# Channel flow instabilities of complex fluids

by

Hugo A. Castillo Sánchez MSc

*A thesis submitted in conformity with the requirements*

*for the degree of Doctor of Philosophy*

Department of Mathematics

Faculty of Mathematical & Physical Sciences

University College London

December, 2019

# Disclaimer

I, Hugo A. Castillo Sánchez, confirm that the work presented in this thesis is my own. Where information has been derived from other sources, I confirm that this has been indicated in the thesis.

*Signature* __________________________

*Date* __________________________

# Abstract

Complex fluids are present in our daily life: food, paints, plastics, pharmaceuticals, to name just a few, and thus, their study is of great interest to the industry. In many industrial processes, raw materials are transformed into finished products with specific rheological properties. Such a transformation may consist of many intermediate physical processes (extruding, melting, coating, pumping, among others). However, the complex nature of these materials might be problematic in many of these operations. More specifically, when complex fluids are under flow conditions, an unexpected behaviour may be observed: for instance, the presence of non-ideal velocity fields during steady flow. In fluid mechanics, we refer to these undesired behaviours as *flow instabilities*; they can occur in a variety of commercially important processing operations.

This thesis is a study of instabilities in inertialess viscoelastic flows, also known as *purely elastic instabilities.* The main research content of the thesis is split into three main chapters. In the first, we extend previous theoretical work on a newly discovered elastic instability in planar channel flow of highly shear-thinning viscoelastic fluids. Our motivation was to answer whether the mechanism of such instability observed is truly elastic or principally as a result of strong shear-thinning; we found that both components were critical for the existence of the instability. In the second chapter, we carried out a similar analysis to study instabilities in channel flow of fluids that exhibit much more complex rheological behaviour: thixotropic-viscoelasto-plasticity (TVEP). For the most unstable flows, we showed that the growth rate of instability scales with the rate of recovery of thixotropic structure. Finally, in a third chapter, we extended the scope of the fluids we could consider by including the shear-banding phenomenon in the flows of TVEP fluids; this allowed us to identify distinct bulk and interfacial modes of instability.

*This thesis was completed under the supervision of* ***Professor Helen J. Wilson****.*

# Impact statement

Many of the complex fluids that are of industrial interest (including polymer solutions or surfactant solutions) exhibit viscoelastic behaviour, i.e. they show both viscous and elastic responses to forces. These viscoelastic fluids generate stresses that are absent in their Newtonian counterpart, which result in interesting but complex flow phenomena.

When viscoelastic fluids are subjected to some given flow conditions, their elastic nature can lead to undesired and secondary flows, commonly known purely elastic instabilities. This kind of instabilities have been investigated in different flow configurations, but in this thesis, we investigate pressure-driven channel flows (also known as planar Poiseuille flow). Due to the different molecular properties that can affect the non-Newtonian character of a fluid (such as molecular weight, concentration, level of entanglement, branching, among others), different effects on the flow stability have been reported both numerically and theoretically. Although some of these instabilities are now well understood, there are still plenty of unanswered questions and open problems.

The theoretical content of this work is expected to contribute to understand the mechanism behind a recently observed instability in channel flows of viscoelastic fluids that exhibit shear-thinning behaviour. We have also extended theoretical research in the field of flow instabilities by carrying out stability analysis of fluids with highly complex behaviour: thixotropic-viscoelasto-plastic (TVEP) fluids. We have also extended the scope of fluids we could consider by incorporating shear-banding phenomenon in TVEP fluids, which are some of the rheological phenomena observed in fluids that have become the centre of attention of many rheologists in recent years: wormlike micellar solutions. Moreover, by using more realistic models in our analysis, we hope to complement and contribute with information that previous theoretical works were unable to report.

We have also provided with analytical and semi-analytical solutions derived from these realistic constitutive models that can calculate the velocity and viscosity profiles in planar Poiseuille steady flow, which are in terms of experimentally-measurable quantities. In addition, groups of dimensionless numbers have been obtained and are of use to facilitate the analysis of stability results. More importantly, we have identified key flow conditions and fluid parameter values for which highly unstable flows are observed. Therefore, this information is expected to be valuable for experimental rheologists (who should avoid flow instabilities to prevent the incorrect measurement of rheological properties) and for engineers (in order to predict difficulties in industrial fluid processing operations).

# Acknowledgments

This thesis marks the end of an amazing PhD journey that started back in October 2015. This four-years adventure has been one of the most rewarding and enjoyable experiences in my life, both personally and academically speaking. And of course, I am greatly indebted to all the people that have helped me during my years as a PhD student.

Firstly, none of this would have been possible without the scholarship awarded by the National Council of Science and Technology (CONACyT) of Mexico. Thanks for providing thousands of students like me the opportunity to accomplish our postgraduate studies in prestigious universities around the world.

Secondly, to Prof. Helen J. Wilson. I simply could not have asked for a better supervisor. My PhD experience was more enjoyable under your supervision. Your kind and attentive guidance throughout all these years are truly unique and inspiring qualities that I humbly aspire to emulate. There are not enough words that can describe how grateful I am for your never-ending patience, your encouragement and for your continuous support in all aspects of my PhD life. Thank you for providing me with the motivation and the elements to become a rheologist/non-Newtonian fluid dynamicist. It has been the greatest pleasure to be your student.

A very special gratitude to University College London (UCL) and all the friendly members of the staff of the Department of Mathematics for providing me with all the facilities to carry out my research. I am also thankful to them for providing me with funding to attend international conferences to present my research results. It is also worth mention all the efforts carried out by the department to make international students academic life easier, including mine. Without a doubt, I can easily say that this institution is one of the best places for an international student to do postgraduate studies. I am deeply honoured to have been part of one of the best universities in the world.

I would also like to express my gratitude to the Mexico's Ministry of Education (SEP) (for the complementary scholarship for doctoral studies granted in 2015 and 2016) and to all the donors/sponsors of the postgraduate scholarships for MPhil/PhD research in Applied Mathematics at UCL that I have been awarded during these years.

My PhD was even more pleasant thanks to the people I met during these wonderful years. To all my friends, colleagues, former and current members from the room 713 and the KLB office: thank you for your friendship, for always being kind to me, for the drinks we shared, the good chats and for letting me share you a piece of knowledge during my (very) long seminars. Special mention to all the members of the SuperKLB group: thank you guys for all the experiences and moments of big excitement we have shared, for the great conversations and the evening pints, for your pieces of advice and the never-ending laughs during lunch breaks. I consider myself lucky to have such great friends.

I am also grateful to the Chalkdust magazine, which helped me to develop and improve some of my technical skills that have been useful in the writing up of this thesis. I am also thankful to them for providing me with space to share my scientific articles. It has been a pleasure to be part of a team full of clever, kind and amazing people.

I am also deeply grateful to my home university, the National Autonomous University of Mexico (UNAM) and to my former colleagues at the Institute for Materials Research (IIM-UNAM) (with special mention to Prof. Octavio Manero) for providing me with the basic knowledge and for giving me the opportunity to begin to construct my career as a researcher. Some of the skills and knowledge gained in these institutions have been of great use in some chapters of the present work. I am and will always be proud to say that I was a student at UNAM.

My Mexican friends from my high school and the Faculty of Chemistry also deserve a special mention here. Wherever you are: thank you for all these years of friendship. Although our lives have changed over the years, I am glad that our friendship is still the same as before. I am grateful for your online support, for always being attentive to my life in London and for welcoming me back when I was in Mexico.

Lastly, I would like to offer my heartfelt thanks to the most important persons in my life: my family. A special dedication to the memory of Raúl Sánchez Aguilar, loved by your daughters, your wife and your grandchildren. You will always be remembered. I would like to express my warmest gratitude to my dear and beloved grandmother Virginia: thank you for your love, your protection, your encouragement and your life lessons. I miss you Vicky!

I will be forever thankful to my aunt Hilda Sánchez and to my uncle Alvaro Orsatti for the unconditional support that you have provided me in all aspects of my life. I could not have achieved any of this without you. I am also extremely grateful for taking care of my siblings and me since the moment we were born and for always being there for us in rather difficult times. Special gratitude to someone that I highly appreciate, my cousin Bruno: thank you for all the memories and moments that we have shared together since we were children, and for making my first months in London more exciting. I will also like to extend my gratitude to my dear brother-in-law, Rene, for being phenomenally wonderful to me since the moment we met.

I would like to express the deepest appreciation to my beloved sisters, Grisel and

Fabiola. Hermanas, I am extremely grateful for always being there for me, for your continuous support and for all the sacrifices that you have made in order to help me fulfill all my dreams. I will be forever indebted to you for all the incredible things you have done for the family and for helping us get through the hardest times. Needless to say, I miss you and I truly admire the two of you.

I also want to thank my dear and funny (but sometimes annoying) brothers. Axel, one the things I probably miss more is spending time together (and of course, teasing each other). I am glad that you have had the opportunity to come and visit us. Thank you for those experiences and for taking care of mom, our sisters and our boys while we were living abroad. You know you can always count on me. Juan, our relationship has been strengthened since we have been living in Europe for years. I want to thank you for being a great elder brother: for all your useful advice, for your guidance, for helping me taking hard decisions, for your encouragement and for all the moments we have shared together. You have been a role model for all of us.

Finally, I want to thank the most important person in my life, my mother, Laura. Mom, everything I have achieved in this life is because of you. I am grateful that you have always been there with me in my happiest and hardest times and for supporting every single decision I have taken in my life. I will be forever thankful for your guidance and for all the sacrifices that you have made to see us succeed. Most importantly, thank you for showing us that by staying strong together and with the love for your children, the purest love of all, the hardest life challenges can be overcome. You are our source of inspiration. I dedicate this milestone to you. I love you, Mom!

Hugo A. Castillo Sánchez, *University College London*, December 2019

*To my beloved family.*

*“Everything flows.”*

—Heraclitus (c. 500 B. C.)

*“We see how quickly through the colander, the wines will flow; how, on the other hand, the sluggish olive-oil delays; no doubt, because ’tis wrought of elements more large, or else more crook’d and intertangled.”*

—Lucretius (96–55 B. C.)

*“The mountains flowed before the Lord.”*

—Prophetess Deborah, Judges 5:5

*“Deborah knew two things. First, that the mountains flow, as everything flows. But, secondly, that they flowed before the Lord, and not before man, for the simple reason that man in his short lifetime cannot see them flowing, while the time of observation of God is infinite.”*

—Markus Reiner, 1964

*“The time has come,” the penguin said, “to speak of many things: of flowing macromolecules, and little beads and springs that join together into ‘chains’, or even ‘stars’ or ‘rings’.”*

—R. Byron Bird (with the assistance of Lewis Carroll), 1987

# Contents

# List of Figures

# Chapter 1

# Introduction

# 1.1 Outline

Complex fluids are present in our daily life: food, personal care products, paints, ink, plastics, oils, cement, adhesives, gels, fluids of biological interest such as blood, pharmaceuticals, just to name a few [66], and thus, their characterisation is particularly important for the industry to estimate the ideal conditions to pump, mix and store them in industrial operations. The complex fluid-characterisation relies on *rheology*, known as the study of the deformation and flow of matter.

One of the objectives of the science of rheology is developing mathematical models (commonly known as *constitutive equations*) to describe the relationships between forces and deformation of complex fluids, which differ from simpler fluids like water and air (known as *Newtonian fluids*) due to the presence of one or more molecular microstructures or particles of other substances dispersed within them. These microstructures can also be a function of physico-chemical bonds and inter/intra molecular interactions, which can drastically affect the flow behaviour of the fluid.

Some of the daily-life products mentioned before and all the fluids that will be studied here exhibit both *viscous* and *elastic*-like characteristics when undergoing deformation, and are known as *viscoelastic* materials. Surprisingly, these complex fluids can also exhibit more than one *non-Newtonian* behaviour simultaneously (see sections 1.4 and 1.7).

As we will see throughout this work, the flow of these fluids can sometimes be problematic; given some flow conditions, their complex behaviour (more specifically, their *elastic* nature) can lead to secondary and undesired flows, known as *flow instabilities*. The main aim of this thesis is to study these instabilities and to predict whether they will become more dangerous or vanish as the nature of the complex fluid varies.

It is extremely important for engineers, scientists and mathematicians to know and understand rheology in order to explain the fluid behaviour they encounter in their work or experiments. In the following sections, we will provide a brief introduction to some of these rheological concepts that will be useful to characterise complex fluids (sections 1.2, 1.3, 1.4 and 1.5). Then we will move on to explore the huge variety of constitutive equations that can mathematically describe their flow behaviour (sections 1.6 and 1.7). Finally, we will review some of the literature (both theoretical and experimental) about flow instabilities in viscoelastic materials and other complex fluids (section 1.8).

## 1.2 General rheological concepts

### 1.2.1 Newtonian fluid

We start by asking the simplest question in rheology: what makes a fluid non-Newtonian? To answer it, we obviously need to understand what is a Newtonian fluid. In a few words, a Newtonian fluid obeys the *Newton's law of viscosity.* Newton carried out experiments by confining a fluid between two plates and measuring the force required to move the upper plate at different speeds. He discovered that the *stress* (force applied per unit of area) is proportional to the *shear rate* (defined as the gradient of velocity). Most importantly, he found that there is a linear relationship between those quantities, and their constant of proportionality is defined as the *viscosity of the fluid.*

### 1.2.2 Simple shear flow

Newton's work provided us with the very basic grounds of fluid mechanics, but also has provided us with one of the main concepts of the present work: the definition of *non-Newtonian* fluid, which are those fluids that do not obey Newton's law of viscosity. One of the most common experiments that any rheologist has to carry out to determine whether a fluid is Newtonian or not, is the *simple shear flow*, see 1.1.

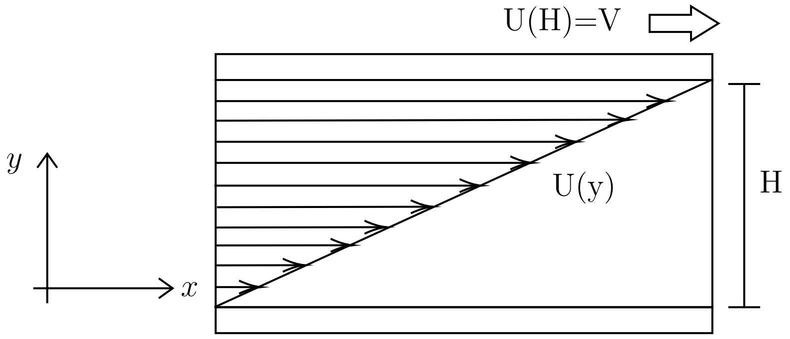

Figure 1.1: Schematic of two-dimensional simple shear flow.

The material is *sandwiched* between two parallel plates, and the top plate will be moved at a constant velocity $V$ in unchanging $x$-direction. In this flow, the fluid moves in parallel layers and they do not mix. In addition, the local velocity $U(y)$ only varies in the vertical direction. The vector velocity profile for steady simple shear flow in Cartesian coordinates is:

$$\underline{u} = (V/H\, y, 0, 0), \tag{1.1}$$

where the velocity in $x$-direction, $U(y)$ is simply the product between the coordinate $y$ and the ratio between the velocity at the top plate $V$ and the gap between plates $H$. In rheology, this quantity $V/H$ is named as the *shear rate*, $\dot{\gamma}$, whose mathematical definition is:

$$\dot{\gamma} = \sqrt{2\underline{\underline{D}} : \underline{\underline{D}}} \qquad \underline{\underline{D}} = \frac{1}{2}\left(\underline{\nabla}\,\underline{u} + \underline{\nabla}\,\underline{u}^{\top}\right) \qquad D_{ij} = \frac{1}{2}\left[\frac{\partial u_i}{\partial x_j} + \frac{\partial u_j}{\partial x_i}\right]. \tag{1.2}$$

The tensor $\underline{\underline{D}}$ is known as the *deformation tensor*. For simple shear flow, using equation (1.1), the shear rate and the deformation tensor are simply reduced to:

$$\underline{\underline{D}} = \frac{1}{2}\begin{pmatrix} 0 & \dot{\gamma} \\ \dot{\gamma} & 0 \end{pmatrix} \qquad \dot{\gamma} = \frac{V}{H}, \tag{1.3}$$

where we can see that the shear rate is independent of the position $x_i$.

The stress tensor is represented with the notation $\sigma_{ij}$, where the index $j$ denotes the direction in which the force is applied on a surface perpendicular to the $i$ direction. As stated before, Newton found a linear relationship between the stress and shear rate, which adopts the following tensor form for an incompressible fluid:

$$\underline{\underline{\sigma}} = 2\,\mu\,\underline{\underline{D}}, \tag{1.4}$$

which in simple shear flow, is reduced to:

$$\underline{\underline{\sigma}} = \begin{pmatrix} \sigma_{11} & \sigma_{12} \\ \sigma_{21} & \sigma_{22} \end{pmatrix} = \begin{pmatrix} 0 & \mu\,\dot{\gamma} \\ \mu\,\dot{\gamma} & 0 \end{pmatrix} \qquad \mu = \frac{\sigma_{12}}{\dot{\gamma}} \tag{1.5}$$

where $\mu$ is the Newtonian viscosity and is independent of the level of deformation but is a function of the temperature, $\mu = \mu(T)$ [15]. Another characteristic of Newtonian fluids is that the elements of the diagonal of the stress tensor have a zero value $\sigma_{11} = \sigma_{22} = \sigma_{33} = 0$, which will not be the case for elastic liquids, as we will discuss later.

## 1.3 Generalised Newtonian fluids: non-Newtonian fluids

Unlike Newtonian fluids, the viscosity of a *non-Newtonian* fluid $\eta$, is allowed to be dependent on the *invariants of the deformation tensor* and on the temperature, $\eta = \eta\,(I_D, II_D, III_D, T)$. Here $I_D$, known as the *first invariant*, is the trace of the deformation tensor $I_D = \mathrm{tr}\,\underline{\underline{D}} = D_{11} + D_{22} + D_{33}$, meanwhile the second invariant is the double dot product of the deformation tensor $II_D = 2 D_{ij} D_{ij}$. Lastly, the third invariant is simply the determinant, $III_D = \det D_{ij}$.

Notice, however, that the first invariant $I_D$ is connected with compressibility through the relation $\mathrm{tr}D_{ij} = \underline{\nabla} \cdot \underline{u}$, thus it will be equal to zero for the incompressible case and $III_D$, which tracks the volume changes in deformations is much more relevant for extensional flows. Here we are only interested in studying incompressible fluids, and in this work, we will only be working with isothermal shear flows. Thus, the non-Newtonian viscosity will only be a function of the second invariant, $\eta = \eta\,(II_D)$ (it can also depend on molecular structural changes, but we will discuss this in section 1.7.1).

Some of the constitutive equations that will be used here are in terms of the *total stress tensor*, $\tau$, defined as the sum of the hydrodynamic contributions and the internal forces that particles of a continuous fluid exert on each other:

$$\underline{\underline{\tau}} = -P\,\underline{\underline{I}} + \underline{\underline{\sigma}}\,(\underline{\underline{D}}), \tag{1.6}$$

where $P$ is the pressure, $\underline{\underline{I}}$ is the *identity* tensor and $\underline{\underline{\sigma}}$ is the stress tensor previously defined, also named as the *extra stress tensor*, *deviatoric tensor* or, if working with polymers, the *polymer* stress tensor.

### 1.3.1 Normal stress differences

In steady simple shear flow, the fluid is moving with velocity $\underline{u}$ from equation (1.1) and the total stress tensor $\tau_{ij}$ of any incompressible fluid will have, in general, four non-zero components:

$$\underline{\underline{\tau}} = \begin{pmatrix} \tau_{22} + N_1 & \sigma_{12} & 0 \\ \sigma_{12} & \tau_{22} & 0 \\ 0 & 0 & \tau_{22} - N_2 \end{pmatrix}. \tag{1.7}$$

The equation above is a more general form of the stress tensor shown in (1.5) and is usually the stress field that a complex fluid will adopt. Moreover, notice that in equation (1.7) we have introduced two more quantities: $N_1$ and $N_2$, commonly named as the *first normal stress* and the *second normal stress* differences, respectively, formally defined as:

$$N_1 = \tau_{11} - \tau_{22} = \Psi_1 \, \dot{\gamma}^2 \qquad N_2 = \tau_{22} - \tau_{33} = \Psi_2 \, \dot{\gamma}^2, \tag{1.8}$$

where $\Psi_1$ and $\Psi_2$ are their respective *coefficients*, which can also be functions of the shear rate. Most of the exciting and surprising phenomena observed in complex fluids, particularly of viscoelastic materials, can be understood and explained by studying the normal stress differences (for some examples, see [18]). We will see in the next chapters that shear flows give rise not only to components outside of the diagonal of the stress tensor, (like the Newtonian case, equation (1.5)), but also to the diagonal elements, $\tau_{ii}$. The rheologists consider normal stress differences rather than pure normal stresses to avoid the indeterminacy of pressure $P$ for incompressible fluids [128].

But what exactly gives rise to normal stress components? Let's take, for instance, a polymer or polymer-*like* fluid flowing under steady simple shear conditions. The polymer chains, which are usually modelled as linear chains that can both store energy like an elastic solid does and also dissipate energy like a viscous fluid, will be stretched under the action of the local shear and will tend on average to align in the direction of the flow ($x$-direction), but at the same time, the *entropic* forces begin to act to return the molecular chain to an undisturbed conformation, which will lead to an extra tension in $x$-direction.

The first normal stress difference tracks the variation in normal stresses between the direction of the flow ($x$-direction) and the direction of flow variation ($y$-direction), meanwhile the second normal stress difference tracks the normal stresses in the $y$-

direction and the neutral direction, $z$.

There are multiple ways in which the normal stress differences can be measured experimentally. In two-dimensional linear shear flows, the only significant component of the normal stresses is $\tau_{11}$. Measuring the normal stress differences is a challenge, but rheologists have developed some experimental techniques that take the advantage of the coupling between the normal stresses and the forces on the boundaries that exist in some curvilinear geometries. For this reason, the most common device used for measuring the material properties of a fluid is the *cone-and-plate* rheometer (described in section 1.8.1), in which a cone is rotated above a horizontal plate with a sample of the fluid filling the gap between them. Using a momentum balance, rheologist have derived a simple equation that measures the first normal stress difference $N_1$ by simply measuring the total force exerted on the plate when the cone is rotating [160].

It has been reported experimentally that $\Psi_1$ is usually positive for viscoelastic fluids, meanwhile $\Psi_2$ is even much more complicated to measure experimentally, but it has been reported that for most polymers, $\Psi_2$ is negative and much smaller in size than $\Psi_1$ [13].

### 1.3.2 Weissenberg number

In the steady flows of complex fluids that will be studied here, there will be present both *elastic* and *viscous* forces, so a dimensionless number will be defined to compare the two effects. This number is known as the *Weissenberg number*, $W$ [172], which is simply the ratio of the elastic forces $N_1$ and viscous forces $\sigma_{12} = \eta\dot{\gamma}$:

$$W = \frac{N_1}{\sigma_{12}} = \frac{\Psi_1 \dot{\gamma}^2}{\eta\,\dot{\gamma}} = \frac{\Psi_1 \dot{\gamma}}{\eta}. \tag{1.9}$$

The Weissenberg number in non-Newtonian fluid mechanics is the analogous to the *Reynolds number Re* in fluid mechanics and it will play a key role in the development of this thesis.

## 1.4 Simple non-Newtonian behaviour

### 1.4.1 Shear-thinning

Shear-thinning behaviour is the most common rheological phenomenon that rheologists encounter when studying the flow of complex fluids, and is the decrease in viscosity when they are driven to flow at high shear rates. The tastiest example of this kind of fluids is chocolate [168]. Figure 1.2a) illustrates the general behaviour of an inelastic shear-thinning fluid in simple shear flow. At low shear rates, there exists a region where the fluid behaves like a Newtonian fluid, which we call the *high viscosity plateau*, characterised by a viscosity value $\eta_0$. With an increase in shear rate, we can observe a decrease in $\eta$, until it reaches a second *plateau* with viscosity $\eta_\infty$ at high shear rates.

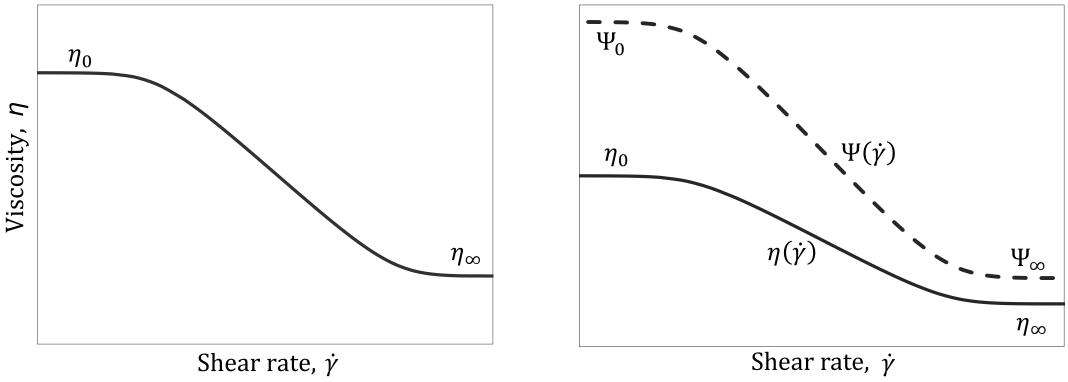

(a) Inelastic shear-thinning behaviour

(b) Elastic shear-thinning behaviour

Figure 1.2: Viscosity and first normal stress difference coefficient profiles for inelastic and elastic shear-thinning materials.

This drop in viscosity is usually due to changes in the internal micro-structure of the fluid as a result of the applied shear, for instance, a breakdown of complex molecular arrangements or physico-chemical bonds or the disentanglement of branched structures, among others.

Although shear-thinning is the most common non-Newtonian behaviour, it is usually not the only one that complex fluids exhibit. Most polymer solutions [116] and polymer melts [101] exhibit elasticity along with some degree of shear-thinning. Figure 1.2b) illustrates the typical behaviour of an elastic-shear thinning material, where we can see that the first normal stress difference coefficient has a non-zero value (unlike the inelastic shear-thinning case shown in 1.2a) and is dependent on the shear rate. Additionally, it follows a similar behaviour to the viscosity curve: it shows two plateau regions at low and high shear rates. In the next sections, we will study this behaviour in more depth and we will see that $\Psi_1$ depends on the physical properties of the material, which can also be shear-dependent. There can also exist some fluids that show an almost constant viscosity, but surprisingly, exhibit a non-zero normal stress difference (*Boger* fluids [17]).

More interestingly, we will also see that shear-thinning behaviour is a particular case of a much more complex non-Newtonian behaviour, where the viscosity is not only dependent on the shear rate but on time (section 1.7.1).

### 1.4.2 Shear-thickening

The complete opposite of shear-thinning behaviour is called *shear-thickening*, where there is an increasing resistance to shear as $\dot{\gamma}$ increases, as illustrated in figure 1.3. Some shear-thickening fluids can also exhibit two plateaus at low and high shear-rates, but with the difference that $\eta_\infty > \eta_0$.

The most popular fluid that exhibits this non-Newtonian behaviour is a mixture of cornstarch and water (named *Oobleck*), but it can also be seen in other suspensions and some pastes.The mechanism that leads to this bizarre behaviour is still not well understood, but recent theoretical research has demonstrated that the phenomenon can be caused by friction (or *something* that resembles friction) between particles within the fluid [157,176,183].

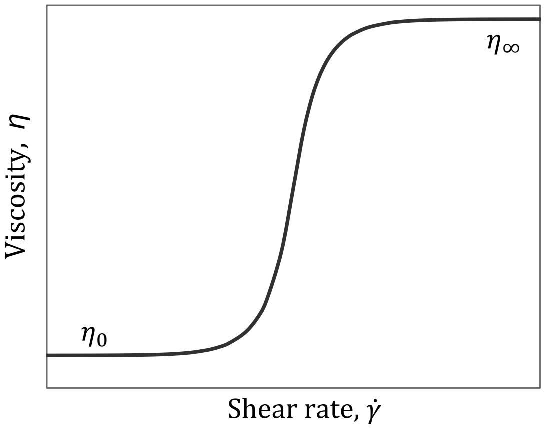

Figure 1.3: Shear-thickening behaviour.

### 1.4.3 Yield stress fluids

Another typical non-Newtonian behaviour also observed in many daily-life products (such as ketchup, mayonnaise, gels, etc) is called *viscoplasticity.* A feature of this type of fluid is that they will be able to flow only if the applied stress is above a *threshold* stress, commonly known as *yield stress.* Below this point, the material will behave as a solid (or a fluid with extremely high viscosity), absorbing the stress-energy without flowing [41]. When processing these fluids, the existence of the yield stress means that large stresses are required to keep the fluid flowing. Figure 1.4 illustrates the typical behaviour of yield stress fluids.

As can be seen, for stresses smaller than the yield stress $\sigma_y$, the material's apparent viscosity will tend to infinity, and therefore, it will not flow. But above $\sigma_y$, the material will flow like a Newtonian liquid (with viscosity $\mu_0$). This kind of material is known as a *Bingham* fluid. However, as we will see, a great majority of yield stress fluids are not Bingham fluids, i.e. they will not flow like a Newtonian fluid above the yielding point but instead, their viscosity will exhibit shear-thinning due to an

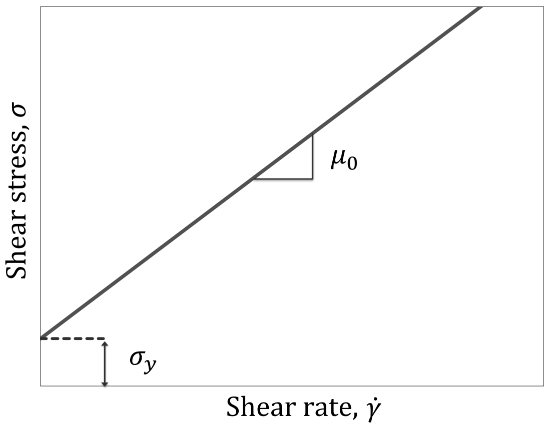

Figure 1.4: Yield stress fluid behaviour.

internal structure breakdown.

Although the concept of yield stress has been widely used among rheologists, it has also been quite a controversial one. For instance, Barnes [6] argued that if the materials flow at high shear rates, they also must flow at low ones, and some experimental information helped to prove his point: with the arrival of modern rheometers that were able to detect more accurately the response of materials at very low shear rates, it was proved that materials that were previously believed to exhibit a yield stress, do not actually, as it was shown that they deform even at low $\dot{\gamma}$.

All of this led to the definition of another concept that we will be using in some chapters of this work: the threshold stress (that was believed to be a yield stress) is named *apparent yield stress*. Above this stress, there is a major change in the material behaviour (such as shear-thinning), but below the threshold, the material will flow with a very high but finite viscosity [49].

Despite this, the debate is still going but the reality is that it would be almost *impossible* to determine whether a fluid poses a *true yield stress* since it would require an infinite observation time to show that indeed the shear rate of the material (at given stress) is zero [55]. Thus, for practical purposes, we will refer here to fluids with a *true yield stress* to those whose viscosity tends to infinity when the shear rate tends to zero.

With the exception of shear-thickening, we will study fluids that can display simultaneously any of the simple non-Newtonian behaviours we have described, which will be discussed in section 1.7, along with the mathematical models that are used to predict their behaviour.

## 1.5 Material functions

In order to solve an isothermal-fluid mechanics problem of any incompressible fluid, we need to solve the following coupled system of equations, normally named as the *governing equations*:

$$\underline{\nabla} \cdot \underline{u} = 0 \tag{1.10}$$

$$\rho\Big(\frac{\partial \underline{u}}{\partial t} + \underline{u} \cdot \underline{\nabla u}\Big) = -P\,\underline{\underline{I}} + \underline{\nabla} \cdot \underline{\underline{\sigma}} + \rho\,\underline{g} \tag{1.11}$$

$$\underline{\underline{\sigma}} = \underline{\underline{\sigma}}\,(\underline{\underline{D}}), \tag{1.12}$$

where $\underline{u}$ is the fluid velocity, $P$ is the pressure, $\rho$ is the fluid density, $\underline{g}$ is the gravitational field and equation (1.10) and (1.11) are the continuity equation and the momentum conservation (or Cauchy or Generalised Navier-Stokes equations) equations, respectively. For equation (1.11), notice that there is a *key* piece of information missing, which is the stress tensor. For Newtonian fluids, the stress adopts the form of equation (1.4). For non-Newtonian fluids, on the other hand, the stress tensor (1.12) is a much more complicated function of material properties and of the level of deformation of the fluid. Thus, rheologists have to carry out a series of experiments to find equations that can accurately describe the flow behaviour of these fluids, which are named *constitutive equations*.

### 1.5.1 Steady shear flow

One of these experiments was already described in section 1.2.2: the steady simple shear flow (also known as *Couette flow*), which provides us with three useful pieces of information that can be measured:

$$\eta(\dot{\gamma}) = \frac{\sigma_{12}}{\dot{\gamma}} \qquad \Psi_1(\dot{\gamma}) = \frac{N_1}{\dot{\gamma}^2} \qquad \Psi_2(\dot{\gamma}) = \frac{N_2}{\dot{\gamma}^2}. \tag{1.13}$$

These deformation-rate-dependent functions are extremely useful to characterise the rheological behaviour of complex fluids and are called *material functions*; the viscosity and the first and second normal stress difference coefficients are said to be material functions of non-Newtonian fluids for steady shear flow.

Notice that we specified that the quantities (1.13) are only material functions in simple shear flow, which means that these functions have to be defined in terms of three important elements: 1) the type of flow, that can be either shear or extensional flow (these flows make the fluid experience volumetric changes, which is something we will not study here) or a combination of the two, 2) the time-dependence on the level of deformation and the imposed dynamic conditions during the flow and 3) the material functions will always be based on the measurable quantities, i.e. $\sigma_{12}$, $N_1$ and $N_2$.

### 1.5.2 Unsteady shear flows

So far we have only described steady flows. Unfortunately, most of the material properties of complex fluids exhibit time-dependence, and therefore, steady flows are not the only rheological tests needed to characterise them. Here, we will present a brief summary of some of the most important unsteady flows (mainly, the ones that will be useful for us) and their respective material functions [108, 128].

### 1.5.2.1 Shear-stress growth

The viscosity of a fluid is usually determined using simple steady shear flow. However, before reaching the steady state, there is a start-up stage where the stress grows from zero (this is when the fluid is at rest) to its steady value. This transition stage is obviously time-dependent, and the unsteady shear-rate function $\dot{\gamma}(t)$ used in this experiment is defined as follows:

$$\dot{\gamma}(t) = \begin{cases} 0 & t < 0 \\ \\ \dot{\gamma}_0 & t \geq 0 \end{cases} \tag{1.14}$$

which tell us that the fluid is initially at rest, but then at $t \geq 0$, a shear rate is imposed on the material, see figure 1.5a). The rheologists then measure the three time-dependent quantities, $\sigma_{12}(t, \dot{\gamma}_0)$ (see figure 1.5b), $N_1(t, \dot{\gamma}_0)$ and $N_2(t, \dot{\gamma}_0)$ and thus, the three new material functions can be defined as:

$$\eta^+(t, \dot{\gamma}) = \frac{\sigma_{12}}{\dot{\gamma}_0} \qquad \Psi_1^+(t, \dot{\gamma}) = \frac{\tau_{11} - \tau_{22}}{\dot{\gamma}_0^2} \qquad \Psi_2^+(t, \dot{\gamma}) = \frac{\tau_{22} - \tau_{33}}{\dot{\gamma}_0^2}. \tag{1.15}$$

When the flow reaches steady-state, the material functions (1.17) will reach their steady values, which are the material functions in simple shear flow (1.13).

In much more complex materials, the behaviour in this unsteady flow might be different: the stress increases until it reaches a maximum value at a given time and then it will decrease towards a steady-state value. This phenomenon is known as *stress overshoot* and it has been extensively studied by rheologists as it is one of the most important non-linear rheological phenomena exhibited by some polymeric liquids [86].

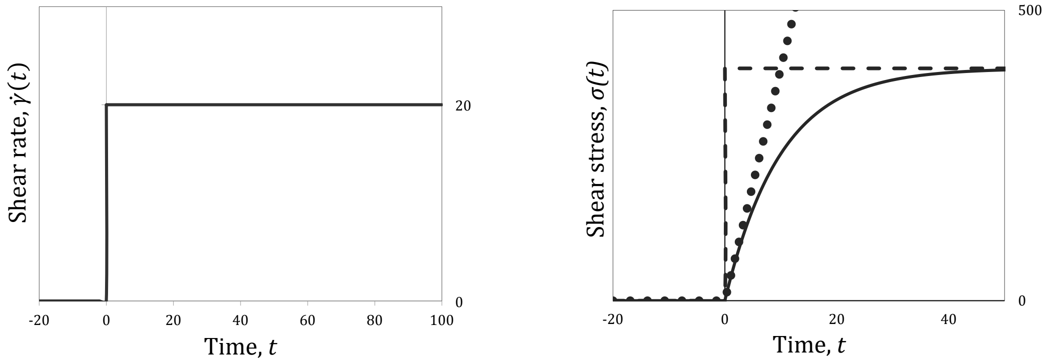

(a) $\dot{\gamma}(t)$ vs $t$

(b) $\sigma(t)$ vs $t$

Figure 1.5: Shear-stress growth experiment. For figure (b), we show the responses of an elastic solid that follows Hooke's law (dotted line), a viscous Newtonian liquid (dashed line) and a material that exhibit both behaviours (solid line), for which it will take some time to fully adjust to the flow happening to it.

### 1.5.2.2 Stress relaxation

Another highly important experiment is the *shear-stress decay* or *stress relaxation*, widely used in rheology to characterise fluids that exhibit some degree of elasticity. The experiment consists in reaching a steady state value (achieved in the shear-stress growth experiment 1.5.2.1), followed by a *cessation* of steady shearing, allowing the stresses to *relax* when the flow is stopped (see figure 1.6a):

$$\dot{\gamma}(t) = \begin{cases} \dot{\gamma}_0 & t < 0 \\ \\ 0 & t \geq 0 \end{cases} \tag{1.16}$$

The rheologists then measure the stresses' decay as a function of time and the material functions for the stress relaxation experiment, known as *stress-decay coefficients*, are defined as:

$$\eta^-(t, \dot{\gamma}) = \frac{\sigma_{12}}{\dot{\gamma}_0} \qquad \Psi_1^-(t, \dot{\gamma}) = \frac{\tau_{11} - \tau_{22}}{\dot{\gamma}_0^2} \qquad \Psi_2^-(t, \dot{\gamma}) = \frac{\tau_{22} - \tau_{33}}{\dot{\gamma}_0^2}. \tag{1.17}$$

In figure 1.6, we illustrate some material responses to the cessation of the steady shearing. As we can see, all Newtonian fluids will relax instantaneously when the

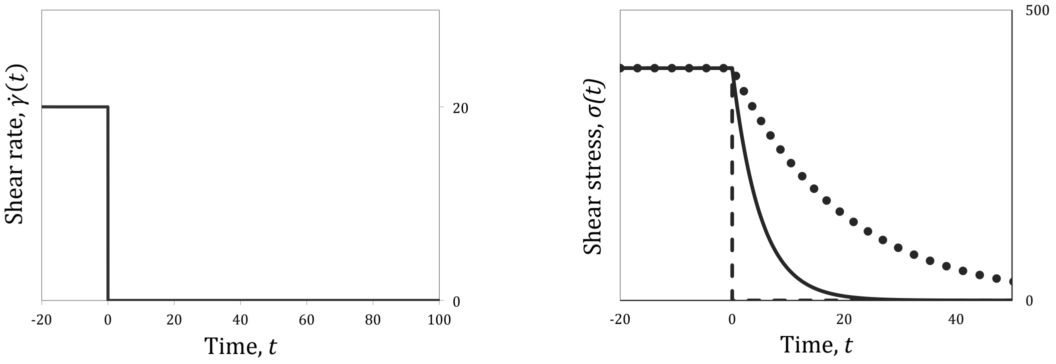

(a) $\dot{\gamma}(t)$ vs $t$

(b) $\sigma(t)$ vs $t$

Figure 1.6: Shear-stress decay experiment. Figure (b) shows the response of a viscous Newtonian liquid (dashed line) and two materials with different relaxation times $\lambda_R$; the material's response with higher $\lambda_R$ is represented with the dotted line.

flow is stopped due to the fact that the stress depends on the rate of deformation. On the other hand, the non-Newtonian fluids will take a *finite* amount of time to decay or *relax* (see figure 1.6b); how quickly or slowly the stress decay will depend on a *characteristic time* of the fluid that is in terms of some material parameters (such as degree of elasticity and viscosity) and is known as the *relaxation time* of the fluid, $\lambda_R$.

In addition, there is a *dimensionless* number widely used to characterise the importance of $\lambda_R$ in the analysis of unsteady flows called the *Deborah number De* [150], which is simply the ratio between the material time-scale $\lambda_R$ and a time-scale of the process or a fluid residence time in a given regime flow $t_{flow}$ [146]:

$$De = \frac{\lambda_R}{t_{flow}}. \tag{1.18}$$

Large values of $De$ mean that the relaxation time will determine the response to a particular deformation. On the other hand, if the time of observation is long or the relaxation of the material is short, then 'fluid-like' behaviour is to be expected when $De \to 0$.

#### 1.5.2.3 Step shear strain

The following rheological test is one of the most interesting experiments and one from which a lot of information can be obtained about the relaxation time of a fluid. It will also help us to define the concept of *memory* of a material. But before that, we need to point out that there are two generic behaviours that we could expect to observe in a material; the first one is a viscous fluid, whose general constitutive equation in shear flows is simply the equation shown in (1.4). On the other hand, there are some materials that follow Hooke's law, whose shear stress depends on the *strain*, $\gamma = \delta x/\delta y$ (unlike Newtonian fluids, which depend on the rate of strain $\dot{\gamma}$) and can be simply calculated as:

$$\sigma_{12} = G\,\gamma, \tag{1.19}$$

where $G$ is the material's resistance to be deformed, known as the *elastic modulus.* For comparison purposes, the material's response will be tested in a *step shear strain*, which consists of placing a sample at rest between parallel plates and then it will be suddenly disturbed by imposing, for a small time $\epsilon$, a constant and large shear rate $\dot{\gamma}_0$. Thus, the shear-rate function of a shear step strain (see figure 1.7a) adopts the form of an *impulse* function:

$$\dot{\gamma}(t) = \lim_{\epsilon \to 0} \begin{cases} 0 & t < 0 \\ \dot{\gamma}_0 & 0 \le t < \epsilon \\ 0 & t \ge \epsilon \end{cases} = \gamma_0 \lim_{\epsilon \to 0} \begin{cases} 0 & t < 0 \\ \epsilon^{-1} & 0 \le t < \epsilon \\ 0 & t \ge \epsilon \end{cases} \tag{1.20}$$

where the limit means that the shearing could occur as quickly as possible. Another condition we specify in the experiment is that after the time $\epsilon$, and although the flow is stopped, $\dot{\gamma}(t > \epsilon) = 0$, the strain will remain constant ($\gamma_0 \approx \dot{\gamma}_0 \epsilon$, see figure 1.7b). Then, the stresses are monitored as functions of time and the material functions of a shear step strain experiment are defined as:

$$G(t,\gamma_0)=\frac{\sigma_{12}}{\gamma_0} \qquad G_{\Psi_1}(t,\gamma_0)=\frac{\tau_{11}-\tau_{22}}{\gamma_0^2} \qquad G_{\Psi_2}(t,\gamma_0)=\frac{\tau_{22}-\tau_{33}}{\gamma_0^2}, \tag{1.21}$$

where $G(t,\gamma_0)$ is the *relaxation modulus* or the unsteady shear modulus. When the steady-state value is reached, the relaxation modulus will only be a function of $\gamma_0$ (or equivalently, of $\dot{\gamma}_0$). This shear-modulus function will be of great use in many of our chapters. The other functions are simply known as the *normal stress step shear relaxation modulus*. Finally, in figure 1.7c) we show some of the material responses to the step strain. The easiest materials to spot are 1) the Newtonian fluid (dashed line), whose stress relaxes instantaneously when the flow is stopped at $t \geq \epsilon$ and 2) the Hooke's elastic solid, whose stress remains constant as the strain after $t \geq \epsilon$ is also constant, i.e. there is no stress relaxation as long as $\gamma \neq 0$. In rheology, elastic solids are said to have *perfect memory*; when the deformation applied to it is released, it will relax back to its original shape, which is the opposite case of a Newtonian fluid, which forgets instantly. For those materials that exhibit both behaviours, we say that they will not remember they shape forever; they exhibit *partial memory*, that is, the stress generated will not relax immediately but will rather decay over time, see, for instance, the thin and thick lines of figure 1.7c). The difference between these two fluids is their respective value of relaxation time $\lambda_R$: for the case with the

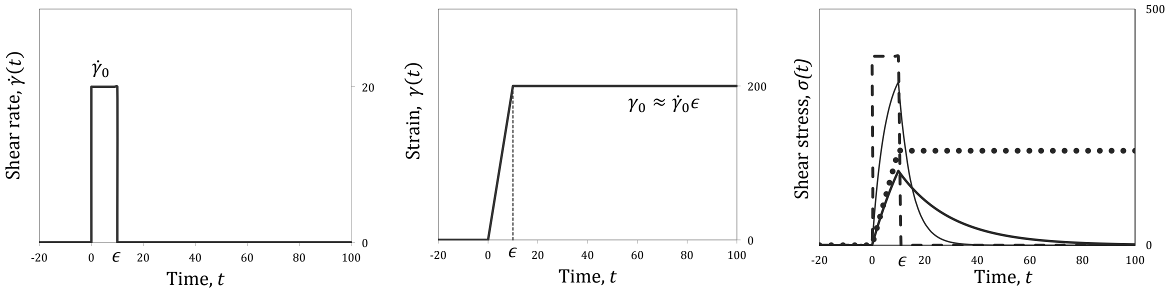

(a) $\dot{\gamma}(t)$ vs $t$ (b) $\gamma(t)$ vs $t$ (c) $\sigma(t)$ vs $t$

Figure 1.7: Shear step strain experiment. Figure (c) shows the response of four materials: an ideal elastic solid (dotted line), a viscous liquid (dashed line), a viscoelastic material (thin line) and an elastoviscous material (thick line).

thin line in figure 1.7c), $\lambda_R$ is very small but greater than zero, which is the case of a viscoelastic fluid. On the other hand, for the case with the thick line, $\lambda_R$ is large but has a finite value, and represents an elastoviscous material.

#### 1.5.2.4 Small-amplitude oscillatory shear (SAOS)

A highly important rheological test widely used by most of rheologists is the *small-amplitude oscillatory shear* (SAOS), where the flow is again shear flow, but the main difference is that the time-dependent shear rate $\dot{\gamma}(t)$ is a periodic function (a cosine function):

$$\dot{\gamma}(t) = \dot{\gamma}_0 \cos(\omega t) \qquad \gamma(t) = \gamma_0 \sin(\omega t), \tag{1.22}$$

where $\dot{\gamma}_0$ is the constant amplitude of the shear rate function and $\omega$ is the frequency. Integrating $\dot{\gamma}(t)$, we obtain the strain function, which is a sine function with amplitude $\gamma_0 = \dot{\gamma}\omega$. The SAOS is usually carried out in cone-and-plate or parallel plate rheometers (described in section 1.8.1).

When a sample of fluid is strained at low amplitudes, the shear stress that is produced is a sine function with the same frequency as the input strain function. However, the shear stress will not be in phase with the strain, which adopts the following form:

$$\sigma_{12} = \sigma_0\, \sin(\omega t + \delta) = \gamma_0\, G' \sin(\omega t) + \gamma_0\, G'' \cos(\omega t), \tag{1.23}$$

where $\delta$ is the phase difference between the strain wave and the stress response. Using trigonometric identities, it is possible to obtain the right-hand side of the equation, where we can see that there is a portion of the stress that is in phase with the imposed strain (proportional to $\sin \omega t$) and another portion that is in phase with the imposed strain rate (proportional to $\cos \omega t$). Recalling that the stress for Newtonian fluids is proportional to the shear rate and the stress for elastic solids is proportional to the strain, we can deduce that the stress response in viscoelastic fluids in SAOS (equation 1.23) flow has both a part that is Newtonian-like and an elastic part, whose contributions can be measured with the following material functions:

$$G'(\omega) = \frac{\sigma_0}{\gamma_0}\cos\delta \qquad G''(\omega) = \frac{\sigma_0}{\gamma_0}\sin\delta, \tag{1.24}$$

where $G'(\omega)$ is the *storage modulus* and $G''(\omega)$ is the *loss modulus*. For a Newtonian fluid in SAOS, $\delta = \pi/2$ and $G'(\omega) = 0$; for an elastic solid, $\delta = 0$ and $G''(\omega) = 0$ and for a viscoelastic fluid, $0 < \delta < \pi/2$ and $G'(\omega)$ and $G''(\omega)$ are non-zero.

There are still plenty of other unsteady shear flows used to characterise viscoelastic materials, such as *shear creep* (where the shear flow is produced by fixing the stress constant instead of the shear rate). In essence, these are the simplest unsteady shear-flows, but rheologists can use a combination of the flows mentioned above to differentiate between different complex rheological behaviours (as we will see in section 1.7.2).

## 1.6 Constitutive equations

Once that experimental information has been collected, it is time to start modelling non-Newtonian flow behaviours. As stated in section 1.5, in order to solve flow problems of complex fluids, we need (along with the continuity and momentum equations) an extra piece of information: this is, tensorial expressions for stress as a function of the rate of deformation (and its history). These are designed to match the observed material behaviour in rheological tests, like the ones described in the previous section. These equations are commonly known as *constitutive equations*.

Due to the huge variety of rheological behaviours observed in complex fluids, there exists a large number of constitutive equations in the literature designed to model different physical materials. Thus, we should expect that there is no *perfect* constitutive equation that is able to describe most of the existent complex non-Newtonian behaviour. However, the validity and usefulness of a constitutive equation will be judged on its ability to predict experimental observation accurately, such as material functions in different unsteady shear flows.

We begin by describing the simplest non-Newtonian constitutive equations, which we categorise as *no-memory* models, which are mostly empirical models and have no formal physical derivation. On the other hand, the constitutive equations with *memory effects* have a more rigorous approach in which the physicochemical structural changes and the interactions between the molecules are taken into account.

## 1.6.1 No-memory constitutive equations

The *no-memory* or the *generalised Newtonian* constitutive equations will adopt the following tensorial form:

$$\underline{\underline{\sigma}} = 2\,\eta(II_D)\,\underline{\underline{D}}, \tag{1.25}$$

where the non-Newtonian viscosity $\eta$ is only a function of the second invariant of the deformation tensor, the generalised shear rate. As we will see, the viscosity function will vary for the different non-Newtonian behaviours.

### 1.6.1.1 Power-law model

The Ostwald-de Waele or *power-law* model is the simplest non-Newtonian model and is able to describe either shear-thinning or shear-thickening behaviour. The power-law viscosity function is proportional to some power of the shear rate and it adopts in shear flows the following form:

$$\eta(\dot{\gamma}) = \mu_0\,\dot{\gamma}^{\,N-1}, \tag{1.26}$$

where $\mu_0$ is the viscosity coefficient and the index $N$ is the power-law coefficient, which have to be determined experimentally; $\mu_0$ is simply the intercept and $N-1$ is the slope of the logarithmic plot of $\eta$ vs $\dot{\gamma}$. If the value of $N > 1$, the fluid exhibits dilatant or shear-thickening behaviour, meanwhile if $N < 1$, the material is called shear-thinning. For the case $N = 1$, the power-law model will simply give Newtonian behaviour, see figure 1.8. Although the power-law model has the ability to reproduce multiple behaviours, it has many limitations: for instance, it cannot predict the low and high viscosity plateaus described in section 1.4. Instead, the power-law model predicts an infinite viscosity in the limit $\dot{\gamma} \to 0$, which is unphysical. This particular limitation of the model will affect us in chapter 3. In addition, it cannot predict stress relaxation phenomenon as it is a purely empirical model and has no molecular derivation. The only advantage is that the model requires just two parameters, $N$ and $\mu_0$ and it can be used to study flow behaviour in simple geometries.

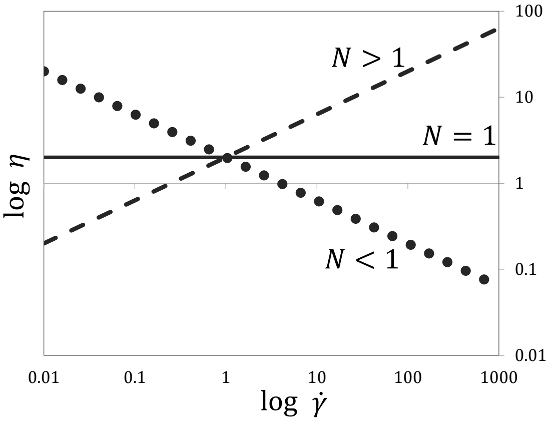

Figure 1.8: Power-law model predictions: Newtonian fluid (solid line), shear-thinning (dotted line) and shear-thickening behaviour (dashed line).

### 1.6.1.2 Carreau-Yasuda model

The *Carreau-Yasuda* modelr [25,185] is able to capture more characteristics of the curves $\eta$ vs $\dot{\gamma}$, such as the low and high-shear rates plateaus and the transition from $\eta_0$ to $\eta_\infty$. The model, which is commonly used to describe shear-thinning behaviour, adopts the following form:

$$\frac{\eta(\dot{\gamma}) - \eta_\infty}{\eta_0 - \eta_\infty} = [1 + (\lambda\dot{\gamma})^a]^{\frac{N-1}{a}} \tag{1.27}$$

where $N$ is, similarly to the power-law model, the coefficient that describes the slope of the decreasing curve $\eta$ vs $\dot{\gamma}$, $a$ is a parameter that affects the shape of the transition between the low and high viscosity plateaus and $\lambda$ is a material's time constant, whose value will determine the value of shear-rate at which the drop in viscosity begins; for instance, if $\dot{\gamma} < \lambda^{-1}$, the fluid will behave approximately as a Newtonian fluid with viscosity $\eta_0$. As can be seen, the Carreau-Yasuda model (1.27) is in some way an extension of the power-law model (1.26) and although it can fit nicely a huge majority of $\eta$ vs $\dot{\gamma}$ curves and it does not present any singularities, there is a disadvantage: the model is governed by five parameters that have to be determined experimentally. In addition, similarly to the power-law model, there is no real molecular insight into the material behaviour (with the exception of $\lambda$, which will be explained soon).

In the present work, we will be using a *time-dependent Carreau-Yasuda-like* model, so it is worth explaining the basics behind this model.

#### 1.6.1.3 Bingham model

The *Bingham* model is the simplest constitutive equation used to describe the flow behaviour of fluids that exhibit yield stress (see section 1.4.3):

$$\eta(\dot{\gamma}) = \begin{cases} \infty & \sigma \leq \sigma_y \\ \mu_0 + \dfrac{\sigma_y}{\dot{\gamma}} & \sigma > \sigma_y \end{cases} \tag{1.28}$$

where $\sigma_y$ is the (true) yield stress. Equation (1.29) is a two-parameter model and it basically predicts that there is no flow $\dot{\gamma} = 0$ if the applied stress is lower than the yield stress: this is due to the solid-behaviour of the material in this region. On the other hand, the material will flow as a Newtonian fluid if $\sigma > \sigma_y$.

#### 1.6.1.4 The Herschel-Bulkley model

There exist materials that behave as solid below a yield stress value, but if the applied stress exceeds the value of $\sigma_y$, the material will not flow as a Newtonian fluid, but will rather exhibit shear-thinning or (in very few cases) shear-thickening behaviour. The *Herschel-Bulkley* model is one constitutive equation used to model the rheological behaviour of these fluids and it consists of a combination of the Bingham (1.29) and power-law (1.26) models:

$$\eta(\dot{\gamma}) = \begin{cases} \infty & \sigma \leq \sigma_y \\ \mu_0 \, \dot{\gamma}^{\,N-1} + \dfrac{\sigma_y}{\dot{\gamma}} & \sigma > \sigma_y \end{cases} \tag{1.29}$$

The model parameters used for this model have exactly the same meaning described above. Lastly, as stated before, all the constitutive equations that we have reviewed so far can predict steady-simple shear flow. Apart from the disadvantages that we already discussed, none of the constitutive equations in this subsection are able to predict elastic effects. The memory-effects constitutive equations, on the other hand, can do.

### 1.6.2 Memory-effects constitutive equations

One serious problem with all the constitutive equations described above is that the stress tensor depends on the *instantaneous* deformation tensor; i.e. the fluid velocity will adjust instantaneously to changes in stresses. Thus, there is a lack of information in the equations that can account for the effect of *history* or *past* deformations on the stress, which is a key element needed to model complex fluids. For instance, the rheological behaviour of polymeric fluids is strongly affected by the deformation history; as we saw in section 1.5.2.1, their stress does not grow instantaneously when the flow is started in a shear-stress growth experiment (unlike ideal elastic solids and viscous fluids which respond instantaneously); and likewise, as seen in 1.5.2.2, when the shearing is stopped, the stress will slowly decay in time (unlike inelastic fluids, whose stress vanishes instantaneously).

Therefore, a new element in the constitutive equations is required to account for *memory* effects that will depend on what happened to a material at some time in the past. We can thin of a term, for instance, such as $\underline{\underline{D}}(t-t_0)$, whose physical meaning is the value of the rate deformation at a time $t_0$ ago. Thus, we can also think of a constitutive equation that can incorporate the current and past deformations, which may adopt the following form:

$$\underline{\underline{\sigma}}(t) = 2\,\eta \left[ \underline{\underline{D}}(t) + a\,\underline{\underline{D}}(t-t_0) \right]. \tag{1.30}$$

The first term on the right is the *current deformation* meanwhile the second term on the right is what the material have experienced in the past. Notice that if the parameter $a$ is zero, we recover a simple Newtonian fluid, but since some fluids are observed to exhibit fading memory of past deformations, it is expected that the *history* term would be less important than the current strain rate. Thus, $0 < a < 1$; for instance, if $a = 0.7$, that means that the fluid will forget 30% of what happened to it $t_0$ seconds (or minutes or hours) ago.

Equation (1.30) is not a real constitutive equation; it is a simple example to illustrate the importance of including the deformation history and memory terms in constitutive equations.

### 1.6.2.1 Maxwell model

In this subsection, we will briefly explain the most basic viscoelastic model, the *Maxwell* model, from which plenty of more complex constitutive equations have been derived.

As we have mentioned already, viscoelastic materials display simultaneously both viscous and elastic responses to forces and the distinction between a viscous fluid and an elastic solid relies on their responses to a sudden deformation: stresses that arise in elastic solids remain constant in time for as long as the deformation is present, while stresses in viscous fluids will dissipate over time.

The typical approach to model a simple viscoelastic material is to combine the constitutive equations of the two type of material responses: Hooke's law (1.19) and Newton's law of viscosity (1.4). The Maxwell fluid is then represented graphically like (in a direct analogy with electric circuits) an *elastic spring* connected in series to a *dashpot* (a container with a viscous fluid inside that resists motion via viscous friction), see figure 1.9. The derivation of the Maxwell constitutive equation simply consists of treating the viscoelastic material as an electrical circuit connected in series: the total stress $\sigma$ is the same for the dashpot and for the spring element ($\sigma = \sigma_s = \sigma_d$) but the total displacement is the sum of their contributions, i.e. $\gamma = \gamma_d + \gamma_s$. Combining the scalar constitutive equations (Hooke's and Newton's law), the Maxwell model is obtained:

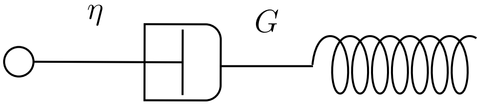

Figure 1.9: Graphical depiction of a Maxwell material.

$$\sigma + \frac{\eta}{G}\frac{\mathrm{d}\sigma}{\mathrm{d}t} = \eta\,\dot{\gamma} \tag{1.31}$$

Equation (1.31) is reduced to Newton's law of viscosity at steady state, and at very short times, the time derivative is dominant and the behaviour observed is a Hooke's solid. The Maxwell model is a differential model and it is one of the first equations reported that accounts for memory effects. This is better seen if the differential equation is solved for the stress:

$$\sigma(t) = \frac{\eta}{\lambda_R} \int_{-\infty}^{t} \mathrm{e}^{-(t-t')/\lambda_R}\, \dot{\gamma}(t')\, \mathrm{d}t', \tag{1.32}$$

where we have introduced the *Maxwell relaxation time*, defined as $\lambda_R = \eta/G$, which is a material time-scale that will essentially determine if a fluid can sustain stress for some time and how quickly or slowly the stresses will decay over time. From the same integral equation (1.32), we can deduce the physical meaning of the terms present there: the current stress in a Maxwell model $\sigma(t)$ is proportional to the integral over all past times of the *deformation history* or shear rate $\dot{\gamma}(t')$ at some past time $t'$, which is multiplied by a *variable forgetting* function of the interval between the current time $t$ and all the past times. In fact, if we use this integral equation for the stress relaxation experiment 1.5.2.2, we obtain an equation of the form $\sigma(t) = \eta\,\dot{\gamma}_0 \exp\left(-t/\lambda_R\right)$, which can nicely predict the stress decay, as shown in figure 1.6.

Another kind of simple viscoelastic model can be derived if instead of considering a serial connection, we use a *parallel* one between the spring and dashpot elements. The models that are derived using this approach are called *Kelvin-Voigt* models, and are used to model viscoelastic behaviour of solids, which we will not consider in the present work. See [160] for some examples.

#### 1.6.2.2 Upper-Convected Maxwell model

Although the Maxwell model can predict the stress relaxation in shear flows of a few fluids (such as extremely dilute polymer solutions), it is not a real constitutive equation, as it cannot deal with general unsteady flow types.

We, therefore, need the tensorial form of equation (1.31) and it would seem obvious to simply rewrite the equation in terms of stress and deformation tensors. However, there is a serious issue in doing it that way: the generalisation $\partial\sigma/\partial t \to \partial\underline{\underline{\sigma}}/\partial t$ is unphysical, since it would lead to a *non-frame invariant equation*, i.e. the equation will depend on what reference frame we are in. All constitutive equations must be frame invariant since the response of a material to an imposed deformation has to be the same for all observers. So instead of using a simple derivative, we need a *convected derivative* of a second-rank tensor [13].

The *Upper-Convected-Maxwell (UCM)* model is in terms of an upper-convected derivative of the stress tensor, which adopts the following form [14]:

$$\overset{\nabla}{\underline{\underline{\sigma}}} = \frac{\partial \underline{\underline{\sigma}}}{\partial t} + u \cdot \underline{\nabla}\,\underline{\underline{\sigma}} - \underline{\underline{\sigma}} \cdot (\underline{\nabla}\,\underline{u}) - (\underline{\nabla}\,\underline{u})^{\top} \cdot \underline{\underline{\sigma}}. \tag{1.33}$$

The tensorial form of the UCM model is:

$$\underline{\underline{\sigma}} + \frac{\eta}{G_0}\,\overset{\nabla}{\underline{\underline{\sigma}}} = 2\,\eta\,\underline{\underline{D}} \tag{1.34}$$

where $G_0$ is the *constant stress modulus.* The UCM model is the first non-linear constitutive equation reported here that is able to predict the first normal stress difference $N_1$, which in simple shear flow adopts the following form:

$$N_1 = 2\,G_0^{-1}\,\eta^2\,\dot{\gamma}^2 = 2\,\lambda_R\,\eta\,\dot{\gamma}^2 = \Psi_1\,\dot{\gamma}^2, \tag{1.35}$$

from which we can deduce that the elastic forces depend, as expected, on the material's relaxation time. Moreover, we can notice that $N_1$ is proportional to $\dot{\gamma}^2$, but this will only be valid for the UCM and other simple models. The UCM model is also able to capture many viscoelastic characteristics, such as stress growth and stress relaxation, shear step-strain among others.

However, like any other model, the UCM model has its disadvantages: some polymer solutions have a $N_2 \neq 0$ but the UCM model cannot be a suitable model for these fluids since it predicts a zero value of second normal stress differences $N_2$ (this will not be a problem for us in the present work though), neither cannot predict shear-dependent viscosity and a shear-dependent elastic-modulus (such as shear-thinning behaviour). Despite these limitations, the model can work for very dilute polymer solutions and some polymer melts in shearing flows.

### 1.6.2.3 White-Metzner model

As we have seen in the past sections, there is a lack of information in most of the constitutive equations reviewed so far as they cannot fully predict most of the complex behaviour described before. And the most common way to tackle these issues is to combine models; in fact, all the equations that we will use in the present work are a combination of different non-Newtonian models.

A clear example of this is the *White-Metzner* model, which is a memory-effect constitutive equation that incorporates a shear-dependent viscosity $\eta(\dot{\gamma})$:

$$\underline{\underline{\sigma}} + \frac{\eta(\dot{\gamma})}{G_0} \overset{\nabla}{\underline{\underline{\sigma}}} = 2\,\eta(\dot{\gamma})\,\underline{\underline{D}}. \tag{1.36}$$

The viscosity function can, for instance, be a power-law function (1.26) and thus, we are now able to describe the flow behaviour of viscoelastic fluids that exhibit shear-thinning or shear-thickening (less common). Notice that by introducing a non-constant viscosity function, the fluid will have a shear-dependent relaxation time $\lambda_R = \eta(\dot{\gamma})/G_0$. For this particular case (1.36), $G_0$ is constant, but it can also be a function of the shear rate.

### 1.6.2.4 Oldroyd-B model

The constitutive model that will be explained in this subsection was derived using a *kinetic theory approach*, i.e. an approach in which the elements of a constitutive equation can be defined in terms of molecular properties. More importantly, it will help us to define a second order tensor that will be of great use in this thesis.

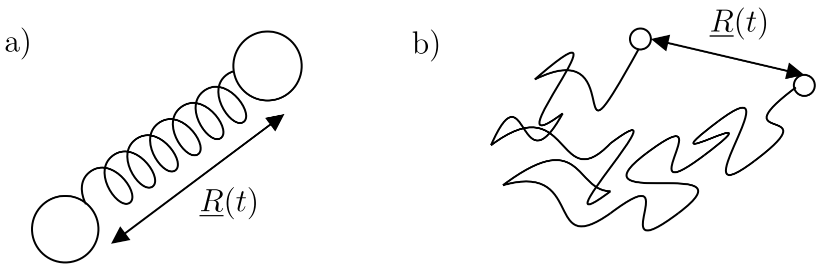

Figure 1.10: Figure (a): Depiction of the bead-spring dumbbell. Figure (b): elastic motion of the ends of a *real* polymer coil in solution that can be seen as a Hookean dumbbell.

The constitutive equation in question models the polymer chains as *dumbbells*: two beads connected by a linear elastic spring and the distance between the beads is $\underline{R}$, known as the *end-to-end vector* (see figure 1.10). These polymer chains are dissolved in a solvent with constant viscosity $\mu$ and the solution is assumed to be dilute so the dumbbells do not interact with each other.

To calculate the polymer extra stress tensor $\underline{\underline{\sigma}}$, it is considered that the dumbbells cross a tiny surface element with area $\delta S$ and unit normal $\underline{n}$, see figure 1.11. If the force associated with a single dumbbell that crosses the surface is proportional to $\underline{R}$, the polymer extra-stress exerted by the dumbbells per unit of volume that cross the surface element is:

$$\underline{\underline{\sigma}} = G\langle \underline{R}\,\underline{R}\rangle = G\underline{\underline{A}}. \tag{1.37}$$

The symbol $\langle \underline{R}\,\underline{R}\rangle$ denotes the *average* vector product of the end-to-end vector of the polymer chains present in a polymer solution, and a new tensor is defined: the conformation tensor $\underline{\underline{A}}$, which will provide us information about the configuration of the polymer chains when a deformation is imposed on them. One important condition of the conformation tensor is that it must be positive definite to remain physically valid.

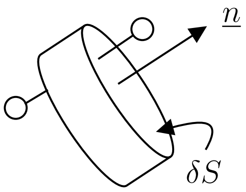

Figure 1.11: A dumbbell crossing a surface element $\delta S$ with normal unit $\underline{n}$.

The equation still lacks information: it is still necessary to introduce the memory effects. Thus, an additional frame-invariant equation is required that will take into consideration the flow history. The equation is derived by carrying out a force balance between three key elements: beads will move under the action of 1) a *drag force*, which is the force acting in opposite direction to the relative motion of the moving polymer chains with respect to the solvent, 2) the spring force and 3) *Brownian motion* (random motion) of the beads. The resulting equation is the evolution of the conformation tensor in terms of a *co-deformational derivative* $\overset{\nabla}{\underline{\underline{A}}}$ (previously defined in section 1.6.2.2), which will represent what happen to fluid-line elements that are deforming with the flow:

$$\overset{\nabla}{\underline{\underline{A}}}= \frac{\partial \underline{\underline{A}}}{\partial t} + \underline{u} \cdot \nabla \underline{\underline{A}} - \underline{\underline{A}} \cdot (\nabla \underline{u}) - (\nabla \underline{u})^{\top} \cdot \underline{\underline{A}} = -\frac{1}{\lambda_R}(\underline{\underline{A}} - \underline{\underline{I}}). \tag{1.38}$$

The *Oldroyd-B model* [137] is the set of equations that defines the stress tensor in terms of the hydrodynamic, viscous solvent and extra-polymer forces:

$$\underline{\underline{\tau}} = -P\,\underline{\underline{I}} + 2\,\mu\,\underline{\underline{D}} + \underline{\underline{\sigma}} = -P\,\underline{\underline{I}} + 2\,\mu\,\underline{\underline{D}} + G\underline{\underline{A}} \tag{1.39}$$

$$\overset{\nabla}{\underline{\underline{A}}}= -\frac{1}{\lambda_R}(\underline{\underline{A}} - \underline{\underline{I}}). \tag{1.40}$$

The Upper-Convected Maxwell model shown in equation (1.34) can also be derived using kinetic theory approach and can be expressed in term of the conformation tensor. In fact, the only difference between the UCM model and the Oldroyd-B model is that the latter one takes into account the solvent contribution to the stress.

The Oldroyd-B model is also a popular viscoelastic model used to describe the behaviour of dilute polymer solutions. However, it has the same disadvantages as the UCM model: it does not predict $\Psi_2$ nor a shear-rate dependent polymer viscosity and elastic modulus. But shear-thinning features can be incorporated in a similar way to the White-Metzner model, see section 1.6.2.3. In fact, a White-Metzner model in terms of the conformation tensor can be derived from equations (1.38)–(1.40) if the solvent viscosity is $\mu = 0$ and if $\lambda_R$ is allowed to depend on $\dot{\gamma}$. Lastly, a modified Oldroyd-B model will be of extreme importance in the development of the content of chapter 3.

## 1.7 More complex rheological behaviour

In the previous sections, we have studied some of the most common non-Newtonian behaviour observed in complex fluids: in section 1.4, we have analysed time-independent phenomena such as the decrease or increase in the viscosity when the fluid is subjected to deformations; we have also studied materials that behave as solids below a critical point, but will flow above that threshold. In section 1.5 we have explored the time-dependent responses of viscoelastic materials to deformations .

Next we will study more complex rheological behaviour that is encountered in *structured fluids*, i.e. those materials that contain more than one phase, such as solid particles dispersed in a liquid, suspensions, surfactant solutions, among others, whose complex behaviour is generally dominated by the interactions between the components of the fluid. Some of the rheological phenomena of structured fluids is a combination of the complex behaviours already described here. However, in some particular cases, the time-dependence (mainly of the viscosity) becomes a strong element to take into consideration, which will make the flow mechanics problems more challenging. And even worse, when the materials are flowing, apart from the shear-rate-and time-dependence, some fluids will exhibit *mechanical instabilities*. All of this will be explored in the following subsections.

### 1.7.1 Thixotropy

In general, *thixotropy* is seen as a generalisation of shear-thinning behaviour and is associated with changes in rheological properties (mainly the viscosity) with time when an applied shear-rate or stress is fixed. In a few words, thixotropy can be seen as a reversible process in which there is a shear-induced decrease of viscosity with time, but when the flow ceases and the fluid is allowed to rest, it has the ability to *rebuild* its viscosity [5]. We will provide a more technical definition later.

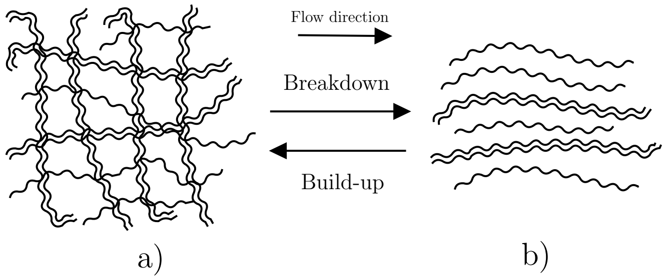

Figure 1.12: (a) Entanglement networks and (b) alignment of molecular chains in the flow direction.

#### 1.7.1.1 General constitutive equation of thixotropic behaviour

In order to explain this rheological behaviour, we need to understand what is happening at a molecular level. As we stated before, structured fluids are liquids with a microstructure within them. This microstructure can mean multiple things, depending on the kind of fluid being studied: it can mean entanglement density, molecular associations in polymer solutions, network junctions, flocculated particles, etc. However, these microstructures can change with time under the action of external and internal forces; for these cases, the microstructure is *bounded* (see figure 1.12), i.e. 1) there is a *maximum level* of microstructure, which is seen when the alignment and spatial distribution of the components of the microstructure (polymer chains, worm-like micelles) are random and entanglement level is at a maximum, and 2) there is a minimum level of microstructure in which there is an alignment of molecular chains in the flow direction or there is a minimum number of entanglements or associations between the chains [5].

These microstructural changes are due to a competition between two kinds of processes: 1) a *breakdown* process of the microstructure caused by flow stresses and 2) a *rebuild* or *build-up* of the microstructure, where the driving force is Brownian motion. Thus, in order to model thixotropic behaviour, we need a governing equation that can be able to describe these two processes, along with a constitutive equation for the stress tensor. We first consider the case of an *ideal* thixotropic fluid: i.e. there are no elastic effects present; when the flow of a thixotropic fluid is ceased, the stress will vanish immediately (viscous response) [98]. The stress tensor can adopt the following form:

$$\underline{\underline{\sigma}} = 2\,\eta(\lambda_s, II_D)\,\underline{\underline{D}}, \tag{1.41}$$

where the viscosity of a thixotropic fluid is not only a function of the second invariant of the deformation tensor; it will now depend on a *structural parameter* $\lambda_s$, which describes the level of organization of the microstructure of the fluid. This parameter can vary within the range between unity (which represents the highest structuring level) and zero (lowest microstructure level) [48]. In some models, like the one we will use in chapter 4, the level of structure can be measured through the viscosity, and thus, $\eta$ can be seen as a structural parameter.

In order to incorporate the structural time-dependent behaviour of the material, an evolution equation for the structural parameter is introduced. For most of the thixotropic models reported in the literature, the evolution equation adopts the following general form [124]:

$$\frac{\mathrm{d}\lambda_s}{\mathrm{d}t} = k_+(1-\lambda_s) - k_-\dot{\gamma}\lambda_s. \tag{1.42}$$

The term of the first right-side of (1.42) describes the build-up process, where $k_+$ stands for the rate of growth of the structure parameter, meanwhile the second term is the breakdown process whose rate is determined by the magnitude of $k_-$.

#### 1.7.1.2 Typical behaviour of thixotropic fluids

Now we will briefly describe some of the most common phenomena observed in thixotropic fluids. Suppose we place a sample of thixotropic material into a rheometer, which carries out a start-up experiment (see section 1.5.2.1), where a constant shear-rate $\dot{\gamma}_0$ is imposed on the material. We will then observe that there is a decrease in the viscosity with time, as shown in figure 1.13, and this is due to the shearing that is breaking down the microstructure (initially with $\lambda_s = 1$), until it reaches its steady-state value (viscosity with $\lambda_s$ within the range $0 \leq \lambda_s < 1$, depending on the value of $k_-$). At this moment, or at least when the viscosity no longer varies with time, the flow is stopped and we allow the fluid to rest for a very long but finite time $t_1$. We call this initial process experiment I. After this, experiment II begins: we switch the shear on again with the same value of shear-rate used before $\dot{\gamma}_0$, and we will observe that the initial viscosity value measured in experiment II ($0 \ll \lambda_s < 1$) will be close to the initial viscosity reported in experiment I, and then decreases with time until it reaches the same steady-state value as in experiment I.

The long rest time of the fluid in experiment I allowed the fluid to rebuild its structure (for instance it allowed the molecular chains of the fluid to become entangled again). However, the fluid did not reach its original microstructure level. In

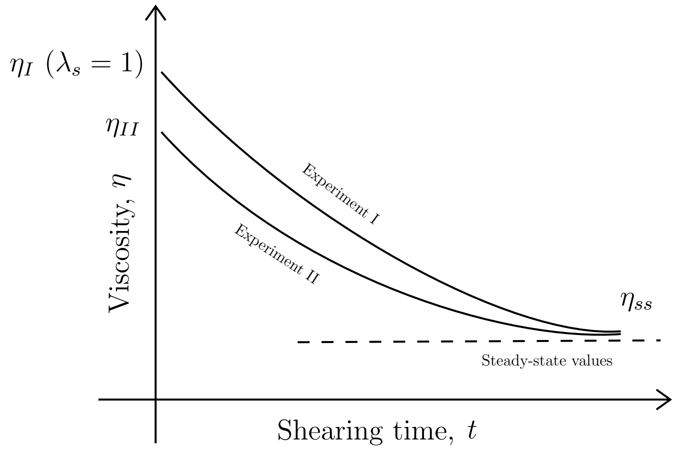

Figure 1.13: Viscosity decrease with time of a thixotropic fluid.

some way, we can say that the fluid exhibits some sort of *structural memory*, and this kind of memory depends on the parameter value of $k_+$ and on how long we have allowed the material to settle and rest.

This structural recovery of the material after the cessation of flow can be mathematically modelled using the following equation:

$$\frac{1}{\eta_{II}} = \frac{1}{\eta_I} + \Big(\frac{1}{\eta_{ss}} - \frac{1}{\eta_I}\Big) \mathrm{e}^{-\, t_1 \, k_+}, \tag{1.43}$$

where $\eta_{ss}$ is the steady-state viscosity value, $\eta_I$ is the initial viscosity value seen in experiment I when the fluid has its highest level of microstructure and $\eta_{II}$ is the viscosity value reached after the fluid was allowed to rest for a time $t_1$. From equation (1.43), we can deduce many conclusions: the parameter $k_+$ from equation (1.42) has units of inverse of time, so we define $\lambda = 1/k_+$ as the material's *structural relaxation time-scale*, which plays a key role in the thixotropic phenomenon: extremely low values of $\lambda$ (high $k_+$) will involve a quick structural recovery, i.e. $\eta_{II} \approx \eta_I$. On the other hand, extremely high values of $\lambda$ (low $k_+$) means that the structural recovery will be extremely slow and thus, $\eta_{II} \approx \eta_{ss}$. Therefore, we say that thixotropic fluids exhibit a slow recovery of structure.

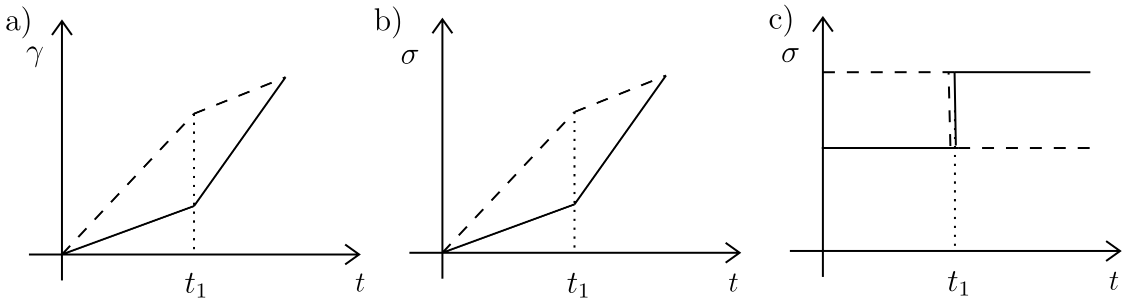

Figure 1.14: Figure (a): Start-up and step-up (solid lines) and step-down (dashed lines) shear. Figure (b): elastic response. Figure (c): viscous fluid response.

## 1.7.2 Thixotropic-viscoelastic materials

Here we will simply provide a brief introduction to fluids that can exhibit both viscoelastic and thixotropic effects. But first, we need to be able to distinguish between the two rheological phenomena.

### 1.7.2.1 Distinction between viscoelasticity and thixotropy

For many years, the term thixotropy was used to describe the decrease in viscosity by flow followed by its structural rebuild over a period of time. However, shear-thinning non-linear viscoelastic fluids can also exhibit these characteristics and thus, a more accurate definition of thixotropy was needed. In 2015, Larson [98], through the publication of his paper, helped to clarify the concept. He argued that viscoelasticity must be seen as a *relaxation of stress*, meanwhile thixotropy is “a slow relaxation of viscosity or other viscoelastic parameters”.

To make clearer the distinction between the two phenomena, Larson states that a series of step experiments (like the one explained in sections 1.5.2.1 and 1.5.2.3) have to be carried out. This experiment, better known as *start-up and step-up or step-down shear*, consists of shearing a sample of fluid for a long period, followed by an increase (or decrease) of the shear rate. The stress and the instantaneous viscosity are then monitored. In figure 1.14, we show some of the responses of simple materials.

Before the time $t_1$, the flow is started and we allow the fluid to reach its steady-state value (stress-growth experiment). At $t = t_1$, the shear rate can either be increased (*step-up*, solid lines) or decreased (*step-down*, dashed lines). The responses of both elastic and viscous materials are straightforward, and therefore, are not interesting. The ones for viscoelastic and thixotropic materials are more interesting and they are depicted in figure 1.15.

Notice in particular, the big differences between the viscoelastic (figure 1.15a) and ideal thixotropic fluid (figure 1.15b) responses to a step-down experiment: for the former case, there is a gradual, monotonic decrease in stress toward the steady value, meanwhile for the latter one, we observe an instantaneous rapid decrease in stress followed by a gradual increase towards the steady-state due to the structure-rebuilding process [118]. For the step-up experiment, the fluids exhibit the same behaviour but in the opposite direction.

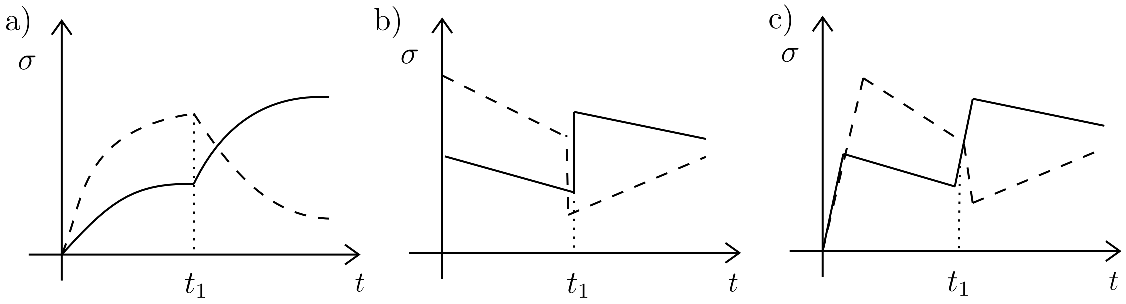

Figure 1.15: Responses to the deformation depicted in figure 1.14) of (a) a viscoelastic fluid, (b) an ideal-thixotropic material and (c) a non-ideal thixotropic (or thixo-elastic) fluid.

We can also notice differences at the start-up of the experiment: for the viscoelastic case, the material takes time to respond to the flow, meanwhile for the ideal-thixotropic case, the fluid reacts instantaneously to the deformation and the microstructure is affected by the flow and it will take some time until it reaches its steady value. More differences can be found, for instance, if we carry out a pure step shear strain experiment, (see section 1.5.2.3): for a viscoelastic fluid, we will observe a stress relaxation over a finite time. On the other hand, the ideal thixotropic fluid will exhibit an instantaneous stress relaxation due to the absence of elastic effects (no elastic recoil).

These remarkable differences are governed by the respective time scales of the two phenomena: the characteristic time-scale for viscoelasticity is the stress relaxation $\lambda_R = \eta/G_0$ and the one for thixotropy is the structural relaxation time, $\lambda$. Real fluids will exhibit both time scales, and whether they will exhibit a thixotropic or viscoelastic response will depend on the magnitude of these time scales: if the structural relaxation time scale is much longer than the stress relaxation one, the thixotropic effects dominate (see figure 1.15b). On the other hand, if $\lambda_R \gg \lambda$, viscoelasticity will dominate (see figure 1.15a). And what happens for intermediate values of these time scales? This is illustrated in figure 1.15c), which depicts the case of a *non-ideal thixotropic fluid*, also known as *thixo-elastic fluid*. We can see that at $t < t_1$, at short times, there is an initial elastic response to the flow and then there is an increase in stress followed by a decrease towards the steady value characteristic of thixotropic materials. For the step-down case $t \geq t_1$, we observe first a stress relaxation followed by a buildup of the structure. The behaviour displayed in figure 1.15c) is seen if the thixotropic time scale is slightly greater than the stress relaxation time scale.

### 1.7.2.2 General constitutive equations

As we saw in section 1.7.1.1, a set of constitutive equations is required to model ideal-thixotropic fluids: Newton's law of viscosity and a kinetic equation that could describe the processes of breakdown and build up of the structure, see equation (1.42). For thixotropic-viscoelastic fluids, the mathematical modelling is similar, but instead of an inelastic stress tensor, we need to incorporate elastic effects by coupling a thixotropic equation with a viscoelastic constitutive equation, such as the ones described in section 1.6.2.

Plenty of thixo-elastic models can be found in the literature [2,7,47,48,129], but as stated by Larson [98], care must be taken: if their viscoelastic relaxation time is much longer than the structural relaxation time, the models would be regarded as models of complex nonlinear viscoelasticity rather than of thixotropy.

In chapter 4, we introduce a complex thixotropic-viscoelastic model that also incorporates plasticity.

### 1.7.3 Shear-banding flow

Now we focus on one of the most interesting properties of some complex fluids, which occurs when an initially homogeneous flow becomes unstable above a critical value of shear rate, leading the system to separate into bands of different internal structure and differing viscosity, which results in a non-monotonic behaviour in the flow curve (shear stress versus shear rate), see figure 1.17a). This complex rheological behaviour has been the subject of both theoretical and experimental research [10, 20, 32, 33, 142, 170]. This kind of behaviour has been observed in both high molecular weight polymeric liquids and *wormlike surfactant* solutions. We will particularly focus on the latter.

#### 1.7.3.1 Surfactant solutions

A surfactant molecule possesses a *hydrophilic* group (water-*loving*) which is chemically bonded to a *hydrophobic* group (water-*hating*). The hydrophilic groups are usually polar groups that can establish interactions with other polar chemical groups (such as water). On the other hand, hydrophobic groups are non-polar groups (i.e. hydrocarbon chains) that will interact with similar groups.

Things get exciting when these molecules are in solution, as they will *self-assemble* into aggregates such as spherical and wormlike micelles and bilayers, among others, see figure 1.16. The surfactants are said to be *polymorphic*, as the formation of these supramolecular structures can depend on many things, such as the amount and type

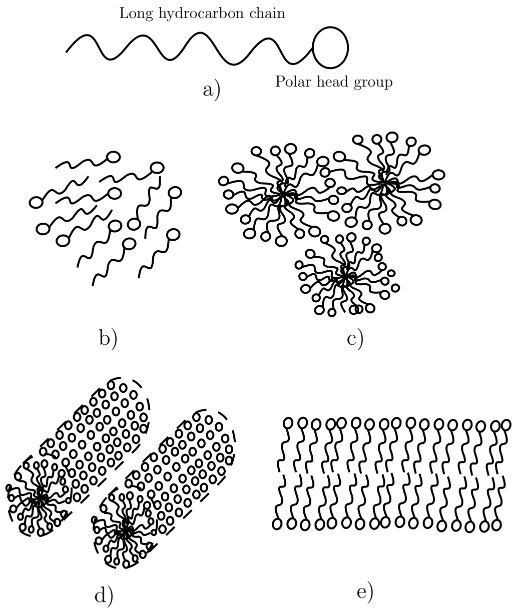

Figure 1.16: Figure (a): Surfactant molecule and different micellar structures: figure (b) surfactant monomers in solution at low concentration; (c) spherical micelles; (d) wormlike chains; (e) a bilayer.

of solvent present, temperature, salinity and concentration [97]. For instance, above a critical concentration, the surfactant supramolecular structures such as the wormlike chains overlap and form an entangled complex network. This process can also be reversible: the entanglements can be destroyed by a strong flow that will lead to an oriented state (i.e. linear wormlike chains). For even higher concentrations, the aggregates can form even more complex structures (hexagonal, cubic, etc).

#### 1.7.3.2 Rheology of wormlike micellar solutions

Entangled solutions of wormlike micelles exhibit viscoelastic effects, but they show a special characteristic: at very low shear rates, their shear viscosity is constant (and slightly larger than that of the solvent), but more importantly, they are characterised by a single relaxation time $\lambda_R$ [97] (unlike some polymer solutions that exhibit a *spectrum* of relaxation times), yielding a near-Maxwell behaviour. The response of these entangled solutions of wormlike surfactant solutions to unsteady shear-flows can be described with the Maxwell model (see sections 1.5 and 1.6.2.1).

However, at higher shear rates, the entanglements may begin to break, so in order to model this kind of complex fluid, it is necessary to account for the reversible assembly and disassembly of the entangled wormlike-chain solution, which is usually modelled using a kinetic equation (like the one shown in 1.7.1).

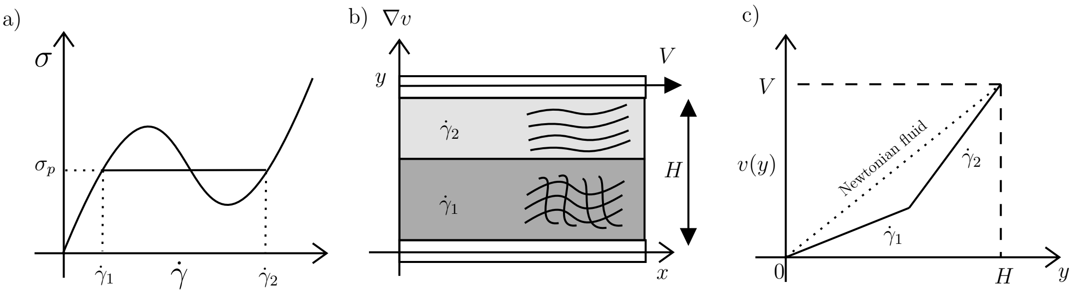

Figure 1.17: Shear-banding flow. Figure (a): flow curve $\sigma$ vs $\dot{\gamma}$; figure (b): steady shear flow; figure (c): velocity profile $v(y)$ vs $y$.

Apart from viscoelasticity, these solutions can show another fascinating rheological property. For instance, the steady simple shear flow of a (initially entangled) wormlike micellar solution is studied. At very low shear rates ($\dot{\gamma} \ll \dot{\gamma}_1$), the fluid exhibits a linear dependence of the shear stress on the shear rate (i.e. Newtonian behaviour with high viscosity). An increase in $\dot{\gamma}$ will cause a drop in viscosity (shear-thinning), as there is a strong dependence of the viscosity (and thus, of the microstructure) on the applied shear rate.

Above a critical value of the shear stress, the initially homogeneous flow becomes unstable, which will lead the system to separate into two different bands with different internal structure and different shear-rates values $\dot{\gamma}_1$ and $\dot{\gamma}_2$, see figure 1.17. These two bands are separated by an interface whose normal is in the flow-gradient direction. This phenomenon is called *shear-banded* flow or *shear-banding* transition, which describes a transition between a homogeneous and non-homogeneous state of flow. This rheological phenomenon is analogous to the liquid-gas transition described by Van-der-Waals [27]. At very high shear rates ($\dot{\gamma} \gg \dot{\gamma}_2$), the theoretical models predict that the flow becomes homogeneous again and the fluid will display a single but a smaller viscosity [111].

The critical stress value described above is called the *stress plateau* $\sigma_p$: below this value, we observe entangled networks of micellar solutions; when the stress applied is $\sigma = \sigma_p$, separation of bands occur and they coexist at this point, and above this stress value, we can idealise that the majority of entanglements will be destroyed, leading to flow-oriented linear wormlike chains. The coexistence of the low and high viscosity bands has been confirmed by different experimental techniques [12, 23, 50, 110].

The non-monotonic curve shown in figure 1.17a), which is the theoretical curve predicted by many constitutive equations, has interesting features: 1) in the banded region ($\dot{\gamma}_1 < \dot{\gamma} < \dot{\gamma}_2$), a negative slope for the flow curve $\sigma$ vs $\dot{\gamma}$ is seen and homogeneous flow is unstable there, triggering the formation of bands with different shear rate values, and 2) a *multivalued region* (i.e. three different possible values of shear rate for a given value of shear stress). However, it has been observed in experiments that real systems have a well-defined stress, which is the stress plateau $\sigma_p$ and thus, the *real* shear flow curve is composed of two increasing stable homogeneous curves of high and low viscosities separated by a stress plateau (horizontal line) extending between two shear rate values $\dot{\gamma}_1$ and $\dot{\gamma}_2$ (see figure 1.18). The mathematical and physical selection criterion which will determine the band coexistence and a more detailed analysis of the constitutive curve is given in chapter 5.

We also illustrate the coexistence of the entangled networks (with shear rate value $\dot{\gamma}_1$) and wormlike linear chains (with $\dot{\gamma}_2$) at the stress plateau and the corresponding velocity profile in figures 1.17b) and 1.17c), respectively, where we can see that the destruction of entangled networks is stronger at the moving wall ($y = H$), leading to linear chains.

It is highly important to understand this phenomenon, as fluids that exhibit the shear-banding transition are highly important in the oil industry [68], drag reducing agents [74] and in many home and personal care products [155, 156]. Experimental

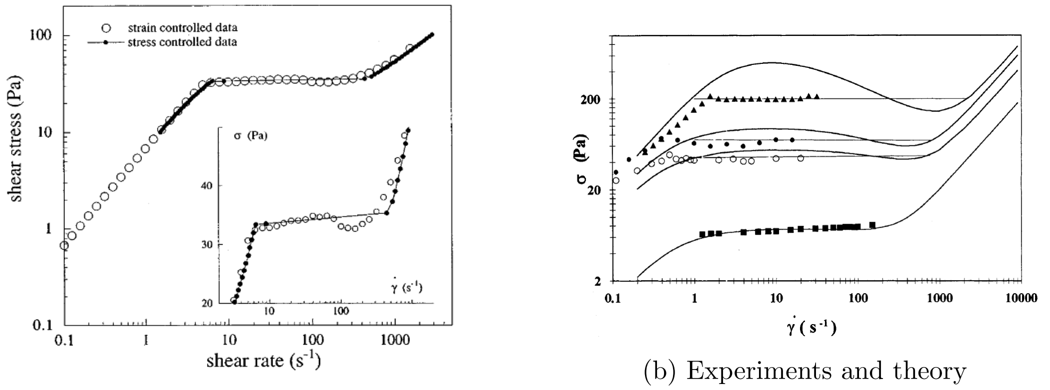

(a) Experiments

(b) Experiments and theory

Figure 1.18: Shear-banded flow on micellar systems. Figure (a): experimental evidence of shear-banding phenomenon of a micellar solution obtained by Cappelaere *et al.* [24]. Figure (b): flow curves $\sigma$ vs $\dot{\gamma}$ for different micellar solutions at different concentrations. The points represent experimental information and the solid lines are the theoretical curves predicted by a constitutive equation [111].

evidence of shear banding in micellar solutions is available in the literature [11,21,24]. However, shear banding is not a phenomenon unique to this kind of fluids; it has also been observed and studied in liquid crystalline polymers [148], soft glasses [42], colloidal suspensions [38] and associative polymers [30,161].

#### 1.7.3.3 Constitutive equations for shear-banded flow

As we have just seen, micellar solutions can separate into coexisting bands with different viscosities and internal structuring when a critical shear stress value is reached, as illustrated in figure 1.17. The modelling of this complex rheological behaviour becomes a challenge but fortunately, this flow curve has been captured by several different constitutive models. As Fielding [62] states, these models can divided into two classes: a) *phenomenological* models, which are able to capture the relevant physics of the phenomenon while using as few parameters as possible and b) models that are derived by considering the dynamics of the molecular chains, i.e. flow-induced changes on the structural level of the fluid. We will review only a few of the many models available in the literature.

One of the most popular phenomenological models is the Diffusive Johnson-

Segalman (DJS) model [45, 87], used to describe shear-banding in dilute solutions of wormlike micelles. The stress tensor of the JS model comprises the pressure, a Newtonian solvent stress and a non-Newtonian stress. The last stress term is governed by a Gordon-Schowalter convected time derivative [95], used to describe *nonaffine* response of polymer chains to an imposed deformation, i.e. the local microscopic strain is not identical to the global macroscopic strain applied to the material. The parameters of the DJS model are the solvent viscosity, an elastic modulus, a stress relaxation time, a diffusion coefficient and a *slip* parameter $a$, which is a measure of the nonaffinity of the polymer deformation. In order to observe shear-banding, $a < 1$, so that the chains will slip relative to the flow field.

Although the DJS model is able to predict non-monotonic curves (such as the one shown in figure 1.17a) and it has been used to understand some features of the band formation, this model cannot describe the breaking and reformation processes of these micellar systems under flow described in section 1.7.3.2, which are important ingredients of a model that need to be considered if one wishes to accurately describe other highly non-linear behaviours of micellar solutions [8, 27, 111].

On the other hand, there are several models in the literature that do consider these kinetic processes. The reason for this is that there are different approaches taken to model this kind of complex fluid [59]. One of the first models that takes into account the reversible breaking and recombination of micellar chains was developed by Cates [31]. His model (which was derived using the fundamentals of the reptation theory of polymers [46]) has two representative time scales: a *reptation time* (the time it takes a polymer chain to pass through a *virtual* tube formed by the surrounding and entwining polymer molecules) and a *breaking time* (a mean time for a molecular chain to break into two pieces). Cates' model can predict nicely the linear rheology behaviour and the onset of shear banding, but fails to predict other non-linear rheological phenomena (such as the *stress overshoot* observed in start up experiments, see section 1.5.2.1). It has also been of little help to completely understand the mechanism behind shear-banding.

Another common approach taken by other models found in the literature is to combine dumbbell models and network theory by coupling viscoelastic governing equations and kinetic equations for the breaking and reformation of micellar solutions. One of the most popular models and also the one that we will be using in Chapters 4 and 5 is the Bautista-Manero-Puig (BMP) model [7, 8, 111], which consists of a codeformational Maxwell constitutive equation (see section 1.6.2.2) coupled to an evolution equation for the internal structural level of the fluid [67]. This model can capture accurately a large variety of complex rheological behaviour, such as shear-thinning and shear-thickening effects, thixotropy, viscoelasticity, plasticity and the shear-banding phenomenon. The mathematical equations, the model parameters and their physical meaning and the model limitations will be discussed in detail in the following chapters.

Another constitutive equation used to model wormlike micellar solutions rheological behaviour was developed by Vazquez *et al.* [145, 169], which is a *two-species reptation-reaction network* model that incorporates the reformation and continuous rate-dependent breakage of the entangled viscoelastic network. More specifically, they consider elastic long chains that can each break to form two short chains, which can also recombine to form the long chain. This model is able to describe linear and non-linear rheological behaviour prior to the onset of shear-banding. It also works well in predicting start-up shearing flow, cessation of steady shear flow, among others, but fails to predict $N_2$ and to describe the onset of the stress plateau observed in experiments.

Other constitutive equations that have been used to describe shear-banding in micellar solutions are the Rolie-Poly [3] and Giesekus [73] models, but they are commonly more used to address polymer solutions and melts and are usually used as an alternative to the DJS model for wormlike micelles, and therefore, they will not be discussed here.

## 1.8 Introduction to flow instabilities in complex fluids

Over the last few sections, we have reviewed some of the multiple complex rheological phenomena exhibited by some fluids of industrial interest, such as polymers and surfactant solutions, among many others.

In the manufactoruing industry, for instance, some processes consist of converting raw polymeric materials into a finished product of a specific shape with specific properties. This transformation from raw materials to the final product involves many physical changes, such as mixing, extruding, moulding, melting, coating, pumping, among others (for further information, see [43]). In addition, rheological tests have to be carried out to determine whether the final product will have the required properties.

However, the complex nature of these fluids might be problematic in many of the industrial processes mentioned above. More specifically, when the complex fluids are under flow, something *might go wrong*; i.e. an unexpected behaviour may be observed, for instance, the presence of non-ideal velocity fields during steady flow (*secondary flows*). In fluid mechanics, we refer to these undesired behaviours as *flow instabilities* and they can occur in a variety of commercially important processing operations. These flow instabilities should be avoided when measuring fluid properties as they might cause a fluid to inaccurately appear as shear-thinning, shear-thickening, shear-banding or having time-dependence, when in reality the fluids do not exhibit any of these behaviours. In addition, these instabilities can badly affect the quality of the desired product.

In the present work, we will be particularly interested in studying instabilities in viscoelastic flows, also known as *purely elastic instabilities*, i.e. instabilities present in inertia-less flows that are not seen in Newtonian fluids. Petrie & Denn [143] were the first to identify such instabilities arising in extensional and shearing flows in polymer processing operations. Since then, extensive theoretical and experimental research has been made by rheologists in order to understand the mechanisms behind these instabilities.

Some reviews of viscoelastic instabilities are available in the literature, such as those by Tanner [164], Larson [96], Shaqfeh [158], Wilson [175] and Muller [130]. As Larson states, the viscoelastic nature of complex fluids has a large variety of complex effects on flow instability. This means that there are plenty of different elastic instabilities that have been observed experimentally and studied theoretically and this is due to the fact that viscoelastic properties vary from fluid to fluid; for instance, the fluids might have different concentration, molecular weight, molecular weight distribution, branching, entanglement between molecular chains, network junctions, kinetic processes that affect the evolution of an internal microstructure (such as destruction and reformation processes, as explained in section 1.7), among others, which can greatly influence the fluid's viscoelastic character. In addition, some elastic instabilities are only observed in given flow geometries (such as Taylor-Couette flows, cone-and-plate and plate-and-plate flows, etc). So in this way, in the present work, we will only focus on flow instabilities in shear flows, leaving aside those that have been observed in extensional flows [35, 64, 122, 125, 187].

In the following subsections, we start with a short explanation of common rheometric flows in rheology (section 1.8.1), and then we will move on to provide a brief introduction to some elastic instabilities commonly observed in experiments (sections 1.8.2, 1.8.3 and 1.8.4). Lastly, we will review both theoretical and experimental research in Couette and pressure-driven channel flows of viscoelastic fluids with and without shear banding that will be extremely useful for the present work (sections 1.8.5 and 1.8.6).

### 1.8.1 Rheometric flows

As we have previously mentioned, the only accurate way to determine whether a constitutive equation is able to predict the behaviour of a material is to measure experimentally some properties of the fluid (such as material functions, see section 1.5) and compare them with the predictions made by the constitutive equations. The set of experimental techniques used to measure the material properties is generally called *rheometry*. In this subsection, we will describe some of the most common rheometric flows used in rheometry to study a fluid's behaviour, see figure 1.19.

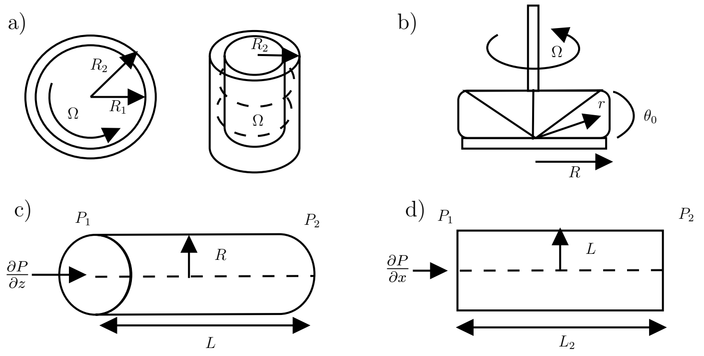

Figure 1.19: Geometric flows commonly used in rheology; figure (a): Taylor-Couette flow, (b): cone and plate flow, (c): Poiseuille flow, (d): channel flow.

The *Taylor-Couette flow* is used to measure a fluid's viscosity and is illustrated in figure 1.19a), which consists of a fluid confined in the gap between two rotating cylinders. The inner cylinder, with radius $R_1$, will rotate with angular velocity $\Omega$ meanwhile the outer cylinder with radius $R_2$ is fixed. The Taylor-Couette flow approaches simple shear in the limit of large $R_1$ (or small gap).

Another popular geometry used is the *cone-and-plate* (see figure 1.19b), where a material is placed on a horizontal plate and then a cone (with radius $R$) is placed into it, which will rotate with angular velocity $\Omega$. The angle between the surface of the cone and the plate is $\theta_0$. This kind of flow is often used to measure the viscosity and the first and second-normal stress differences [79]: the resistance to the rotation of the cone produces a torque that is proportional to the shear stress in the fluid and thus, viscosity can be calculated from the known geometric constants of the cone, the rate of rotation and the stress related torque.

In figure 1.19c), we show the *cylindrical Poiseuille flow*, which is a pressure-induced flow in a pipe with radius $R$ and length $L$. It is assumed that there is laminar flow induced by a constant pressure drop $\partial P/\partial z \approx (P_1 - P_2)/L$.

Finally, in figure 1.19d), we have the *pressure-driven channel flow*, also known as *planar Poiseuille flow*. The only difference with respect the cylindrical Poiseuille flow is obviously the geometry used. In the present work, we will be particularly interested in this geometry. The motion of different viscoelastic fluids in planar Poiseuille flow will be described in the following chapter 2.

### 1.8.2 Curved streamlines elastic instabilities

We start by reviewing some of the most common instabilities encountered by experimental rheologists: purely elastic instabilities in flows having curved streamlines. Two key *ingredients* are necessary to observe these instabilities: high Weissenberg numbers (see the definition in section 1.3.2) and elastic fluids flowing in rotational geometries, such as concentric cylinders, cone-and-plate and plate-and-plate (in which the cone is replaced by a disk). The combined effect of the fluid elasticity and the curvature of the streamlines *generates* tension that causes instability.

There is an extensive literature on curved streamline instabilities, see [140, 158]. For instance, a complete experimental and theoretical work about purely elastic instabilities in different rotational geometries was carried out by McKinley *et al.* [115]. They defined a new dimensionless group that unifies theory and experiments that can be used to determine the critical conditions required for the onset of purely elastic instabilities for simple geometries (such as Taylor-Couette and cone-and-plate flows) and more complicated ones (such as planar contraction, eccentric rotating cylinders and lid-driven cavity, among others).

#### 1.8.2.1 Instabilities in Taylor-Couette flow

One of the first reported instabilities in Newtonian fluids is the Taylor-Couette instability [167], which is observed in the flow having the same name (see figure 1.19a). This instability is characterised by the formation of toroidal cellular structures (also known as *Taylor cells*) in the axial direction, and its mechanism is well understood: the inertial motion along with the centrifugal forces acting on the fluid are the main source of this instability [52]. The stability criterion for Newtonian fluids has been established and it is based on a dimensionless number called the *Taylor number*, $Ta$, which is the ratio between inertial forces due to rotation and viscous forces; above a critical value of $Ta$, the flow will be unstable. This dimensionless number can be expressed in terms of the density and viscosity of the fluid, the angular velocity and the diameters of the inner and outer cylinders.

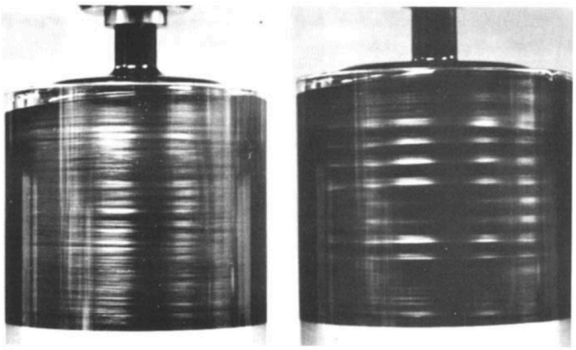

Figure 1.20: Visualisation of the purely elastic Taylor-Couette instability. The left picture shows the onset of the instability, meanwhile we see a fully developed instability at the right one. Picture taken from Muller *et al.* [131].

A similar instability is seen in elastic fluids, such as dilute and moderately entangled polymer solutions: the *purely elastic Taylor-Couette instability* (see figure 1.20), in which toroidal cells are also observed even at very low Reynolds number values. This inertialess viscoelastic instability was first observed experimentally by Giesekus in 1966 [71] and it brought the attention of many groups of researchers, including Muller *et al.* [131], whose work demonstrated experimentally the existence of a purely elastic mode that occurs at negligibly small Reynolds numbers. Their work was relevant as they focused on identifying this elastic mode rather than studying the effect of elasticity on the inertial Taylor-Couette instability (see, for instance [51, 162]).

In a subsequent paper by the same research group (Larson (1990) [100]), they successfully managed to predict theoretically the purely elastic instability that they observed in experiments. For their analysis, they simply used linear stability theory and the Oldroyd-B model constitutive equation. They concluded that the instability is driven by the interaction between the first normal stress difference $N_1$ and a velocity fluctuation.

Further theoretical work about how different fluid properties can affect the purely elastic Taylor Couette instability can be found in the literature. For instance, Shaqfeh [159] studied the effects of various dilute polymer solution properties (such as the ratio of the second to the first normal stress difference coefficients and the ratio of the solvent to the polymer viscosity) and gap width on the previously described instability, and Larson (1994) [99] extended previous theoretical work to consider fluids with a distribution of relaxation times and also fluids that exhibit shear-thinning behaviour.

### 1.8.3 Instabilities in cone-and-plate and plate-and-plate flows

As previously mentioned, the cone-and-plate and plate-and-plate geometries are often used to measure rheological properties of fluids and both consist of a rotating upper surface (cone or a plate) and a bottom fixed surface (a plate). A fluid is confined to the gap between the upper and bottom surfaces and it will be sheared.

However, these geometries are vulnerable to instabilities. For instance, it is well known that centrifugal forces, for given geometric conditions and above a critical Reynolds number, can produce a secondary flow in some Newtonian fluids [39]. It has also been reported that if the ratio between the inertial forces and the surface tension forces is above a threshold value, the fluid (Newtonian fluids and some polymeric liquids) will experience inertial expulsion, or in other words, will be ejected from the rheometer due to the effect of centrifugal forces [165].

#### 1.8.3.1 Meniscus distortions

At low Reynolds number values, other type of instabilities are observed for polymeric fluids, which are usually called *elastically-driven meniscus distortions* [96]. These are classified in two different types: the *fracture*, an irregular, non-axisymmetric distortion whose effect on the fluid makes it look like surface vortices, and the *edge fracture*, characterised by an axisymmetric smooth indentation of the meniscus located in the middle between the plate and the cone (or the other plate).

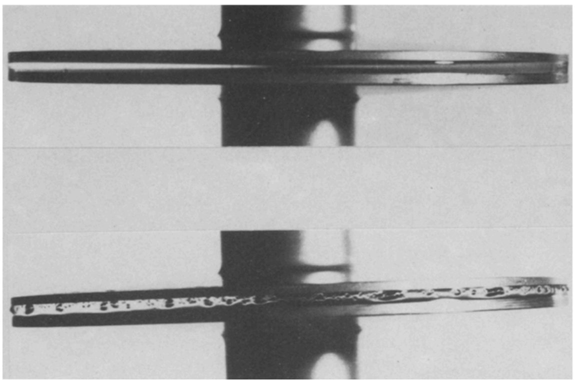

Figure 1.21: Cone-and-plate flow of a polymer solution. Top picture: a smooth meniscus; bottom picture: the *fracture* meniscus distortion. Pictures taken by Kulicke *et al.* [91].

The *fracture* instability (see figure 1.21) is commonly observed in polymer melts and entangled polymeric solutions at moderate Weissenberg numbers. Kulicke *et al.* reported many experimental observations of this phenomenon in cone-and-plate devices (see [91–93]). They found that the fluid elasticity is responsible for the distortion and that the ratio between the first normal stress difference and the shear stress can be used as a critical parameter to predict the onset of the fracture.

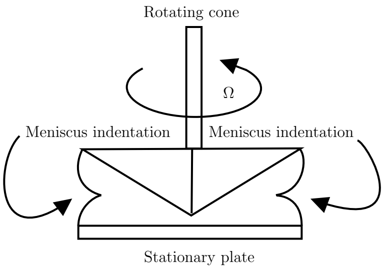

Figure 1.22: Schematic diagram of edge fracture.

The *edge fracture* (see figure 1.22), on the other hand, is often present in entangled polymeric solutions and it was first experimentally observed by Hutton [84]. Edge fracture occurs when the free surface of the fluid meets the outside air, which destabilises the flow. One of the disadvantages of the presence of this instability is that it makes stress measurements inaccurate as it lowers the effective shearing surface area. In 1983, Tanner & Keentok [166] proved that the edge fracture will be seen if the second normal stress difference $N_2$ is negative (which differs from the fracture instability described above, that is dependent on $N_1$). In addition, they provided a criterion for instability (dependent on $N_2$, the surface tension and the size of the fracture) that correctly predicts the critical shear-rate at which the fracture occurs. Lee *et al.* [103] studied the edge fracture for six different polymer solutions with different ratio values of $N_2/N_1$, and experimentally confirmed Tanner's observations: the edge fracture correlates with $N_2$ and not with $N_1$.

In recently published papers, Hemingway *et al.* [76, 77] used stability theory to derive an analytical expression for the onset of the edge fracture that is in terms of the fluid rheological properties, the jump in shear stress between the fluid and the air, surface tension of the air-fluid interface and the gap size of the cone-and plane rheometer. In addition, they were the first to provide with a full mechanistic understanding of the edge fracture, which was validated by their numerical simulations.

In a subsequent paper, Hemingway & Fielding [75] demonstrated numerically that in shear-thinning polymeric fluids, modest disturbances of the sample edge (which may go unnoticed experimentally and are the precursors of the true edge fracture instability) can lead to strong secondary flows that are able to penetrate the fluid bulk and form shear bands. Most importantly, they found that this is also true even for a fluid whose flow curve is monotonic (no manifestation of shear-banding). They also proved that flatter constitutive curves will tend to produce more edge-induced pseudo-shear-banding.

#### 1.8.3.2 Bulk instabilities

Another instability that differs from the meniscus distortions has been observed for unentangled and moderately entangled fluids. Jackson *et al.* [85] discovered an unusual rise in both the shear stress and first normal stress difference of a Boger fluid [17] after being sheared for a finite time, which might imply that the fluid becomes time-dependent. Further experiments carried out by Magda & Larson [109] in both cone-and-plate and plate-and-plate flows concluded that the dramatic rise in $\sigma_{12}$ and $N_1$ were caused by the appearance of a secondary flow, which is even present at low Reynolds number values.

Magda & Larson also found that the instability occurs at shear rates values that exceed a critical value, and that the threshold value is dependent on the gap between the plates. McKinley's experiments [113, 114] confirmed this conclusion, who also found the geometric and flow conditions for the onset of instability in terms of a critical Deborah number.

Some theoretical works can be found in the literature: Öztekin *et al.* [139] and Olagunju [136] used a multi-mode viscoelastic model and the Oldroyd-B model, respectively, to study instabilities in cone-and-plate geometries. Öztekin [138] also used the Oldroyd-B model to theoretically predict instabilities in parallel-plate devices. Further analysis and discussion about this elastic instability in these geometries can be found in [96].

### 1.8.4 Interfacial instabilities

Now we focus on reviewing interfacial instabilities present in viscoelastic liquids, which are of major concern in many practical applications that involve *multi-layer flows*, i.e. the flow of inmiscible liquids that are in contact but in distinct layers (for instance, in polymer processing such as coating, coextrusion and others). The main purpose of the applications that involve this kind of flows is to obtain materials that can combine properties of two (or more) different components. For these materials, uniformity is desired and thus, instabilities must be avoided.

The interfacial instabilities brought the attention of researchers: in 1991, Yih [186] studied the stability of two fluids with different viscosities in both Couette and Poiseuille flows; in 1987, Waters *et al.* [171] carried out a stability analysis of two Oldroyd-B liquids flowing in distinct layers in Couette flow and in 1991, Chen [36] did a similar research but using and Upper-Convected Maxwell (UCM) model instead. Further analysis of instabilities of Newtonian fluids and UCM liquids in Couette flow was carried out by Renardy [152, 153]. All these papers have something in common: the instabilities occur if stratification of fluid properties is present (i.e. differences in density, viscosity and elasticity).

However, Chen [36] found that Waters [171] got erroneous interfacial conditions which led him to wrong conclusions about the effect of elasticity on the instability. After correcting the boundary conditions, Chen demonstrated that instabilities can occur in fluids having matched viscosities and densities in Couette flow at low Reynolds number and this is due to a *jump* in the first normal stress difference $N_1$ at the fluid-fluid interface, $\kappa$. However, the elastic stratification can be stabilising or destabilising, depending on the volume ratios of both liquids. The mechanism of this instability is discussed in detail by Hinch *et al.* [80]. Similar results were found by Wilson & Rallison, who studied pressure-driven channel flow of two-layer Oldroyd-B fluids [120, 179].

Wilson & Rallison [181] extended the previous theoretical work and they found the presence of a *co-extrusion instability* (i.e. an instability whose mechanism depends on the jump in $N_1$ at the interface) in inertialess channel-flow of elastic liquids with continuously stratified properties (i.e. a continuous variation of stress relaxation time or polymer concentration over a thin enough region).

Other researchers have focused on studying the effect of shear-thinning behaviour in two-layer flows: for instance, Khomami [88] studied instabilities in channel-flow and Waters & Keely in Couette flow [171]. Experimental work has also been carried out (see [89,102,173], to name a few) and they have observed some of the theoretical predictions made by the previously mentioned articles.

Recent works have been focused on, for instance, studying both pressure-driven channel and pipe flows of Oldroyd-B and UCM liquids having matched viscositites at very high Weissenberg numbers [119,121], the interfacial instability in a pressure-driven two-layer flow with moving boundaries (Couette-Poiseuille flow) of viscoelastic fluids [40] and the effect of the presence of a surfactant on the coextrusion instability [141].

### 1.8.5 Instabilities in channel flow of shear-thinning viscoelastic fluids.

One of the most important characteristics of polymers and other complex fluids is their shear-thinning behaviour (see section 1.4), which can be caused by disentanglement of molecular chains during flow. This complex behaviour (along with viscoelasticity) is encountered in multiple industrial processes, such as polymer processing.

The steady Poiseuille flow of these kinds of fluids in different geometries, such as pipes or channels, is of great interest and it has been extensively studied. However, under determined conditions, the flow of these materials might become unstable. In this subsection, we will review some of the theoretical and experimental works about stability in channel flows.

The stability of inertialess planar Poiseuille flow (or pressure-driven channel flow) of Maxwell (liquids that obey the UCM model) and Oldroyd-B fluids (see section 1.6.2) was studied first by Ho & Denn [81] in 1977. They found theoretically that the flow is linearly stable but the stability can be *weak* at high Weissenberg number values.

In 2004, Meulenbroek *et al.* [117] showed both experimentally and theoretically that Poiseuille flow of UCM fluids can exhibit a nonlinear *subcritical* instability (i.e. behaviour seen in polymers where the flow is linearly stable but non-linearly unstable) due to normal stress effects. Atalik *et al.* [4] found similar results for the Oldroyd-B and other viscoelastic models. These subcritical instabilities are also seen in Plane Couette [1, 127, 149] and planar Poiseuille flows [19, 126]. Inertial instabilities of inelastic shear-thinning fluids have also been the subject of study in the past [34, 134, 135].

The previously mentioned works considered only channel flow of either purely elastic liquids (with no manifestation of other complex rheological behaviours) or of inelastic shear-thinning fluids. Wilson & Rallison [180] were the first ones to study theoretically the stability of pressure-driven channel flows of shear-thinning viscoelastic fluids. Using a White-Metzner fluid having power-law viscosity, they found a purely elastic instability (which differs from the curved streamlines and the interfacial instabilities seen in sections 1.8.2 and 1.8.4), whose mechanism involves both strong variations of the normal stresses close to the channel-wall and a stress relaxation time $\lambda_R$ that depends instantaneously on the shear rate. More specifically, the flow becomes linearly unstable if the power-law exponent is smaller than 0.3, which is the case of a fluid with a high degree of shear-thinning behaviour.

No experimental evidence of their predicted instability was reported until 2015, where Bodiguel *et al.* [16] observed experimentally a purely elastic instability similar to the one predicted by Wilson & Rallison [180]. Bodiguel studied channel flows of highly shear-thinning viscoelastic polymeric solutions (with shear-thinning power-law exponent equal to 0.21) at different flow rate values. They found that above a critical shear stress value, the experimentally measured velocities no longer match the theoretical predictions. In addition, they detected strong fluctuations of the velocity field along the channel and they were able to measure a velocity component in the gradient direction. A more detailed analysis is given in chapter 2.

The major difference between Wilson and Bodiguel research is that the latter studied channel-flows of fluids with non-constant shear modulus $G(\dot{\gamma})$. Motivated by this, Wilson & Loridan [178] extended the previous theoretical work, where they used a constitutive model that could match the rheometry of the fluid used by Bodiguel [16]. Despite the many limitations of their model (which we will discuss in chapter 3), they found a reasonable agreement between theoretical predictions and experiments.

Similar experiments were carried out by Poole [147] in 2016, who studied pipe and channel flows of viscoelastic polymer solutions that exhibit shear-thinning behaviour. The results obtained by Poole are identical to the ones reported by Bodiguel: at high flow rates, evidence of an elastic instability is seen for both geometries.

Picaut *et al.* [144] also studied experimentally the effect of shear-thinning behaviour on the flow stability of viscoelastic entangled polymer solutions being extruded through capillaries with different aspect ratios $R/L$ ($R$ and $L$ are the radius and length, respectively), and they found that the flow becomes linearly unstable above a critical value of Weissenberg number. Most importantly, they found that the nature of the instability is controlled by the degree of shear-thinning of the fluid.

### 1.8.6 Instabilities in shear-banded flows

The phenomenon of shear banding has been probed using a huge variety of techniques, such as rheometry, velocimetry, flow birefringence and others. However, many of the data obtained experimentally for shear-banded flows of wormlike micellar solutions exhibit spatio-temporal fluctuations in . As Fardin [58] states, these fluctuations could be caused by either 1) a purely elastic bulk instability of the high shear rate band, 2) interfacial instability between the bands or 3) wall slip [9, 60, 105–107].

Similarly to the instabilities present in polymeric solutions discussed in the previous sections, wormlike micellar solutions with and without shear-banding are susceptible to the development of elastic instabilities and turbulence. These flow instabilities driven by elasticity have been observed in micellar solutions in different geometries, such as Taylor-Couette rheometers [57, 104, 123], cone-and-plate [26], microchannel [72, 90, 132] and pipe flows [184], to name a few. We will review a few of the articles focusing mainly on the shear-banding phenomenon.

Early work by López-González *et al.* [82, 106, 107] demonstrated, using magnetic-resonance velocimetry techniques, the existence of erratic motions in the interface between bands in Couette flow, which are correlated to shear stress fluctuations. By analysing individual velocity profiles, they also showed that the magnitude of local velocity fluctuations was much larger in the high shear-rate band. Similar results were observed by Manneville *et al.* [105, 112]. In these experiments, most of the data revealed a strong correlation between the slip dynamics at the moving wall and the bulk dynamics. However, they could not distinguish which of these phenomena was driving the other one.

For the case of microchannels, Nghe *et al.* [132] studied the shear-banding flow of a micellar surfactant solution and they found an instability of the interface between the bands. More specifically, they observed undulations along the interface in the gradient/neutral plane. Similar behaviour was observed in pipe Poiseuille flow of a wormlike micellar solution [184].

These experimental observations have motivated a huge number of rheologists to develop theoretical research. For instance, linear stability analysis of the diffusive Johnson-Segalman model in both planar and curved Couette geometries carried out by Fielding [63]. She showed that, depending on the level of the cell curvature and on the material's constitutive properties, it is possible to find either a bulk viscoelastic Taylor-Couette instability in the high shear rate band driven by large values of $N_1$ or an instability of the interface between the bands driven by a jump in $N_2$ across it. Nicolas & Morozov [133] found similar results in Taylor-Couette flow: they found that at the beginning of the stress plateau (where the proportion of the high shear rate band is small), an interfacial instability is present, while most of the plateau is occupied by a bulk instability.

Unstable shear banded flows have also been studied theoretically by Fielding & Wilson [61, 177] in planar Couette flow of both diffusive and non-diffusive Johnson-Segalman fluids. For the non-diffusive case, they found that the flow is unstable to long waves for most of the arrangements between the bands, while weak diffusion has a small stabilising effect. In addition, they identified two key ingredients that cause the interfacial instability predicted by them: a jump in the first normal stress difference at the interface and a discontinuity in the shear rate.

The stability of pressure-driven channel flows of shear-banding micellar solutions was also studied by Wilson & Filelding [65] and by Cromer *et al.* [44]; the former used a diffusive Johnson-Segalman model and the latter a two-species reptation-reaction network model. Both works predicted an interfacial instability similar to the one described in [61, 177]. The disadvantage of these works, as discussed before, are the limitations of the models used by them (see section 1.7.3.3).

Lastly, a recently published paper by Renardy *et al.* [154] studied the stability of two-dimensional plane Couette flow of a viscoelastic fluid with thixotropic yield stress behaviour that exhibits the shear-banding phenomenon. Using a thixotropic model that can describe non-monotonic behaviour of the flow curve, and in which the yield stress arises naturally as a limiting case of the model itself [94, 151], they found a bulk mode in the yielded phase (i.e. in the high-shear rate band) which is present even in the absence of shear banding. When an interface appears, interfacial and bulk modes are present, but the latter ones become the dominant mechanism of instability in shear-banded flows. They also showed that interfacial modes are driven by a jump in the first normal stress difference in the interface between the bands.

# Chapter 2

# Theoretical formulation of channel flow stability problems

## 2.1 Introduction

In the previous chapter, we briefly described some of the extensive literature on both experimental evidence and theoretical research of flow instabilities of complex fluids. This field, which is of great interest for rheologists, is continuously growing over time thanks to the development of both new experimental techniques and numerical simulations, which have helped to understand the mechanism behind some of these instabilities. However, there are still multiple questions that remain unanswered and plenty of unexplored topics, which are the main motivations of the present work. From now on, we will study theoretically the instabilities of elastic fluids. More specifically, we will focus on instabilities in pressure-driven channel flow of complex fluids such as polymeric liquids and wormlike micellar solutions, which exhibit highly non-linear rheological behaviour.

In this chapter, we provide with an introduction to the general theoretical approach that will be taken to study flow stability in planar Poiseuille flow of elastic fluids, which consists of the following elements: governing equations of the motion of the fluid, section 2.2, experimental information about the fluid behaviour in simple shear flow, section 2.3, geometry in 2.4, base-state quantities, section 2.5, nondimensionalisation of the governing equations in section 2.6, linear stability theory and perturbed equations of motion in 2.7, boundary conditions that need to be satisfied, section 2.8 and a numerical method in order to solve the stability problem, described in 2.9.

## 2.2 Governing equations

As mentioned in section 1.5, we need to solve the governing equations of the motion of an incompressible fluid, which are the continuity and momentum-conservation equations (1.10)–(1.11) along with a constitutive equation that relates the stress field with the deformation tensor.

For comparison purposes, we solve the governing equations of four different fluids in order to obtain their velocity profile in pressure-driven channel flow. Three of the fluids that will be briefly studied are inelastic liquids: Newtonian, shear-thinning and Bingham fluids, whose scalar constitutive equations are:

$$\sigma = \mu\,\dot{\gamma} \qquad \sigma = \mu_0\,\dot{\gamma}^N \qquad \dot{\gamma} = \begin{cases} 0 & \sigma \leq \sigma_y \\ \dfrac{1}{\mu_0}\,(\sigma - \sigma_y) & \sigma > \sigma_y. \end{cases} \tag{2.1}$$

The parameter of the models were described in sections 1.6.1, 1.6.1.1 and 1.6.1.3. Considering that $Pa$ is the unit of stress $\sigma$ and $\dot{\gamma}$ has units of $s^{-1}$, the coefficients $\mu$ and $\mu_0$ have therefore units of $Pa\,s$ and $Pa\,s^N$, respectively.

The fourth fluid, on the other hand, is of viscoelastic nature, and its constitutive equation is the White-Metzner model (see section 1.6.2.3). However, we use here a version of the model that is in terms of the conformation tensor $\underline{\underline{A}}$ (defined in section 1.6.2.4), which adopts the following form:

$$\underline{\underline{\tau}} = -p\underline{\underline{I}} + \underline{\underline{\sigma}} = -p\underline{\underline{I}} + G_M\,\underline{\underline{A}} \tag{2.2}$$

$$\overset{\nabla}{\underline{\underline{A}}} = \frac{\partial \underline{\underline{A}}}{\partial t} + \underline{u}\cdot\nabla\,\underline{\underline{A}} - \underline{\underline{A}}\cdot(\nabla\,\underline{u}) - (\nabla\,\underline{u})^{\top}\cdot\underline{\underline{A}} = -\frac{1}{\lambda_R(\dot{\gamma})}(\underline{\underline{A}} - \underline{\underline{I}}), \tag{2.3}$$

where $G_M$ is a constant shear modulus, $\overset{\nabla}{\underline{\underline{A}}}$ is the Upper-Convected derivative of the conformation tensor, $\nabla\,\underline{u}$ and $(\nabla\,\underline{u})^{\top}$ are the velocity gradient and its transpose, respectively and $\lambda_R(\dot{\gamma})$ is the stress relaxation time that depends instantaneously on the shear rate:

$$\lambda_R(\dot{\gamma}) = K_M\dot{\gamma}^{n-1}, \tag{2.4}$$

where $K_M$ and $n \in [0,1]$ are relaxation-time coefficients. It is important to point out that in the absence of flow, $\underline{\underline{A}} = \underline{\underline{I}}$, the constant $G_M$ will be absorbed into the isotropic pressure $P$. There are multiple reasons why we chose this model as a study case. Firstly, it is one of the simplest models used to describe the shear-thinning viscoelastic behaviour of polymer solutions. Secondly, it will help us as an introduction to the content of the next chapters. And lastly, this model was used by Wilson & Rallison [180] to study elastic instabilities in channel flow, and that research is the theoretical starting point of this dissertation.

## 2.3 Simple shear flow

Simple shear flow (section 1.2.2) is a fundamental rheological test that provides us with useful information about the fluid's behaviour in simple conditions, which can give us clues of what to expect in more complex rheometric flows. In all the following chapters, a simple shear flow section will be given, in which we will briefly describe the rheological behaviour of the complex fluid in question, including the material functions such as the viscosity and the normal stress differences.

Using Cartesian coordinates $(x, y)$, and considering steady simple shear flow conditions, $\underline{u} = \dot{\gamma} y \underline{e}_x$ with $\dot{\gamma} > 0$, it is possible to obtain $\sigma(\dot{\gamma})$, $\eta(\dot{\gamma})$, $N_1(\dot{\gamma})$ and $N_2(\dot{\gamma})$. For the case of inelastic liquids, the equations (2.1) happen to be the equations that describe the stress fields in steady shear flow conditions, meanwhile equations (1.26) and (1.29) are the viscosity functions for a shear-thinning fluid and a Bingham fluid, respectively (for the Newtonian case, $\eta = \mu$). The other material functions, $\Psi_1(\dot{\gamma})$ and $\Psi_2(\dot{\gamma})$ (equations (1.13)) have a zero value, as these fluids are inelastic.

On the other hand, the stress tensor for the elastic fluid is derived from the White-Metzner model, equations (2.2)–(2.3):

$$\underline{\underline{\tau}} = \begin{pmatrix} -P_0 + G_M\,(1 + 2\,\lambda_R^2\,\dot{\gamma}^2) & \lambda_R\,G_M\dot{\gamma} \\ \lambda_R\,G_M\dot{\gamma} & -P_0 + G_M \end{pmatrix}, \tag{2.5}$$

from which the material functions can be calculated as:

$$\eta(\dot{\gamma}) = \frac{\sigma_{12}}{\dot{\gamma}} = \lambda_R \, G_M \qquad \Psi_1 = \frac{\tau_{11} - \tau_{22}}{\dot{\gamma}^2} = 2 \, G_M \, \lambda_R^2, \qquad \Psi_2 = \frac{\tau_{22} - \tau_{33}}{\dot{\gamma}^2} = 0. \quad (2.6)$$

From the equations above, we can see that the viscosity of an elastic fluid is simply the product of the shear modulus and the stress relaxation time. Most importantly, we can see that the first normal stress difference coefficient $\Psi_1$ has a non-zero value and a quadratic dependence on $\lambda_R$. However, notice that $\Psi_2 = 0$. In fact, most of the elastic models that we will use predict the same result for $\Psi_2$ and thus, the conclusions obtained in the present work will not consider the effects of $\Psi_2$ on the flow instabilities.

If we now substitute the power-law function (2.4), into equations (2.7), we obtain:

$$\eta(\dot{\gamma}) = G_M \, K_M \, \dot{\gamma}^{n-1} \qquad \Psi_1 = 2 \, G_M \, K_M^2 \, \dot{\gamma}^{2(n-1)} \qquad (2.7)$$

We are interested in studying shear-thinning behaviour, so $n < 1$. For these cases, equations (2.7) show a decrease in both $\eta$ and $\Psi_1$. However, as illustrated in section 1.6.1.1, the viscosity and the first normal stress difference coefficient will tend to infinity as the shear rate tends to zero. Therefore, these power-law functions cannot predict the viscosity plateaus at low and high $\dot{\gamma}$ values (described in section 1.4.1), which are important features of many complex fluids. Despite these limitations, we will still carry the work out using these power-law functions, as they allow us to study shear-thinning viscoelastic fluids using as few parameters as possible. More realistic models will be used in Chapter 4.

## 2.4 Geometry: pressure-driven channel flow

The geometry we are interested in studying here is planar Poiseuille flow, also known as pressure-driven channel flow, sketched in figure 2.1. This rheometric flow (initially described in section 1.8.1) has been used to investigate the flow of complex fluids in different microrheological devices.

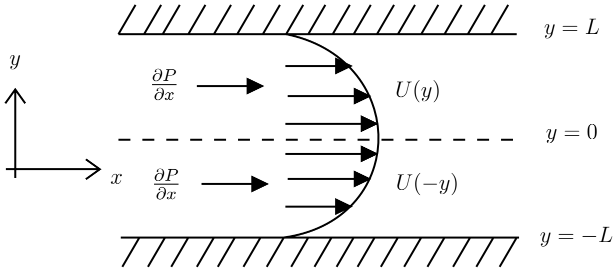

Figure 2.1: Flow geometry: two-dimensional pressure-driven channel flow or planar Poiseuille flow.

The steady planar Poiseuille flow is laminar and consists of two infinitely long, parallel plates separated by a fixed distance ($2L$). The plates will remain at rest and the flow will be caused by a pressure gradient $\mathscr{P} \equiv -\mathrm{d}P/\mathrm{d}x$ in the $x$-direction, giving, as a result, a symmetric velocity profile $U$ dependent on the gradient-direction-position $y$, whose maximum value is located at the centreline ($y = 0$) and non-slip conditions are satisfied at the wall, $U(\pm L) = 0$. Lastly, if the fluid is moving in horizontal motion, gravitational effects are neglected or if the fluid is moving in vertical motion, they can be rolled into the pressure gradient term as $\mathscr{P} \equiv -\mathrm{d}P/\mathrm{d}x - \rho g x$.

## 2.5 Base state solutions

We assume a steady, unidirectional flow profile $\underline{u} = U(y)\underline{e}_x$, whose gradient is expected to be negative $U'(y) < 0$ if $y > 0$. By symmetry, we consider only the upper half-channel $0 \leq y \leq L$, and thus, $U'(0) = 0$ (here, the prime will denote differentiation with respect to the coordinate $y$). With the conditions established in section 2.4, the momentum balance in $x$-direction (1.11) becomes:

$$\frac{\mathrm{d}\sigma_{12}}{\mathrm{d}y} + \mathscr{P} = 0. \tag{2.8}$$

From (2.8), we can deduce that the shear stress for any fluid in planar Poiseuille flow is proportional to the pressure gradient. In fact, by integrating the equation and discarding the constant of integration by symmetry arguments, the stress takes the following form:

$$\sigma_{12} = -\mathscr{P}\, y. \tag{2.9}$$

## Inelastic fluids

The equation above can provide us with information about the velocity field of a fluid, as long as we have information about the shear stress $\sigma_{12}$. For our three inelastic liquids, this information is given by equations (2.1). Defining $\dot\gamma_0$ as the base state shear-rate, $\dot\gamma_0 = |U'|$, we solve the differential equation for $U(y)$ and we obtain the following profiles:

### Newtonian fluid

$$U(y) = \left(\frac{\mathscr{P}}{\mu}\right)\left(\frac{1}{2}\right)\left[L^2 - |y|^2\right], \tag{2.10}$$

$$\dot\gamma_0 = |U'| = \left(\frac{\mathscr{P}\,|y|}{\mu}\right) \tag{2.11}$$

### Shear-thinning fluid

$$U(y) = \left(\frac{\mathscr{P}}{\mu_0}\right)^{1/N}\left(\frac{N}{N+1}\right)\left[L^{(N+1)/N} - |y|^{(N+1)/N}\right] \tag{2.12}$$

$$\dot\gamma_0 = |U'| = \left(\frac{\mathscr{P}\,|y|}{\mu_0}\right)^{1/N} \tag{2.13}$$

**Bingham fluid**

$$U(y) = \begin{cases} \left(\dfrac{\mathscr{P}}{\mu_0}\right)\left(\dfrac{1}{2}\right)\left[L^2 - |y|^2\right] + \dfrac{\sigma_y}{\mu_0}\left[L - |y|\right] & h \leq y \leq L \\ \left(\dfrac{\mathscr{P}}{\mu_0}\right)\left(\dfrac{1}{2}\right)L^2 + \dfrac{\sigma_y L}{\mu_0} - \dfrac{3}{2}\dfrac{\sigma_y^2}{\mathscr{P}\mu_0} & 0 \leq y \leq h. \end{cases} \tag{2.14}$$

$$\dot{\gamma}_0 = |U'| = \begin{cases} \left(\dfrac{|y|}{\mu_0}\right)(\mathscr{P} + \sigma_y) & h \leq y \leq L \\ 0 & 0 \leq y \leq h. \end{cases} \tag{2.15}$$

Equations (2.10), (2.12) and (2.14) are the velocity profiles in pressure-driven channel flow of a Newtonian, shear-thinning and Bingham fluid, respectively. For the latter case, $|y| = h$ is the location in the channel that separates the *unyielded region* (where the fluid behaves as a rigid solid) from the *yielded region* (where the material flows). In order to see continuity of $U(y)$ between the two regions, $h = \sigma_y/\mathscr{P}$.

Also, it is important to mention that the units of the coefficients $\mu$, $\mu_0$ and $\sigma_y$ are $Pa\, s$, $Pa\, s^N$ and $Pa$, respectively, which will lead to units of $m/s$ for the velocity $U(y)$. Although we have three different fluids, we can see that there are some similarities between their velocity profiles; for instance, the centreline velocity $U_0 = U(y = 0)$ for each fluid has at least one term that is proportional to $(\mathscr{P}/\mu)L$ and the shear rate at the centreline has a zero-value (see equations (2.11), (2.13) and (2.15)). Notice that we recover the Newtonian velocity profile if $N = 1$ and $\sigma_y = 0$.

In figure 2.2a), we illustrate some examples of velocity profiles for each fluid using equations (2.10)–(2.14). For their calculation, the viscosity coefficients are taken to be equal to the Newtonian one $\mu = \mu_0 = 1\,\text{Pa s}$, and the pressure gradient is the same for all cases $\mathscr{P} = 10\,\text{Pa/cm}$. We use $N = 0.7$ for the shear-thinning fluid and a yield stress value $\sigma_y = 5\,\text{Pa}$ for the Bingham fluid. Lastly, we assume a channel half-width $L = 1\,\text{cm}$.

We notice that the shape of the velocity profiles is different for each fluid: a)

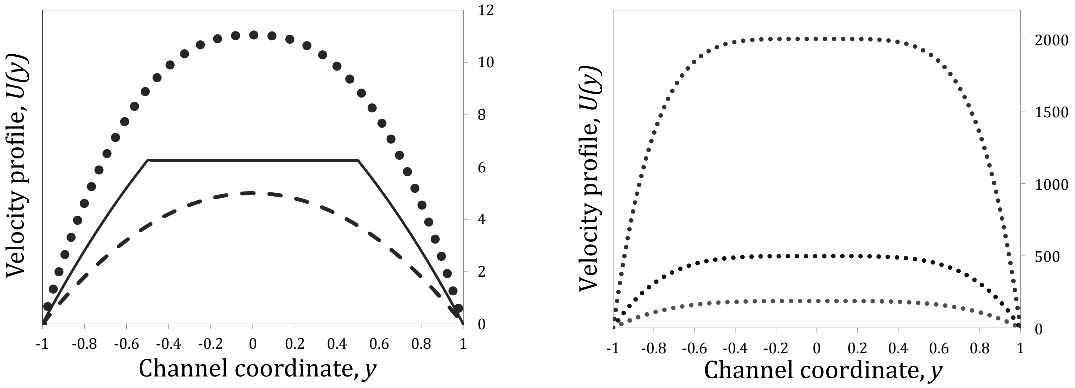

(a) Newtonian, shear-thinning and Bingham (b) Shear-thinning fluids with different $N$

Figure 2.2: Velocity profiles in pressure-driven channel flow calculated using equations (2.10)–(2.14) with fixed $\mathscr{P} = 10\,\mathrm{Pa/cm}$. Figure (a): Newtonian (dashed line), Bingham (solid line) and shear-thinning (dotted line) fluids. Figure (b): shear-thinning fluids with different $N$; from bottom to top, $N = 0.35, 0.30$ and $0.25$.

the Newtonian case has the typical parabolic shape, b) the Bingham fluid exhibits a *plug-flow* near the centreline, i.e. an unyielded region in which the fluid behaves a solid. At $|y| > h = 0.5$, we find the yielded region. And for the last case, c) the shear-thinning fluid has a smooth shape like the Newtonian flow but with higher-order dependence on $y$, causing the fluid to move much faster compared to the rest.

In figure 2.2b), we explore the dependence of the velocity profile on the power-law coefficient $N$, so we take three different values of highly shear-thinning fluids, $N = 0.35, 0.30$ and $0.25$. We can see that for a decrease of $N$ (from bottom to top), the centreline velocity of the fluid is becoming higher and higher. Moreover, notice how a plug-flow like region is forming near the centreline: this is due to an increase in viscosity at low shear rate values as $N$ decreases. This is clearly seen in the centreline velocity $U(0)$ equation (2.16) obtained from (2.12):

$$U(y) = \left(\frac{\mathscr{P}}{\mu_0}\right)^{1/N} \left(\frac{N}{N+1}\right) \left[L^{(N+1)/N}\right]. \tag{2.16}$$

### White-Metzner fluid

The reason we illustrate the base state solutions of some inelastic fluids is because we will encounter some of these behaviours in the next chapters. From now on, we will focus only on obtaining the base state solutions for elastic fluids that are of interest for the present work, and we start with the White-Metzner fluid.

Solving the governing equations (2.2)–(2.4) and (2.8) for planar Poiseuille flow conditions, we obtain the following base state solutions:

$$U(y) = \left(\frac{\mathscr{P}}{G_M\,K_M}\right)^{1/n}\left(\frac{n}{n+1}\right)\left[L^{(n+1)/n} - |y|^{(n+1)/n}\right] \tag{2.17}$$

$$\dot{\gamma}_0 = |U'| = \left(\frac{\mathscr{P}\,|y|}{G_M\,K_M}\right)^{1/n} \qquad N_1 = 2\,G_M^{-1}\,\mathscr{P}^2\,|y|^2. \tag{2.18}$$

It can be clearly seen that the velocity profile (2.17) derived using the White-Metzner constitutive equation is identical to the one obtained for the inelastic shear-thinning fluid (2.12). This observation gives us an important conclusion: elasticity does not have any effect on the steady velocity profile. However, it is important to distinguish the differences between the two fluids, which is the reason we are using different power-law coefficients ($N$ is for the inelastic case and $n$ for the viscoelastic fluid). More importantly, the White-Metzner fluid has a non-zero first normal stress difference, see (2.18), which tells us that the there is extra tension in the direction of the flow.

## 2.6 Nondimensionalisation of the governing equations

In the analysis of flow stability of complex fluids, it is convenient to carry out a *nondimensionalisation* of the governing equations, i.e. remove the units from an equation involving physical quantities in order to reduce the number of parameters, which helps to simplify the problem.

The first step is to scale the physical quantities of our system: we scale lengths by the channel half-width $L$, times by the average shear rate in the channel $(U_0/L)^{-1}$, velocities by the centreline velocity $U_0$, and stresses by $\eta_N(U_0/L)$, where $\eta_N$ is a typical viscosity of the fluid being studied, and it is entirely up to the author to choose a characteristic value of $\eta_N$. During all the chapters of this thesis, we will be using different values of $\eta_N$, but for the case of a White-Metzner fluid, we choose $\eta_N = G_M K_M (U_0/L)^{n-1}$.

With the scaling proposed above, the continuity, momentum and White-Metzner constitutive equations become dimensionless:

$$\underline{\nabla} \cdot \underline{u} = 0 \tag{2.19}$$

$$Re\Big(\frac{\partial \underline{u}}{\partial t} + \underline{u} \cdot \underline{\nabla u}\Big) = \underline{\nabla} \cdot \underline{\underline{\tau}} \tag{2.20}$$

$$\underline{\underline{\tau}} = -P\underline{\underline{I}} + \underline{\underline{\sigma}} = -P\underline{\underline{I}} + \frac{1}{W}\underline{\underline{A}} \tag{2.21}$$

$$\overset{\nabla}{\underline{\underline{A}}} = -\frac{1}{\mathcal{W}}(\underline{\underline{A}} - \underline{\underline{I}}) \tag{2.22}$$

$$\mathcal{W} = W\dot{\gamma}^{n-1} \qquad W = K_M\Big(\frac{U_0}{L}\Big)^n \qquad Re = \frac{\rho U_0 L}{G_M K_M (U_0/L)^{n-1}}, \tag{2.23}$$

where $\mathcal{W}$ is the dimensionless stress-relaxation time. From the nondimensionalisation, we have obtained two important dimensionless numbers that will be of extremely great use in this dissertation: the Reynolds and the Weissenberg numbers, shown in equation (2.23). The former compares the inertial effects to the viscous ones and the latter is the ratio between elastic and viscous forces. Here we are interested in inertialess flows, and thus, $Re = 0$. The importance of this assumption is that the left-hand side of equation (2.20) vanishes, which will simplify our calculations.

Using the now dimensionless governing equations, and considering only the up-

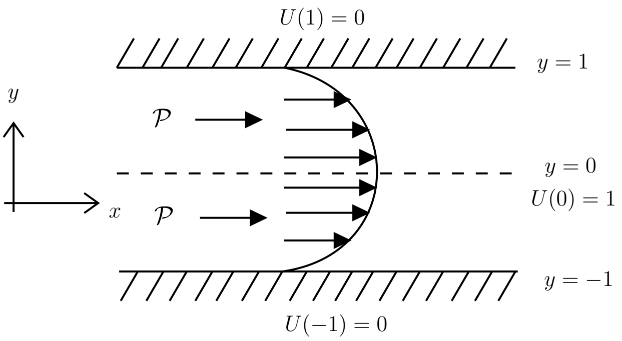

Figure 2.3: Dimensionless flow geometry.

per half-channel $0 \leq y \leq 1$, we look for the dimensionless base state quantities that satisfy the non-slip $U(1) = 0$ and channel-symmetry $U'(0) = 0$ conditions (see figure 2.3). Additionally, we want the velocity profile of all the fluids that will be studied here to be bounded $0 \leq U(y) \leq 1$, so an additional boundary condition is $U(0) = 1$. The dimensionless base state solutions in pressure-driven channel flow of a White-Metzner fluid become:

$$\underline{u} = (U(y), 0) \qquad U(y) = 1 - y^{(n+1)/n} \qquad \dot{\gamma}_0 = |U'| = -U' = \left(\frac{n+1}{n}\right) y^{1/n}. \tag{2.24}$$

$$\mathcal{W}_0 = W \dot{\gamma}_0^{n-1} = W \left(\frac{n+1}{n}\right)^{n-1} y^{(n-1)/n} \tag{2.25}$$

$$\underline{\underline{A}} = \begin{pmatrix} A_{11} & A_{12} \\ A_{21} & A_{22} \end{pmatrix} = \begin{pmatrix} 1 + 2\,W^2\,\mathcal{P}^2\,y^2 & -W\mathcal{P}y \\ -W\mathcal{P}y & 1 \end{pmatrix}. \tag{2.26}$$

Here, $\mathcal{W}_0$ is the base state relaxation time and the tensor $A_{ij}$ is the conformation tensor, which describes the stretch in molecular chains. A new quantity has also been defined, $\mathcal{P}$, which is the dimensionless pressure gradient, whose value is dictated by the normalisation of the velocity profile ($U(0) = 1$):

$$\mathcal{P} = \left(\frac{n+1}{n}\right)^n. \tag{2.27}$$

The pressure $P$ can be found by solving the momentum balance equation in the

$y$-direction:

$$P = P_\infty - \mathcal{P}x + \frac{1}{W}, \tag{2.28}$$

where $P_\infty$ is a baseline pressure. Lastly, the base state polymeric stress tensor is:

$$\underline{\underline{\sigma}} = \begin{pmatrix} \sigma_{11} & \sigma_{12} \\ \sigma_{21} & \sigma_{22} \end{pmatrix} = \begin{pmatrix} W^{-1} + 2\,W\,\mathcal{P}^2\,y^2 & -\mathcal{P}y \\ -\mathcal{P}y & W^{-1} \end{pmatrix}. \tag{2.29}$$

In figure 2.4, the dimensionless velocity profiles calculated using (2.24) are sketched for different values of $n$. As we can notice, one of the advantages of using dimensionless equations is that we do not need specify the values of pressure gradient or the width of the channel to calculate $U(y)$ (unlike the dimensional equation (2.17)).

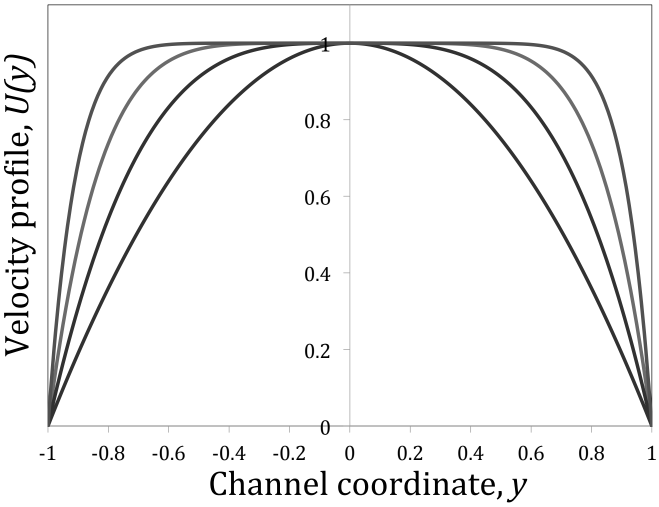

Figure 2.4: Dimensionless velocity profiles calculated using equation (2.24). From bottom to top: $n = 1, 0.4, 0.2$ and $0.1$. For $n = 1$, we observe a parabolic profile, meanwhile smaller values of $n$ exhibit a plug-like flow through most of the channel.

# 2.7 Linear stability

## 2.7.1 General description of the linear stability problem

Now we briefly describe the fundamentals of linear stability theory. For a full detailed analysis, see [83,174]. In a few words, *linear stability analysis* consists of assuming the existence of disturbances to a *base state* (also called a background, initial or equilibrium state), which is the flow whose stability is investigated. For our case, the base state consists of the steady velocity profile $U(y)$ and other flow quantities defined in equations (2.24)–(2.29). These quantities are solutions of our governing equations and thus, are the reference flow around which the stability analysis will be performed.

Some of the instabilities of complex fluids described in section 1.8 are caused by disturbances (such as noise), so we are interested in studying the evolution of these disturbances superimposed on the selected base state. Taking this into account, a system is said to be *stable* if it remains close to the base state after being disturbed by sufficiently small initial perturbations. On the other hand, if these perturbations drastically alter the flow evolution, the system is *unstable*.

In the context of linear stability theory, the perturbations are restricted to be *infinitesimal*, which will be useful to linearise around the base state to arrive at a new set of equations for the linear stability problem. Mathematically speaking, we add an infinitesimal perturbation $\epsilon \ll 1$ to the base flow, modifying every flow variable (velocity, viscosity, stress relaxation time, pressure, conformation and stress tensors) in a similar way. To illustrate this, we take velocity as an exemplar:

$$\underline{u} = (U, 0) + \epsilon(\hat{u}, \hat{v}), \tag{2.30}$$

where the perturbation quantities $\hat{u}$ and $\hat{v}$ can depend on space and time. We can then expand our governing equations (continuity, momentum and constitutive equations) in powers of $\epsilon$. Discarding terms of order $\epsilon^2$ allows us to investigate the *linear* stability of the system. The leading-order terms involve only base-state quantities, which are derived by solving the governing equations in steady-pressure-driven channel flow conditions. The remaining terms are linear in perturbation quantities, and because the base state variables are independent of $x$ and $t$, it is helpful to take a Fourier transform with respect to those variables. We then use the theory of *normal modes* to argue that perturbations of a given wavelength do not interact (at linear order) with those of any other wavelength. This is equivalent to assuming that our perturbation quantities are of the form:

$$\hat{u}(x, y, t) = \mathrm{Real}\left(u(y) \exp\left[\mathrm{i}kx - \mathrm{i}\,\omega t\right]\right), \tag{2.31}$$

$$\hat{v}(x, y, t) = \mathrm{Real}\left(v(y) \exp\left[\mathrm{i}kx - \mathrm{i}\,\omega t\right]\right), \tag{2.32}$$

in which i is the imaginary number ($\mathrm{i} = \sqrt{-1}$), $k$ is the wavenumber and $\omega$ the frequency. These perturbation quantities are then substituted into the leading-order governing equations, where all the spatial ($x$-direction) and temporal derivatives become terms that are proportional to i$k$ and i$\omega$, respectively. The resulting system is a set of linear ordinary differential equations (ODE's).

For simplicity, we will find it convenient to introduce an extremely useful function commonly used to solve two-dimensional flow problems in fluid mechanics, which is called the *streamfunction*, $\psi$. This function will allow us to express the perturbed velocity components $u$ and $v$ as derivatives of $\psi$. By using this definition, we can combine the system of ODE's into a single fourth-order ODE for $\psi$, which is in terms of $k$, $\omega$, the channel coordinate $y$ and the parameters of the constitutive equation. Four boundary conditions are necessary to solve the ODE, which will depend on the flow in question. For our case, we need to establish two boundary conditions at the wall and two at the centreline. We will see that all the boundary conditions will be zero. In this way, the system will be overdetermined for specified $k$ and $\omega$, and therefore, nontrivial solutions will only exist for certain pairs $(k, \omega)$. The boundary conditions, as well as the numerical method used to solve the ODE, will be discussed in the following subsection.

The linear stability problem above is reduced to an *eigenvalue* problem, and there are two ways to proceed to solve it: the *spatial* and the *temporal* stability. We will briefly describe these two approaches, but in this dissertation, we will use the latter case, as this is the most common method used in the literature, which is usually easier.

In spatial stability analysis, a disturbance is imposed upstream at a fixed frequency, and observing its evolution at it moves downstream to see whether it grows. This is achieved by fixing a real value of $\omega$ and solving for complex wavenumber $k$. If $\Im(k) > 0$, the perturbations will grow in space and the flow is unstable.

On the other hand, in the temporal stability analysis, the flow is given a disturbance of fixed wavenumber (real $k$) and its growth in time is found from the complex value of the frequency $\Im(\omega)$. The eigenvalue system is then expressed as $\omega = \omega(k)$, commonly known as the *dispersion relation.* Our goal in the present dissertation is to find either analytically or numerically this function, as it will provide us with information about the flow stability: if the imaginary part of the complex frequency, $\Im(\omega)$ is positive for any value of $k$, then the exponential term of the perturbed quantities (see equation (2.31)) will grow in time, and then the base flow is said to be unstable. The real part of the eigenvalue, $\Re(\omega)$, will provide us with information about the location of the perturbation in the channel.

In the analysis of channel-flow instabilities, we will see that the dispersion relaxation is not only a function of $k$; it will also depend on the fluid properties, such as the level of shear-thinning, elasticity, among others.

### 2.7.2 Perturbation flow

To illustrate the method described above, we carry out the stability analysis of a White-Metzner fluid, whose base state quantities were already calculated (2.24)–(2.29). We now add an infinitesimal perturbation to the base flow:

$$\underline{u} = (U + u\varepsilon, v\varepsilon) \tag{2.33}$$

$$\dot{\gamma} = \dot{\gamma}_0 + \dot{\gamma}_p\varepsilon \tag{2.34}$$

$$P_p = P + p\varepsilon \qquad \mathcal{W} = \mathcal{W}_0 + w\varepsilon \tag{2.35}$$

$$\underline{\underline{A}} = \begin{pmatrix} A_{11} + a_{11}\varepsilon & A_{12} + a_{12}\varepsilon \\ A_{21} + a_{21}\varepsilon & A_{22} + a_{22}\varepsilon \end{pmatrix} \tag{2.36}$$

$$\underline{\underline{\sigma}} = \begin{pmatrix} \sigma_{11} + \Sigma_{11}\varepsilon & \sigma_{12} + \Sigma_{12}\varepsilon \\ \sigma_{21} + \Sigma_{21}\varepsilon & \sigma_{22} + \Sigma_{22}\varepsilon \end{pmatrix}, \tag{2.37}$$

where our perturbed quantities are denoted by either lower case letters ($u$ and $v$ for the velocity components, $\underline{\underline{a}}$ for the conformation tensor, $p$ for the pressure and $w$ for the stress relaxation time), capital case letters ($\underline{\underline{\Sigma}}$ for the polymeric stress tensor) or subscripts ($\dot{\gamma}_p$ for the shear rate).

The reason we are restricting our attention to two-dimensional modes is because according to *Squire's theorem*, we only need to consider two-dimensional $(x, y)$ perturbations in order to determine the first occurrence of instability [53].

As stated in section 2.7.1, we consider a single Fourier mode with the form:

$$\varepsilon = \epsilon \exp[\mathrm{i}\, kx - \mathrm{i}\, \omega t]. \tag{2.38}$$

Now substituting (2.33) and (2.38) into the continuity equation (2.19), we obtain the following:

$$\mathrm{i}\,ku + \frac{\mathrm{d}v}{\mathrm{d}y} = 0. \tag{2.39}$$

And here is where we introduce the concept of the streamfunction, $\psi$, whose mathematical definition is:

$$u = \frac{\partial \psi}{\partial y} \qquad v = -\frac{\partial \psi}{\partial x}. \tag{2.40}$$

For our problem, these equations become:

$$u = \frac{\mathrm{d}\psi}{\mathrm{d}y} \qquad v = -\mathrm{i}\,k\psi, \tag{2.41}$$

and thus, the continuity equation of the perturbed quantities (2.39) is automatically satisfied with the introduction of the streamfunction.

For simplicity, we also introduce the notation D to denote differentiation with respect to $y$. Now we substitute the perturbed forms (2.33)–(2.38) into the governing equations (2.19)–(2.23), and discarding terms of order $\varepsilon^2$, we obtain a linearised system of equations:

$$\underline{\underline{\Sigma}} = \frac{1}{W}\underline{\underline{a}} \tag{2.42}$$

$$\begin{aligned} Re(-\mathrm{i}\omega \mathrm{D}\psi - \mathrm{i}k\psi \mathrm{D}U + \mathrm{i}kU\mathrm{D}\psi) &= -\mathrm{i}kp + \mathrm{i}k\Sigma_{11} + \mathrm{D}\Sigma_{12} &(2.43)\\ Re(-k\omega\psi + k^2U\psi) &= -\mathrm{D}\,p + \mathrm{i}k\Sigma_{12} + \mathrm{D}\Sigma_{22}. &(2.44) \end{aligned}$$

Considering that we are interested in studying inertialess flows, $Re = 0$, the perturbed pressure $p$ can be eliminated from equations (2.42)–(2.44), and the resulting equation is:

$$\mathrm{D}^2 a_{12} + k^2 a_{12} + \mathrm{i}\,k\,\mathrm{D}(a_{11} - a_{22}) = 0. \tag{2.45}$$

The evolution equations for the perturbations $\underline{\underline{a}}$ are:

$$\begin{aligned}(-\mathrm{i}\,\omega+\mathrm{i}\,kU+\mathcal{W}_0^{-1})a_{11} &= \mathrm{i}\,k\psi\mathrm{D}A_{11}+2a_{12}\mathrm{D}U+2A_{11}\mathrm{i}\,k\mathrm{D}\psi \\ &+ 2A_{12}\mathrm{D}^2\psi+\frac{w}{\mathcal{W}_0^2}(A_{11}-1) \qquad (2.46)\\ (-\mathrm{i}\,\omega+\mathrm{i}\,kU+\mathcal{W}_0^{-1})a_{12} &= \mathrm{i}\,k\psi\mathrm{D}A_{12}+a_{22}\mathrm{D}U+A_{11}k^2\psi \\ &+ \mathrm{D}^2\psi+\frac{w}{\mathcal{W}_0^2}A_{12} \qquad (2.47)\\ (-\mathrm{i}\,\omega+\mathrm{i}\,kU+\mathcal{W}_0^{-1})a_{22} &= 2A_{12}k^2\psi-2\,\mathrm{i}\,k\mathrm{D}\psi. \qquad (2.48)\end{aligned}$$

In order to determine the perturbation to the shear-rate, we limit our domain to the upper half of the channel $0 \leq y \leq 1$, in which $\mathrm{D}U < 0$ and thus $\dot{\gamma}_0 = -\mathrm{D}U$. This allows us to calculate $\dot{\gamma}_p$ using the definition of shear rate (1.2):

$$\dot{\gamma}_0+\dot{\gamma}_p\,\varepsilon=\left(2\,[\underline{\underline{D}}_0+\varepsilon\underline{\underline{d}}]:[\underline{\underline{D}}_0+\varepsilon\underline{\underline{d}}]\right)^{1/2}+O(\varepsilon^2).$$

The perturbation shear rate $\dot{\gamma}_p$ and the perturbed form of the stress relaxation time $w$ are:

$$\begin{aligned}\dot{\gamma}_p &= -(\mathrm{D}^2+k^2)\psi, \qquad (2.49)\\ w &= W(n-1)\dot{\gamma}_0^{n-2}\dot{\gamma}_p. \qquad (2.50)\end{aligned}$$

The system defined by equations (2.45)–(2.50) can be combined to give the fourth-ordinary differential equation we need.

## 2.8 Boundary conditions

As stated in section 2.7.1, in order to solve the fourth-order ODE, four boundary conditions are needed. In our channel geometry (see figure 2.3), there are two zero boundary conditions on $\underline{u} = (U + u\varepsilon, v\varepsilon)$ at each wall: *slip velocity* (the fluid moves with the wall's velocity) and *penetration velocity* (flow through the walls). For our case, we consider non-slip and no-penetration boundary conditions for the perturbation flow: $u(1) = 0$ and $v(1) = 0$. In terms of the streamfunction (2.41), they become:

$$\psi = \mathrm{D}\psi = 0 \text{ at } y = \pm 1. \tag{2.51}$$

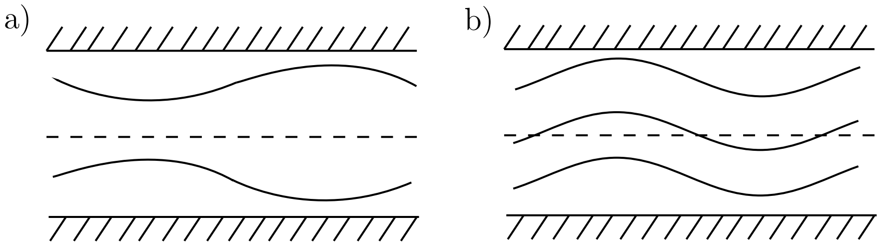

Figure 2.5: Sketch of the shape of the perturbed streamlines for (a) varicose modes, for which $\psi$ is an odd function of $y$; (b) sinuous modes, for which $\psi$ is an even function of $y$.

As we consider only the upper-half channel, $0 \leq y \leq 1$, the remaining two boundary conditions are to be placed on the centreline $y = 0$, and depend on the kind of perturbation that is disturbing the flow. If the perturbation is *sinuous*, there is a *snake-like* motion. Mathematically speaking, the $x$-perturbed velocity at the centreline remains unchanged under the transformation $y \to -y$, and thus, its value is zero, so $\psi$ is an even function of $y$. On the other hand, for a *varicose* perturbation, no cross-channel motion is observed; i.e. there must not be $y$-perturbed velocity on the centreline of the channel, and therefore, $\psi$ is an odd function. To illustrate this, we sketch the shape of the perturbed streamlines for both varicose and sinuous modes in figure 2.5.

Since we are solving a linear problem, any solution $\psi$ can be split into its even and odd components, each of which will also be a solution to our system. For this reason, we will consider separately the two cases of varicose modes and sinuous modes. For each of these, we can solve over the half-channel $0 \leq y \leq 1$ with the appropriate symmetry boundary conditions at $y = 0$:

$$\psi = \mathrm{D}^2\psi = 0 \text{ at } y = 0 \qquad \text{for varicose modes,} \tag{2.52}$$

$$\mathrm{D}\psi = \mathrm{D}^3\psi = 0 \text{ at } y = 0 \qquad \text{for sinuous modes.} \tag{2.53}$$

As we mentioned in section 2.7.1, because all these boundary conditions are zero, the condition that we are looking for a nontrivial solution provides the over-determination of the problem.

It is worth mentioning that for the flow of a single fluid (which is the case of the White-Metzner fluid, and also the case for the content of Chapters 3 and 4), we only need to satisfy the non-slip and no penetration boundary conditions along with the perturbation conditions at the centreline (for either a varicose or sinuous mode). However, for the two-fluids flow or shear-banded flow (see section 1.7.3), there exists a fluid-fluid interface, for which more boundary conditions need to be satisfied at the interface location. This will be discussed with more detail in chapter 5.

Our goal is to determine the complex eigenvalue $\omega(k)$ for a nontrivial solution of the equations (2.45)–(2.50) subject to the non-slip conditions (2.51) and the boundary conditions for either varicose (2.52) or sinuous (2.53) perturbations.

### 2.8.1 A mathematical difficulty for power-law models

When forming the fourth-order ODE for $\psi$, we have to take the derivatives of the term $-\mathrm{i}\,\omega + \mathrm{i}\,kU + \mathcal{W}_0^{-1}$ that appears in the evolution equation of the elements of $a_{ij}$ (2.48), which involve derivatives of $y^{(1-n)/n}$, resulting in terms proportional to $y^{(1-2n)/n}$ and $y^{(1-3n)/n}$, causing a problem near the centreline $y = 0$ if $n < 1$.

This difficulty arises from using power-law models for the stress-relaxation time function $\mathcal{W}_0$ (2.25), where a weakly singular behaviour occurs when $\dot{\gamma}_0 = 0$, which for our case is seen at the centreline $y = 0$. This singularity also affects the perturbed viscometric function $w \propto \dot{\gamma}_0^{n-2}\dot{\gamma}_p$, see (2.50). This difficulty was encountered first by Wilson and colleagues [178, 180], which was one of the many limitations of their work, as mentioned in section 1.8.5.

However, despite the presence of the singularity in the governing equations, they were able to proceed by limiting themselves to study only varicose modes, and the reason for this has physical validation: notice that the perturbation to the shear rate $\dot{\gamma}_p$ is proportional to $\psi'' + k^2\psi$, and for a varicose mode (see (2.52)), $\psi$ is an odd function of $y$ and $\dot{\gamma}_p = 0$ at the centreline. Therefore, the system of equations has a removable singularity at $y = 0$ and sensible conclusions could be obtained.

In chapter 3 we will also encounter this singularity, so we will only focus on studying varicose modes. But for the last chapters, a much more realistic model with bounded viscosity will be used, and no singular behaviour at the centreline will be observed, which will allow us to study both sinuous and varicose perturbations.

## 2.9 Numerical method

For very specific cases, an analytic solution of the system of equations shown above can be found. But on most occasions (especially for the complex models that we will use on the following chapters), it is necessary to solve these equations numerically. The method we will use was developed by Ho & Denn [81], and here we briefly explain it.

As described in section 2.7.1, we are interested in carrying out a temporal linear stability analysis. That means that for a given value of wavenumber, we look for the complex frequency. We start by fixing a value of $k$ and we choose as an initial guess an estimated value of $\omega$. Ho and Denn's method is iterative, so it is convenient to select a value of frequency that is *close* to the *true* solution. This initial guess could obtained from solving the governing equations where analytic solutions are tractable or from cases in which the solutions to the equations are available in the literature.

Using this value of $k$ and the estimate of $\omega$, we have a fourth-order ODE for $\psi$ with boundary conditions at the wall and at the centreline. Now let us suppose we are looking for only a sinuous mode. Then the boundary conditions that need to be satisfied are:

$$\psi'(0) = \psi'''(0) = 0 \tag{2.54}$$

$$\psi(1) = \psi'(1) = 0. \tag{2.55}$$

Since the system of equations is linear, any solution to it can be specified by the values of $\psi$ and its derivatives at the centreline:

$$\underline{\psi} = (\psi(0), \psi'(0), \psi''(0), \psi'''(0)). \tag{2.56}$$

Therefore, any solution along the channel must be a linear combination of two functions:

$$\underline{\psi} = a\,\underline{\psi_1} + b\,\underline{\psi_2}, \tag{2.57}$$

where $\underline{\psi_1}$ and $\underline{\psi_2}$ are defined as:

$$\underline{\psi_1} = (1, 0, 0, 0) \qquad \underline{\psi_2} = (0, 0, 1, 0). \tag{2.58}$$

We wish to satisfy the non-slip conditions (2.55), so the equations above become:

$$\begin{pmatrix} \psi_1(1) & \psi_2(1) \\ \psi_1'(1) & \psi_2'(1) \end{pmatrix} \begin{pmatrix} a \\ b \end{pmatrix} = \begin{pmatrix} 0 \\ 0 \end{pmatrix} \tag{2.59}$$

If $\omega$ is the true value, then there exists some linear combination of $\psi_1$ and $\psi_2$ for which the two wall boundary conditions (2.55) are satisfied (using a nonzero vector $(a, b)$):

$$\begin{vmatrix} \psi_1(1) & \psi_2(1) \\ \psi_1'(1) & \psi_2'(1) \end{vmatrix} = 0. \tag{2.60}$$

Here |...| denotes the determinant. Thus, the numerical method consists of integrating the two basis functions $\psi_1$ and $\psi_2$ numerically across the channel from the centreline to the channel wall (from 0 to 1). With the information obtained from the integration, the determinant (2.60) can be calculated. And finally, in order to find the true value of $\omega$, we will use a Newton-Raphson method to find a zero of the determinant as a function of $\omega$.

Lastly, in order to avoid spurious numerical instabilities, the integration routine also involves renormalisation of the two basis vectors at several stations across the channel. A more detailed explanation of this can be found in [174].

## 2.10 Summary of previous results in instabilities of shear-thinning viscoelastic flows

Now we provide with a brief summary of the results of the stability analysis of a White-Metzner fluid obtained by Wilson & Rallison [180]. As stated in section 1.8.5, the first experimental evidence of the instability predicted by them was reported by Bodiguel *et al.* [16], whose results are also going to be briefly discussed here. Finally, we will summarise some of the most remarkable observations from the theoretical analysis of Wilson & Loridan [178], who extended previous work by using a model that matches the rheology of the fluid used by Bodiguel. The content of this section and some of the numerical techniques used by these authors are going to be useful for the development of the content of the next chapters.

### 2.10.1 Wilson & Rallison predictions

One of the particular cases where an analytic solution of equations (2.45)–(2.50) can be obtained is the long-wave limit case $k \to 0$. In this way, Wilson & Rallison proposed to expand the eigenvalue $\omega$ in power of $k$. Thus, the leading- and first-order calculation can be written in the following way:

$$\omega = \omega_0 + k\omega_1 + O(k^2) \qquad \psi = \psi_0 + k\psi_1 + O(k^2). \tag{2.61}$$

For the leading order, the solution to the governing equations that satisfy the boundary conditions for varicose perturbations is:

$$\omega_0 = -\frac{\mathrm{i}}{W}\left(\frac{n}{n+1}\right)^{n-1}\frac{3n}{2n+1}. \tag{2.62}$$

From the equation above, an important conclusion was obtained: infinitely long waves $k \to 0$ are stable for any value of Weissenberg number $W$ and power-law coefficient $n$. In addition, equation (2.62) is reduced to the solution for the Maxwell case if $n = 1$.

The order-$k$ case was solved from substituting the leading order quantities into the first order expansion in small $k$, giving as result a third-order ODE for $\psi_1$, which is independent of $W$. The order-$k$ solution $\omega_1$ for varicose perturbations was only possible to find in the Maxwell limit ($n = 1$), which adopts the following form:

$$\omega_1 = \begin{cases} 0.29039769 \pm 0.05012283\mathrm{i} \\ \\ 0.89882760 \pm 0.12682973\mathrm{i}. \end{cases} \tag{2.63}$$

These equation proves that there exist four stable modes for varicose perturbations at long waves for a Maxwell fluid. With the information obtained above, Wilson & Rallison were able to make parameter continuation for $n$, $W$ and $k$, taking as a starting point the Maxwell case. We show some of their numerical results in figure 2.6. The imaginary part of the complex frequency $\omega$, which we call the *growth rate*, is plotted against the power-law coefficient $n$ for fixed values of Weissenberg number and wavenumber $k = W = 2$ (see figure 2.6a). It can be seen that there exist multiple modes of stability for $n < 1$. From these modes, three of them are stable: two of them (C and D) cease to exist at $n \approx 0.7$, and the other one (A) remains stable for smaller values of $n$. On the other hand, five modes (B, E, F, G and H) become unstable at $n \leq 0.3$, which is the range of highly shear-thinning behaviour. Notice that it was not possible to obtain a numerical solution near the limit $n \to 0$, and this is due to the mathematical difficulties described in section 2.8.1. These results are evidence that an instability is present in viscoelastic fluids with a high level of shear-thinning and its mechanism differs from the curved streamlines, shear-banding and interfacial instabilities discussed in section 1.8. In addition, non-zero values of $W$ and $k$ are necessary conditions to observe unstable flows.

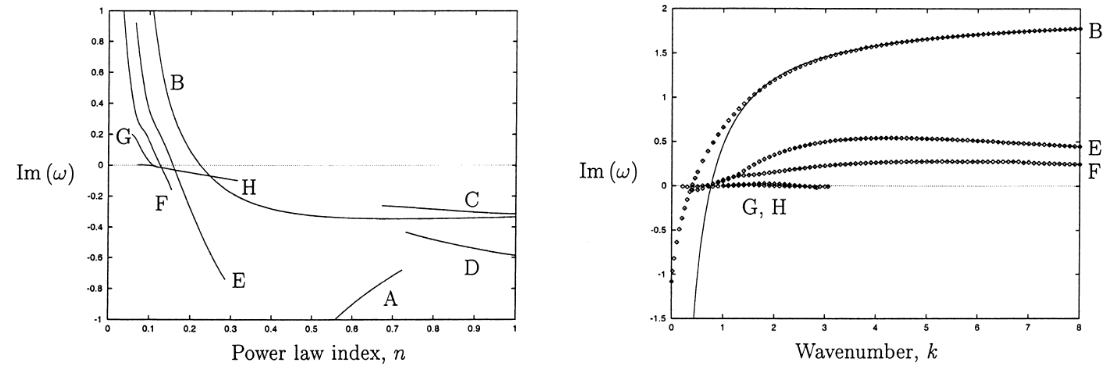

(a) $\Im(\omega)$ vs $n$ (b) $\Im(\omega)$ vs $k$

Figure 2.6: Stability analysis results of varicose perturbations of a White-Metzner fluid obtained by Wilson & Rallison [180]. Figure (a): growth rate against power-law coefficient $n$ with $W = k = 2$. Figure (b): wavenumber-dependence of the growth rate of the five unstable roots of figure a) with $W = 2$ and $n = 0.1$.

Wilson & Rallison also carried out parameter continuation in $k$ for the five unstable roots (B, E, F, G and H) shown in figure 2.6a) with $W = 2$ and $n = 0.1$ fixed. Their results can be seen in figure 2.6b) and they demonstrated that this instability can still be seen at short waves $k \to \infty$ (see root B). These calculations were confirmed by their short-waves analysis, which will be discussed with more detail in chapter 4.

## 2.10.2 Bodiguel's experiment

In section 1.8.5, we briefly described the experiments carried out by Bodiguel *et al.* [16], which provided with the first experimental evidence of the instability initially predicted by Wilson and Rallison.

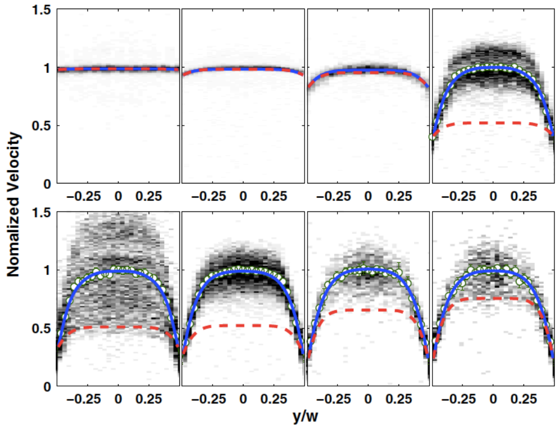

Figure 2.7: Experimental results reported by Bodiguel *et al.* [16]. The figures are the velocity profiles in channel flows obtained for different pressure gradients; from left to right, the pressure drop increases. It can be seen that above a critical stress value $\sigma_w \geq 4.86$ Pa (fourth picture at the top-right), the theoretical prediction (dashed line) no longer matches the experiments.

Bodiguel studied the flow of an aqueous solution of polyacrylamide, HPAM (concentration of 4000 ppm and molecular weight of $18 \times 10^6$ g/mol). They obtained the global flow curve (simple shear flow) using a rheometer with cone-and-plate geometry. Their experimental results can be matched nicely using simple power-law models:

$$\sigma_{12} = 3.73\dot{\gamma}^{0.21} \qquad W = \lambda_R\,\dot{\gamma} = 3.63\,\dot{\gamma}^{0.43}. \tag{2.64}$$

where the power-law coefficient is 0.21 and according to Wilson's prediction (see figure 2.6), an instability was likely to be observed for this polymeric fluid.

The pressure-driven flow of these solutions was studied in straight channels of 5.5 cm of length, 1 mm of height and $2L = 152\,\mu m$ width. Using particle image velocimetry (PIV) techniques, velocity profiles were obtained for different values of pressure gradient $\mathscr{P}$. The experiments could be separated into two different regimes: for shear stress values at the wall $|\sigma_w| = \mathscr{P}L \geq 4.86$ Pa, the measured velocity $U(y)$ did not match the theoretical predictions of equation (2.17), and this is due to the appearance of large fluctuations in the $x$-direction and an apparent slippage at the wall. For very low values of $\sigma_w$, no velocity fluctuations are observed and the theory matches the experiments (see figure 2.7).

The experiments were also able to measure fluctuations along the $y$-direction, and they observe that for $4.6\,\text{Pa} < \sigma_w < 8$ Pa, a periodic variation of the transverse velocity $v_y$ as a function of time is seen.

### 2.10.3 Wilson & Loridan observations

A major difference between Wilson's theoretical work and Bodiguel's experiments is that the former studied stability analysis of a fluid with constant shear-modulus $G = G_M$, meanwhile the experiments carried out by Bodiguel suggested that the shear modulus is a function of the shear rate $G(\dot{\gamma})$. This motivated Wilson & Loridan [178] to extend Wilson & Rallison's wok [180] by using a constitutive model that could match the rheometry of the fluid used in Bodiguel's experiments (see equations (2.64)). In order to satisfy this, they used a modified UCM model, in which the shear-modulus $G$ and the stress-relaxation time $\lambda_R$ were allowed to depend instantaneously on the local shear rate.

Their model adopts the following form:

$$\underline{\underline{\tau}} = -p\underline{\underline{I}} + \underline{\underline{\sigma}} = -p\underline{\underline{I}} + G(\dot{\gamma})\,\underline{\underline{A}} \tag{2.65}$$

$$\overset{\nabla}{\underline{\underline{A}}} = \frac{\partial \underline{\underline{A}}}{\partial t} + \underline{u}\cdot\nabla\,\underline{\underline{A}} - \underline{\underline{A}}\cdot(\nabla\,\underline{u}) - (\nabla\,\underline{u})^{\top}\cdot\underline{\underline{A}} = -\frac{1}{\lambda_R(\dot{\gamma})}(\underline{\underline{A}} - \underline{\underline{I}}). \tag{2.66}$$

#### 2.10.3.1 Simple shear flow

In simple shear flow $\underline{u} = \dot{\gamma} y \underline{e}_x$, the stress tensor derived from Wilson's and Loridan's model (2.65)–(2.66) adopts a similar form to the one obtained using the White-Metzner model (2.5), but the terms of the equations with $G_M$ (constant shear-modulus) is replaced with $G(\dot{\gamma})$ instead, giving the following material functions:

$$\eta(\dot{\gamma}) = \frac{\sigma_{12}}{\dot{\gamma}} = \lambda_R\, G \qquad \Psi_1 = \frac{\tau_{11} - \tau_{22}}{\dot{\gamma}^2} = 2\,G\,\lambda_R^2. \tag{2.67}$$

Wilson & Loridan found it reasonable to approximate both $\eta(\dot{\gamma})$ and $\Psi_1(\dot{\gamma})$ with power-law functions of the shear rate of the form $A\dot{\gamma}^n$ in order to match the rheology of Bodiguel's fluid, and thus, $G(\dot{\gamma})$ and $\lambda_R(\dot{\gamma})$ adopted the following form:

$$G(\dot{\gamma}) = G_M\,\dot{\gamma}^{m-n} \qquad \lambda_R = K_M\,\dot{\gamma}^{n-1}. \tag{2.68}$$

The indices $m$ and $n$ were selected to match the definition of stress-relaxation time used in [180], see equation (2.4). The shear stress then becomes $\sigma_{12} = G_M K_M \dot{\gamma}^m$. If $m < 1$, the fluid exhibits shear-thinning behaviour and if $n < 1$, the stress-relaxation time will decrease with an increase in shear rate. Lastly, notice that if $m = n$, $G(\dot{\gamma}) = G_M$, and thus, this model is reduced to the original one used by Wilson and Rallison.

## Base state solutions

In pressure-driven channel flow conditions (see section 2.4), the base state solutions predicted by the Wilson & Loridan model (2.65)–(2.66) are:

$$U(y) = \left(\frac{\mathscr{P}}{G_M\, K_M}\right)^{1/m} \left(\frac{m}{m+1}\right) \left[L^{(m+1)/m} - |y|^{(m+1)/m}\right] \tag{2.69}$$

$$\dot{\gamma}_0 = |U'| = \left(\frac{\mathscr{P}\,|y|}{G_M\, K_M}\right)^{1/m} \qquad N_1 = 2\, G(\dot{\gamma})^{-1}\, \mathscr{P}^2\, |y|^2. \tag{2.70}$$

The obvious differences between these equations and the ones by Wilson & Rallison (2.17)–(2.18) are that these are in terms of $m$ (which is the viscosity power-law coefficient) and of the non-constant shear modulus $G(\dot{\gamma})$.

### 2.10.3.2 Dimensionless equations

The process of nondimensionalisation of the constitutive equation (2.65)–(2.66) along with continuity (1.10) and momentum equations (1.11) is the same as the one described in section 2.6: we use the same scaling for times, velocities, stresses and lengths. The governing equations (in the absence of gravitational forces) become:

$$\underline{\nabla} \cdot \underline{u} = 0 \tag{2.71}$$

$$Re\left(\frac{\partial \underline{u}}{\partial t} + \underline{u} \cdot \underline{\nabla u}\right) = \underline{\nabla} \cdot \underline{\underline{\tau}} \tag{2.72}$$

$$\underline{\underline{\tau}} = -P\underline{\underline{I}} + \underline{\underline{\sigma}} = -P\underline{\underline{I}} + \frac{C}{\mathcal{W}}\underline{\underline{A}} \tag{2.73}$$

$$\overset{\nabla}{\underline{\underline{A}}} = -\frac{1}{\mathcal{W}}(\underline{\underline{A}} - \underline{\underline{I}}) \tag{2.74}$$

$$\mathcal{W} = W\dot{\gamma}^{n-1} \qquad C = \dot{\gamma}^{m-1}. \tag{2.75}$$

The Reynolds and Weissenberg numbers and the dimensionless stress-relaxation time were already defined in equations (2.23). For this model, a new viscometric function appeared by introducing a non-constant shear modulus: the dimensionless shear viscosity $C$.

The base-state solution of these governing equations in conditions of pressure-driven channel flow is:

$$\underline{u} = (U(y), 0) \qquad U(y) = 1 - y^{(m+1)/m} \qquad \dot{\gamma}_0 = |U'| = -U' = \Big(\frac{m+1}{m}\Big)\, y^{1/m}. \tag{2.76}$$

$$\mathcal{W}_0 = W\dot{\gamma}_0^{n-1} = W\Big(\frac{m+1}{m}\Big)^{n-1} y^{(n-1)/m} \tag{2.77}$$

$$C_0 = \dot{\gamma}_0^{m-1} = \Big(\frac{m+1}{m}\Big)^{m-1} y^{(m-1)/m} \tag{2.78}$$

$$\underline{\underline{A}} = \begin{pmatrix} A_{11} & A_{12} \\ A_{21} & A_{22} \end{pmatrix} = \begin{pmatrix} 1 + 2\,W^2\,[\mathcal{P}y]^{2n/m} & -W[\mathcal{P}y]^{n/m} \\ -W[\mathcal{P}y]^{n/m}y & 1 \end{pmatrix}. \tag{2.79}$$

For these equations, $\mathcal{P}$ now is in terms of $m$ (rather than the index $n$ in equation (2.27)):

$$\mathcal{P} = \Big(\frac{m+1}{m}\Big)^{m}. \tag{2.80}$$

The pressure $P$ is:

$$P = P_\infty - \mathcal{P}x + \frac{C_0}{\mathcal{W}_0}, \tag{2.81}$$

and the base state polymeric stress tensor, which is now in terms of $m$ and $n$ is:

$$\underline{\underline{\sigma}} = \begin{pmatrix} \sigma_{11} & \sigma_{12} \\ \sigma_{21} & \sigma_{22} \end{pmatrix} = \begin{pmatrix} \frac{C_0}{\mathcal{W}_0} + 2\,W\,[\mathcal{P}y]^{(m+n)/m)} & -\mathcal{P}y \\ -\mathcal{P}y & \frac{C_0}{\mathcal{W}_0} \end{pmatrix}. \tag{2.82}$$

#### 2.10.3.3 Perturbed quantities

As described in section 2.7.2, an infinitesimal perturbation is added to the base flow quantities. The perturbed-quantities definition used for the White-Metzner fluid (2.33)–(2.38) are also valid for the Wilson & Loridan model, with the exception of the new viscometric function $C$ (2.78), which is defined as:

$$C = C_0 + c\varepsilon, \tag{2.83}$$

where $c$ is the perturbation to the dimensionless shear-viscosity $C_0$. Using Fourier modes and the streamfunction (2.41), the governing equations for order $\epsilon$ are:

$$\underline{\underline{\Sigma}} = \frac{C_0}{\mathcal{W}_0}\underline{\underline{a}} + \Big(\frac{c}{\mathcal{W}_0} - \frac{C_0 w}{\mathcal{W}_0^2}\Big)\underline{\underline{A}}. \tag{2.84}$$

$$\begin{aligned} 0 &= -\mathrm{i}kp + \mathrm{i}k\Sigma_{11} + \mathrm{D}\Sigma_{12} && (2.85)\\ 0 &= -\mathrm{D}\,p + \mathrm{i}k\Sigma_{12} + \mathrm{D}\Sigma_{22}, && (2.86) \end{aligned}$$

where $w$ and $c$ are:

$$\begin{aligned} c &= -(m-1)\dot{\gamma}_0^{m-2}(\mathrm{D}^2 + k^2)\psi, && (2.87)\\ w &= -W(n-1)\dot{\gamma}_0^{n-2}(\mathrm{D}^2 + k^2)\psi. && (2.88) \end{aligned}$$

The evolution equations of the perturbation to the conformation tensor $a_{ij}$ for the Wilson & Loridan model adopt exactly the same form that of the White-Metzner fluid (2.45)–(2.48), but the base state quantities $U(y), DU, \mathcal{W}_0, A_{ij}$ in terms of the coefficients $m$ and $n$ (2.76)–(2.82) have to be used instead. As described before, the system of equations can be combined, resulting in a fourth-order ODE for $\psi$ with non-slip boundary conditions (2.51). The singularity at the centreline as result of using power-law models discussed in section 2.8.1 is still present in the Wilson & Loridan model, so they limit themselves to study only varicose perturbations (2.52). The ODE was then solved using the numerical method described in section 2.9.

#### 2.10.3.4 Critical Weissenberg number

The most important results obtained by Wilson & Loridan [178] are briefly discussed in this subsection, but for comparison purposes, we will refer to more of their specific results in chapter 3.

They were interested in finding theoretically the instability observed experimentally by Bodiguel, so they needed to calculate at what flow rate the flow would become unstable. In other words, they were looking for the dimensionless flow rate below which the flow is stable to perturbations of all wavenumbers, also known as the *critical Weissenberg number*, $W_{crit}$ [178].

From the model parameters that match the rheology of Bodiguel's fluid ($m = 0.21$, $n = 0.43$, $K_M = 3.63\,\mathrm{s}^{0.43}$ and $G_M = 1.03\,\mathrm{Pa\,s}^{-0.22}$) and from the critical shear stress value at the wall $\sigma_w^{crit} = 4.7 \pm 0.2\,\mathrm{Pa}$, it was possible to calculate the critical value of pressure gradient $\mathscr{P}$ and the theoretical value of centreline velocity $U(y = 0) = U_0$ (see equation (2.17)). With these values, the critical Weissenberg number of the experiments was obtained, which is $W_{crit} = K_M(U_0/L) = 2.75 \pm 0.25$.

On the other hand, Wilson and Loridan's calculation predicted instability at $W_{crit} = 1.8$. Although this result was not in perfect agreement with the experimental value and considering the many limitations of their model, the discrepancy was not massive, which led them to conclude that the same mechanism is driving both the theoretical and experimental instabilities. However, no insight into the mechanism of instability was given.

In addition, the experiments showed that the velocity perturbations cross the centreline of the channel (presence of sinuous modes), and therefore, the perturbations are not purely varicose. As we have previously discussed 2.8.1, one of the primary weaknesses of Wilson & Loridan's work is that their stability analysis could not capture sinuous perturbations. Thus, the next step would be to use a model that allows to study both varicose and sinuous perturbations.

A secondary issue is that their viscometric functions, such as the stress-relaxation time and the shear modulus, depend instantaneously on the shear rate, which led them to suggest that a structural model (one in which the fluid properties would depend on the evolution of a structural parameter) could be used to carry out stability analysis for greater understanding of the instabilities present in shear-thinning viscoelastic fluids. One of our goals in the present thesis is to tackle some of these issues encountered by Wilson *et al.* [178, 180].

# Chapter 3

# Channel flow stability of highly shear-thinning viscoelastic fluids

## 3.1 Introduction

In recent experimental work, Bodiguel and coworkers [16] discovered an instability in channel flow of a viscoelastic shear-thinning fluid (a high molecular weight polymer solution). The steady rheometry of their fluid suggested that both the shear viscosity and the relaxation time of the fluid could be modelled with a power-law dependence on shear-rate. The experiments were described in section 2.10.2.

This scenario was modelled theoretically by Wilson & Loridan [178] using linear stability theory and a modified UCM model whose physical parameters (relaxation time $\lambda_R$ and shear modulus $G$) were allowed to depend instantaneously on the local shear rate (see section 2.10.3). They had some success in reproducing the experimental observations, but no real insight into the mechanism of the instability.

It is clear that the instability is neither inertial (since it exists at zero Reynolds number) nor the well-known curved-streamline instability (disccussed in section 1.8.2) since the streamlines are straight. The stability of shear-thinning flows without elasticity has been studied extensively [34,134,135] and no instability has ever been found in the absence of inertia. A natural question to ask is whether the mechanism of this instability is truly elastic or principally a result of strong shear-thinning. To address this, we will augment the fluid model of Wilson & Loridan [178] (equations (2.65)–(2.66)) in the simplest way possible, and study the effect of reducing elasticity while maintaining the shear-thinning velocity profile.

Our research contributions to the field of flow instabilities in elastic fluids begin in this chapter, and the bulk of this work has been published in the *Journal of Non-Newtonian Fluid Mechanics* [28]. We start by introducing the new model in section 3.2. The material and viscometric functions in simple shear flow are shown in section 3.2.2. The dimensionless governing equations are derived in 3.2.4. We then obtain our base state solutions in section 3.3.1 and the perturbed quantities in 3.3.2. Finally, we discuss our results in section 3.4 and draw conclusions 3.5.

# 3.2 Model fluid

We want a fluid which models the constitutive behaviour seen in experiments [16] using as few disposable parameters as possible, while also allowing some exploration of the importance of viscoelastic effects in triggering the observed instability; it is also useful to have a model which reduces to that used by Wilson and Loridan [178] in some limit.

We choose to add just one term to the model used by them (see section 2.10.3). We add a "solvent" contribution to the stress, which shear-thins at the same rate as the polymer contribution, in order to retain the simple power-law dependence of the shear viscosity. This will introduce only one new dimensionless parameter to the problem.

## 3.2.1 Governing equations

The set of governing equations for the incompressible shear-thinning fluid (in the absence of external body forces such as gravity) is:

$$\underline{\nabla} \cdot \underline{u} = 0 \tag{3.1}$$

$$\rho\Big(\frac{\partial \underline{u}}{\partial t} + \underline{u} \cdot \underline{\nabla u}\Big) = \underline{\nabla} \cdot \underline{\underline{\tau}} \tag{3.2}$$

$$\underline{\underline{\tau}} = -P\underline{\underline{I}} + 2\,\mu(\dot{\gamma})\underline{\underline{D}} + \underline{\underline{\sigma}} = -p\underline{\underline{I}} + 2\,\mu(\dot{\gamma})\underline{\underline{D}} + G(\dot{\gamma})\underline{\underline{A}} \tag{3.3}$$

$$\overset{\nabla}{\underline{\underline{A}}} = -\frac{1}{\lambda_R(\dot{\gamma})}(\underline{\underline{A}} - \underline{\underline{I}}) \tag{3.4}$$

in which the upper-convected derivative was defined in (2.3). Recalling that $\rho$ its density, the tensor $\underline{\underline{A}}$ is the conformation tensor, describing the stretch in the polymer chains; $\underline{\underline{I}}$ is the identity tensor, $\underline{\underline{\tau}}$ and $\underline{\underline{\sigma}}$ are the total and polymer stress tensors, respectively and we have introduced the symmetric flow gradient tensor $\underline{\underline{D}}$ defined in (1.2). The scalar functions $G$ (the shear modulus), $\lambda_R$ (the relaxation time) and $\mu$ (the viscosity of the solvent) are all empirical functions of the shear-rate $\dot{\gamma}$. The only difference between this model and that used by Wilson and Loridan [178] is the addition of the solvent term $2\mu(\dot{\gamma})\underline{\underline{D}}$ in equation (3.3). This additional term will give us a shear-thinning modification of the Oldroyd-B model, which will allow us to separate elastic from viscous effects.

### 3.2.2 Rheometry

We now consider the behaviour of our fluid in a simple shear flow, $\underline{u} = \dot{\gamma} y \underline{e}_x$ with $\dot{\gamma} > 0$, using Cartesian coordinates. The stress tensor for our system is:

$$\underline{\underline{\tau}} = \begin{pmatrix} -P_0 + G(1 + 2\lambda^2\dot{\gamma}^2) & (\mu + \lambda_R G)\dot{\gamma} \\ (\mu + \lambda_R G)\dot{\gamma} & -P_0 + G \end{pmatrix}. \tag{3.5}$$

The viscometric functions accessible in experiment are:

$$\tau_{12} = \sigma_{12} = (\mu + G\lambda_R)\dot{\gamma}, \qquad N_1 = \tau_{11} - \tau_{22} = 2G\lambda_R^2\dot{\gamma}^2, \tag{3.6}$$

in which the parameters $\mu$, $G$ and $\lambda_R$ depend on the shear-rate $\dot{\gamma}$. In the original experiments of Bodiguel [16], both these viscometric functions were observed to have a power-law dependence on $\dot{\gamma}$, so we follow the same power-law functions defined by Wilson & Loridan (see section 2.10.3.1):

$$G(\dot{\gamma}) = G_M \dot{\gamma}^{m-n} \qquad \lambda_R(\dot{\gamma}) = K_M \dot{\gamma}^{n-1} \tag{3.7}$$

and, to keep the shear stress $\sigma_{12}$ a simple power-law, we introduce

$$\mu(\dot{\gamma}) = \mu_0 \dot{\gamma}^{m-1}. \tag{3.8}$$

The one new parameter of this model, $\mu_0$, is the solvent-viscosity coefficient. The resulting rheological response of our model fluid is:

$$\sigma_{12} = (\mu_0 + G_M K_M)\dot{\gamma}^m \tag{3.9}$$

$$\frac{\tau_{11} - \tau_{22}}{2\sigma_{12}} = \left(\frac{G_M K_M^2}{\mu_0 + G_M K_M}\right)\dot{\gamma}^n. \tag{3.10}$$

The fluid rheology of a viscoelastic shear-thinning fluid reported by Bodiguel in [16] is:

$$\sigma_{12} = 3.73\dot{\gamma}^{0.21}\mathrm{Pa} \qquad \frac{\tau_{11} - \tau_{22}}{2\sigma_{12}} = 3.63\dot{\gamma}^{0.43}. \tag{3.11}$$

Matching these experimental fits to our model (equations (3.9–3.10)), and taking $\mu_0$ in units of $\mathrm{Pa\,s}^{0.21}$, we obtain:

$$m = 0.21 \qquad n = 0.43 \tag{3.12}$$

$$G_M = \Big(\frac{3.73 - \mu_0}{K_M}\Big)\mathrm{Pa\,s}^{0.22} \qquad K_M = 3.63\Big(1 + \frac{\mu_0}{3.73 - \mu_0}\Big)\mathrm{s}^{0.43} \tag{3.13}$$

The power-law parameters $m$ and $n$ are unchanged from their values in Wilson and Loridan's model [178], but now the parameters $K_M$ and $G_M$ are only determined once a value has been chosen for $\mu_0$ (which must lie between 0 and $3.73\,\mathrm{Pa\,s}^{0.21}$). As $\mu_0$ increases, $K_M$ also increases but $G_M$ decreases, as shown in figure 3.1. If $\mu_0 = 0$ we regain the values used in [178], namely $G_M = 3.73\,\mathrm{Pa\,s}^{0.22}$ and $K_M = 3.63\,\mathrm{s}^{0.43}$.

### 3.2.3 Steady channel flow

We consider the same geometry specifications explained before in section 2.4. The following velocity profile is then obtained:

$$U(y) = \left(\frac{\mathcal{P}}{\mu_0 + G_M K_M}\right)^{1/m}\Big(\frac{m}{m+1}\Big)\Big[L^{(m+1)/m} - |y|^{(m+1)/m}\Big], \tag{3.14}$$

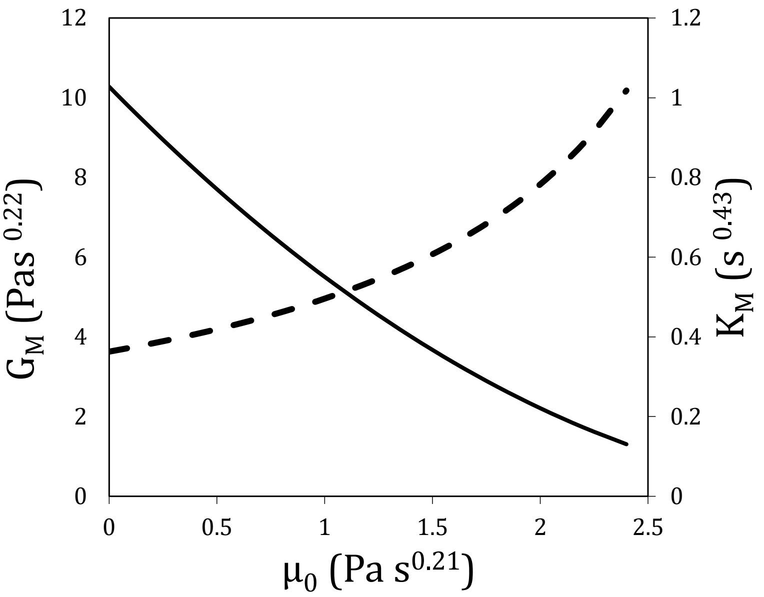

Figure 3.1: Plot of the required behaviour of the parameters $G_M$ (solid line) and $K_M$ (dashed line) as the solvent coefficient $\mu_0$ varies, in order to correctly replicate the experimental data from [16]. Curves specified by equation (3.13).

from which an important flow measure is the centreline velocity

$$U_0 = U(0) = \left(\frac{\mathcal{P}}{\mu_0 + G_M K_M}\right)^{1/m} \left(\frac{m}{m+1}\right) L^{(m+1)/m}. \tag{3.15}$$

The only difference here with respect to the velocity profile obtained by Wilson and Loridan (see equation (2.69)) is the addition of the solvent viscosity $\mu_0$, that appears in the denominator of the first term of the equation (3.14).

### 3.2.4 Dimensionless form of the governing equations

In order to reduce our parameter space, we derive dimensionless forms of our equations using a similar scaling to the one proposed for the White-Metzner and the Wilson & Loridan models (section 2.6): recalling that we scale lengths with $L$, we use the average shear rate $U_0/L^{-1}$ to scale times. For our new model, we now scale stresses with a typical shear stress, which is $(\mu_0 + G_M K_M)(U_0/L)^m$. In terms of dimensionless variables, the governing equations become:

$$\underline{\nabla} \cdot \underline{u} = 0 \tag{3.16}$$

$$Re\Big(\frac{\partial \underline{u}}{\partial t} + \underline{u} \cdot \underline{\nabla u}\Big) = -\underline{\nabla} P + \underline{\nabla} \cdot \underline{\underline{\sigma}} \tag{3.17}$$

$$\underline{\underline{\sigma}} = 2\Big(\frac{\beta}{1+\beta}\Big) C \underline{\underline{D}} + \Big(\frac{1}{1+\beta}\Big)\frac{C}{\mathcal{W}}\underline{\underline{A}} \tag{3.18}$$

$$\overset{\triangledown}{\underline{\underline{A}}} = -\frac{1}{\mathcal{W}}(\underline{\underline{A}} - \underline{\underline{I}}) \tag{3.19}$$

$$C = \dot{\gamma}^{m-1} \qquad \mathcal{W} = W\dot{\gamma}^{n-1} \qquad W = K_M\Big(\frac{U_0}{L}\Big)^n \tag{3.20}$$

The functions $C$ and $\mathcal{W}$ are the dimensionless *viscometric functions* (which also appeared in section 2.10.3.2), and there are three dimensionless physical constants: $W$, $Re$ and $\beta$: $W$ is the purely elastic Weissenberg number; the Reynolds number $Re$ is expressed as:

$$Re = \frac{\rho U_0 L}{(1+\beta) G_M K_M (U_0/L)^{m-1}}; \tag{3.21}$$

and we have introduced a new dimensionless parameter, $\beta$, which is the *retardation parameter*: the ratio between the solvent viscosity and the polymer viscosity:

$$\beta = \frac{\mu_0}{G_M K_M}. \tag{3.22}$$

The domain of values of $\beta$ is $[0, \infty)$, with the limit $\beta = 0$ corresponding to the earlier work of Wilson & Loridan [178]. We will mostly concern ourselves with the weak effects of solvent, $0 < \beta < 1$, but will consider some cases of larger $\beta$ (corresponding to solvent-dominated flow).

## 3.3 Stability calculation

### 3.3.1 Base state

In order to study the stability of the flow, we first need a steady solution. In dimensionless form, the velocity profile, shear rate and viscometric functions become:

$$U = 1 - |y|^{\frac{m+1}{m}} \qquad y \in [-1, 1] \tag{3.23}$$

$$\dot{\gamma}_0 = |U'| = \frac{m+1}{m} |y|^{1/m} \tag{3.24}$$

$$C_0 = \dot{\gamma}_0^{m-1} = \left[\frac{m+1}{m}\right]^{m-1} |y|^{(m-1)/m} \tag{3.25}$$

$$\mathcal{W}_0 = W \dot{\gamma}_0^{n-1} = W \left[\frac{m+1}{m}\right]^{n-1} |y|^{(n-1)/m}. \tag{3.26}$$

Equations (3.23)–(3.26) are exactly the same as the equations predicted by the Wilson & Loridan model (2.76)–(2.78). The pressure, conformation and polymer stress tensor are:

$$P_0 = P_\infty + \frac{1}{1+\beta} \frac{C_0}{\mathcal{W}_0} - \mathcal{P} x \tag{3.27}$$

$$\underline{\underline{A}} = \begin{pmatrix} A_{11} & A_{12} \\ A_{21} & A_{22} \end{pmatrix} = \begin{pmatrix} 1 + 2W^2 [\mathcal{P} y]^{2n/m} & -W [\mathcal{P} y]^{n/m} \\ -W [\mathcal{P} y]^{n/m} & 1 \end{pmatrix} \tag{3.28}$$

$$\underline{\underline{\sigma}} = \begin{pmatrix} \sigma_{11} & \sigma_{12} \\ \sigma_{21} & \sigma_{22} \end{pmatrix} = \begin{pmatrix} \frac{1}{1+\beta} \frac{C_0}{\mathcal{W}_0} + \frac{2W}{(1+\beta)} [\mathcal{P} y]^{\frac{m+n}{m}} & -\mathcal{P} y \\ -\mathcal{P} y & \frac{1}{1+\beta} \frac{C_0}{\mathcal{W}_0} \end{pmatrix}, \tag{3.29}$$

and the first normal stress difference is:

$$N_1 = \sigma_{11} - \sigma_{22} = \frac{2W}{(1+\beta)} [\mathcal{P} y]^{\frac{m+n}{m}} \tag{3.30}$$

where $P_\infty$ was previously defined as a baseline pressure and $\mathcal{P} = [(m+1)/m]^m$ is the dimensionless pressure gradient whose value was dictated by the normalization of the velocity profile.

These differ from the previous work [178] only in the normal stress component $\Sigma_{11}$ (see equation (2.82)). This term is reduced here by a factor of $(1+\beta)$ because of the presence of the solvent (which does not contribute to the normal stress difference but does contribute to the shear stress we use as our stress scale). In the limit $\beta \to \infty$, the solvent dominates and we have a simple power-law fluid: a generalised Newtonian Fluid having no viscoelastic effects.

### 3.3.2 Perturbation flow

The base flow quantities of our new model are modified by an infinitesimally small change in the same way as it was done with the White-Metzner and the Wilson and Loridan models (see section 2.7.2):

$$\underline{u} = (U + u\varepsilon, v\varepsilon) \qquad \dot{\gamma} = \dot{\gamma}_0 + \dot{\gamma}_p \varepsilon \tag{3.31}$$

$$C = C_0 + c\varepsilon \qquad \mathcal{W} = \mathcal{W}_0 + w\varepsilon \tag{3.32}$$

$$\underline{\underline{A}} = \begin{pmatrix} A_{11} + a_{11}\varepsilon & A_{12} + a_{12}\varepsilon \\ A_{21} + a_{21}\varepsilon & A_{22} + a_{22}\varepsilon \end{pmatrix} \tag{3.33}$$

$$\underline{\underline{\sigma}}^{tot} = \underline{\underline{\sigma}} + \varepsilon \underline{\underline{\Sigma}} \qquad \underline{\underline{\sigma}}^{tot} = \begin{pmatrix} \sigma_{11} + \Sigma_{11}\varepsilon & \sigma_{12} + \Sigma_{12}\varepsilon \\ \sigma_{21} + \Sigma_{21}\varepsilon & \sigma_{22} + \Sigma_{22}\varepsilon \end{pmatrix} \tag{3.34}$$

where $\varepsilon$ is a Fourier mode (2.38). The continuity equation (3.16) is automatically satisfied if we use the Fourier mode and the streamfunction definition (2.41).

Substituting the perturbed forms into the governing equations, and discarding terms of order $\varepsilon^2$, we obtain a linearised system of equations for inertialess flows:

$$\begin{aligned} 0 &= -\mathrm{i}kp + \mathrm{i}k\Sigma_{11} + \mathrm{D}\Sigma_{12} && (3.35) \\ 0 &= -\mathrm{D}\,p + \mathrm{i}k\Sigma_{12} + \mathrm{D}\Sigma_{22}, && (3.36) \end{aligned}$$

$$\underline{\underline{\Sigma}} = -2\left(\frac{\beta}{1+\beta}\right)\left[c\underline{\underline{D}}_0 + C\underline{\underline{d}}\right] + \frac{1}{(1+\beta)}\left[\frac{C}{\mathcal{W}}\underline{\underline{a}} + \left(\frac{c}{\mathcal{W}} - \frac{Cw}{\mathcal{W}^2}\right)\underline{\underline{A}}\right] \tag{3.37}$$

$$\underline{\underline{D}}_0 = \frac{1}{2}\begin{pmatrix} 0 & \mathrm{D}U \\ \mathrm{D}U & 0 \end{pmatrix} \qquad \underline{\underline{d}} = \frac{1}{2}\begin{pmatrix} 2\mathrm{i}k\mathrm{D}\,\psi & \mathrm{D}^2\psi + k^2\psi \\ \mathrm{D}^2\psi + k^2\psi & -2\mathrm{i}k\mathrm{D}\,\psi \end{pmatrix} \tag{3.38}$$

$$\begin{aligned} (-\mathrm{i}\,\omega + \mathrm{i}\,kU + \mathcal{W}^{-1})a_{11} &= \mathrm{i}\,k\psi\mathrm{D}A_{11} + 2a_{12}\mathrm{D}U + 2A_{11}\mathrm{i}\,k\mathrm{D}\psi \\ &+ 2A_{12}\mathrm{D}^2\psi + \frac{w}{\mathcal{W}^2}(A_{11}-1) && (3.39) \\ (-\mathrm{i}\,\omega + \mathrm{i}\,kU + \mathcal{W}^{-1})a_{12} &= \mathrm{i}\,k\psi\mathrm{D}A_{12} + a_{22}\mathrm{D}U + A_{11}k^2\psi \\ &+ \mathrm{D}^2\psi + \frac{w}{\mathcal{W}^2}A_{12} && (3.40) \\ (-\mathrm{i}\,\omega + \mathrm{i}\,kU + \mathcal{W}^{-1})a_{22} &= 2A_{12}k^2\psi - 2\,\mathrm{i}\,k\mathrm{D}\psi && (3.41) \end{aligned}$$

As explained in section 2.7.2, we limit our domain to the upper half of the channel $0 \le y \le 1$, in which $\mathrm{D}U < 0$ and thus $\dot{\gamma}_0 = -\mathrm{D}U$. This allows us to calculate $\dot{\gamma}_p$ using the definition:

$$\dot{\gamma}_0 + \dot{\gamma}_p\,\varepsilon = \left(2\left[\underline{\underline{D}}_0 + \varepsilon\underline{\underline{d}}\right] : \left[\underline{\underline{D}}_0 + \varepsilon\underline{\underline{d}}\right]\right)^{1/2} + O(\varepsilon^2).$$

The perturbation shear rate and the perturbed form of the viscometric functions are:

$$\begin{aligned} \dot{\gamma}_p &= -(\mathrm{D}^2 + k^2)\psi, && (3.42) \\ c &= (m-1)\dot{\gamma}_0^{m-2}\dot{\gamma}_p, && (3.43) \\ w &= W(n-1)\dot{\gamma}_0^{n-2}\dot{\gamma}_p. && (3.44) \end{aligned}$$

### 3.3.3 Boundary conditions and centreline singularity

We have a coupled system of equations (3.35)–(3.44). Those equations can be combined and the resulting equation is a fourth-order ODE in $\psi$ dependent on $y$. The boundary conditions are conditions of no flow on the boundaries (2.51).

The system is governed by six dimensionless parameters: the five introduced in Wilson & Loridan model [178] (the indices $m$ and $n$, the Weissenberg and Reynolds numbers, and the wavenumber $k$) along with the new parameter $\beta$. We solve the ODE using the shooting method of Ho & Denn [81], which was briefly explained here in section 2.9.

As described in a previous sections 2.8.1, we face a common problem as result of using power-law models, which happens at the centreline $y = 0$: the viscometric functions become singular at that point, which is unphysical. However, if we limit ourselves to varicose perturbations (2.52), for which $\psi$ is an odd function of $y$, then the value of the perturbed shear rate $\dot{\gamma}_p$ will be zero at the centreline, allowing us to draw some conclusions without having to further complicate the model. Note that we are not claiming that the varicose modes are the most unstable – indeed, the experimental observations of Bodiguel [16] suggest that sinuous modes may be more dangerous. Rather, the limitations of the power-law model restrict the modes to which linear stability theory can be applied. In the following chapter (chapter 4), we intend to study models which do not suffer from the power-law singularity, and thereby answer the question of the relative stability of sinuous and varicose modes.

# 3.4 Results

## 3.4.1 Effect of solvent on growth rate

### 3.4.1.1 Fluid to match experiments

For a direct comparison with the experimental instability reported by Bodiguel [16], we fix $m = 0.20$ and $n = 0.40$. The physical parameters $G_M$ and $K_M$ must be chosen to match equation (3.13) for a given value of $\mu_0$; however, in the dimensionless equation set the variation of these physical quantities is all captured within the dimensionless parameter $\beta$.

The case $\beta = 0$ was studied by Wilson & Loridan [178], see section 2.10.3, who found instability in the absence of inertia for Weissenberg numbers above 1.8; increasing the flow rate to $W = 2$ they found (their figure 6(a)) a broad peak in the plot of growth rate against wavenumber, with the most unstable mode at $k = 4.18$ but instability being seen over the large range $2.2 < k < 24$. Here we choose an indicative wavenumber $k = 3$ (giving a wavelength, $2\pi/k$, of the same magnitude as the channel) and investigate the effect of increasing $\beta$ from zero: that is, increasing the solvent contribution and correspondingly decreasing the viscoelastic contribution to the stress. The results are shown in figure 3.2.

We see that the growth rate of the instability is reduced monotonically by the introduction of solvent, and the flow becomes stable to perturbations of this wavelength for $\beta > 0.0695$. In the complex plane, we see that as the unstable mode becomes stable, its advection rate $\Re(\omega)$ increases, suggesting that it localises closer to the centre of the channel. If the convection rate would have remained finite for vary large values of $k$, that would mean that the perturbations is localised in the wall region [178, 180].

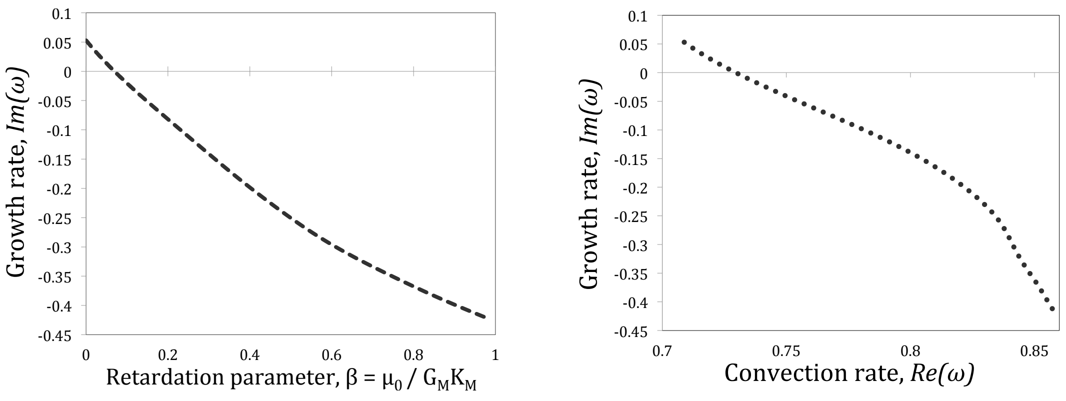

(a) $\Im(\omega)$ vs $\beta$

(b) $\Im(\omega)$ vs $\Re(\omega)$

Figure 3.2: Variation of the instability with the retardation parameter $\beta$ at $m = 0.2$, $n = 0.4$, $W = 2$, $Re = 0$ and $k = 3$. (a) Plot of growth rate $\Im(\omega)$ against $\beta$. (b) Behaviour of the eigenvalue $\omega$ in the complex plane.

### 3.4.1.2 Fluid having constant shear modulus

Our second case study fluid is a highly shear-thinning fluid whose shear modulus $G$ is constant: we set $m = n = 0.2$ to have

$$C = \dot{\gamma}^{-0.8} \qquad \mathcal{W} = W\dot{\gamma}^{-0.8}. \tag{3.45}$$

This fluid was shown by Wilson & Rallison [180] to be unstable to waves of wavenumber $k \approx 3$ at a Weissenberg number $W = 2$ without inertia, though the growth rate is lower than for the fluid discussed in section 3.4.1.1 above.

We see the stability behaviour of this fluid as function of the retardation parameter $\beta$ in figure 3.3: as before, although the initial instability observed at $\beta = 0$ remains present at small values of retardation parameter, the growth rate decreases and reaches stability at $\beta > 0.0135$.

### 3.4.1.3 Critical retardation parameter value

In the previous sections, we analysed the stability of two fluids to perturbations of a fixed wavenumber $k = 3$. It is more useful to determine the critical value of retardation parameter for each fluid: the value of $\beta$ above which the fluid is stable

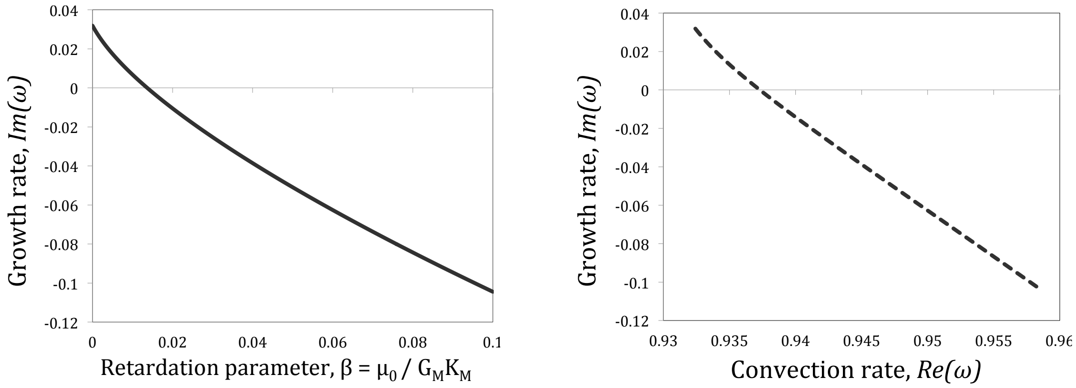

(a) $\Im(\omega)$ vs $\beta$

(b) $\Im(\omega)$ vs $\Re(\omega)$

Figure 3.3: Variation of the instability with the retardation parameter $\beta$ for a fluid with constant shear modulus constant: $m = n = 0.2$, $W = 2$, $k = 3$ and $Re = 0$. (a) Plot of growth rate $\Im(\omega)$ against $\beta$. (b) Behaviour of the eigenvalue $\omega$ in the complex plane.

to perturbations of all wavelengths. In this section we fix a value of the relaxation time power-law coefficient $m = 0.2$, along with Weissenberge number $W = 2$ and zero Reynolds number $Re = 0$, and for a range of values of $n$, we have calculated the critical $\beta$ above which the flow is unconditionally linearly stable. The results are shown in figure 3.4.

We see that if $n > 0.5235$ (fluids whose shear modulus is strongly shear-thinning) or $n < 0.1846$ (shear-thickening modulus), the flow is stable for any value of $\beta$: i.e. these fluids are stable even without the addition of solvent. As $n$ decreases from a starting point $n = 0.5234$ (where a tiny addition of solvent is sufficient to stabilise the flow) we see an increase in the critical retardation parameter. The curve reaches its maximum value at $n = 0.42$: for this rheology, a value of $\beta = 0.0804$ would be required to completely stabilise the flow. This fluid is not very different from that used in the experiments of [178].

A local minimum is observed at $n = 0.246$. After this point, the plot rises again and a second maximum is located at $n = 0.216$ (a very weakly shear-thinning shear modulus). Below this second maximum, the critical retardation parameter value decreases monotonically until at the point $n \approx 0.1846$ (a slightly shear-thickening modulus) the instability is lost even when there is no solvent viscosity.

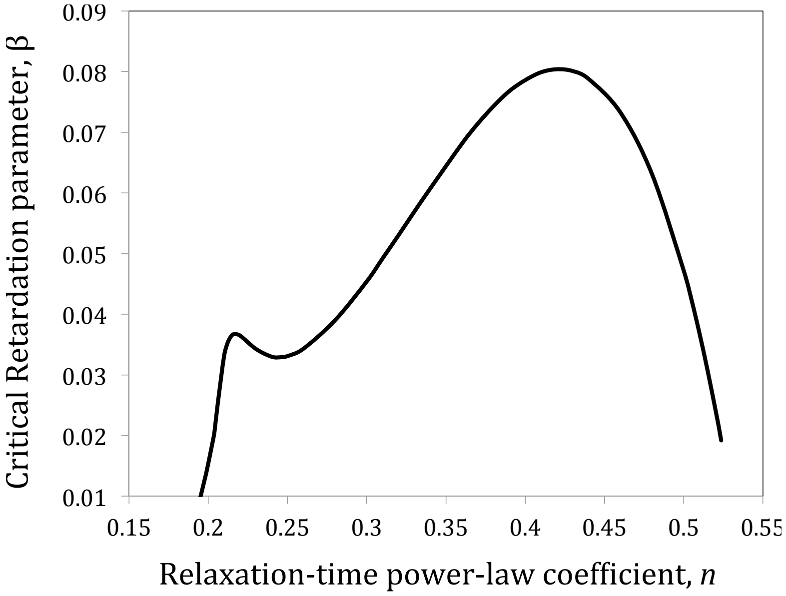

Figure 3.4: Critical retardation parameter value $\beta$ plotted against relaxation time power-law $n$; the other parameters are fixed as $m = 0.2$, $Re = 0$, $W = 2$.

Note that both the fluids discussed in the previous sections have the same value of $m = 0.2$, which means they exhibit the same flow profile; the constant-modulus fluid ($n = 0.2$), which is only marginally more stable than the experimentally-matched fluid ($n = 0.4$) in the absence of solvent, becomes stable much sooner as solvent viscosity is added to both fluids.

From figures 3.2–3.4 it is clearly seen that, at least for these test cases, the first effect of adding a solvent that shear thins at the same rate than the polymer is to *stabilise* the flow. This suggests that viscoelasticity, rather than shear-thinning alone, is a critical component of the mechanism of instability.

### 3.4.2 Critical Weissenberg number

In the previous section we showed that adding solvent can stabilise flows at a fixed Weissenberg number. However, for a more systematic picture of the instability, and particularly of onset, it is of interest to know the *critical Weissenberg number*:

the dimensionless flow rate below which the flow is stable to perturbations of all wavenumbers.

One such calculation was carried out by Wilson & Loridan [178] (see section 2.10.3.4): there was no solvent ($\beta = 0$), inertial terms were neglected ($Re = 0$), the power-law coefficient $m = 0.2$ was fixed, and a range of values of the timescale power-law $n$ was considered. They found that the lowest critical Weissenberg number (the most unstable fluid at this value of $m$) was located at $n = 0.2$, with a second local minimum around $n = 0.4$, close to the fluid used in experiments [16]. These results are reproduced in figure 3.5, along with the corresponding curves for nonzero retardation parameter.

We see that, in all cases, the critical Weissenberg number increases with increasing $\beta$: that is, as we had already postulated, the presence of inelastic solvent is stabilising. At $\beta = 0$ (the case presented in [178]) there is a sharp minimum in the curve at $n = 0.2$ (for which the shear modulus is constant, $n = m$) and a broader minimum around $n = 0.4$ (a shear-thinning modulus similar to the fluid used by Bodiguel. The constant-modulus case $n = 0.2$ becomes unstable at a lower critical Weissenberg number than any other fluid. The critical Weissenberg number increases markedly for large or small $n$.

As $\beta$ is increased, the sharp minimum first becomes broader and more stable (this happens very quickly; even a very small solvent contribution $\beta = 0.01$ is enough to make this fluid more stable than the shear-thinning modulus case $n \approx 0.4$), moves to slightly larger values of $n$, and then disappears completely at $\beta = 0.046$ (shown in figure 3.5b). Beyond this value, the dominant instability is the broad minimum which started at $n \approx 0.4$; this also shifts slightly to higher $n$.

As $\beta$ increases further, there are no more exciting developments in the critical Weissenberg number curve, which has one simple minimum. The flow becomes more stable (the critical Weissenberg number increases), and the most dangerous fluid (at

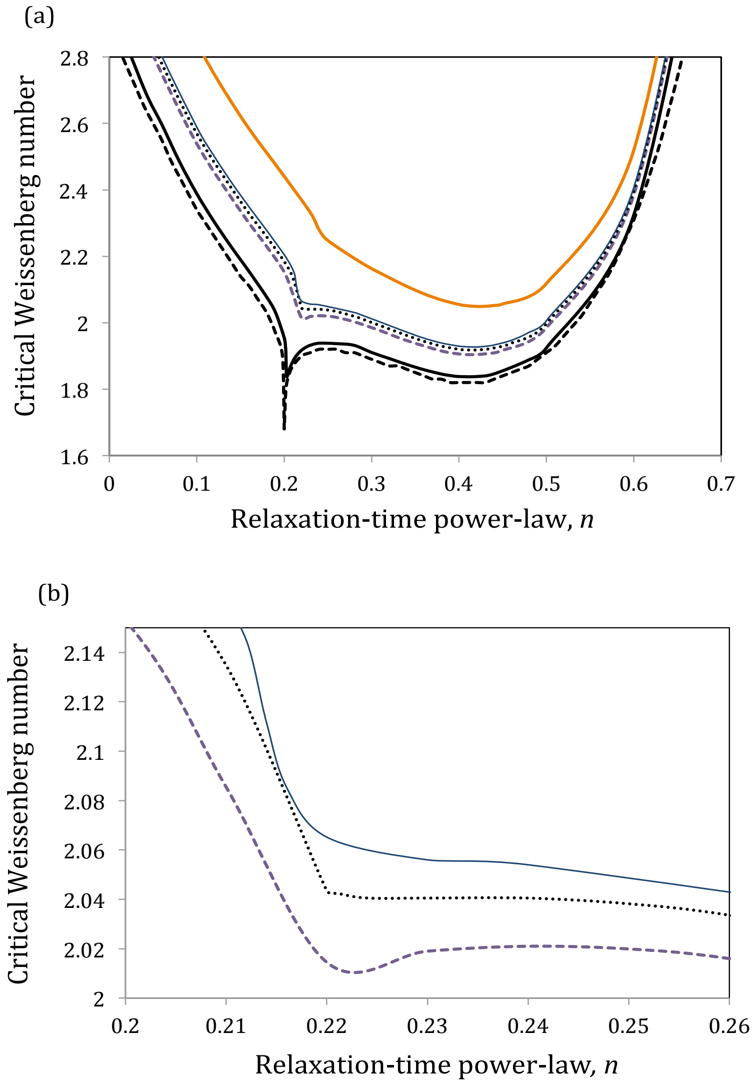

Figure 3.5: Critical Weissenberg number plotted against the relaxation time power-law, $n$, for different values of the retardation parameter $\beta$, in the absence of inertia ($Re = 0$). We have fixed $m = 0.2$. (a) Increasing from bottom: $\beta = 0$, 0.01, 0.04, 0.046, 0.05, 0.1; (b) the disappearance of the local minimum near $n = 0.2$: (from bottom) $\beta = 0.04$, 0.046, 0.05.

$m = 0.2$) is found at increasingly larger values of $n$.

The results shown in figure 3.5 are consistent with those we saw in figure 3.4: the local minimum located at $n = 0.4$ in the plot of critical Weissenberg number stabilises relatively slowly with the addition of solvent, so requires a larger value of $\beta$ to stabilise the flow. On the other hand, for the lowest $W_{\text{crit}}$ seen at $m = n = 0.2$ when $\beta = 0$, the effect of solvent is more dramatic and a much lower value of $\beta$ is sufficient to banish the instability.

#### 3.4.2.1 Case study fluid: Experimental matching

In this section we take the fluid rheology measured for the fluid used in the experiments of Bodiguel [16], that is, $m = 0.2$, $n = 0.4$, and examine the evolution of the critical Weissenberg number with changing the retardation parameter $\beta$. We have seen already that $W_{\text{crit}}$ increases with increasing $\beta$ when $\beta$ is small; in figure 3.6 we plot it against $\beta$ for a wider range.

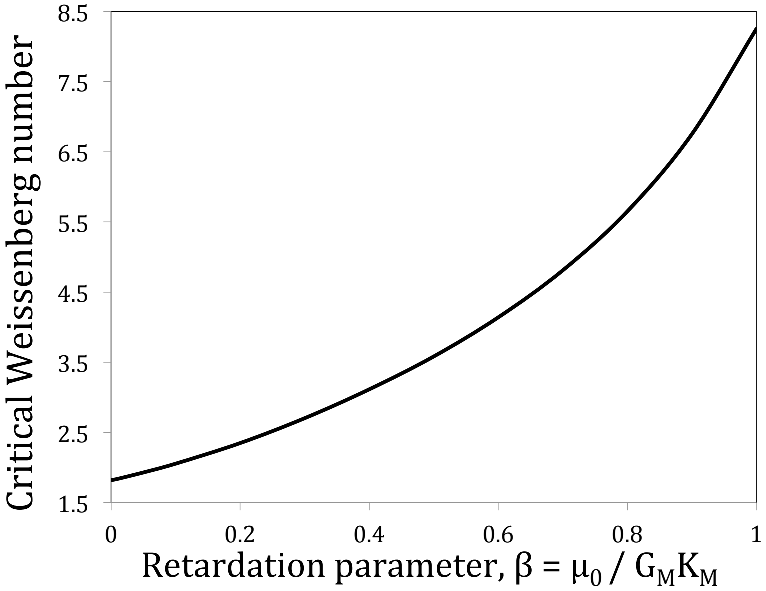

Figure 3.6: Plot of the critical Weissenberg number against the retardation parameter $\beta$ for an exemplar fluid defined by $m = 0.2$, $n = 0.4$.

At values of $\beta < 0.1$, the growth of $W_{\text{crit}}$ with $\beta$ is approximately linear ($W_{\text{crit}} \approx 1.82 + 2.3\beta$), but for larger $\beta$ the growth is faster and by a value of $\beta = 1$ (when the total shear viscosity has equal components from the solvent and elastic contributions) we have $W_{\text{crit}} = 8.25$.

At much higher values of $\beta$, the required flow rate for instability becomes very large; and extrapolating from the data shown in figure 3.6, we expect that in the limit $\beta \to \infty$, for which there is no elastic contribution to the stress, the flow will be unconditionally stable at all Weissenberg numbers.

#### 3.4.2.2 Dependence of critical Weissenberg number on shear stress power law, $m$

We have seen in previous sections that the effect of adding solvent viscosity is purely stabilising: that is, the mechanism of this instability must be in some part elastic. However, shear-thinning must also be a critical component of the instability, since the non-shear-thinning case $m = n = 1$, the Oldroyd-B fluid, is known to be linearly stable in this flow at $Re = 0$ [81, 163].

The following question then arises: how strongly does shear-thinning affect this instability? To address this, we now study the dependence of the critical Weissenberg number on the power-law coefficient $m$, which governs the level of shear-thinning in the shear viscosity.

In this section we set $\beta = Re = 0$; we vary both the remaining fluid parameters $m$ and $n$, and we determine the critical Weissenberg number $W_{\text{crit}}$ for each flow: the Weissenberg number below which the flow is linearly stable to perturbations of all wavenumbers, $k$.

In figure 3.7a) and b) we show the results: a plot of $W_{\text{crit}}$ against $n$ for three different values of the power-law coefficient, $m = 0.20$, $0.19$ and $0.18$. The shape of the three curves is similar: $W_{\text{crit}}$ is large when the relaxation time power-law $n$ is either large or small, and the most unstable scenario (lower $W_{\text{crit}}$) occurs at $m = n$. The case $m = 0.18$ is the most unstable of the three.

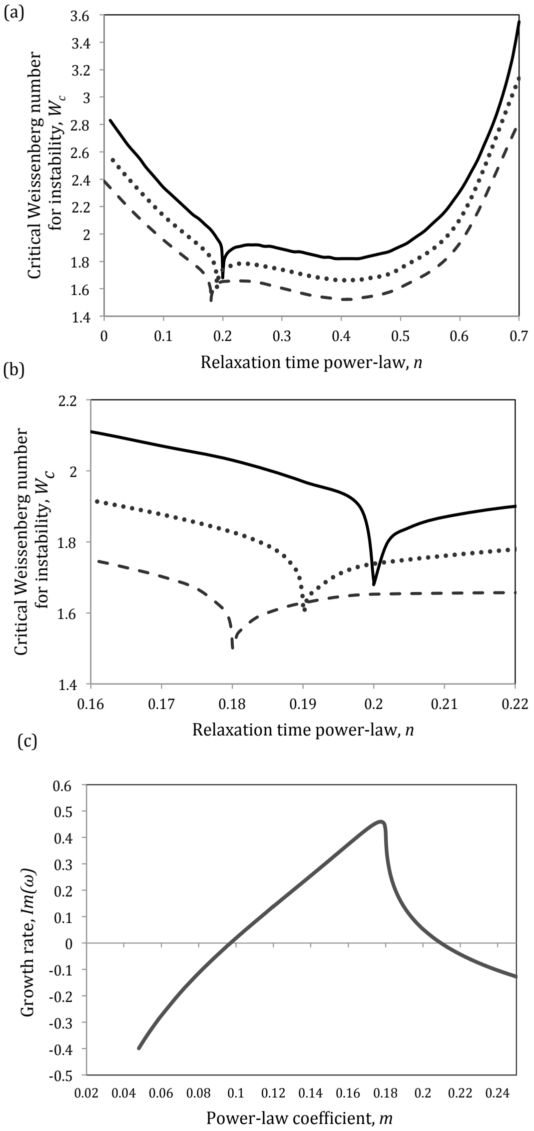

Figure 3.7: The effect of shear-thinning when $\beta = Re = 0$. (a) Plot of the critical Weissenberg number $W_{crit}$ against relaxation time power-law $n$, for three different values of the shear-stress power law $m$. Solid line: $m = 0.20$ (identical to figure 5 of [178]; dotted line: $m = 0.19$; dashed line: $m = 0.18$. (b) Small region of plot (a). (c) Dependence of the growth rate on $m$ for specific values of the other parameters: $n = 0.4$, $W = 2$, $k = 3$, $Re = 0$, $\beta = 0$

The less sharp minimum in the $W_{\text{crit}}$ curve, which for the case $\beta = 0$ is seen at $n = 0.4$, remains located at the same value of timescale $n$ for the cases $m = 0.19$ and $m = 0.18$, but with different values of $W_{\text{crit}}$ for each.

If we now add solvent viscosity, the general behaviour of the curves of $W_{\text{crit}}$ against $n$ will not be different from that observed for $m = 0.2$ (figure 3.5): the flow will be more stable as the retardation parameter increases, the lowest point seen at $m = n$ when $\beta = 0$ will no longer be the most unstable scenario, and the lowest point of the global curves will be located in a zone of weakly-shear thinning modulus near $n = 0.4$. The main difference between the three cases ($m = 0.20, m = 0.19$ and $m = 0.18$) is that the most unstable curves will be found when the power-law coefficient $m$ is equal to 0.18.

From these observations, we might be tempted to conclude that decreasing the power-law coefficient $m$ would produce fluids that are less and less stable; we might guess that the most unstable scenarios would be found in strongly shear-thinning fluids ($m \to 0$). However, this is not the case: in figure 3.7c) we give a plot of growth rate against power-law coefficient $m$, having fixed the other parameters $n = 0.4$, $\beta = Re = 0$, $W = 2$, $k = 3$. We chose these parameters to match one of the most unstable scenarios in figure 3.7a).

The instability only exists in the small region $0.1 < m < 0.205$; the strongest instability occurs at $m \approx 0.18$, while very strongly shear-thinning fluids having $m \to 0$ are fully stable, which is consistent with the observations originally made by Wilson & Loridan [178]. In that limit, we also observed that the flow is stable for any value of Weissenberg number (and therefore, no critical Weissenberg number was found).

## 3.5 Conclusions

We have investigated the stability of channel flow of a strongly shear-thinning viscoelastic fluid, modelled to imitate the experiments of Bodiguel *et al.* [16]. Extended the existing model of Wilson & Loridan [178], we introduced a non-Newtonian solvent contribution to the fluid stress, which does not change the shear-rate dependence of the fluid's shear viscosity but reduces the effect of viscoelasticity.

We introduced a new parameter: the retardation parameter, $\beta$, defined as the ratio the solvent to polymer contributions to the shear viscosity of the fluid. We found out that for a wide range of values of the other key parameters in the problem, the addition of solvent (the increase of $\beta$) has a *stabilising effect* on the flow. Since the solvent effectively reduces the size of the elastic terms in the system, we can conclude that elasticity is a key factor in the mechanism of this instability.

Two specific fluid models stand out in our analysis: the case in which the shear modulus is constant, originally studied by Wilson & Rallison [180]; and a shear-thinning modulus fluid close to that used in the experiments of Bodiguel *et al.* [16]. These fluids are both extreme in the sense that any fluid whose physical parameters are very close to one of these specific cases will be marginally more stable than our specific fluid. In the absence of solvent, the constant-shear-modulus fluid is the more unstable of the two; but it is stabilised more quickly than the shear-thinning modulus case, which rapidly becomes the dominant instability for finite values of $\beta$.

We also assessed the dependence of the instability on the degree of shear-thinning in the shear stress, described by the power-law $m$; it was observed that there is a critical level of shear-thinning for which the instability is strongest; for either weak shear-thinning $m \to 1$ or very strong shear-thinning $m \to 0$, the flow is unconditionally linearly stable. Even strong elastic shear-thinning is not the only component of this instability: some complex coupling between shear and normal stress effects is at work.

The instability cannot be caused by inertial terms, as it appears even when we fix a Reynolds number of zero. Nor is it exclusively caused by inelastic non-Newtonian effects (shear-thinning), as the addition of a shear-thinning solvent term is strongly stabilising. We conclude that the instability is of *purely elastic nature*; and we observe that its strongest effects may be observed for a fluid whose shear viscosity thins very strongly (with a power-law coefficient $m \approx 0.2$) and whose elastic modulus is weakly shear-thinning ($G \sim \dot{\gamma}^{-0.2}$).

# Chapter 4

# Channel flow stability of thixotropic-viscoelasto-plastic fluids

## 4.1 Introduction

As we have described in section 1.8, extensive theoretical and experimental research has been made by rheologists in order to understand the mechanisms behind flow instabilities of viscoelastic fluids.

Several categories of non-inertial instabilities are more or less understood: curved streamline (section 1.8.2) interfacial (section 1.8.4) and shear-banding (section 1.8.6) instabilities. Early work by Wilson & Rallison [180] (see section 2.10.1) predicted theoretically an instability that had not previously been seen, for pressure-driven channel flows of highly shear-thinning viscoelastic fluids having a constant elastic modulus and a single polymer relaxation time that depends instantaneously on the shear rate. No experimental evidence of this instability was found until 2015, when Bodiguel and his team [16] (section 2.10.2) demonstrated an elastic instability, occurring at a reproducible critical flow rate, in a channel flow of a high molecular weight polymer solution having neither curved streamlines, nor an interface, nor any evidence of shear-banding. Similar results were seen in experiments by Poole [147] in 2016, who also identified an instability for a shear-thinning viscoelastic polymer (1% polyacrylamide). However, theoretical work at that stage was restricted to a very simple model which could not capture the non-constant shear modulus of Bodiguel's polymer.

The theoretical work was subsequently extended by Wilson & Loridan [178] (section 2.10.3) and by ourselves [28] (see chapter 3) to decouple shear and normal stresses and incorporate a solvent viscosity. However, all these studies were restricted to instability modes with no cross-channel motion at the centreline because of their use of power-law rheometric functions. An additional issue is that the models they used have fluid properties (such as the relaxation time) that depend instantaneously on the flow environment. Therefore in this paper we consider a *structural* parameter (such as molecular entanglements, network junctions, or micelle length) that is changing with deformation history and on which the material properties depend. A finite value of the zero shear viscosity will permit cross-channel motion at the centreline, and the model also captures more complex rheological behaviours: thixotropic-viscoelasto-plasticity. Our chosen model, which satisfies all these requirements, is the BMP model [7], a structural model which has been proven to accurately reproduce the complex rheological behaviour of viscoelastic systems that also exhibit plasticity and thixotropy (see section 1.7.1). In addition, the model is capable of matching the flow curve of shear-thickening and shear-thinning fluids, non-vanishing normal stress differences, shear-banding [8] and even yield stress behaviour [22].

A paper similar to our research presented here was recently published by Renardy [154], who studied the linear stability of a shear-banded flow with viscoelasticity and thixotropic yield stress behaviour in a two-dimensional plane Couette flow; they identified bulk instabilities in the yielded phase (high shear rate zone) along with long wave interfacial instabilities.

In this work, we will stay away from shear-banded flows (which will be studied in chapter 5) and focus on identifying only bulk instabilities present in thixotropic-viscoelasto-plastic materials in pressure-driven channel flows. In section 4.2 we introduce the simplest version of the BMP model and the behaviour of our fluid in steady simple shear (see 4.2.2). We derive dimensionless equations in section 4.2.4 and construct a group of dimensionless numbers recently proposed by Ewoldt [56] that allow us to compare the effects of thixotropy, viscoelasticity and plasticity in our fluid. In section 4.3 we obtain an analytic solution for the velocity profile, and derive the perturbed governing equations for linear stability analysis. In section 4.4 we present our results and discuss them in terms of the dimensionless groups introduced in section 4.2.4. Finally, in sections 4.5 and 4.6, we make general observations and draw our conclusions.

The bulk of this chapter has also been successfully published in the *Journal of*

*Non-Newtonian Fluid Mechanics* [29].

## 4.2 Model fluid: The BMP model

Many of the materials we use in our daily life — such as foods, personal care products, paints, ink, adhesives, waxy oils, gels, biological fluids such as blood, and pharmaceuticals — fall into the category of *thixotropic-viscoelasto-plastic* materials (TVEP) (see section 1.7). These are structured fluids that display a combination of three time-dependent complex rheological behaviours: viscoelasticity, thixotropy and plasticity. Unlike Newtonian fluids (that simply consist of an homogeneous phase), these kinds of materials are usually composed of multiple phases, such as solid particles or a microstructure dispersed in a viscous (or viscoelastic) continuous phase. The rheological response of these structured fluids usually depend on multiple *characteristic time scales* of the material and on the level of deformation imposed.

TVEP materials show a complex combination of rheological behaviours. Under steady shear, the microstructure will reach a steady configuration that is determined by an equilibrium between the microstructure breakdown and build up processes. After a step change of either shear rate or shear stress, they may exhibit time dependence if a new equilibrium is not reached instantaneously. Above some threshold shear rate or shear stress, they can show microstructure collapse, with a dramatic drop in both elasticity and viscosity; and of course the viscoelastic nature of the fluid can both store energy elastically and dissipate it through viscosity. The mathematical modelling of this kind of fluid is challenging, but there has been progress in recent years. Most models rely on introducing a *structural* parameter, used as a measure of the microstructure, which evolves according to a kinetic equation including both breakdown and buildup processes.

As discussed in section 1.7.2, care needs to be taken when modelling these fluids, to distinguish the effects of thixotropy from nonlinear viscoelasticity. Thixotropy is often defined as a reversible decrease in viscosity over time during flow, but Larson [98] argues that we should instead define thixotropy as a memory that viscosity has of past *strain rate*, and viscoelasticity as a memory that stress has of past *strain*.

Existing TVEP models have been grouped by de Sousa Mendes [48] into two types. Type I models are based on the Bingham model, with thixotropy and viscoelasticity are introduced (as in [129]). On the other hand, Type II models incorporate thixotropy into a viscoelastic stress equation based on the Maxwell model. For these models, no additional equations are required to describe plasticity, as it is implicitly introduced by expressing the bulk model parameters as a function of the level of structure (when the fluid is completely structured, the viscosity is unbounded). Type II models are more robust than Type I, and are able to describe a wider range of cases, including viscoelasto-plastic fluids with no thixotropy, inelastic thixotropic viscoplastic materials, and of course, thixotropic viscoelasto-plastic or viscoelasto thixo-plastic fluids.

There are several Type II models available in the literature that can successfully describe TVEP behaviour, including de Sousa Mendes' [47] thirteen-parameter model, which is commonly used in the oil and polymer industry due to its ability to model multiple rheological flows. Seeking a simpler model that can still distinguish between thixotropy and nonlinear viscoelasticity, we select the Bautista–Manero–Puig (BMP) model [7]. The BMP model can accurately describe rheological flows of associative polymers, worm-like micellar solutions, dispersions of lamellar liquid crystals, and blood. It has five rheological parameters, which can be estimated from simple rheological experiments in steady and unsteady flows. For various choices of the parameters, it can reproduce shear thinning or shear thickening behaviour, apparent yield stress and actual yield stress.

The simplest version of the model consists of a coupled system of equations:

the Upper Convected Maxwell constitutive equation, which calculates the polymer contribution to the stress tensor, along with a kinetic equation proposed by Fredrickson [67], which introduces a *structural parameter*. In thixotropic systems it is observed that the instantaneous rheological properties (such as viscosity) depend on the level of internal structure of the system, and this level changes with deformation history. The evolution of the internal microstructure of the fluid (and therefore, the viscosity) depends on the balance between two processes. The first, *structural reformation* (or *spontaneous build up of viscosity*), occurs whenever the fluid is not perfectly structured, at a rate that is assumed to be independent of the rate at which shear work is done on the material, but instead depends on a characteristic recovery timescale of the material. The second process, *structural destruction* (or *breakdown of viscosity*), occurs only under flow, at a rate that depends on the shear work applied to the material. Fredrickson [67] initially coupled his kinetic equation with a Newtonian stress equation to predict inelastic thixotropic behaviour of suspensions under shear flow. Bautista and colleagues [7] simply introduced the Upper-Convected Maxwell model instead of the Newtonian constitutive equation to incorporate nonlinear viscoelasticity.

A family of models originating from the BMP model have been developed in recent years, introducing extra parameters to predict even more complex rheological phenomena. Examples include shear-banding flows in wormlike micellar solutions [8], and diffusion of species [69]. For the current work we have selected the original BMP for simplicity, and in order to focus on bulk, rather than interfacial, instabilities. Another complication we can avoid is the addition of a solvent viscosity, as it has been shown in our previous work [28] (see chapter 3) that the addition of an inelastic solvent stabilises the flow. Although we will not consider shear banding effects, the model we use is still valid for, for instance, micellar systems above the critical temperature, for which shear-banding is not observed [27].

### 4.2.1 Governing equations

The stress tensor $\underline{\underline{\sigma}}$ for a BMP fluid flowing with velocity $\underline{u}$ evolves according to the UCM model (discussed in section 1.6.2.2):

$$\underline{\underline{\sigma}} + \frac{1}{G_0\varphi} \overset{\triangledown}{\underline{\underline{\sigma}}} = \frac{2}{\varphi}\underline{\underline{D}}, \tag{4.1}$$

in which the upper-convected derivative is defined as:

$$\overset{\triangledown}{\underline{\underline{\sigma}}} = \frac{D\underline{\underline{\sigma}}}{Dt} - \underline{\underline{\sigma}} \cdot (\underline{\nabla}\,\underline{u}) - (\underline{\nabla}\,\underline{u})^{\top} \cdot \underline{\underline{\sigma}}, \tag{4.2}$$

and $D/Dt$ denotes the material derivative [14] (for any scalar, vector or tensor quantity $A$):

$$\frac{DA}{Dt} = \frac{\partial A}{\partial t} + \underline{u} \cdot \underline{\nabla}\, A, \tag{4.3}$$

and $\underline{\underline{D}}$ is the symmetric part of the flow gradient tensor: The parameters here are $G_0$, the stress modulus, and the variable $\varphi$, which is our structural parameter called *fluidity*, simply defined as the inverse of the viscosity ($\equiv \eta$). It evolves according to Fredrickson's equation:

$$\frac{D\varphi}{Dt} = \frac{1}{\lambda}(\varphi_0 - \varphi) + K_0(\varphi_\infty - \varphi)\underline{\underline{\sigma}} : \underline{\underline{D}}, \tag{4.4}$$

The right hand side of (4.4) consists of two terms: the reformation process (build up of viscosity or breakdown of fluidity), parametrised by $\lambda$, the *structural relaxation time* and $\varphi_0$, the plateau fluidity observed at low shear rates; and the destruction process (breakdown of viscosity or build up of fluidity), described by $K_0$, a rate parameter for structure destruction, $\varphi_\infty$, the fluidity at high shear rates, and $\sigma_{ij}D_{ij}$, the rate of energy dissipation in the fluid.

Equations (4.1) and (4.4) are then coupled with the continuity and momentum equations, which are (in the absence of external forces such as gravity):

$$\underline{\nabla} \cdot \underline{u} = 0 \tag{4.5}$$

$$\rho \left( \frac{\partial \underline{u}}{\partial t} + \underline{u} \cdot \underline{\nabla u} \right) = -\underline{\nabla} P + \underline{\nabla} \cdot \underline{\underline{\sigma}}. \tag{4.6}$$

### 4.2.2 Behaviour in steady simple shear

For simple steady shear flow, given in cartesian coordinates by $\underline{u} = \dot{\gamma} y \underline{e}_x$ with $\dot{\gamma} > 0$, equations (4.1) and (4.4) give:

$$\underline{\underline{\sigma}} = \begin{pmatrix} 2\dot{\gamma}^2 G_0^{-1} \varphi^{-2} & \varphi^{-1}\dot{\gamma} \\ \varphi^{-1}\dot{\gamma} & 0 \end{pmatrix}, \tag{4.7}$$

$$0 = \frac{1}{\lambda}(\varphi_0 - \varphi) + K_0(\varphi_\infty - \varphi)\frac{\dot{\gamma}^2}{\varphi}. \tag{4.8}$$

Equation (4.8) is a quadratic equation for the fluidity, whose solution is:

$$\varphi = \frac{-(K_0\lambda\dot{\gamma}^2 - \varphi_0) \pm \sqrt{(K_0\lambda\dot{\gamma}^2 - \varphi_0)^2 + 4(K_0\lambda\dot{\gamma}^2\varphi_\infty)}}{2}, \tag{4.9}$$

For a given set of parameters $K_0$, $\lambda$, $\varphi_0$ and $\varphi_\infty$, equation (4.9) has exactly one real positive root. If the product $K_0\lambda$ is zero (this is *no destruction of structure*), we have a simple Maxwell fluid with constant viscosity $\eta_0$ ($\equiv \varphi_0^{-1}$). On the other hand, if the product $K_0\lambda \to \infty$ (this is *dominant reformation of structure*), we reach the other extreme $\varphi = \varphi_\infty$ for any nonzero shear rate.

The viscometric functions (viscosity $\eta$, shear stress $\sigma_{12}$ and the first normal stress difference coefficient $\Psi_1$) are given as:

$$\eta = \varphi^{-1} \qquad \sigma_{12} = \eta\dot{\gamma} \qquad \Psi_1 = \frac{\sigma_{11} - \sigma_{22}}{\dot{\gamma}^2} = 2G_0^{-1}\eta^2. \tag{4.10}$$

Figure 4.1 illustrates the behaviour of these viscometric functions with shear rate, using parameter values $\varphi_\infty = 15\,\text{Pa}^{-1}\text{s}^{-1}$, $\varphi_0 = 1.3\,\text{Pa}^{-1}\text{s}^{-1}$, $G_0 = 68\,\text{Pa}$ and $K_0\lambda = 7 \times 10^{-6}\,\text{Pa}^{-1}\,\text{s}$ chosen to fit a shear-thinning low-concentration micellar solution of CTAT above the shear-banding temperature [27].

#### 4.2.2.1 Shear viscosity and critical shear stress

Figure 4.1(a) shows the nonlinear global behaviour of the shear stress as a function of shear rate. There are two distinct Newtonian-like regions, which correspond (figure 4.1(b)) to regions of near-constant fluidity. The low-shear rate phase of complex entangled networks (fully structured state) has $\varphi \approx \varphi_0$, and the unstructured state (or highly oriented flow region) has $\varphi \approx \varphi_\infty$. The shear stress is a monotonic function of shear rate, and for moderate shear rates there is a small *transition* zone between the phases.

Fredrickson [67] observed that under the sudden startup of shear (with imposed shear stress, see section 1.5.2.1) there are two different types of behaviour: *primary creep*, at low shear stress, in which the strain rate decreases over time; and *accelerating flow*, in which the strain rate increases monotonically towards its steady value. He defined a critical stress $\sigma_c$ separating these two regimes, which can be calculated as:

$$\sigma_c = \frac{1}{\sqrt{K_0\,\lambda\,\varphi_\infty\,(1 - 2\varphi_0/\varphi_\infty)}}. \tag{4.11}$$

This critical stress value is marked in figure 4.1a) by a black circle. At small values of $\varphi_0$, an *apparent yield stress* is observed, and at $\varphi_0 = 0$, the first Newtonian region (located at low values of shear rate) vanishes and a non-zero stress $\sigma_y$ is found even for vanishing values of shear rates:

$$\sigma_y = (K_0\,\lambda\,\varphi_\infty)^{-1/2}. \tag{4.12}$$

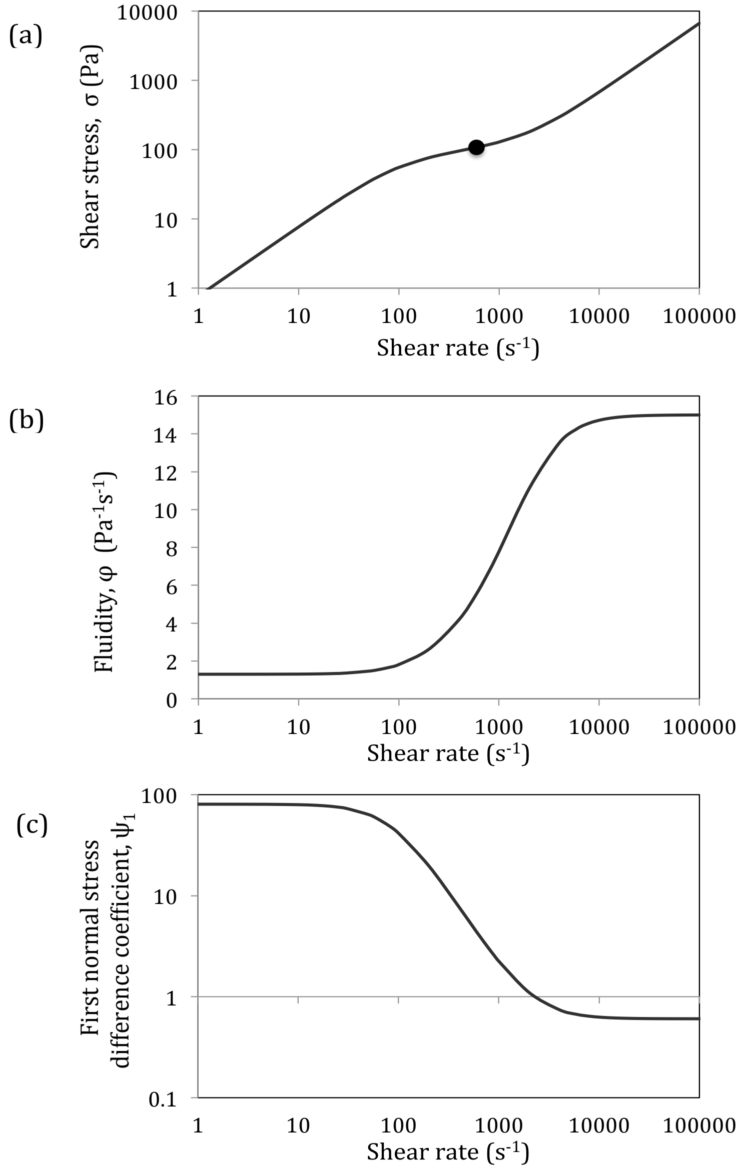

Figure 4.1: Plots of viscometric functions against shear rate for the BMP model: (a) shear stress, (b) fluidity and (c) first normal stress difference coefficient. In all cases, $\varphi_\infty = 15\,\mathrm{Pa}^{-1}\mathrm{s}^{-1}$, $\varphi_0 = 1.3\,\mathrm{Pa}^{-1}\mathrm{s}^{-1}$, $G_0 = 68\,\mathrm{Pa}$, and $K_0\lambda = 7 \times 10^{-6}\,\mathrm{kg\,m}^{-1}\mathrm{s}^{-2}$. The point marks the critical shear stress defined by equation (4.11). The BMP model parameter values shown here are the best fit to experimental values of a simple shear flow of a micellar solution [27].

Calderas [22] and his team showed experimentally that the yield stress measured for Kaolin suspensions can be modelled using the BMP model.

#### 4.2.2.2 Fluidity and first normal stress difference coefficient

Unlike the power-law functions shown in the previous chapters, the BMP model exhibits plateaus at low and high shear rates for both the fluidity $\varphi$ and the first normal stress difference coefficient $\Psi_1$ (shown in figures 4.1b) and 4.1c)). We can think of a viscoelastic relaxation time $\lambda_R$ defined via the shear viscosity as

$$\lambda_R = \frac{\eta}{G_0} = \frac{1}{G_0\varphi}; \tag{4.13}$$

in that case, the normal stress coefficient is

$$\Psi_1 = \frac{2\eta^2}{G_0} = 2G_0\lambda_R^2. \tag{4.14}$$

In the transition region, if we fit the fluidity curve with a power law $\varphi \sim \dot{\gamma}^{1-n}$ then $\lambda_R$ will follow the same power law and it follows that $\Psi_1$ grows as $\dot{\gamma}^{2(1-n)}$.

Returning to the plateaus, we can use equation (4.9) to estimate the range of shear rates applying to each:

$$\varphi \approx \varphi_0 \text{ when } \dot{\gamma}^2 \ll \frac{\varphi_0}{K_0\lambda}; \qquad \varphi \approx \varphi_\infty \text{ when } \dot{\gamma}^2 \gg \frac{\varphi_\infty}{K_0\lambda}. \tag{4.15}$$

### 4.2.3 Dimensional velocity profile

The steady velocity gradient profile for a BMP model fluid flowing in a two-dimensional channel of infinite extent in the $x$-direction and with $-L \le y \le L$ under pressure gradient $\mathscr{P}$ (sketched in section 2.4) is given by:

$$\dot{\gamma}_0 = |U'| = \frac{1}{2}\varphi_\infty \mathscr{P} y - \frac{1}{2K_0\lambda\mathscr{P}y} \pm \frac{\sqrt{b_0 y^4 - c_0 y^2 + 1}}{2K_0\lambda\mathscr{P}y}, \tag{4.16}$$

where the coefficients $b_0$ and $c_0$ are:

$$b_0 = K_0^2\lambda^2\varphi_\infty^2\mathscr{P}^4 \qquad c_0 = 2K_0\lambda\mathscr{P}^2(\varphi_\infty - 2\varphi_0). \tag{4.17}$$

Integrating equation (4.16) and applying non-slip boundary conditions at the channel-wall ($y = \pm L$), we obtain the velocity profile:

$$U = \frac{1}{4}\varphi_\infty\mathscr{P}(L^2 - y^2) - \frac{1}{4K_0\lambda\mathscr{P}}(U_{01} + U_{02} + U_{03}), \tag{4.18}$$

where:

$$U_{01} = \sqrt{b_0 y^4 - c_0 y^2 + 1} - \sqrt{b_0 L^4 - c_0 L^2 + 1} \tag{4.19}$$

$$U_{02} = \frac{1}{2}\frac{c_0}{\sqrt{b_0}} \ln\left[\frac{2\sqrt{b_0}\sqrt{b_0 L^4 - c_0 L^2 + 1} + 2b_0 L^2 - c_0}{2\sqrt{b_0}\sqrt{b_0 y^4 - c_0 y^2 + 1} + 2b_0 y^2 - c_0}\right] \tag{4.20}$$

$$U_{03} = \ln\left[\frac{2 - c_0 L^2 + 2\sqrt{b_0 L^4 - c_0 L^2 + 1}}{2 - c_0 y^2 + 2\sqrt{b_0 y^4 - c_0 y^2 + 1}}\right]. \tag{4.21}$$

The centreline velocity $U(0) = U_0$ is:

$$\begin{aligned} U_0 = \frac{1}{4}\varphi_\infty\mathscr{P}L^2 - \frac{1}{4K_0\lambda\mathscr{P}} \Bigg(1 - \sqrt{b_0 L^4 - c_0 L^2 + 1} \\ + \frac{c_0}{2\sqrt{b_0}} \ln\left[\frac{2\sqrt{b_0}\sqrt{b_0 L^4 - c_0 L^2 + 1} + 2b_0 L^2 - c_0}{2\sqrt{b_0} - c_0}\right] \\ + \ln\left[\frac{2 - c_0 L^2 + 2\sqrt{b_0 L^4 - c_0 L^2 + 1}}{4}\right]\Bigg). \end{aligned} \tag{4.22}$$

The velocity profiles will be discussed with more detail in the following sections.

### 4.2.4 Dimensionless form of the governing equations

For this stability problem, we scale lengths with $L$, times using the average shear rate $U_0/L$, and fluidities with the high-shear rate value $\varphi_\infty$. The natural stress scale then becomes $\varphi_\infty^{-1}(U_0/L)$. In terms of dimensionless variables, the governing equations become:

$$\underline{\nabla} \cdot \underline{u} = 0 \tag{4.23}$$

$$Re\left(\frac{\partial \underline{u}}{\partial t} + \underline{u} \cdot \underline{\nabla u}\right) = -\underline{\nabla} P + \underline{\nabla} \cdot \underline{\underline{\sigma}} \tag{4.24}$$

$$\underline{\underline{\sigma}} + \frac{W}{\varphi} \overset{\nabla}{\underline{\underline{\sigma}}} = \frac{2}{\varphi} \underline{\underline{D}} \tag{4.25}$$

$$\frac{D\varphi}{Dt} = \frac{1}{\Lambda}(\Phi - \varphi) + \Gamma(1-\varphi)\underline{\underline{\sigma}} : \underline{\underline{D}} \tag{4.26}$$

Five dimensionless numbers appear in our system of equations, being the well-known Reynolds number $Re$ and Weissenberg number $W$:

$$Re = \rho\, U_0\, L\, \varphi_\infty \qquad W = \lambda_{ve}\left(\frac{U_0}{L}\right) = \frac{1}{G_0 \varphi_\infty}\left(\frac{U_0}{L}\right). \tag{4.27}$$

along with the extra parameters required by the model:

$$\Phi = \frac{\varphi_0}{\varphi_\infty} = \frac{\eta_\infty}{\eta_0} \qquad \Lambda = \lambda\left(\frac{U_0}{L}\right) \qquad \Gamma = \left(\frac{1}{\varphi_\infty}\frac{U_0}{L}\right) K_0 \tag{4.28}$$

$\Phi$, the *thixotropic ratio*, is simply the ratio between zero and high shear rate fluidities. Despite its simplicity, this dimensionless number is highly important to distinguish between shear-thinning ($\Phi < 1$) and shear-thickening ($\Phi > 1$) fluids. The thixotropic ratio is analogous to the exponent $n$ used in power-law models [180]; both indicate the strength the shear-thinning behaviour: for low values of both parameters ($\Phi$ and $n \ll 1$) we have a strongly shear-thinning fluid. The remaining parameters $\Lambda$ and

$\Gamma$ are timescale and stress ratios, which we discuss in the following sections. They are crucial in defining the key dimensionless quantities of thixo-elasto-plasticity: the thixoelastic, thixoplastic and elastoplastic numbers.

#### 4.2.4.1 Thixoviscous and thixoelastic numbers

A recently published paper by Ewoldt & McKinley [56] shows how plasticity and thixotropy can be incorporated with viscoelasticity. Each one of these complex rheological behaviours has a characteristic timescale. These timescales allow us to form dimensionless groups that can be mapped into a three dimensional space to represent thixotropic elastoviscoplastic material responses. In this section we form Ewoldt and McKinley's three dimensionless groups for the BMP model.

The first grouping is $\Lambda$, as defined in equation (4.28), and is the ratio of the fluid's reformation time to a typical flow time. It is known as the *thixoviscous number*; its form looks similar to the Weissenberg number of equation (4.27), but critically, the timescale $\lambda$ here is not the viscoelastic relaxation time but the time over which structure recovers from flow. For high values of the thixoviscous number ($\Lambda \to \infty$), the fluid will exhibit a slow or null recovery of viscosity after the cessation of flow; fast structural recovery is seen for the opposite case ($\Lambda \to 0$).

The next grouping is the *thixoelastic number*. In section 1.7.2, we discussed that there is often confusion in the literature between non-ideal thixotropy and non-linear viscoelasticity. Larson [98] states that pure thixotropic behaviour can only occur when the viscoelastic relaxation time $\lambda_{ve}$ is much shorter than the thixotropic timescale $\lambda$. We define the thixoelastic number as

$$W_{te} = \frac{\lambda_{ve}}{\lambda} = \frac{W}{\Lambda}. \tag{4.29}$$

Large values of $W_{te}$ correspond to pure viscoelasticity, with any thixotropic response happening very quickly; strong thixotropy is the opposite limit $W_{te} \to 0$.

#### 4.2.4.2 Dimensionless critical stress and thixoplastic number

The parameter $\Gamma$ in equation (4.28) is associated with the destruction or breaking down of structure. $K_0$ has units $(\text{stress})^{-1}$, which indicates that $\Gamma$ is in some way a ratio of stresses. When we come to solve for steady channel flow, the parameter $\Gamma$ only appears in the combination $\Gamma\Lambda$, which has been defined by Herrera *et al.* [78] as the ratio between viscous work and kinetic structural work:

$$\Gamma\Lambda = \frac{\eta_\infty (U_0/L)^2}{(K_0\lambda)^{-1}}. \tag{4.30}$$

This means that for high values of $\Gamma\Lambda$ the structural destruction dominates over reformation and we have a highly thixotropic material. For small $\Gamma\Lambda$, we have either weak destruction or quick structural reformation.

For a steady, homogeneous flow, the limit $\Lambda \to \infty$ (no fluidity recovery) yields a viscoelastic fluid having a dimensionless fluidity equal to 1 (i.e. a value of the dimensional fluidity equal to the high-shear rate fluidity, $\varphi_\infty$). If, on the other hand, the destruction parameter $\Gamma = 0$ (this is no breaking down of structures), we have a similar scenario: a viscoelastic fluid but with a fluidity $\varphi_0$.

The dimensionless form of the critical stress in (4.11) can be defined in terms of $\Gamma$, $\Lambda$ and $\Phi$:

$$\tau_c = \frac{1}{\sqrt{\Gamma\Lambda\,(1-2\Phi)}}. \tag{4.31}$$

If the product $\Gamma\Lambda$ is large, only a small stress is required to destroy the complex structural networks. Note that yield stress behaviour is recovered when $\Phi = 0$, and equation (4.31) is reduced to:

$$\tau_y = (\Gamma\Lambda)^{-1/2}. \tag{4.32}$$

As discussed in [56], for thixo-plastic fluids in which the (apparent) yield stress $\sigma_c$ or $\sigma_y$ is re-established after the cessation of flow, we can define the (dimensionless) timescale over which this process occurs:

$$\lambda_{tp} = \frac{\eta_\infty}{\sigma_c} \qquad W_{tp} = \lambda_{tp}\left(\frac{U_0}{L}\right) = \sqrt{\Gamma\Lambda\left(1-2\Phi\right)}. \tag{4.33}$$

This new dimensionless number $W_{tp}$ is the *thixoplastic number*, and is simply the inverse of the Bingham number. If $W_{tp} \to 0$, an apparent yield stress is observed; for higher values of $W_{tp}$ the recovery of critical stress after flow is slower, and in the limit $W_{tp} \to \infty$ no critical stress is observed.

We have now derived all the dimensionless groups described in [56] in terms of our dimensionless numbers from equation (4.28). Of course, other combinations of these can be made; but these three parameters $\Lambda$, $W_{te}$ and $W_{tp}$, serve to link our results to the framework introduced by [56].

## 4.3 Stability calculation

### 4.3.1 Base state

Under pressure-driven channel flow conditions (see section 2.6), and denoting $U' = \mathrm{d}U/\mathrm{d}y$, equations (4.23)–(4.26) become:

$$0 = \mathcal{P} + \frac{\mathrm{d}\sigma_{12}}{\mathrm{d}y} \tag{4.34}$$

$$\sigma_{12} = \frac{1}{\varphi}\frac{\mathrm{d}U}{\mathrm{d}y} \qquad \varphi = \frac{\Phi + \Gamma\Lambda\sigma_{12}U'}{1+\Gamma\Lambda\sigma_{12}U'}. \tag{4.35}$$

Equation (4.34) immediately gives:

$$\sigma_{12} = -\mathcal{P}y + C, \tag{4.36}$$

where we can discard the constant $C$ by symmetry arguments. Substituting equation (4.36) into equation (4.35), we obtain an equation for the velocity gradient:

$$\dot{\gamma}_0 = |U'| = \frac{1}{2}\mathcal{P}y - \frac{1}{2\Gamma\Lambda\mathcal{P}y} \pm \frac{\sqrt{by^4 - cy^2 + 1}}{2\Gamma\Lambda\mathcal{P}y}, \tag{4.37}$$

in which

$$b = \Gamma^2\Lambda^2\mathcal{P}^4, \qquad c = 2W_{tp}^2\mathcal{P}^2 = 2\Gamma\Lambda(1-2\Phi)\mathcal{P}^2. \tag{4.38}$$

Equation (4.37) (which has only one physically possible root) is the analytic form of the shear rate $\dot{\gamma}_0$. For the case no structural breakdown, or of fast recovery, we are in the limit $\Gamma\Lambda = 0$ and equation (4.37) is reduced to $\dot{\gamma}_0 = \Phi\mathcal{P}|y|$, which is the profile of a Maxwell fluid with our low-shear viscosity. In that case we have a simple velocity profile $U = (1/2)\Phi\mathcal{P}(1-y^2)$. In the opposite limit of null structural relaxation $\Gamma\Lambda \to \infty$ the fluid takes on the high-shear viscosity and the shear rate and velocity profiles are $2|y|$ and $(1-y^2)$, respectively.

Integrating equation (4.37) and applying the no-slip boundary conditions on the channel walls, we have an analytic equation for the velocity profile:

$$U = \frac{1}{4}\mathcal{P}(1-y^2) - \frac{1}{4\Gamma\Lambda\mathcal{P}}(U_1 + U_2 + U_3), \tag{4.39}$$

where:

$$\begin{aligned}
U_1 &= \sqrt{by^4 - cy^2 + 1} - \sqrt{b - c + 1} && (4.40)\\
U_2 &= \frac{c}{2\sqrt{b}}\ln\left[\frac{2\sqrt{b}\sqrt{b-c+1} + 2b - c}{2\sqrt{b}\sqrt{by^4 - cy^2 + 1} + 2by^2 - c}\right] && (4.41)\\
U_3 &= \ln\left[\frac{2 - c + 2\sqrt{b-c+1}}{2 - cy^2 + 2\sqrt{by^4 - cy^2 + 1}}\right], && (4.42)
\end{aligned}$$

with centreline velocity:

$$U_0 = \frac{1}{4}\mathcal{P} - \frac{1}{4\Gamma\Lambda\mathcal{P}}\Bigg(1 - \sqrt{b-c+1} + \frac{c}{2\sqrt{b}}\ln\left[\frac{2\sqrt{b}\sqrt{b-c+1}+2b-c}{2\sqrt{b}-c}\right] + \ln\left[\frac{2-c+2\sqrt{b-c+1}}{4}\right]\Bigg). \qquad (4.43)$$

Equations (4.39) and (4.43) allow us to calculate the velocity profile, and along with the fluidity (4.35) and shear rate (4.37) equations, we can fully describe the base state for our system. However, the value of the dimensionless gradient pressure gradient $\mathcal{P}$ has to be determined numerically to satisfy the constraint that the dimensionless centreline velocity $U_0$ of equation (4.43) is equal to 1.

## 4.3.2 Velocity profiles

### 4.3.2.1 Dependence on the thixotropic ratio

In this section we will illustrate some of the different velocity and fluidity profiles that can be obtained for various values of our model parameters.

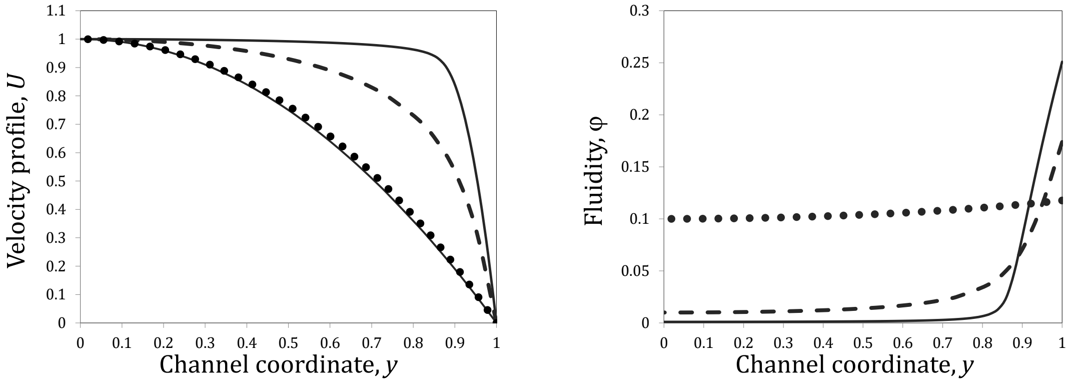

(a) Velocity profile

(b) Fluidity profile

Figure 4.2: Velocity and fluidity profiles from equations (4.39)–(4.42) and (4.35) with $\Gamma\Lambda = 0.005$. For both panels, dotted line ($\Phi = 0.1$), dashed line ($\Phi = 0.01$) and top solid line ($\Phi = 0.001$, highly shear-thinning fluid). The bottom solid line in (a) is the velocity profile for the Maxwell case, $\Phi = 1$).

In figure 4.2 we show profiles of velocity and fluidity different values of the thixotropic ratio $\Phi$, keeping the structural evolution parameter constant, $\Gamma\Lambda = 0.0005$. The bottom solid line in (4.2a), which we have not included in the fluidity plot, represents the case $\Phi = 1$, for which the fluidity is constant: the Maxwell model. As the thixotropic ratio decreases, the curves approach a plug flow near the centreline of the channel; this is most evident for the case when $\Phi = 0.001$ (solid line), where a Bingham-like behaviour is observed (see section 2.5). A higher value of the dimensionless pressure gradient is required to keep the centreline velocity at 1 as $\Phi \to 0$.

We see in figure 4.2b) that the fluidity at the centreline is given by $\Phi$; and that the fluidity increases as we move away from the centreline. For the case $\Phi = 0.1$ (dotted-line), the fluidity is almost constant across the channel, yielding a nearly-parabolic velocity profile similar to the Maxwell model. For the particular case $\Phi = 0.001$, the critical stress $\tau_c$ (calculated with equation (4.31)) is reached within the channel (at $y \approx 0.867$), giving a higher value of fluidity at the wall than the other cases.

#### 4.3.2.2 Extremes of structural destruction and reformation

In this section, we focus on a fixed value of the thixotropic ratio ($\Phi = 0.001$, highly shear-thinning) to study the dependence of the velocity and fluidity on the product $\Gamma\Lambda$. Since the parameters $\Gamma$ (structural destruction rate) and $\Lambda$ (structural reformation timescale) only affect the flow profiles through their product, it follows that the effect of increasing destruction by increasing $\Gamma$ is *exactly* equivalent to decreasing structural recovery by increasing $\Lambda$; in dimensional terms, for a given material this corresponds to increasing the flow rate.

In figure 4.3 we show velocity and fluidity profiles for the two extreme cases. In the case of fast recovery and slow destruction, $\Gamma\Lambda \to 0$, shown in figures (4.3a)–(4.3b), the fluidity retains its zero-shear value of $\Phi$ across the whole channel, giving constant viscosity and a parabolic velocity profile. Because our $\Phi = 0.001$ is so small, the fluid

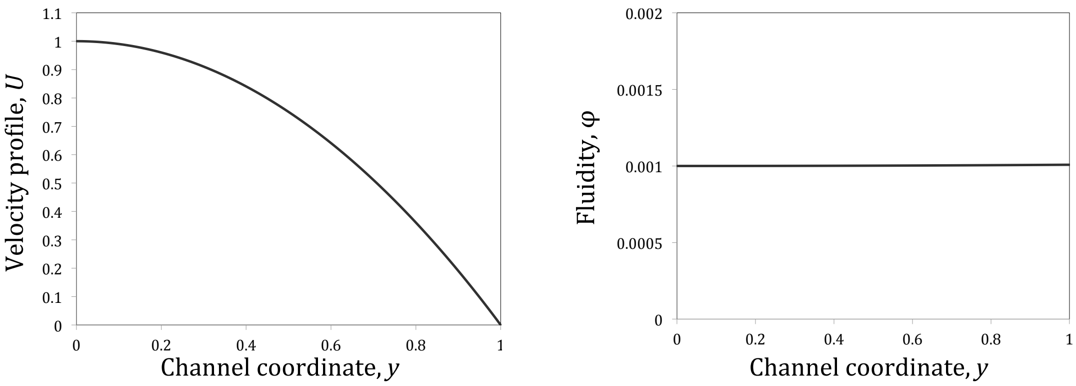

(a) Velocity profile with $\Gamma\Lambda = 0$.

(b) Fluidity profile with $\Gamma\Lambda = 0$.

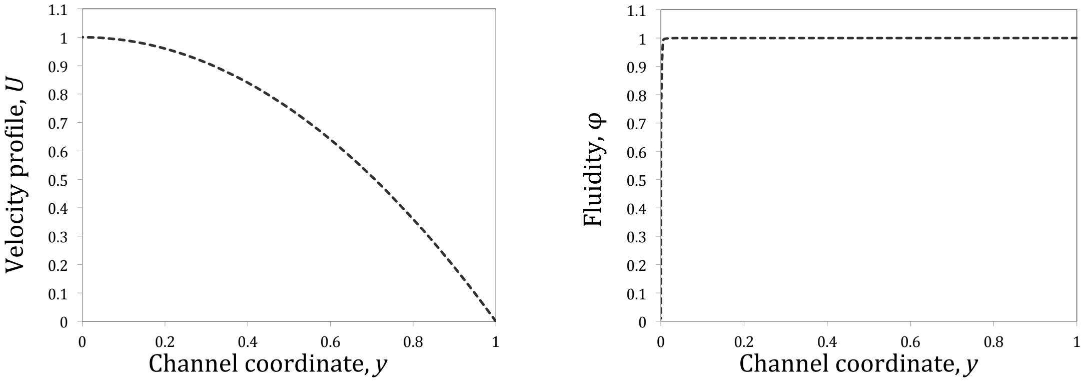

(c) Velocity profile with high $\Gamma\Lambda$.

(d) Fluidity profile with high $\Gamma\Lambda$.

Figure 4.3: Velocity and fluidity profiles from equations (4.39)–(4.42) and (4.35) with $\Phi = 0.001$. Parts (a) and (b) shows a fluid with extremely quick structural recovery or null destruction, $\Gamma\Lambda \to 0$. Part (c) and (d) show a fluid that exhibits fast destruction and slow reformation ($\Gamma\Lambda = 10^6$).

is very viscous and we require a large dimensionless pressure gradient $\mathcal{P} = 2/\Phi$ to drive a flow with unit velocity at the centreline. In the opposite case $\Gamma\Lambda \gg 1$, shown in figures (4.3c)–(4.3d), there is a very small zone around the centreline where the dimensionless fluidity is equal to $\Phi = 0.001$ (*unyielded zone*), but the bulk of the channel falls in the *yielded zone*, i.e. the zone where highly oriented structures have been reached and $\varphi \approx 1$. Again, the viscosity is constant across almost all of the channel, so the velocity profile is approximately parabolic; but the fluidity is much higher than the previous case so the required pressure gradient is much smaller ($\mathcal{P} = 2$).

#### 4.3.2.3 Strong to moderate destruction

In figure 4.4 we show velocity and fluidity profiles at $\Phi = 0.001$, over a range $0.025 \leq \Gamma\Lambda \leq 0.4$. Here the central "plug flow" region where $\varphi \approx \Phi$, that we could just make out in figure 4.3d) when destruction was strong, becomes much wider as the fairly low shear rates near the centre of the channel fail to break down the fluid structure. On the velocity profiles in figure 4.4a) we have marked the channel location of the critical stress $\tau_c$ defined in equation (4.31); we see that it is a good proxy for the edge of the plug flow. As $\Gamma\Lambda$ decreases, so does the fluidity at the walls.

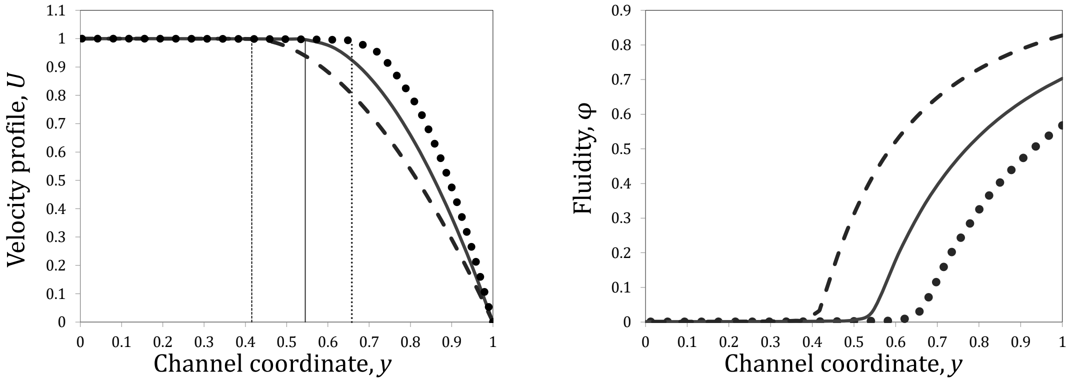

(a) Velocity profile

(b) Fluidity profile

Figure 4.4: Velocity and fluidity profiles calculated using (4.39)–(4.42) and (4.35) with $\Phi = 0.001$. For both figures, dotted line ($\Gamma\Lambda = 0.025$), solid line ($\Gamma\Lambda = 0.10$) and dashed line ($\Gamma\Lambda = 0.40$). The vertical lines in figure 4.4a) indicate the location of the critical stress $\tau_c$ calculated with (4.31).

#### 4.3.2.4 Weak destruction

When the destruction is very weak indeed, or the flow very slow (e.g. the dotted lines in figure 4.5, which correspond to $\Gamma\Lambda = 10^{-6}$) we do not see a yielded region as the whole channel is below the critical stress. The fluidity is almost constant across the channel and the velocity profile is almost parabolic. If we increase $\Gamma\Lambda$ to $7 \times 10^{-6}$, the critical stress is reached close to the channel wall (as marked in figure 4.5c) and the fluidity increases markedly in the wall region. As we increase $\Gamma\Lambda$ further, this

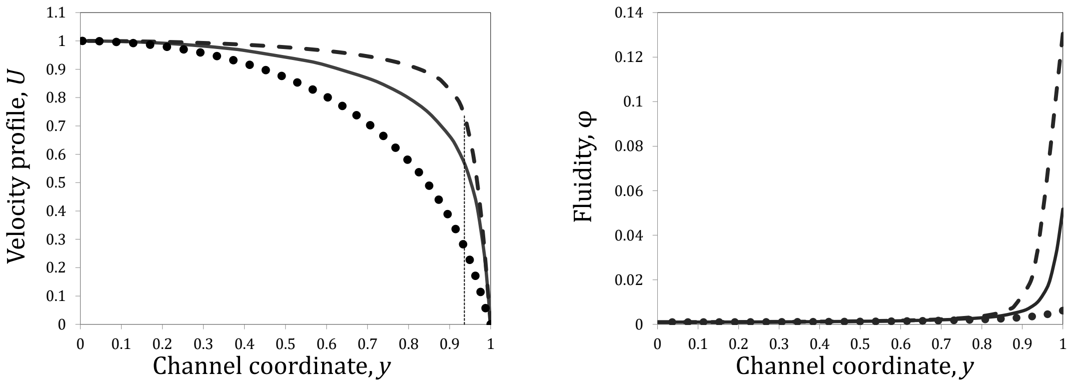

(a) Velocity profiles (b) Fluidity profiles

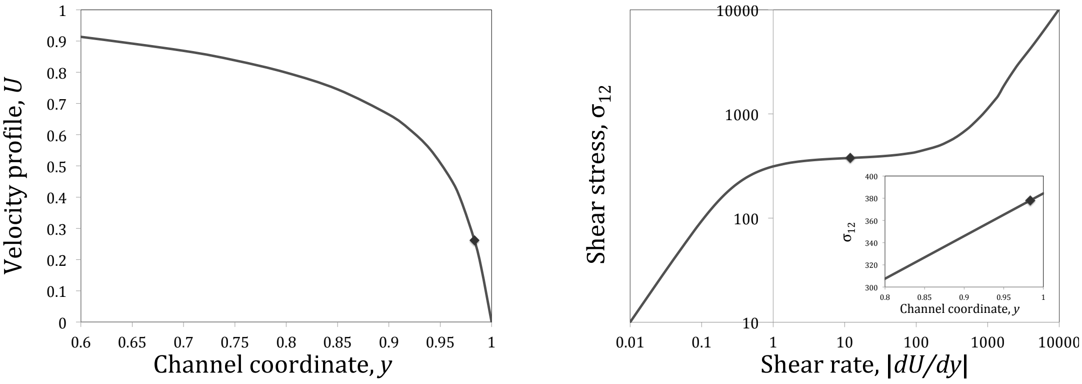

(c) Velocity profile with $\Gamma = 0.00007$. (d) Simple shear flow and shear stress vs $y$

Figure 4.5: (a) Velocity and (b) fluidity profiles from equations (4.39)–(4.42) and (4.35) with $\Phi = 0.001$. Dotted line: $\Gamma\Lambda = 10^{-6}$; solid line $\Gamma\Lambda = 7 \times 10^{-6}$; dashed line $\Gamma\Lambda = 5 \times 10^{-5}$. (c) Velocity profile at $\Gamma\Lambda = 7 \times 10^{-6}$ again, with the critical stress $\tau_c$ marked; it lies just within the channel at $y \approx 0.983$. (d) Flow curve (shear stress against shear rate) for the same parameters as (c), with (inset) the stress profile across the channel.

trend continues until eventually (as seen in section 4.3.2.3) the wall fluidity saturates at a value close to 1.

## 4.3.3 Equation formulation: perturbation flow

The perturbed quantities are obtained in a similar way as we did with the previous channel flow stability problems (sections 2.7.2 and 3.3.2); an infinitesimal perturbation is added to the perturbation flow:

$$\underline{u} = (U + u\varepsilon, v\varepsilon) \tag{4.44}$$

$$\underline{\underline{\sigma}}^{tot} = \underline{\underline{\sigma}} + \varepsilon \underline{\underline{\Sigma}} \qquad \underline{\underline{\sigma}}^{tot} = \begin{pmatrix} \sigma_{11} + \Sigma_{11}\varepsilon & \sigma_{12} + \Sigma_{12}\varepsilon \\ \sigma_{21} + \Sigma_{21}\varepsilon & \sigma_{22} + \Sigma_{22}\varepsilon \end{pmatrix} \tag{4.45}$$

$$\varphi_p = \varphi + \phi\varepsilon \tag{4.46}$$

$$\underline{\underline{D}} = \underline{\underline{D}}_0 + \underline{\underline{d}}\varepsilon, \tag{4.47}$$

in which all the perturbation quantities are functions of the cross-channel coordinate $y$, and $\varepsilon$ denotes a single Fourier mode (equation (2.38)). The continuity equation (4.23) is automatically satisfied if we use the Fourier mode and the streamfunction $\psi$ definiton (2.41). The remaining governing equations become:

$$Re(-\mathrm{i}\omega \mathrm{D}\psi - \mathrm{i}k\psi \mathrm{D}U + \mathrm{i}kU\mathrm{D}\psi) = -\mathrm{i}kp + \mathrm{i}k\Sigma_{11} + \mathrm{D}\Sigma_{12} \tag{4.48}$$

$$Re(-k\omega\psi + k^2U\psi) = -\mathrm{D}\,p + \mathrm{i}k\Sigma_{12} + \mathrm{D}\Sigma_{22} \tag{4.49}$$

$$\phi = \frac{(1-\varphi)\Gamma\left[\mathrm{i}k\sigma_{11}\mathrm{D}\psi + \sigma_{12}(\mathrm{D}^2 + k^2)\psi + \Sigma_{12}\mathrm{D}U\right] + \mathrm{i}k\psi\mathrm{D}\varphi}{(-\mathrm{i}\omega + \mathrm{i}kU + \Lambda^{-1} + \Gamma\sigma_{12}\mathrm{D}U)} \tag{4.50}$$

$$\Sigma_{22}(-\mathrm{i}\omega W\eta + \mathrm{i}kUW\eta + 1) = 2\eta(W\sigma_{12}k^2\psi - \mathrm{i}k\mathrm{D}\psi) \tag{4.51}$$

$$\begin{aligned} \Sigma_{12}(-\mathrm{i}\omega W\eta + \mathrm{i}kUW\eta + 1) &= \eta(\mathrm{D}^2 + k^2)\psi - \xi\mathrm{D}U + \mathrm{i}k\psi W\eta\mathrm{D}\sigma_{12} \\ &+ W\eta(\sigma_{11}k^2\psi + \Sigma_{22}\mathrm{D}U) \end{aligned} \tag{4.52}$$

$$\begin{aligned} \Sigma_{11}(-\mathrm{i}\omega W\eta + \mathrm{i}kUW\eta + 1) &= 2\eta\mathrm{i}k\mathrm{D}\psi - 2W\xi\sigma_{12}\mathrm{D}U + \mathrm{i}k\psi W\eta\mathrm{D}\sigma_{11} \\ &+ 2W\eta(\mathrm{i}k\sigma_{11}\mathrm{D}\psi + \sigma_{12}\mathrm{D}^2\psi + \Sigma_{12}\mathrm{D}U) \end{aligned} \tag{4.53}$$

in which:

$$\xi = \frac{\phi}{\varphi^2} \tag{4.54}$$

and the base state quantities $\eta$ and $\sigma_{ij}$ are:

$$\eta = \varphi^{-1} = \frac{1 + \Gamma\Lambda\sigma_{12}\mathrm{D}U}{\Phi + \Gamma\Lambda\sigma_{12}\mathrm{D}U} \qquad \underline{\underline{\sigma}} = \begin{pmatrix} 2W\mathcal{P}^2y^2 & -\mathcal{P}y \\ -\mathcal{P}y & 0 \end{pmatrix}. \tag{4.55}$$

Note that if $W = 0$, the term $(-\mathrm{i}\omega W\eta + \mathrm{i}kUW\eta + 1)$ in equations (4.51)–(4.53) is equal to one, in which case the system of equations (4.48)–(4.54) would just describe temporal stability analysis for a simple inelastic-thixotropic fluid.

### 4.3.4 Boundary conditions

The coupled system of equations (4.48)–(4.54) can be combined and the resulting equation is a fourth-order ODE in $\psi$ dependent on $y$. The boundary conditions are conditions of no flow on the boundaries (2.51). This system is governed by six dimensionless parameters: the Reynolds and Weissenberg numbers, the wavenumber $k$, the thixotropic ratio $\Phi$ and the reformation/destruction parameters $\Lambda$ and $\Gamma$. We solve the ODE for inertialess flows ($Re = 0$) using the shooting method of Ho & Denn [81] (see section 2.9).

As described in Chapters 2 and 3, previous theoretical work on shear-thinning instabilities [28, 178, 180] used power law models, and as a result had to deal with with a singularity in the viscometric functions at the centreline $y = 0$ where the base-state shear rate is zero (see section 2.8.1). Their solution was to limit themselves to perturbations for which the streamfunction $\psi$ is an *odd* function of $y$, for which the perturbation also has zero shear rate at the centreline. These perturbations are called *varicose* because of the form of the perturbations to streamlines, sketched in figure 2.5. With the BMP model there is no zero-shear singularity, so we are no longer constrained in which forms of $\psi$ are allowed.

Since we are solving a linear problem, any solution $\psi$ can be split into its even and odd components, each of which will also be a solution to our system. For this reason, we will consider separately the two cases of varicose modes ($\psi$ odd) and sinuous modes ($\psi$ even), shown in figure 2.5. For each of these, we can solve over the half-channel $0 \leq y \leq 1$ with the appropriate symmetry boundary conditions at $y = 0$: equation (2.52) for varicose perturbations and (2.53) for sinuous modes. The limit $\Phi = 1$ of our system is the UCM model, whose dispersion relation is well known. We use parameter continuation to obtain the eigenvalue $\omega$ for any given set of physical parameters.

# 4.4 Results

## 4.4.1 Wavelength dependence

### 4.4.1.1 Long waves

As explained in section 2.10.1, Wilson and Rallison [180] expanded $\omega$ and $\psi$ in the long wave limit ($k \to 0$) in terms of $k$:

$$\omega = \omega_0 + k\omega_1 + O(k^2) \qquad \psi = \psi_0 + k\psi_1 + O(k^2). \tag{4.56}$$

If we consider the case of small destruction ($\Gamma \to 0$), the leading order solution ($k \to 0$) can be obtained from solving equation (4.52) using the non slip boundary conditions established in (2.51), which gives the following dispersion relation:

$$\omega_0 = -\frac{\mathrm{i}}{W}\Phi, \tag{4.57}$$

from which we conclude that long waves are stable in this limit, since $\Phi$ and $W$ are positive. The Maxwell model solution ($\Phi = 1$) is simply $\omega_0 = -\mathrm{i}/W$.

The order $k$ solution is obtained from substituting the leading order quantities into the first order expansion, giving as result a third-order ODE for $\psi_1$. For each mode (varicose or sinuous), a characteristic equation is obtained by scaling all the quantities, then taking superposition of the solutions of the ODE and applying their respective boundary conditions [182]. For varicose modes, the polynomial $f(\omega_1)$ has four roots that are independent of $W$, which were already calculated by Wilson and Renardy [182]:

$$\omega_1 = \begin{cases} 0.29039769 \pm 0.05012283\mathrm{i} \\ 0.89882760 \pm 0.12682973\mathrm{i}. \end{cases} \tag{4.58}$$

On the other hand, the characteristic equation for sinuous modes $g(\omega_1)$ has only two roots, which are:

$$\omega_1 = 0.3257438 \pm 0.171948\mathrm{i}. \tag{4.59}$$

#### 4.4.1.2 Scaling for short waves

Now we study the other extreme of the wavelengths: the short wave case $k \to \infty$, which was first considered by Chen & Joseph [37]. In this limit, the size of the boundary layer where the shear rate changes near the wall is greater than the wavelength $O(k^{-1})$, and therefore, any disturbance will be localised in a region of size $k^{-1}$. We therefore scale all lengths with the wavelength, as in [37], and assume that modes will be localised near the channel walls.

We define a new variable $z$ as $z = k(y-1)$, the symbol d will denote derivatives w.r.t. $z$, and we take the limit $k^{-1} \to 0$. The relevant timescale is the wall shear rate, $\dot{\gamma}_w$, and we scale the dimensionless stresses $\Sigma_{ij}$ by a factor of $k^2\dot{\gamma}_w^{-1}$. Applying these transformations to equations (4.55)–(4.54), and assuming $Re = 0$, we obtain:

$$\sigma_{12} = -\mathcal{P} \qquad \dot{\gamma}_w = -\mathrm{D}U_w = \frac{1}{2}\mathcal{P} - \frac{1}{2\Gamma\Lambda\mathcal{P}} + \frac{\sqrt{b-c+1}}{2\Gamma\Lambda\mathcal{P}} \tag{4.60}$$

$$\eta_w = \frac{1}{\varphi_w} = \frac{1+\Gamma\Lambda\mathcal{P}\dot{\gamma}_w}{\Phi+\Gamma\Lambda\mathcal{P}\dot{\gamma}_w} \qquad \mathcal{W} = W\eta_w \tag{4.61}$$

$$\chi = -\mathrm{i}\omega\dot{\gamma}_w^{-1} - \mathrm{i}z + \Lambda^{-1}\dot{\gamma}_w^{-1} - \Gamma\mathcal{P} \tag{4.62}$$

$$\Theta = \frac{(1-\varphi_w)\Gamma}{\chi\varphi_w^2\dot{\gamma}_w}\left[2\mathrm{i}\mathcal{W}\mathcal{P}\dot{\gamma}_w\mathrm{d}\psi - \mathcal{P}(\mathrm{d}^2+1)\psi\right] \tag{4.63}$$

$$\zeta = \frac{(1-\varphi_w)\Gamma\left[2\mathrm{i}\mathcal{W}\mathcal{P}\dot{\gamma}_w\mathrm{d}\psi - \mathcal{P}(\mathrm{d}^2+1)\psi - \Sigma_{12}\right]}{\dot{\gamma}_w\varphi_w^2\chi} \tag{4.64}$$

$$\Sigma_{22}(-\mathrm{i}\omega\dot{\gamma}_w^{-1} - \mathrm{i}z + \mathcal{W}^{-1}\dot{\gamma}_w^{-1}) = -2\mathcal{P}\psi - \frac{2\mathrm{i}}{W}\mathrm{d}\psi \tag{4.65}$$

$$\begin{aligned}\Sigma_{12}\left(-\mathrm{i}\omega\dot{\gamma}_w^{-1} - \mathrm{i}z + \mathcal{W}^{-1}\dot{\gamma}_w^{-1} + (1-\varphi_w)\Gamma\mathcal{W}^{-1}\varphi_w^{-2}\chi^{-1}\right) &= \frac{1}{W}(\mathrm{d}^2+1)\psi \\ &- \Sigma_{22} + 2\mathrm{i}\mathcal{W}\mathcal{P}\dot{\gamma}_w\psi - \mathcal{W}^{-1}\mathrm{D}U_w\Theta \end{aligned} \tag{4.66}$$

$$\begin{aligned}\Sigma_{11}(-\mathrm{i}\omega\dot{\gamma}_w^{-1} - \mathrm{i}z + \mathcal{W}^{-1}\dot{\gamma}_w^{-1}) &= \frac{2}{W}\mathrm{id}\psi - 2\dot{\gamma}_w^2\zeta + 4\mathrm{i}\mathcal{W}\mathcal{P}\dot{\gamma}_w\mathrm{d}\psi \\ &- 2\mathcal{P}\mathrm{d}^2\psi - 2\Sigma_{12}, \end{aligned} \tag{4.67}$$

$$(\mathrm{d}^2+1)\Sigma_{12} + \mathrm{id}(\Sigma_{11} - \Sigma_{22}) = 0. \tag{4.68}$$

## Boundary conditions for the short-waves case

Recalling that $z = k(y-1)$, the system above has to satisfy non-slip boundary conditions at $y = 1$, or for this case, at $z = 0$:

$$\psi(0) = \mathrm{d}\psi(0) = 0. \tag{4.69}$$

In addition, the perturbation has to decay away from the channel, and therefore:

$$\psi \to 0 \text{ as } z \to -\infty. \tag{4.70}$$

In the limit $z \to -\infty$, the system of equations obtained above (4.60)–(4.68) is reduced to a 4th order ODE with the following form:

$$\frac{\mathrm{d}^4\psi}{\mathrm{d}z^4} + A_0\frac{\mathrm{d}^3\psi}{\mathrm{d}z^3} + B_0\frac{\mathrm{d}^2\psi}{\mathrm{d}z^2} + C_0\frac{\mathrm{d}\psi}{\mathrm{d}z} + E_0\psi = 0, \tag{4.71}$$

where the coefficients are:

$$A_0 = -2\mathrm{i}W\mathcal{P} \qquad B_0 = -(2+W^3\mathcal{P}^2) \qquad C_0 = 2\mathrm{i}W\mathcal{P}\dot{\gamma}_w \qquad E_0 = 1+W^3\mathcal{P}^2. \tag{4.72}$$

The solution of (4.71) adopts the following form:

$$\psi = A_1\exp(r_1 z) + A_2\exp(r_2 z), \tag{4.73}$$

where $A_1$ and $A_2$ are constants and $r_1$ and $r_2$ are two roots of the characteristic polynomial of (4.71). Moreover, $r_1$ and $r_2$ have to be positive so when $z \to -\infty$, the exponential terms of (4.73) will decay and then we can satisfy condition (4.70).

In order to integrate our short-wave equations (4.60)–(4.68), we apply the far-field boundary condition at a finite value of our modified channel coordinate $z$ so that $\psi(z_s) = 0$. To find the solution $\omega$ to our eigenvalue problem, we use a Ho & Denn [81] method (section 2.9), but instead of integrating from the centreline, we integrate from $z_s < 0$ to the channel wall $z = 0$.

As before, the limit $\Phi = 1$ reduces to the Maxwell model, (which is stable), which is our starting point. We show results for this short-wave calculation in figure 4.7a) along with the results for other wavelengths.

We have assumed here that short-wave modes will localise near the channel wall. However, there are other possibilities: in particular, we will see later that there is some potential for modes that localise close to the position where the base state attains the critical stress $\tau_c$.

#### 4.4.1.3 Intermediate waves: sinuous and varicose modes

We use numerical parameter continuation to find the eigenvalue $\omega(k)$ for each new set of physical parameters. Our starting point is the long-wave results of equations (4.57) and (4.58) or (4.59) for the UCM model. In figure 4.6 we show this dispersion relation for the UCM model, calculated using our BMP code with $\Phi = 1$. These results agree with those already available in the literature [180] (see section 2.10.1).

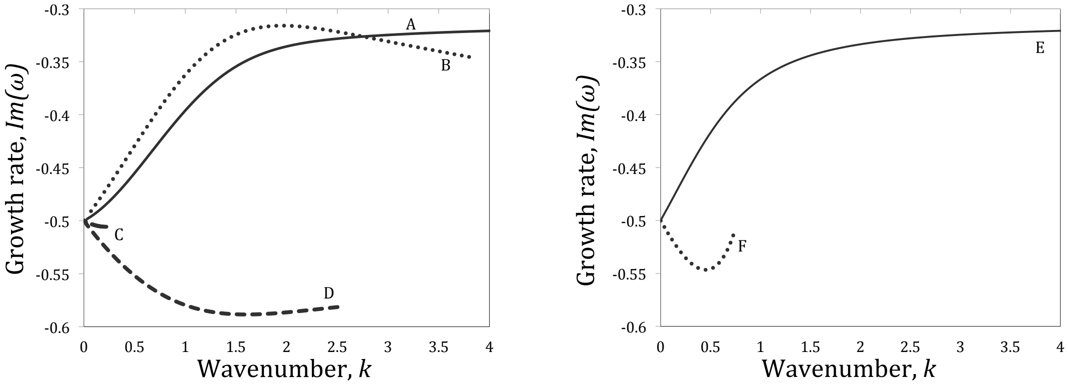

(a) Varicose mode (b) Sinuous mode

Figure 4.6: Growth rate against wavenumber for both varicose and sinuous modes for a UCM model, calculated using the BMP model parameters: $W = 2$, $\Lambda = 1$, $\Phi = 1$ and $\Gamma = 0.0005$. Inertia is neglected ($Re = 0$).

For varicose modes, there are four stable modes for very long waves. Two of them (C and D) cease to exist at moderate $k$ (one of them at $k \approx 0.5$, and the other one at $k \approx 2.5$). The two remaining roots are still seen at larger values of wavenumber; one of them (A) matches the short-wave solution for a wall mode, while root B localises around the centreline as $k \to \infty$.

Two roots are seen for sinuous modes in figure 4.6b); one root (F) vanishes at small $k$, while the other (E) still exists at large values of the wavenumber. Root E is less stable than root A, but they are equivalent in the limit $k \to \infty$, where wall modes are no longer aware of the centreline boundary conditions.

We use these results as a starting point to move away from the UCM limit $\Phi = 1$.

### 4.4.2 Growth rate as function of the thixotropic ratio

Moving away from the UCM limit, we begin by studying the effect of the thixotropic ratio $\Phi$ on the growth rate, keeping all other parameters fixed. Initially we look at long waves ($k = 0.1$), with the BMP parameters $\Lambda = 1$ and $\Gamma = 0.0005$ and a Weissenberg number of $W = 2$. The results are shown in figure 4.7.

For both sinuous and varicose modes (figures 4.7a and 4.7b), decreasing the thixotropic ratio is destabilising; the greater the difference between $\varphi_0$ and $\varphi_\infty$, the more unstable the flow. This is in agreement with earlier work in instabilities in shear-thinning viscoelastic fluids [28, 178, 180]. For sinuous modes (figure 4.7a) there are initially two roots, but one of them (labelled B) ceases to exist at $\Phi \approx 0.263$. The other one (A) becomes unstable for values of the thixotropic ratio below 0.043. A third mode (labelled C) appears at $\Phi \approx 0.03148$ and it becomes unstable at very low thixotropic ratio values. However, the root C will always be more unstable than the mode A for any parameter model value. The mode C will be studied deeply in chapter 5.

We have chosen a small value of $\Gamma\Lambda = 0.0005$ here; at these values, we saw in section 4.3.1 that the base state velocity profile is close to plug flow for small values of $\Phi$, which is where we now see instability. We cannot calculate growth rates in the true plug flow limit $\Phi = 0$ because of numerical difficulties associated with the yield stress surface; however, we can approximate it very closely. For the case $k = 0.1$, we reached $\Phi = 5.1 \times 10^{-5}$, where an instability is still present.

The behaviour for varicose modes is similar to the sinuous behaviour but the detailed picture is more complex as we have at least seven roots. Four remain stable (only three of which are shown in figure 4.7b) as the other ceases to exist at $\Phi \approx 0.62$) but the other three become unstable as $\Phi$ decreases. We have labelled the

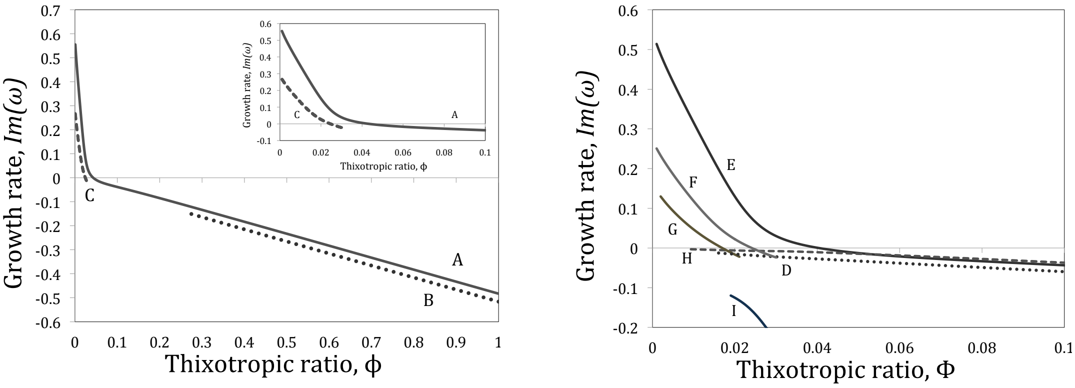

(a) Long waves: sinuous modes

(b) Long waves: varicose modes

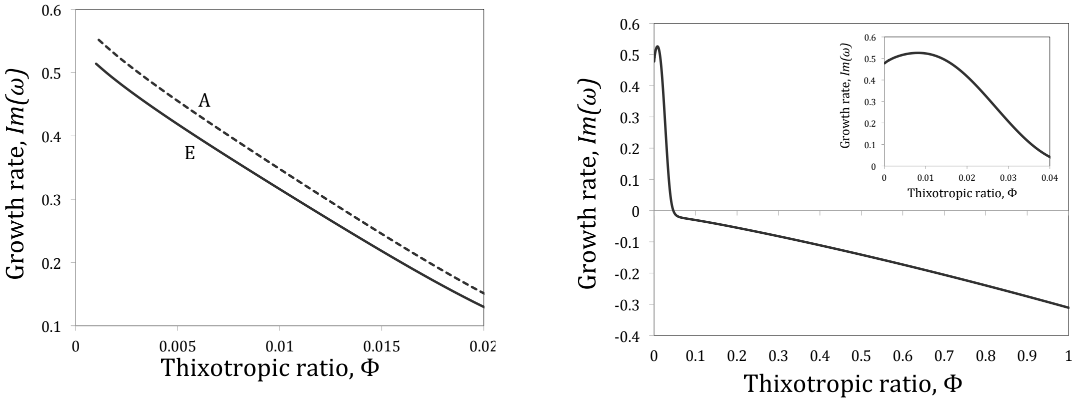

(c) Long waves: sinuous and varicose modes in the unstable region

(d) Short waves, $k \to \infty$

Figure 4.7: Growth rate plotted against thixotropic ratio, at fixed values of the other parameters: $W = 2$, $\Lambda = 1$, $\Gamma = 0.0005$ and (a)–(c) long waves $k = 0.1$ and (d) short waves $k \to \infty$. (a) Sinuous modes; (b) Varicose modes; (c) Comparison between the two unstable modes at low $\Phi$.

most dangerous mode E.

In figure 4.7c) we compare the most dangerous roots (A and E); the sinuous modes are more unstable than the varicose ones here.

Finally, in figure 4.7d) we move away from long waves. Our instability persists as the wavenumber increases, and the root obtained for very short waves has a similar behaviour to roots A and E: the mode remains stable as the thixotropic ratio decreases until $\Phi$ becomes very small ($\Phi < 0.046$), when an instability appears.

However, in the short wave case the growth rate has a maximum value located at $\Phi \approx 0.007$, and decreases slightly as we approach $\Phi \to 0$ (see inset). We found similar behaviour at moderate wavelengths $k > 1$.

### 4.4.3 Most dangerous wavenumber

In figure 4.8 we fix our physical parameters (using three sample values of $\Phi$) and vary the wavelength. We see that very long waves ($k \to 0$) are always stable, but as the wavenumber increases, the flow can become unstable. For the roots with the smaller values of $\Phi$ (upper curves), the curve passes through a maximum value (most dangerous wavenumber) in the range $0.35 < k < 0.6$. The growth rate then decreases for shorter waves until it reaches an asymptotic value which matches the short-wave limit solution calculated from equations (4.60)–(4.72).

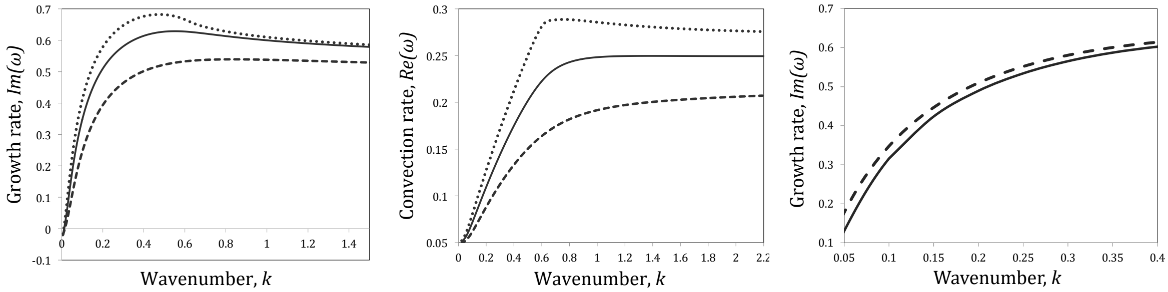

(a) Sinuous modes (b) Sinuous modes (c) Sinuous and varicose modes

Figure 4.8: Plots of the eigenvalue $\omega$ against wavenumber $k$ for different values of thixotropic ratio. Parameters: $W = 2$, $\Lambda = 1$, $\Gamma = 0.0005$. Left: sinuous modes, with $\Phi = 0.007, 0.01, 0.015$ (top to bottom): (a) growth rate (imaginary part of $\omega$) and (b) convection rate (real part of $\omega$); Right (c): comparison between sinuous modes (dashed line) and varicose modes (solid line) at $\Phi = 0.01$.

According to Wilson [178], if the real part of the eigenvalue $\Re(\omega)$ remains finite as the wavenumber tends to infinity, it means that the short wave perturbations are localised in the wall region rather than localising at a cross-channel position $\overline{y}$ and convecting with the flow at velocity $U(\overline{y})$, which would yield the real part of the eigenvalue to follow the relation $\Re(\omega) \sim kU(\overline{y})$. In figure 4.8b), we can see that the values $\Re(\omega)$ do indeed remain finite in the limit $k \to 0$ and thus, the short wave perturbations follow the scaling proposed in section 4.4.1.2.

In figure 4.8c) we compare the curve of growth rate against wavenumber for the most unstable sinuous and varicose perturbations with $W = 2$, $\Lambda = 1$, $\Gamma = 0.0005$ and $\Phi = 0.01$. As before, we see that sinuous modes are more unstable than varicose ones;

however, the difference between their growth rates becomes much less significant for shorter waves: at intermediate values of wavenumber $1 < k < 2$, the difference is less than 0.32%. We will focus on sinuous modes henceforth.

### 4.4.4 Dependence on the Weissenberg number

In this section we show how the Weissenberg number affects the growth rate for different values of thixotropic ratio with the other parameters fixed (figure 4.9). We are looking at relatively long waves, $k = 0.1$, and BMP parameters $\Lambda = 1$, $\Gamma = 0.0005$, and three different values of $\Phi$. Again, the smaller the value of $\Phi$ (the stronger the shear thinning), the more unstable the flow is. As the Weissenberg number increases, the instability remains, and the growth rate increases but remains bounded. In all cases small values of the Weissenberg number $W < 0.15$ yield a stable flow, indicating that elasticity is an important component of the instability.

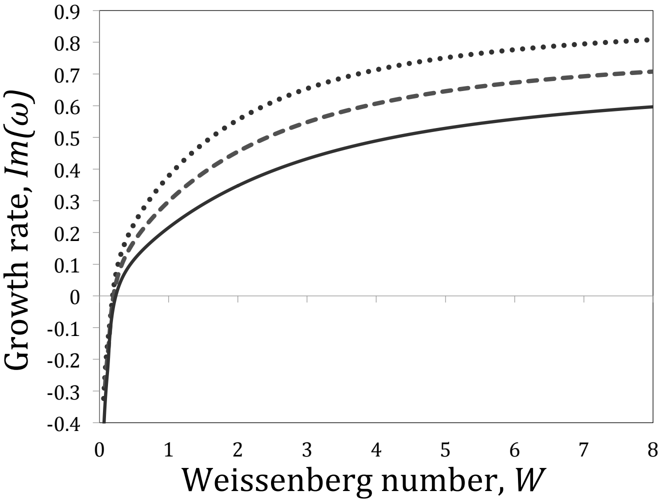

Figure 4.9: Growth rate against Weissenberg number with $\Lambda = 1$, $\Gamma = 0.0005$ and $k = 0.1$. Bottom to top: $\Phi = 0.01, 0.005$ and $0.001$.

### 4.4.5 Thixotropic timescales

Now that we have identified the range of values for $\Phi$, $k$ and $W$ where the instability has its strongest effects, we will discuss the effects of the parameters governing structural reformation ($\Lambda$) and destruction ($\Gamma$).

#### 4.4.5.1 Thixoviscous number $\Lambda$

In figure 4.10 we plot the growth rate against the thixoviscous number $\Lambda$ for different values of the thixotropic ratio $\Phi$, with $W = 2$, $\Gamma = 0.0005$ and $k = 0.1$ fixed.

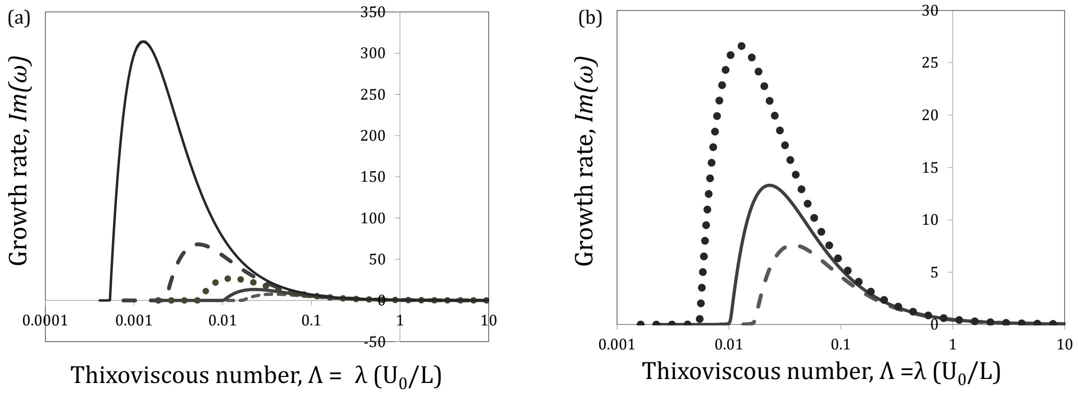

Figure 4.10: Growth rate plotted against the thixoviscous number $\Lambda$ for $W = 2$, $\Gamma = 0.0005$ and $k = 0.1$. (a) Bottom to top: $\Phi = 0.005, 0.004, 0.003, 0.002$ and $0.001$. (b) Lower three curves from (a) for clarity.

The flow is linearly stable at both extremes of the thixoviscous number: both for $\Lambda > 30$, which applies highly thixotropic fluids (slow structural recovery) and in the limit $\Lambda \to 0$ (rapid structural relaxation, a Maxwell fluid). However, for intermediate values of $\Lambda$ we see an instability with an extremely high growth rate, which is higher for smaller values of $\Phi$. Both the maximum growth rate and the value of $\Lambda$ at which this growth is seen, vary with the thixotropic ratio $\Phi$.

We see this instability for flows in which the critical stress $\tau_c$ is either located near the wall or has not been reached within the channel; as we reduce $\Lambda$ the thixoplastic number $W_{tp}$ reduces and the critical stress increases relative to the stress in the channel. In the limit $\Lambda \to 0$, we regain the Maxwell limit and the instability vanishes.

#### 4.4.5.2 Thixoelastic number

The thixoelastic number (section 4.2.4.1) is defined as $W_{te} = W/\Lambda$ the ratio between the viscoelastic $\lambda_{ve}$ and structural relaxation times $\lambda$. Unlike the parameter $\Lambda$ itself, the thixoelastic number is a material parameter which does not depend on the timescale of the flow.

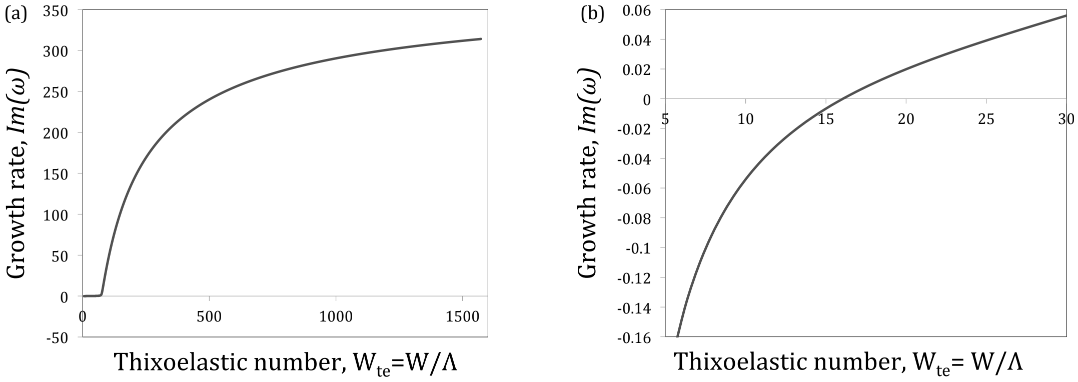

Figure 4.11: Effect of the thixoelastic number on the instability. Fixed parameters: $\Lambda = 0.001271$, $\Gamma = 0.0005$, $\Phi = 0.001$ and $k = 0.1$; the Weissenberg number varies. Part (b) is a small region of (a).

We choose our parameters to include the maximum growth rate in figure 4.10: $W = 2$, $\Lambda = 0.001271$, $\Gamma = 0.0005$, $\Phi = 0.001$ and $k = 0.1$, then allow the Weissenberg number to vary. We plot the resulting growth rates against the thixoelastic number $W_{te}$ in figure 4.11.

Large values of the thixoelastic number lead to the highest growth rates. In these cases, the relaxation time associated with elastic recoil, $\lambda_{ve}$, is much longer than the structural relaxation time $\lambda$. This is the case, according to Larson, where the fluid will exhibit complex non-linear viscoelasticity rather than non-ideal thixotropy. This verifies our earlier conclusions obtained in chapter 3: that the instability initially predicted by Wilson and Rallison [180] is purely elastic in nature. Here, though, we have captured sinuous modes, which are the perturbations most commonly observed in experiments.

The growth rate remains positive for $W_{te} \geq 15.72$, below which the instability vanishes (see figure 4.11b). Here, though $\lambda_{ve} > \lambda$, the viscoelastic effects are less dominant. When structural recovery is slower than viscoelastic relaxation, $W_{te} < 1$, the flow is unconditionally stable.

### 4.4.5.3 Destruction parameter Γ; thixoplastic number

In figure 4.12 we fix the thixoviscous number $\Lambda = 1$ and study the effect of the destruction parameter $\Gamma$ on the growth rate. These results can also be framed in terms of the thixoplastic number $W_{tp} = \sqrt{\Gamma\Lambda(1-2\Phi)}$, since both $\Lambda$ and $\Phi$ are constant for each curve.

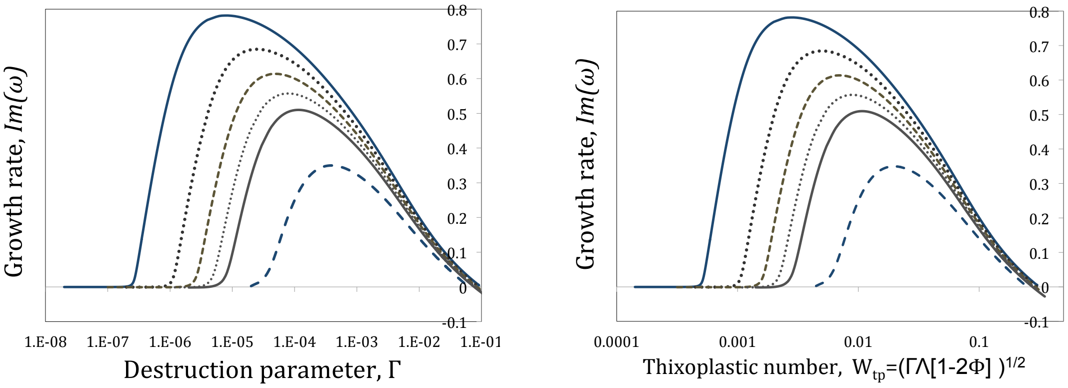

Figure 4.12: Growth rates at fixed $W = 2$, $\Lambda = 1$ and $k = 0.1$ with $\Gamma$ varying. (a) Growth rate $\Im(\omega)$ against destruction parameter $\Gamma$; (b): Growth rate against thixoplastic number $W_{tp}$. Top to bottom: $\Phi = 0.001, 0.002, 0.003, 0.004, 0.005$ and $0.01$.

There is an unstable maximum for each root, and the limits $\Gamma \to 0$ and $\Gamma \to \infty$ stabilise the flow. These stable limits are to be expected as either limit reduces to a Maxwell fluid (albeit with very different viscosities), which is stable.

When we plot against the thixoplastic number $W_{tp}$ the figure looks similar but the interpretation changes: constant values of $W_{tp}$ mean fixed base state velocity profiles. As we increase $W_{tp}$ beyond the most dangerous value, the yielded region near the walls grows, and this is associated with a decrease in growth rate. However, there is a most dangerous value of $W_{tp}$, associated with a most dangerous flow profile. In the case $\Phi = 0.001$, the maximum growth rate occurs when $W_{tp} = 0.0028$, a case where we have a small yielded region and the critical stress $\tau_c$ in the base state is located near the wall, at $y \approx 0.98$.

#### 4.4.5.4 Thixoplastic number at fixed thixoviscous number

In the previous section, we observed that intermediate values of thixoplastic number can destabilise flows as long as the viscoelastic time scale is greater than the structural reformation one ($W_{te} = W/\Lambda \gg 1$ or $\lambda_{ve} \gg \lambda$). However, we should note that the thixoplastic number $W_{tp}$ depends on both $\Gamma$ and $\Lambda$, but in section 4.4.5.3 we kept the structural reformation parameter fixed at $\Lambda = 1$. In this section, we will study the effect of the thixoplastic number on the growth rate with multiple combinations of the destruction and reformation parameters.

We take a set of fixed values for $\Lambda = \{0.1, 0.2, 0.5, 1, 2, 10\}$. In each case we calculate the growth rate as function of the thixoplastic number, by varying the destruction parameter $\Gamma$. The results can be seen in figure 5.23a).

As in figure 4.12, we see that the extreme limits $W_{tp} \to 0$ and large $W_{tp}$ are stable, and instability can occur for intermediate values. However, we now see a strong dependence of the growth rate of the instability on the reformation parameter $\Lambda$. The least unstable curve shown here is $\Lambda = 10$, whose maximum value of the growth rate is $\Im(\omega) \approx 0.08$, obtained at $W_{tp} \approx 0.003$; but as $\Lambda$ is decreased, the growth rate increases so that at $\Lambda = 0.1$ (top solid line in figure 5.23), the maximum value of growth rate is $\Im(\omega) = 7.73$ at $W_{tp} = 0.00269$. In this most unstable case, the velocity profile in the base state was shown in figure 4.5c), where we observed an apparent yield region near the channel wall, between $0.9833 < y < 1$.

If we consider the most unstable values of $W_{tp}$ for all the values of $\Lambda$ in figure 5.23, in all cases the critical stress $\tau_c$ is obtained near the wall (at $y \approx 0.98$).

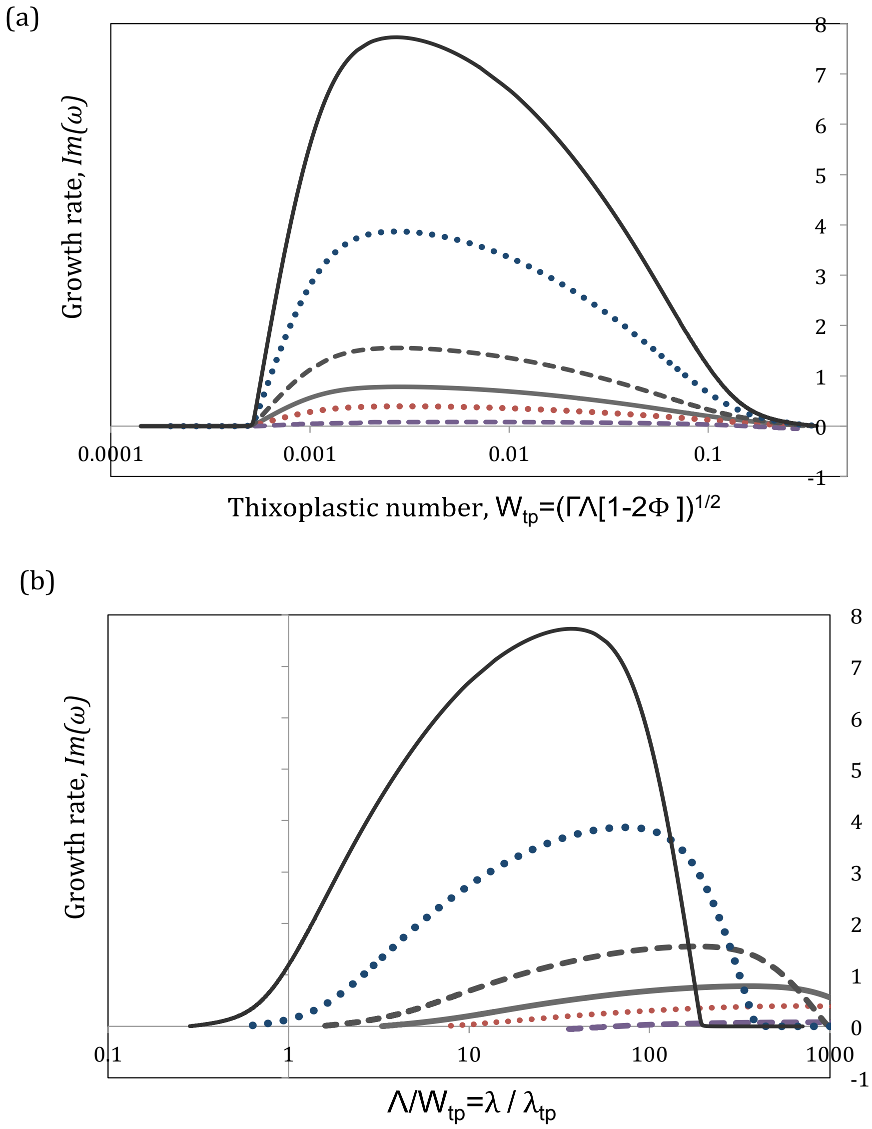

Figure 4.13: Dependence of growth rate on thixoplastic number, at fixed $W = 2$, $\Phi = 0.001$ and $k = 0.1$. For each curve $\Lambda$ is constant and $\Gamma$ varies. Top to bottom: $\Lambda = 0.1$, 0.2, 0.5, 1, 2 and 10. (a) Growth rate against thixoplastic number; (b): growth rate against the ratio $\Lambda/W_{tp}$.

If we reframe these results instead in terms of a material parameter $\Lambda/W_{tp}$, which compares the structural relaxation time $\lambda$ and the time scale associated to the destruction of structures, $\lambda_{tp}$, we obtain figure 5.23b). Now the maximum growth rate shifts to the right as $\Lambda$ increases; this follows from the universality of the most critical value of $W_{tp}$ that we saw in figure 5.23a). For very large values of $\Lambda/W_{tp}$ the flow tends to be stable; this is a limit where thixotropy dominates and we reach the high-shear limit across almost all of the channel: the Maxwell limit again. However, if $\Lambda$ is small (weak thixotropy) we need exceedingly high values of $\Lambda/W_{tp}$ to attain this limit.

Figure 5.23 makes it clear that we cannot define stability in terms of material parameters alone: for fixed values of $k$, $W$ and $\Phi$ the unstable region is best characterised by $W_{tp} = \sqrt{\Gamma\Lambda(1-\Phi)}$, which for our parameter choices gives instability in the range $0.0005 < W_{tp} < 0.15$.

We can characterise the unstable region and the most dangerous situation in terms of the thixoplastic number $W_{tp}$. For our parameters $W = 2$, $\Phi = 0.001$ and $k = 0.1$ this most dangerous value is $W_{tp} = 0.002695$. This value determines the critical stress value ($\tau_c \approx 370$), and its location in the channel (located at $y \approx 0.9823$) which is also the edge of the yielded region. The base-state velocity profile and the flow curve for simple shear are illustrated in figures 4.5c) and 4.5d) for this case.

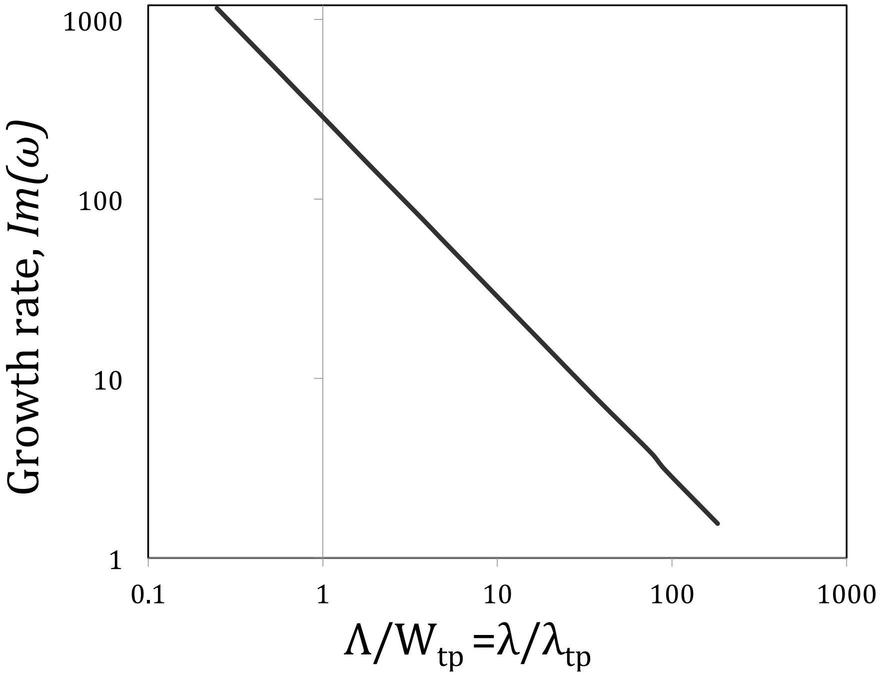

Figure 4.14: Log-log plot of growth rate plotted against the timescale ratio $\Lambda/W_{tp}$. Fixed values $W = 2$, $\Phi = 0.001$, $k = 0.1$, and the most dangerous thixoplastic number $W_{tp} = 0.002695$. The points are fit with the line $370.92(\lambda/\lambda_{tp})^{-1}$.

However, the growth rate of the instability clearly depends on $\Lambda$ even at fixed

$W_{tp}$. In figure 4.14 we use the value above, $W_{tp} = 0.002695$, and plot the growth rate against the material parameter $\Lambda/W_{tp} = \lambda/\lambda_{tp}$, the ratio of the structural and thixoplastic relaxation times. The curve can be fitted to a power-law equation: $\Im(\omega) = 370.92(\lambda/\lambda_{tp})^{-1}$ with $R^2 = 0.9999$. Thus we can characterise the growth rate at fixed $W_{tp}$ (or fixed $\Gamma\Lambda$) by

$$\Im(\omega) \propto \frac{1}{\Lambda} \propto \Gamma. \tag{4.74}$$

Recall that the base flow is defined by the parameters $W$, $\Gamma\Lambda$ and $\Phi$ and does not depend on $\Lambda$ separately from the combination $\Gamma\Lambda$. Thus *for a given unstable base flow*, the rate $\Lambda^{-1}$ will determine the growth rate of the instability.

Fluids having $\Lambda/W_{tp} \gg 1$, i.e. slow structural recovery, will exhibit much weaker instability than those for which structural recovery is fast *given the same base flow*; however, to obtain the same base flow in a fluid having fast structural recovery requires higher flow rates. Though the overall picture is difficult to express briefly in terms of pure material parameters, it is clear that the thixoviscous number $\Lambda$ is a key player in the strength of the instability.

### 4.4.5.5 Elastoplastic number

We have seen that the instability is most dangerous when $\lambda \ll \lambda_{tp}$ (section 4.4.5.4) and $\lambda \ll \lambda_{ve}$ (section 4.4.5.2). In this section we assess the behaviour of the instability as viscoelastic effects are reduced. We will use the *elastoplastic number* $\lambda_{ve}/\lambda_{tp} = W/W_{tp}$ to compare the viscoelastic and plastic effects of our fluid. The elastoplastic number is a ratio of two time scales: the relaxation time associated with the elastic recoil of the material chains $\lambda_{ve}$ over the time scale associated with destruction, $\lambda_{tp}$.

The results are shown in figure 4.15. We see that the instability is present only if the viscoelastic timescale $\lambda_{ve}$ is much longer than the plastic timescale $\lambda_{tp}$, i.e.

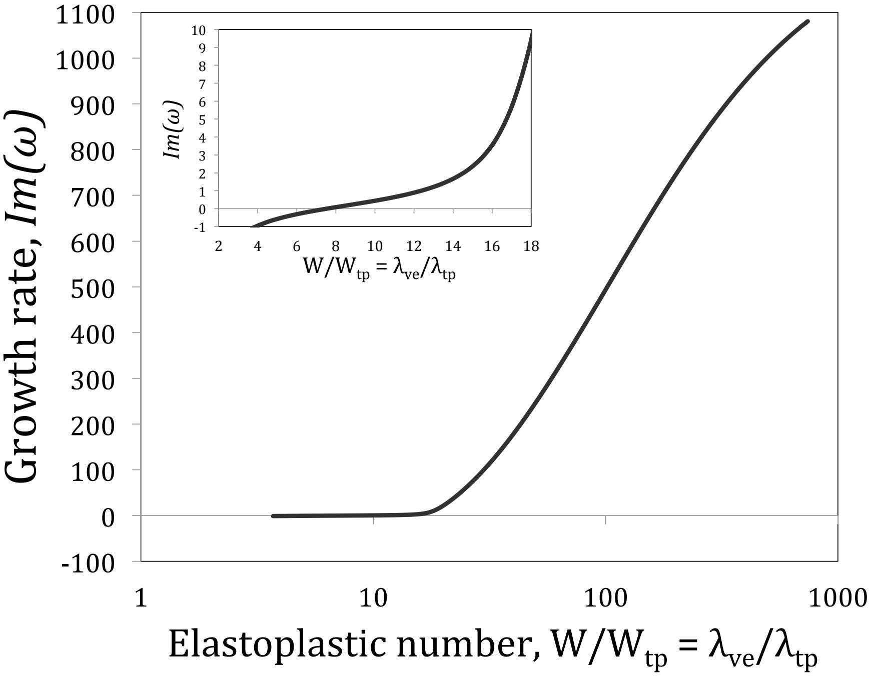

Figure 4.15: Plot of growth rate $\Im(\omega)$ against elastoplastic number $W/W_{tp}$ with fixed values of $\Phi = 0.001$, $\Gamma = 0.010175$, $\Lambda = 7.143 \times 10^{-4}$ and $k = 0.1$.

the elastic recoil process is slow compared to structural destruction, $W/W_{tp} \gg 1$. Decreasing the elastoplastic number makes the flow less unstable, until it stabilises at $W/W_{tp} \approx 8$, below which the viscoelastic effects are no longer strong enough to cause flow instability.

### 4.4.6 Streamfunctions and $x$-velocity

In this final results section, we show the shape of the streamfunction $\psi$ (proportional to cross-channel velocity) and $x$-velocity $\mathrm{D}\psi$ for both sinuous and varicose perturbations at the most dangerous thixoplastic number.

We choose the values used in figure 4.14 ($k = 0.1$, $W = 2$, $\Phi = 0.001$) for which the most dangerous thixoplastic number is $W_{tp} = 0.002695$. Choosing $\Lambda = 1$ then fixes $\Gamma = 7.5 \times 10^{-6}$. The resulting streamfunctions can be seen in figure 4.16.

Both sinuous and varicose modes are unstable for these parameters, but the shape of the two streamfunctions is completely different, as one would expect. Most

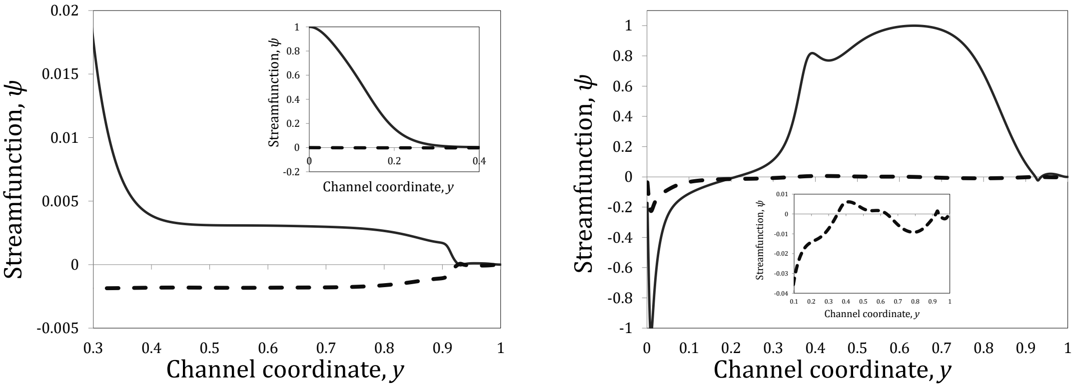

(a) $\psi$ vs $y$: sinuous mode (b) $\psi$ vs $y$: varicose mode

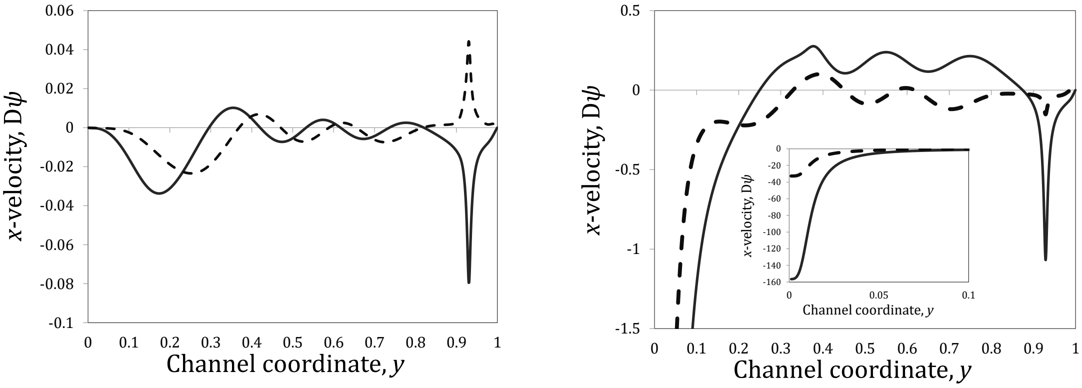

(c) D$\psi$ vs $y$: sinuous mode (d) D$\psi$ vs $y$: varicose mode

Figure 4.16: Form of the unstable complex streamfunction $\psi$ for sinuous and varicose perturbations with $k = 0.1$, $W = 2$, $\Gamma = 7.5 \times 10^{-6}$, $\Lambda = 1$ and $\Phi = 0.001$. The thixoplastic number is $W_{tp} = 0.002695$. The curves are normalised so that the maximum value of $|\psi|$ is 1. For each graph, the solid line is the real part and the dashed line, the imaginary part. Insets show the behaviour near the wall, except in (b) where it shows the shape of the imaginary part of the streamfunction.

surprising, though, is the peak in the $x$-velocity D$\psi$ for both modes near the channel wall (figures 4.16c and 4.16d). This peak occurs roughly where the base state is at the critical stress level $\tau_c$ (for this fluid at $y \approx 0.983$). At this point, where the gradient $d\sigma_{12}/d\dot{\gamma}$ of the constitutive curve (figure 4.5d) is low, the effective viscosity seen by perturbations is also low, so a perturbation can generate large local flows while incurring minimal dissipation of energy.

## 4.5 Comparison with experiments

In this section, we will briefly compare our results with experiments reported by Bodiguel *et al.* [16] (summarised in section 2.10.2), who observed a supercritical instability in microchannel flow of shear-thinning viscoelastic fluids. We begin by finding the BMP model parameters that roughly match the simple shear flow data for their fluid, which was an aqueous solution of polyacrylamide, HPAM (concentration of 4000 ppm and molecular weight of $18 \times 10^6$ g/mol).

The experimental steady shear flow curve $\eta(\dot{\gamma})$ allows us to fit our parameters $\varphi_0$, $\varphi_\infty$ and the combination $K_0\lambda$ (see figure 4.17a). We then use our shear modulus $G_0$ to match the experimental first normal stress difference coefficient $N_1/\dot{\gamma}^2$ (see 4.17b). As only steady rheometry is reported by [16], we have no way to determine $\lambda$ separately from $K_0$; but all the remaining parameters may be derived from combinations of these four parameters determined from the rheology, and simple physical measurements such as the centreline velocity $U_0$ and the channel half-width $L$. The resulting parameters are given in table 4.1.

| Parameter | Value |
|---|---|
| $\varphi_0$ | $0.046\,\mathrm{Pa}^{-1}\,\mathrm{s}^{-1}$ |
| $\varphi_\infty$ | $10.17\,\mathrm{Pa}^{-1}\,\mathrm{s}^{-1}$ |
| $K_0\lambda$ | $3.2 \times 10^{-3}$ $\mathrm{Pa}^{-1}$ s |
| $G_0$ | 0.455 Pa |
| $L$ | $7.6 \times 10^{-5}$ m |
| $\lambda_{ve}$ | 0.21 s |
| $\lambda_{tp}$ | 0.017 s |
| $\Phi$ | 0.0045 |
| $\Gamma\Lambda$ | $5.45 \times 10^4\, U_0^2$ |
| $W$ | $2844\, U_0$ |

Table 4.1: Physical and dimensionless parameters used to fit our analysis to the experiments of Bodiguel [16], with centreline velocity $U_0$ in m/s.

Similar experiments have been carried out by Poole [147]. The fluid used in those experiments does exhibit a central power-law like behaviour of both viscosity and normal stress for moderate shear rates; however, we cannot fit it with the BMP model. In our model, the first normal stress difference coefficient is $2\eta^2 G_0^{-1}$, but Poole's fluid has very different power laws for the viscosity and the first normal stress difference coefficient (or, equivalently, a strongly varying stress modulus). For that reason, we do not attempt a quantitative comparison with Poole's experiments here.

Indeed, even the fit with Bodiguel's fluid is not perfect, as the experimental value of the elastic modulus is not quite constant; however, the parameters given in table 4.1 give a reasonable match over the range $1 < \dot{\gamma} < 100$ (see figure 4.17b).

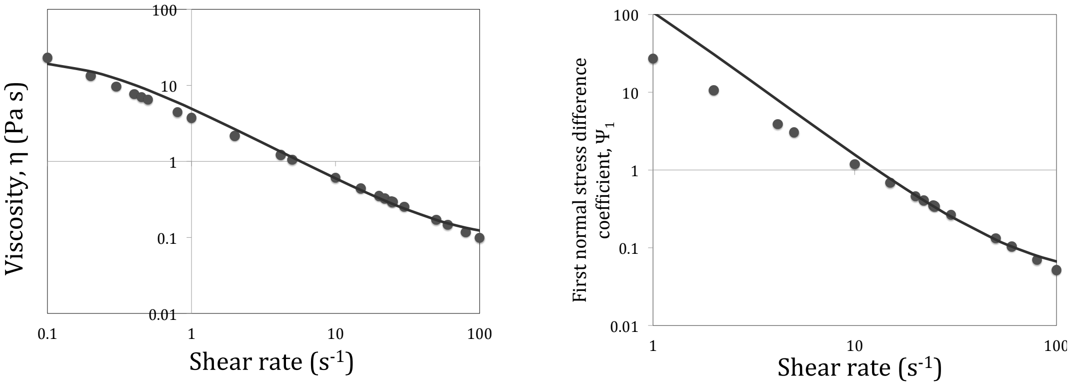

(a) $\eta$ vs $\dot{\gamma}$

(b) $\Psi_1$ vs $\dot{\gamma}$

Figure 4.17: Simple shear flow curves for Bodiguel's fluid [16]. Solid lines are the BMP model predictions, meanwhile the experimental data is depicted in points. Figure (a): simple shear flow viscosity plotted against shear rate; (b) first normal stress difference against shear rate.

From the parameters values shown above, we immediately observe that the thixotropic ratio for the fluid is $\Phi = 0.0045$, within the range of values of $\Phi$ where our theory predicts an instability.

Using the model parameters derived above and for a small set of likely dangerous values of the wavenumber $k = \{0.1, 0.46, 1\}$, we look for the *stability boundary*; this is the pressure gradient $\mathscr{P}$ (or the wall shear stress $\sigma_w = \mathscr{P}L$) above which the flow becomes unstable. Knowing the value of the pressure gradient, we can calculate the dimensional centreline velocity (as in appendix 4.2.3) and therefore the Weissenberg number and the product $\Gamma\Lambda$. As we observed in section 4.4.5.4, at a fixed value of $\Gamma\Lambda$, changing $\Lambda$ does not affect the stability boundary but rather modifies the growth rate of unstable modes; so we are not affected by our inability to separate $K_0$ and $\lambda$ using the fluid rheometry.

We have found that for $k = 0.1$, the critical shear stress at the wall $\sigma_w$ is 5.4609 Pa, meanwhile for $k = 0.46$ (the most dangerous wavenumber for $\Phi = 0.0045$) it is $\sigma_w = 4.3593$ Pa and for $k = 1$ it is $\sigma_w = 4.2938$ Pa. These results are consistent with the values reported by Bodiguel [16], who found that the critical wall shear stress ranged between 3.5 and 4.7 Pa.

## 4.6 Conclusions

We have studied the stability in pressure-driven channel flow of materials that exhibit viscoelasto-thixo-plasticity. We used the BMP model, which has been extensively used to describe this kind of complex rheological behaviour using only a modest number of parameters.

We derived an analytic equation for the steady-state velocity profile in channel flow, which depends on physically measurable quantities (such as low and high shear rate viscosities, structural relaxation time and a structure breakdown parameter).

We obtained a set of dimensionless groups ($\Phi$, $\Lambda$, $\Gamma$) from which we could construct the key dimensionless quantities for analysis of the results in terms of the phenomena of viscoelasticity, thixotropy and plasticity present in our material.

We have made a thorough exploration of the conditions for instability/stability and its growth rate, depending on our model parameters. We have found that viscoelastic effects are the main cause of instability, and that sinuous modes are always more unstable than varicose modes (though sometimes the growth rates of instability are very similar between the modes). We found that a low thixotropic ratio $\Phi$

(strong shear thinning) is needed to trigger the instability, and identified that the most dangerous wavenumber is located in a range of values of $0.35 < k < 0.6$, though the instability persists even at large values of $k$, which we validated using short wave calculations. It was not possible to study a fluid with a true yield stress, but the short wave results suggest that the limiting case $\Phi = 0$ might possibly be stable. Flow stability is seen if either $k \to 0$ or $W \to 0$ for any value of $\Phi$, $\Lambda$ and $\Gamma$.

We can characterise the instability in terms of the thixoplastic number; in doing so, we found that the instability is strongest if the base-state critical stress $\tau_c$ is located near the channel-wall (at $y \approx 0.98$).

Under these conditions, the instability grows fastest when the viscoelastic relaxation time $\lambda_{ve}$ is much longer than both the structural destruction timescale $\lambda_{tp}$ and the thixotropic timescale $\lambda$, and also when the structural destruction occurs over a longer timescale than the thixotropic recovery $\lambda_{tp} \gg \lambda$:

$$\lambda \ll \lambda_{tp} \ll \lambda_{ve}. \tag{4.75}$$

Fluids that satisfy this ordering of timescales exhibit complex non-linear viscoelasticity with shear-thinning characteristics rather than thixotropy, as stated by Larson [98].

Extremes of many parameters cause linearly stable flow: in particular, very large or very small values of the thixoviscous number or the thixoplastic number. Instability is enhanced by large values of the elastoplastic number or the thixoelastic number, which drive the scalings in equation (4.75) above.

# Chapter 5

# Channel flow stability of thixotropic-viscoelasto-plastic fluids with shear-banding

## 5.1 Introduction

In chapter 4, we studied elastic instabilities in planar Poiseuille flow of thixotropic-viscoelasto-plastic fluids, and we found that instability is seen when viscoelastic effects dominate. On the other hand, thixotropy has a stabilising effect. More importantly, we found that the structural relaxation time determines the growth rate of instability.

In this final chapter, we extend the scope of the fluids we can consider by including the shear-banding phenomenon in the flows of thixotropic-viscoelasto-plastic fluids. This kind of complex rheological behaviour has been experimentally observed multiple times in wormlike micellar solutions (see section 1.7.3). These fluids have been the center of numerous experimental and theoretical studies, and this is because they are of industrial relevance as their use is commonly found in household items, in the oil industry, and many other applications such as drag reducing agents. However, as reported in the literature (section 1.8.6), shear-banded fluids are susceptible to the development of elastic instabilities, and thus, it is of great interest to predict the flow conditions for which the flow of these fluids become highly unstable in order to avoid incorrect measurements of rheological data and in order to predict difficulties in industrial flows.

The stability of shear-banding fluids has been mostly studied in Couette geometries (such as Taylor-Couette and planar Couette flows [61, 63, 133, 154, 177]), but it has also recently been studied in pressure-driven channel flows [44, 65]. However, as discussed in sections 1.7.3.3 and 1.8.6, the disadvantages of these theoretical works are the models used by them, which are either phenomenological or have physical limitations.

In the present chapter, we use a much more realistic constitutive model, which is an extension of the model used in chapter 4: *the generalised BMP model*, which is able to predict the shear-banding phenomenon of micellar solutions, along with thixotropic, viscoelastic and plastic behaviours. We introduce this model in section 5.2 and show the behaviour in simple shear flow, where we illustrate the characteristic flow curve of shear-banded fluids predicted by the model in section 5.2.2. The dimensionless governing equations and the dimensionless groups are derived in section 5.2.3. We show the base-state quantities and illustrate the velocity and fluidity profiles for different model parameter values in 5.3.1. The perturbed governing equations, the boundary conditions and a description of the numerical methods to be used to solve our stability problem are found in sections 5.3.3 and 5.3.4, respectively. Finally, we show our results in section 5.4 and draw conclusions in 5.5.

The bulk of this chapter will form a paper to be submitted soon to the *Journal of Non-Newtonian Fluid Mechanics.*

## 5.2 Model fluid: The generalised BMP model

### 5.2.1 Governing equations

In order to study the flow instabilities of TVEP fluids that exhibit the shear-banding phenomenon, we consider the *generalised BMP* model [111], which was derived using an extended irreversible thermodynamics formalism. The set of equations for this model consists of a viscoelastic constitutive equation coupled to an evolution equation of a structural parameter (fluidity $\varphi$ or the inverse of viscosity) that represents the process in which the internal structure of the fluid is modified by an external flow.

For this model, the fluid flows with velocity $\underline{u}$, and its stress tensor $\underline{\underline{\sigma}}$ evolves according to the Upper-Convected Maxwell (UCM) model:

$$\underline{\underline{\sigma}} + \frac{1}{G_0 \varphi} \overset{\nabla}{\underline{\underline{\sigma}}} = \frac{2}{\varphi} \underline{\underline{D}}, \tag{5.1}$$

recalling that $G_0$ is the elastic modulus, and $\underline{\underline{D}}$ is the symmetric part of the flow gradient tensor $\underline{\nabla}\, \underline{u}$, defined in equation (1.2).

Equation (5.1) is coupled to a Fredrickson's-like equation, which describes the process in which a fluid undergoes a process of structure modification characterised by destruction and reformation processes:

$$\frac{D\varphi}{Dt} = \frac{1}{\lambda}(\varphi_0 - \varphi) + K(II_D)(\varphi_\infty - \varphi)\underline{\underline{\sigma}} : \underline{\underline{D}}. \tag{5.2}$$

As described in chapter 4, the first term of the right side of the equation represents the reformation process (build-up of viscosity or breakdown of fluidity), where $\lambda$ is the *structural relaxation time* and $\varphi_0$, the plateau fluidity observed at low shear rates; and the second term is the destruction process (breakdown of viscosity or build up of fluidity), described by $K$, a rate parameter for structure destruction, $\varphi_\infty$, the fluidity at high shear rates, and $\sigma_{ij} D_{ij}$, the rate of energy dissipation in the fluid.

The main difference between the model we will be using here and the one used in the previous chapter is that in equation (5.2), the destruction parameter $K$ is a function of the second invariant of the rate of deformation tensor $II_D = 2\, D_{ij}\, D_{ij}$ and adopts, in the simplest version, the following form (see [2, 8]):

$$K = K_0 \left( 1 + \vartheta \sqrt{II_D} \right). \tag{5.3}$$

Here, $K$ is a first order linear expression where $K_0$ is a kinetic parameter at zero-shear strain, and $\vartheta$ is a coefficient that can be determined experimentally and is known as *shear-banding* parameter, which according to extended irreversible thermodynamics principles, it will determine the location of the *stress plateau* observed in fluids that exhibit formation of shear bands. In simple shear flow, equation (5.3) can be written as $K = K_0(1 + \vartheta\dot{\gamma})$. In the absence of shear-banding flow ($\vartheta = 0$), we recover the original model [7], which was used in chapter 4. A much more general version of the BMP model, which incorporates diffusive terms, concentration gradients and non-zero values of the normal stress differences can be found in the literature [70] and is discussed shortly in 6. However, we will use the model shown in equations (5.1)–(5.3) as it requires less parameters to describe shear-banding phenomenon than the one from [70].

Finally, the constitutive equations (5.1) and (5.2) are coupled with the continuity and momentum equations (in the absence of external forces such as gravity), which were shown in equations (4.5) and (4.6).

## 5.2.2 Behaviour in steady simple shear

For simple steady shear flow, and considering cartesian coordinates $\underline{u} = \dot{\gamma} y \underline{e}_x$ with $\dot{\gamma} > 0$, the equations (5.1) and (5.2) become:

$$\underline{\underline{\sigma}} = \begin{pmatrix} 2\,\dot{\gamma}^2\, G_0^{-1}\,\varphi^{-2} & \varphi^{-1}\dot{\gamma} \\ \varphi^{-1}\dot{\gamma} & 0 \end{pmatrix} \tag{5.4}$$

$$0 = \frac{1}{\lambda}(\varphi_0 - \varphi) + K_0(1 + \vartheta\,\dot{\gamma})(\varphi_\infty - \varphi)\,\sigma_{12}\,\dot{\gamma}. \tag{5.5}$$

Combining equation (5.5) and (5.4), we get a cubic equation for the fluidity:

$$\varphi^3 + a_0\,\varphi^2 + b_0\,\varphi - c_0 = 0 \tag{5.6}$$

$$a_0 = \frac{1}{\sigma_{12}\,\vartheta} - \varphi_\infty \qquad b_0 = \frac{1}{K_0\,\lambda\,\vartheta\,\sigma_{12}^3} - \frac{\varphi_\infty}{\sigma_{12}\,\vartheta} \qquad c_0 = \frac{\varphi_0}{K_0\,\lambda\,\vartheta\,\sigma_{12}^3}. \tag{5.7}$$

Additionally, using Cardano's method to find the solution of the cubic equation, we derive the following expressions:

$$Q_0 = \frac{3\,b_0 - a_0^2}{9} \qquad R_0 = \frac{9\,a_0\,b_0 - 27\,c_0 - 2\,a_0^3}{54} \qquad H_0 = Q_0^3 + R_0^2. \tag{5.8}$$

For fixed value of shear stress $\sigma_{12}$, and a given set of parameters $K_0$, $\lambda$, $\varphi_0$, $\varphi_\infty$ and $\vartheta$, we can solve the cubic equation, for which we can either get a positive real root and two imaginary ones (if $H_0 > 0$), three real roots of which two are equal ($H_0 = 0$) or three different real roots if $H_0 < 0$. The analytic solution of (5.6) for the case $H_0 > 0$, where there is only one real solution $\varphi_{1i}$, is:

$$\varphi_{1i} = -\frac{1}{3}\,a_0 + (S_0 + T_0) \tag{5.9}$$

where $S_0$ and $T_0$ are:

$$S_0 = \sqrt[3]{R_0 + \sqrt{H_0}} \qquad T_0 = \sqrt[3]{R_0 - \sqrt{H_0}}. \tag{5.10}$$

On the other hand, we have the case $H_0 < 0$, where all three solutions are real:

$$\begin{aligned}
\varphi_{1r} &= 2\sqrt{-Q_0}\cos\left(\frac{\Theta_0}{3}\right) - \frac{1}{3}\,a_0 \\
\varphi_{2r} &= 2\sqrt{-Q_0}\cos\left(\frac{\Theta_0 + 2\pi}{3}\right) - \frac{1}{3}\,a_0 \\
\varphi_{3r} &= 2\sqrt{-Q_0}\cos\left(\frac{\Theta_0 + 4\pi}{3}\right) - \frac{1}{3}\,a_0,
\end{aligned} \tag{5.11}$$

where $\Theta_0$ is:

$$\Theta_0 = \cos^{-1}\left(\frac{R_0}{\sqrt{-\,Q_0^3}}\right). \tag{5.12}$$

For the specific case $H_0 = 0$, $\varphi_{2r}$ and $\varphi_{3r}$ are equal. Lastly, authors in [27] demonstrated, using chaos theory and irreversible thermodynamics, that the *shear stress*

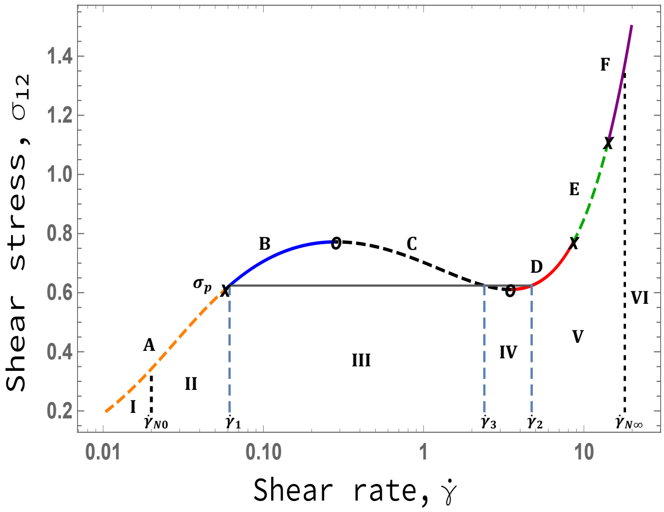

Figure 5.1: Simple shear flow curve predicted by the generalised BMP model. The parameters used are: $K_0\,\lambda = 0.09\,\mathrm{Pa}^{-1}\,\mathrm{s}$, $\varphi_0 = 0.05\,\mathrm{Pa}^{-1}\mathrm{s}^{-1}$, $\varphi_\infty = 13.5\,\mathrm{Pa}^{-1}\mathrm{s}^{-1}$, $G_0 = 0.38\,\mathrm{Pa}$ and $\vartheta = 0.8\,\mathrm{s}$.

*plateau* $\sigma_p$ satisfies the condition $R_0 = 0$.

When solving equations (5.4) and (5.6), the simple shear flow material functions (viscosity $\eta$, shear stress $\sigma_{12}$ and the first normal stress difference coefficient $\Psi_1$) can be obtained as follows:

$$\eta = \varphi^{-1} \qquad \sigma_{12} = \eta\,\dot{\gamma} \qquad \Psi_1 = \frac{\sigma_{11} - \sigma_{22}}{\dot{\gamma}^2} = 2\,G_0^{-1}\,\eta^2. \tag{5.13}$$

### 5.2.2.1 Simple shear flow curve

Figure 5.1, 5.2 and 5.3 illustrate the behaviour of the viscometric functions, using as an example the following parameter values reported in [54, 111]: $K_0\,\lambda = 0.09\,\mathrm{Pa}^{-1}\,\mathrm{s}$, $\varphi_0 = 0.05\,\mathrm{Pa}^{-1}\mathrm{s}^{-1}$, $\varphi_\infty = 13.5\,\mathrm{Pa}^{-1}\mathrm{s}^{-1}$, $G_0 = 0.38\,\mathrm{Pa}$ and $\vartheta = 0.8\,\mathrm{s}$.

As shown in figure 5.1, the generalised BMP model predicts a non-monotonic behaviour for the shear stress against shear rate curve (initially described in section 1.7.3.2) and it can be seen that there are characteristic regions of the curve that will be briefly explained in the following lines. Firstly, we have the line A, where the condition $H_0 > 0$ is satisfied. Within A, we find region I, for which a Newtonian-like behaviour (with viscosity $\eta = 1/\varphi_0$) is observed at very small shear rates. Thus, a low fluidity plateau $\varphi = \varphi_0$ is observed in the following range of shear rates:

$$\varphi \approx \varphi_0 \;\text{ when }\; \dot{\gamma}^2(1+\vartheta\dot{\gamma}) \ll \frac{\varphi_0}{K_0\,\lambda} \tag{5.14}$$

An increase in $\dot{\gamma}$ will lead to a shear-thinning behaviour (region II) until the fluid reaches a value of shear rate equal to $\dot{\gamma}_1$. The crosses marked in the plot represent *bifurcation* points that satisfy the equation $H_0 = 0$, where we have three real solutions for the fluidity but two of them are equal (depicted as circles).

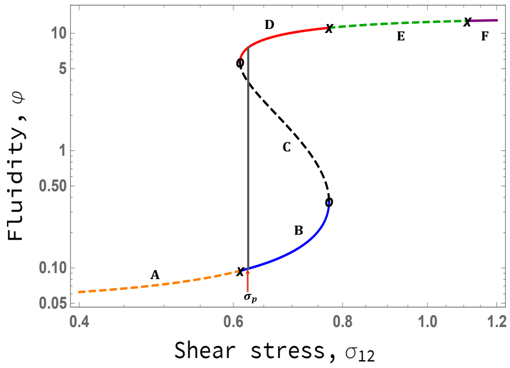

Figure 5.2: Fluidity vs shear stress calculated using equations (5.6) and (5.13). The parameter values used here are the same used in figure 5.1. The vertical line represents the location of the shear stress plateau $\sigma_p$ and the crosses are the bifurcation points.

Secondly, the points located in B, C and D correspond to the *multi-valued* region (where $H_0 < 0$), which is that region where the BMP model predicts that there are three possible values of shear-rate for a fixed value of shear stress. The most common example of this is the *shear stress plateau* $\sigma_p$ and is represented here by the solid horizontal line. The vertical dashed lines indicate the location of its respective shear rate values, $\dot{\gamma}_1, \dot{\gamma}_2$ and $\dot{\gamma}_3$. The points of B located in region III, whose interval is $[\dot{\gamma}_1, \dot{\gamma}_3]$, are said to be meta-stable states, and the points that are also within region III and belong to C (characterised by a negative slope $\mathrm{d}\sigma_{12}/\mathrm{d}\dot{\gamma}$) are said to be mechanically unstable. Something similar is observed in region IV $[\dot{\gamma}_2, \dot{\gamma}_3]$, where there are also present unstable and meta-stable states (those to belong to D).

At higher values than $\dot{\gamma}_2$ (region V), the disentangled state (in which structure is being destroyed by flows) begins to take over. After the second bifurcation point, we have the region E ($H_0 > 0$), where the cubic equation predicts again a single real root. Finally, a third bifurcation point is predicted, and again three real solutions are obtained, but two of them are negative and just one is positive (plot line F). For values of shear rate higher than $\dot{\gamma}_\infty$ (region VI), we will observe a high fluidity plateau $\varphi = \varphi_\infty$, where the molecular networks have been completely destroyed. The condition that needs to be satisfied to observe region VI is the following:

$$\varphi \approx \varphi_\infty \quad \text{when} \quad \dot{\gamma}^2(1 + \vartheta\dot{\gamma}) \gg \frac{\varphi_\infty}{K_0\,\lambda} \tag{5.15}$$

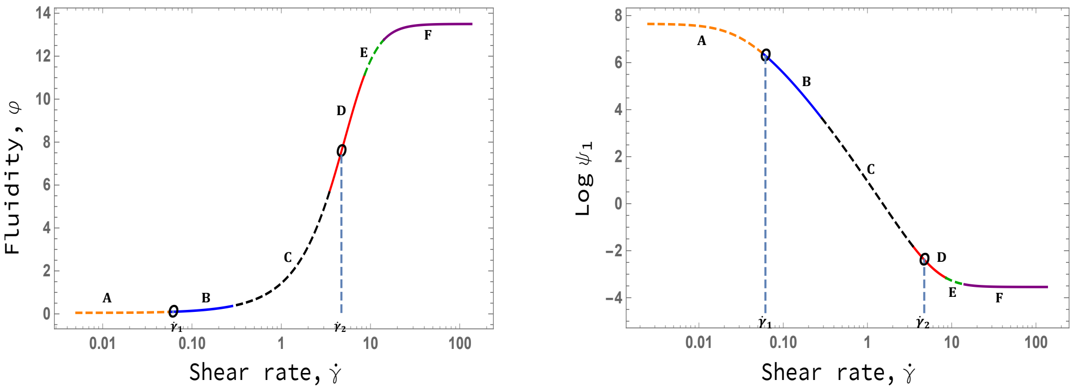

(a) Fluidity versus shear rate

(b) $\Psi_1$ versus shear rate

Figure 5.3: Fluidity and first normal stress difference coefficient versus shear rate. The parameter values used here are the same used in figure 5.1. The circles are the binodals of the system, $\dot{\gamma}_1$ and $\dot{\gamma}_2$.

The shear-stress plateau $\sigma_p$ (the point that satisfies the condition $R_0 = 0$ and in which the areas below and above the plateau of the curve $\sigma_{12}$ vs $\dot{\gamma}$ are equal) is one of the main characteristics of complex fluids that exhibit shear-banding, along with $\dot{\gamma}_1$ and $\dot{\gamma}_2$, known as binodals of the system. These three values are constantly observed and measured in experiments, and the reason for it is that when the fluid reaches the value of $\sigma_p$, there is a thermodynamically stable phase-coexistence between two bands of fluid that have different shear rates: the entangled phase (where there exists branched networks) is seen for values smaller than $\dot{\gamma}_1$, and the disentangled phase (where there are polymer-like linear chains) appears at shear rates higher than $\dot{\gamma}_2$. The value $\dot{\gamma}_3$ is thermodynamically unfavourable and mechanically highly unstable. For a full detailed analysis of the flow curve 5.1, see [27].

#### 5.2.2.2 Fluidity and first normal stress difference coefficient

In figure 5.2, we show the fluidity vs shear stress curve obtained in simple shear flow using the same parameter values as those used in figure 5.1. It can be clearly seen the that for a fixed value of shear stress, there might exist multiple values of fluidity, such as the case of the stress *plateau* (solid vertical line). As indicated in figure 5.1, the crosses are the bifurcation points, and the small circles indicate the location of the minimum and the maximum seen in the simple shear flow curve. Outside the multi-valued zone, and at low shear stress (region A), we observe a low fluidity plateau with $\varphi \approx \varphi_0 = 0.05$, and similarly, $\varphi \to \varphi_\infty$ at high shear stresses values (region F).

These fluidity plateaus can also be seen in the fluidity and first normal stress difference coefficient profiles, shown in figure 5.3. For both figures, the circles indicate the location of the binodals $\dot{\gamma}_1$ and $\dot{\gamma}_2$. The slope of these curves is much more pronounced than those seen in the equivalent model without shear-banding [29]. With an increase in shear rate, the fluid viscosity and elasticity drop.

### 5.2.3 Dimensionless form of the equations

#### 5.2.3.1 Flow geometry

We now consider a two-dimensional channel flow of a fluid that satisfies the governing equations (constitutive equation (5.1)–(5.3) along with continuity and momentum equations (4.5)–(4.6)). Our channel has infinite extent in the $x$-direction and half-height $L$. The fluid is driven by a constant pressure gradient $\mathscr{P}$ in the $x$-direction, and flows with centreline velocity $U_0$. The flow geometry was sketched in section 2.4.

#### 5.2.3.2 Dimensionless form of the governing equations

We scale lengths with $L$, times using the average shear rate $U_0/L$, and fluidities with the high-shear rate value $\varphi_\infty$. The natural stress scale then becomes $\varphi_\infty^{-1}(U_0/L)$. In terms of dimensionless variables, the governing equations become:

$$\underline{\nabla} \cdot \underline{u} = 0 \tag{5.16}$$

$$Re\left(\frac{\partial \underline{u}}{\partial t} + \underline{u} \cdot \underline{\nabla u}\right) = -\underline{\nabla} P + \underline{\nabla} \cdot \underline{\underline{\sigma}} \tag{5.17}$$

$$\underline{\underline{\sigma}} + \frac{W}{\varphi} \overset{\triangledown}{\underline{\underline{\sigma}}} = \frac{2}{\varphi} \underline{\underline{D}} \tag{5.18}$$

$$\frac{D\varphi}{Dt} = \frac{1}{\Lambda}(\Phi - \varphi) + \Gamma \left(1 + \theta \sqrt{II_D}\right)(1 - \varphi)\, \underline{\underline{\sigma}} : \underline{\underline{D}} \tag{5.19}$$

The dimensionless governing equations (5.16)–(5.18) obtained here are the same used in chapter 4, where $Re$ and $W$ are the Reynolds and Weissenberg numbers, respectively, defined as:

$$Re = \rho\, U_0\, L\, \varphi_\infty \qquad W = \lambda_{ve}\left(\frac{U_0}{L}\right) = \frac{1}{G_0 \varphi_\infty}\left(\frac{U_0}{L}\right). \tag{5.20}$$

Equation (5.19) differs from the original Fredrickson's kinetic equation [67] by the shear-banding terms that appear in the right side of the equation. The other dimensionless numbers are:

$$\Phi = \frac{\varphi_0}{\varphi_\infty} \qquad \Lambda = \lambda\left(\frac{U_0}{L}\right) \qquad \Gamma = \left(\frac{1}{\varphi_\infty}\frac{U_0}{L}\right) K_0 \qquad \theta = \vartheta\left(\frac{U_0}{L}\right), \tag{5.21}$$

where $\Phi$, $\Lambda$ and $\Gamma$ are the thixotropic ratio, the structural relaxation time and the destruction parameter, respectively, whose physical meaning was already discussed in section 4.2.4. We have introduced in this work, a new number, which is the *dimensionless shear-banding* parameter $\theta$, defined as the ratio between $\vartheta$ and the characteristic time-scale of the flow. Its physical meaning is simple: for the cases where $\theta \to 0$, no phase coexistence is observed, and high values of $\theta$ will lead to the formation of bands with different shear rates. In the next sections, we will illustrate the effect of the shear-banding parameter in the rheology of the fluid.

## 5.3 Stability calculation

### 5.3.1 Base state

We study the stability of a TVEP fluid with shear-banding flowing through a two-dimensional channel flow of infinite extent in the $x$-direction, which has dimensionless height 2 (in the $y$-direction) and is being driven by a dimensionless constant pressure gradient $\mathcal{P}$ in the $x$-direction. Assuming a steady, unidirectional flow profile $\underline{u} = U(y)\underline{e}_x$ that satisfies a no-slip condition at $y = \pm 1$ (and denoting $U' = \mathrm{d}U/\mathrm{d}y$), equations (5.16)–(5.19) become:

$$0 = \mathcal{P} + \frac{\mathrm{d}\sigma_{12}}{\mathrm{d}y} \tag{5.22}$$

$$\sigma_{12} = \frac{1}{\varphi}\frac{\mathrm{d}U}{\mathrm{d}y} \qquad \varphi = \frac{\Phi + \Gamma\Lambda(1+\theta\,\dot{\gamma})\sigma_{12}U'}{1 + \Gamma\Lambda(1+\theta\,\dot{\gamma})\sigma_{12}U'}. \tag{5.23}$$

Considering channel symmetry, the momentum equation (5.22) gives:

$$\sigma_{12} = -\mathcal{P}y. \tag{5.24}$$

Combining (5.24) into (5.23), we obtain a cubic equation for our dimensionless fluidity, whose coefficients are position-$y$ dependent:

$$\varphi^3 + a\,\varphi^2 + b\,\varphi - c = 0 \tag{5.25}$$

$$a\,(y) = \frac{1}{\mathcal{P}y\,\theta} - 1 \qquad b\,(y) = \frac{1}{\Gamma\,\Lambda\,\theta\,\mathcal{P}^3 y^3} - \frac{1}{\mathcal{P}y\,\theta} \qquad c\,(y) = \frac{\Phi}{\Gamma\,\Lambda\,\theta\,\mathcal{P}^3 y^3}. \tag{5.26}$$

As demonstrated in section 5.2.2, we used Cardano's method to get an analytic solution for the fluidity and some parameters that are useful to determine whether we will observe only one or more real solutions. These parameters have the same basic form as those for steady simple shear:

$$Q(y) = \frac{3b - a^2}{9} \qquad R(y) = \frac{9ab - 27c - 2a^3}{54} \qquad H(y) = Q^3 + R^2. \tag{5.27}$$

Using (5.24)–(5.27), we obtain a fluidity profile that resembles reported experimental information of shear-banding fluids, and is shown below:

$$\varphi(y) = \begin{cases} -\dfrac{1}{3}\,a\, + (S+T) & H(y) > 0 \\ 2\sqrt{-Q}\cos\left(\dfrac{\Theta}{3}\right) - \dfrac{1}{3}\,a & H(y) \leq 0 \text{ and } R(y) \geq 0 \\ 2\sqrt{-Q}\cos\left(\dfrac{\Theta + 2\pi}{3}\right) - \dfrac{1}{3}\,a & H(y) \leq 0 \text{ and } R(y) < 0, \end{cases} \tag{5.28}$$

where $S$, $T$ and $\Theta$ are:

$$S(y) = \sqrt[3]{R + \sqrt{H}} \qquad T(y) = \sqrt[3]{R - \sqrt{H}} \qquad \Theta\,(y) = \cos^{-1}\left(\frac{R}{\sqrt{-\,Q^3}}\right). \tag{5.29}$$

The shear rate $\dot{\gamma}_0$ and the velocity profile $U(y)$ are simply calculated as follows:

$$\dot{\gamma}_0(y) = |U'| = \mathcal{P}\,y\,\varphi(y) \qquad U(y) = \int_0^1 \dot{\gamma}_0(y)\,\mathrm{d}y = \mathcal{P}\int_0^1 y\,\varphi(y)\,\mathrm{d}y \tag{5.30}$$

As can be seen, an analytic equation for the velocity profile $U(y)$ of a fluid that exhibits shear-banding cannot be obtained (unlike the case without shear-banding, see equations (4.39)–(4.42) in chapter 4). Instead, we have to integrate $\dot{\gamma}_0(y)$ from the centreline to the channel wall. Additionally, the viscosity $\eta$ and the stress tensor $\sigma_{ij}$ are calculated as follows:

$$\eta = \varphi^{-1} = \frac{1 + \Gamma\Lambda(1 + \theta\,\dot{\gamma})\sigma_{12}U'}{\Phi + \Gamma\Lambda(1 + \theta\,\dot{\gamma})\sigma_{12}U'} \qquad \underline{\underline{\sigma}} = \begin{pmatrix} 2W\mathcal{P}^2y^2 & -\mathcal{P}y \\ -\mathcal{P}y & 0 \end{pmatrix}. \tag{5.31}$$

The first and second normal stress differences $N_1$ and $N_2$ are simply:

$$N_1 = \sigma_{11} - \sigma_{22} = 2W\mathcal{P}^2y^2 \qquad N_2 = 0. \tag{5.32}$$

Lastly, the low ($\varphi = \Phi$) and high ($\varphi = 1$) dimensionless fluidity plateaus are seen when the following conditions are satisfied:

$$\varphi \approx \Phi \;\text{ when }\; \dot{\gamma}^2(1 + \theta\dot{\gamma}) \ll \frac{\Phi}{\Gamma\,\Lambda} \qquad \varphi \approx 1 \;\text{ when }\; \dot{\gamma}^2(1 + \theta\dot{\gamma}) \gg \frac{1}{\Gamma\,\Lambda} \tag{5.33}$$

In the next section, we will illustrate the behaviour of the fluidity, velocity and normal stress difference profiles predicted by the equations shown above.

### 5.3.2 Base state profiles

In this section, we show some of the velocity and fluidity profiles that can be obtained for various values of our model parameters. We begin with figure 5.4, where we illustrate characteristic base state profiles that are commonly observed in pressure-driven channel flow of fluids that exhibit shear-banding.

#### 5.3.2.1 Base state profiles with shear banding

Firstly, in figure 5.4a) we have the velocity profile that was calculated from the integration of the shear rate profile (5.30). An extra calculation had to be done in order to satisfy the condition $U_0(0) = 1$: Newton-Raphson iterations are used to determine the required value of pressure gradient, which is $\mathcal{P} = 17.5927$ for this case.

As we can see, two regions can be identified in figure 5.4a): 1) a plug flow region of low fluidity (or high viscosity) that covers the channel from the centreline to a specific location close to the wall $y \approx \pm 0.8765$ and 2) a region near the wall ($|y| > 0.8765$) where the velocity drastically decreases towards its zero value at $y = \pm 1$. The regions are separated by an interface located at $y = \kappa = 0.8765$, where the high and low shear rate regions coexist. As stated above, the location of the interface can be simply obtained when $R(\kappa) = 0$ is satisfied, which means that the location of the interface depends on our model parameters such as $\Gamma$, $\Lambda$, $\Phi$ and $\theta$.

The resulting fluidity profile is shown in figure 5.4b). This time we will only show half the channel. For the low-shear-rate band, it can be seen that near the centreline $y \approx 0$ the fluidity has a value of $\varphi = \Phi = 0.001$. As we move along the channel, the fluidity exhibits some shear thinning behaviour, which leads to an increase in fluidity until the interface is reached, where there is a clear *jump* in the fluidity at $y = \kappa = 0.8765$ (see dotted lines and circles). The second band with a much lower viscosity than the first one appears, and its viscosity will increase until the channel wall is reached. The shear rate profile $\dot{\gamma}$ vs $y$ looks qualitatively very similar to the fluidity one, so we will not show it here.

A particularity of the BMP model (compared to other viscoelastic models) is that there is continuity at the interface in the first normal stress difference for fluids that exhibit shear-banding, as can be seen in figure 5.4c) (see black circle), which shows a parabolic profile for $N_1$ as a function of the channel coordinate. The discontinuity that we saw for $\Psi_1$ in section 5.2.2 is due to the jump in shear rate, or equivalently

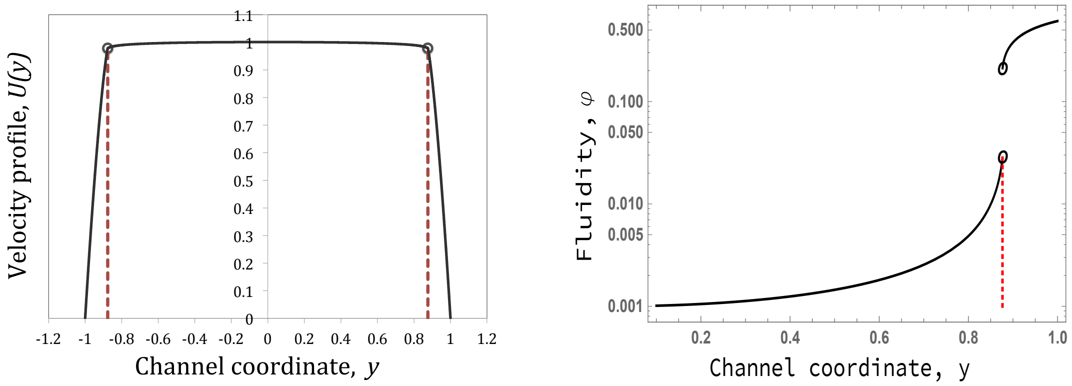

(a) Velocity profile.

(b) Fluidity profile.

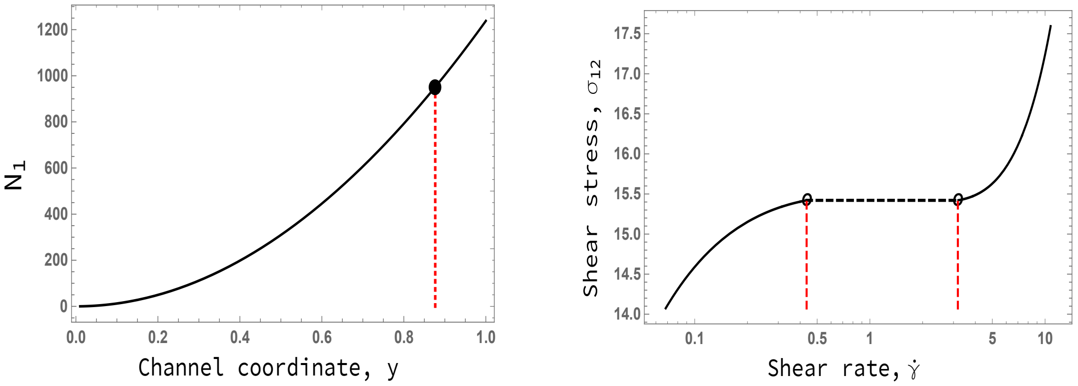

(c) First normal stress difference.

(d) Flow curve.

Figure 5.4: Velocity, fluidity and first normal stress difference profiles and flow curve calculated using equations (5.25)–(5.32) with $\Phi = 0.001$, $\Gamma\Lambda = 0.004$, $W = 2$ and $\theta = 0.10$. For all the panels, the vertical dotted lines represent the location of the interface $\kappa$ between the low and high shear rate bands and the circles are the binodals of the system and their respective value of velocity (a), fluidity (b), $N1$ (c), and shear stress plateau between the two values of shear rate which meet at $y = \kappa$ (d).

to a jump in fluidity. Also, as we have mentioned before, the BMP model predicts a zero value of $N_2$ (see equation (5.32))

The last figure is 5.4d), which illustrates the flow curve for pressure-driven channel flow of our fluid, where we show the only physically-possible dynamic states of the system (unlike figure 5.1 that shows metastable and unstable regions). The interface appears when the flow reaches a shear stress plateau value of $\sigma_p = 15.42$ (see horizontal dashed line), which will lead to a band of fluid with $\dot{\gamma}_1 = 0.4353$ and another one with $\dot{\gamma}_2 = 3.1785$ at $y = \kappa = 0.8765$.

Lastly, an important flow condition that needs to be satisfied in order to see shear-banding within the channel (even though the shear-banding parameter has a non-zero value), is that the wall shear stress $\sigma_w$ has to be greater than the stress plateau $\sigma_p$ (for this case, $\sigma_w = 17.59 > \sigma_p$), otherwise, the low shear rate band will fill the whole channel.

#### 5.3.2.2 Transition to shear-banding

In this section, we will show the effect of the dimensional shear-banding parameter $\theta$ on the base state quantities in pressure-driven channel flow of our fluid. We choose fixed values of $\Phi = 0.001$ and $\Gamma\Lambda = 0.004$ and a set of values of $\theta = [0, 0.05, 0.08, 0.1, 1, 3, 10]$ to illustrate the transition from non-shear banding to the formation of bands. The results can be seen in figure 5.5.

Firstly, we focus on small values of $\theta$. We show the velocity profiles predicted by our equations in figure 5.5a), where the bottom curve depicts the case for a fluid with a value of $\theta = 0$, with a plug-flow along the channel commonly observed in shear-thinning fluids, which is the case that we studied in chapter 4. An increase in the shear-banding parameter (from bottom to top) slowly leads to a wider region of the high viscosity region near the channel wall, until an interface between two bands of fluid with different shear rates is seen at $y = \kappa \approx 0.8765$ (case $\theta = 0.1$).

This transition can be better appreciated in the fluidity profile along the channel, see figure 5.5c). For the case $\theta = 0$, we observe a continuous increase for the fluidity from the centreline towards the channel-wall. Although the same behaviour is observed for the cases $\theta = 0.05$ and $\theta = 0.08$, notice how the slope of the curves increases (rapid increase in $\varphi$ between $y = 0.7$ and $y = 0.9$), until we observe a discontinuity in the curve $\varphi$ vs $y$, indicating that two bands of fluid with different viscosities have been formed. The jump in the fluidity value is represented with a dashed line when $\theta = 0.10$.

The transition from a monotonic to non-monotonic flow curves can be seen in figure 5.5e). Notice how an increase in $\theta$ leads to a stress plateau $\sigma_p$, with two representative binodals: $\dot{\gamma}_1$ at low shear rates and $\dot{\gamma}_2$ at high shear rates.

For the cases with high shear-banding parameter values, the flow behaviour is similar to the one reported with $\theta = 0.1$. However, there are gradual changes; for instance, we have the velocity profiles in figure 5.5b). From right to left, the values are $\theta = 0.3, 1, 3$ and 10. For all cases, there exists an interface that separates the low viscosity band from the high one (see vertical dashed lines), but we can see that an increase in the shear-banding parameter moves the location of the interface, $\kappa$, away from the channel wall. This is consistent with the flow curves shown in 5.5f), where the stress plateau $\sigma_p$, and the binodals $\dot{\gamma}_1$ and $\dot{\gamma}_2$ shift to lower values as $\theta$ grows.

The fluidity profiles 5.5d) are also in agreement with the velocity profiles. We observe that a rise in the shear-banding parameter value causes a jump in the fluidity curves to increase for large $\theta$. The limit will be when the fluidity in the low region $\varphi_1$ is equal to the thixotropic ratio $\Phi$ (fully entangled state), and the high region fluidity $\varphi_2$ reaches a value of 1 (fully destroyed state). As we will see in the next section, how quick or slow the transition from non-shear-banding to shear-banding is will depend on the values of the destruction parameter $\Gamma$, thixoviscous number $\Lambda$ and thixotropic ratio $\Phi$.

#### 5.3.2.3 Dependence of transition on destruction parameter and thixoviscous number

In this section, we focus on fixed values of the thixotropic ratio $\Phi = 0.001$ and shear-banding parameter $\theta = 0.1$ to study the effect of a variable product $\Gamma\Lambda$ on the formation of shear bands. As we previously explained, the destruction parameter $\Gamma$ and the structural reformation parameter $\Lambda$ will only affect the base state quantities through their product (this will not be true for the flow instability, as we will show in the next sections). Small values of $\Gamma\Lambda$ involves slow destruction (or equivalently,

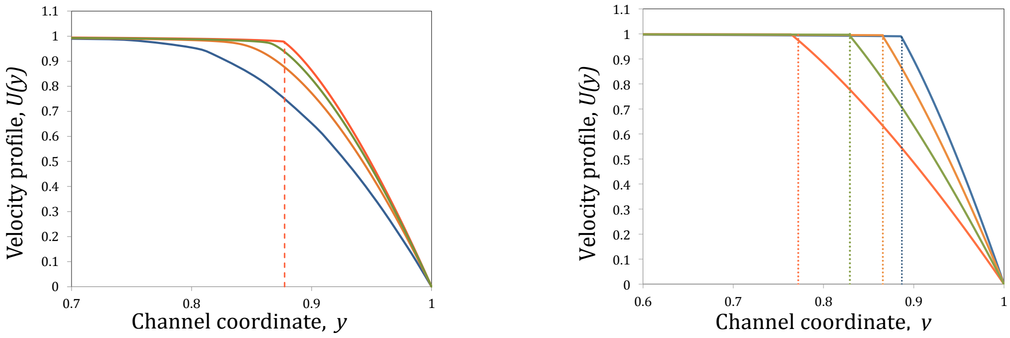

(a) Velocity profile with small $\theta$.

(b) Velocity profile with high $\theta$.

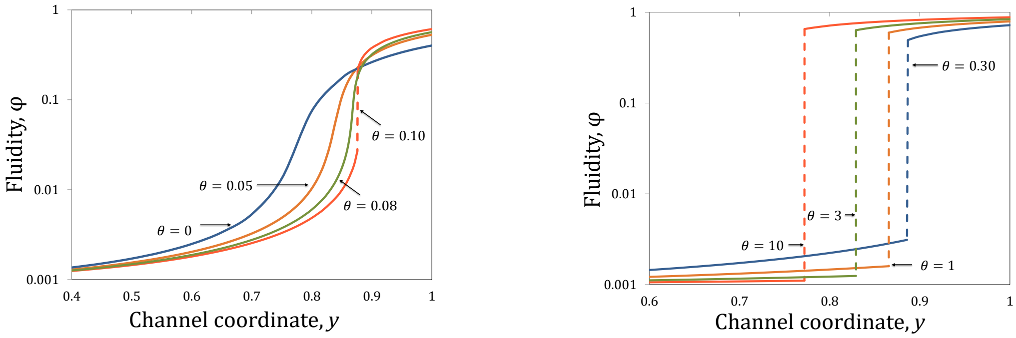

(c) Fluidity profile with small $\theta$.

(d) Fluidity profile with high $\theta$.

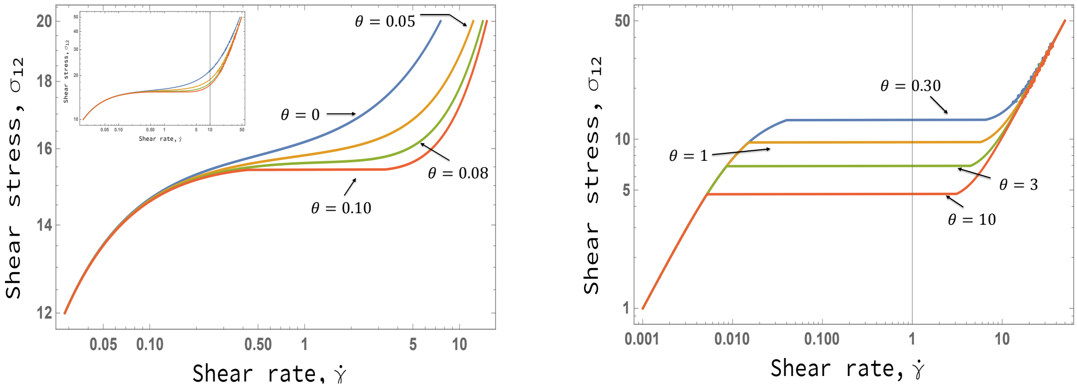

(e) Flow curve with small $\theta$.

(f) Flow curve with high $\theta$.

Figure 5.5: Base state profiles for different values of shear-banding parameter, with $\Phi = 0.001$ and $\Gamma\Lambda = 0.004$ fixed. Figure (a) velocity profile for small $\theta$ values; from bottom to top $\theta = 0, 0.05, 0.08$ and $0.1$. Figure (b) velocity profile for high $\theta$ values; from top to bottom $\theta = 0.3, 1, 3$ and $10$. The vertical dashed lines represent the location of the interface $\kappa$. Figures (c) and (d) are the fluidity profiles for low and high $\theta$ values , and finally, figures (e) and (f) show their respective flow curves $\sigma_{12}$ vs $\dot{\gamma}$.

quick structural reformation), while high structural destruction or high thixotropy will be observed for large values of $\Gamma\Lambda$. In order to explore these structural changes in our fluids, we choose a set of values of $\Gamma\Lambda = [1.6 \times 10^{-4}, 0.001, 0.004, 0.01, 0.05]$. Results are shown in figure 5.6.

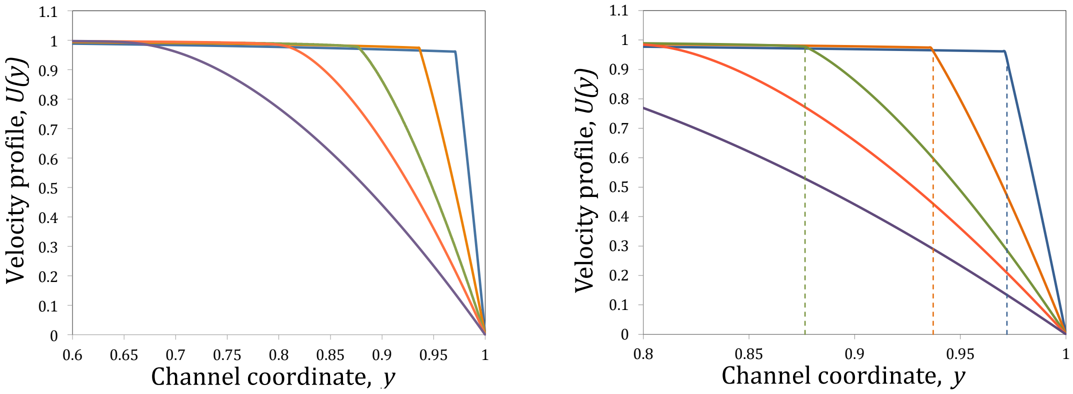

(a) Velocity profiles (b) Small region of a)

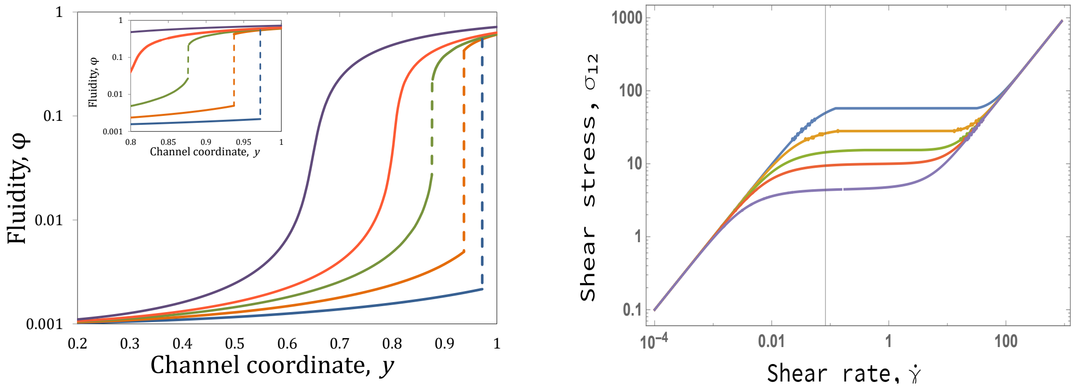

(c) Fluidity profiles (d) Flow curve $\sigma_{12}$ vs $\dot{\gamma}$

Figure 5.6: Base state profiles for different values of $\Gamma\Lambda$, with $\Phi = 0.001$ and $\theta = 0.10$ fixed. Figure (a) Velocity profile; from right to left: $\Gamma\Lambda$=$1.6 \times 10^{-4}, 0.001, 0.004, 0.01$ and 0.05. Figure (b): small region of figure (a). The dashed lines here indicate the location of the shear-banding interface $\kappa$. (c) Fluidity profiles; from left to right, the shear-banding parameter is increasing, with the same parameter values indicated above. The dashed lines represent the discontinuity (or jump) in the fluidity values. Figure (d): flow curve for the same parameters used in (a); from top to bottom, $\Gamma\Lambda$ increases.

Figure 5.6a) illustrates the velocity profiles for different values of the product $\Gamma\Lambda$. For the limit $\Gamma\Lambda \approx 0$, no jump in fluidity is reported, as the interface location would appear outside the channel. The smallest value of $\Gamma\Lambda$ here is $1.6 \times 10^{-4}$, whose curve is located farthest to the right of the plot. We can see for this case that a plug-flow is almost all over the channel, with an interface located very close to the channel wall ($y \approx 0.973$) and with an extremely narrow high-fluidity region. These observations can be seen more clearly in figure 5.6b), which is a *zoom* of the bigger figure. As we increase the value of $\Gamma\Lambda$ (from right to left), the interface location $\kappa$ (vertical dashed line) moves away from the channel wall, meaning that the low-viscosity band becomes wider and the plug-flow occupies less of the flow width.

The fluidity profiles shown in figure 5.6c) are useful to appreciate the transition better. For instance, we can clearly see that an increase in $\Gamma\Lambda$ (i.e. a rise in structural destruction and/or thixotropy of the fluid) is increasing the high-shear rate band width and reducing the *jump* in the fluidity curves, until a *critical* value of $\Gamma\Lambda \approx 0.0045$ is reached, which is where the interface disappears, or in other words, the fluidity profiles are no longer discontinuous. For $\Gamma\Lambda > 0.0045$, the fluidity profiles will always be continuous (but with a high slope) and the high-shear rate band will get wider and wider. It is important to point out that this critical value of $\Gamma\Lambda \approx 0.0045$ is only valid for $\theta = 0.1$ and $\Phi = 0.001$, and therefore, the formation of the bands will depend on these parameters.

We also show the flow curves 5.6d), where we observe that an increase in $\Gamma\Lambda$ (from top to bottom) decreases the values of the shear stress plateau $\sigma_p$ and binodals $\dot{\gamma}_1$ and $\dot{\gamma}_2$, until we no longer see a plateau (two bottom curves).

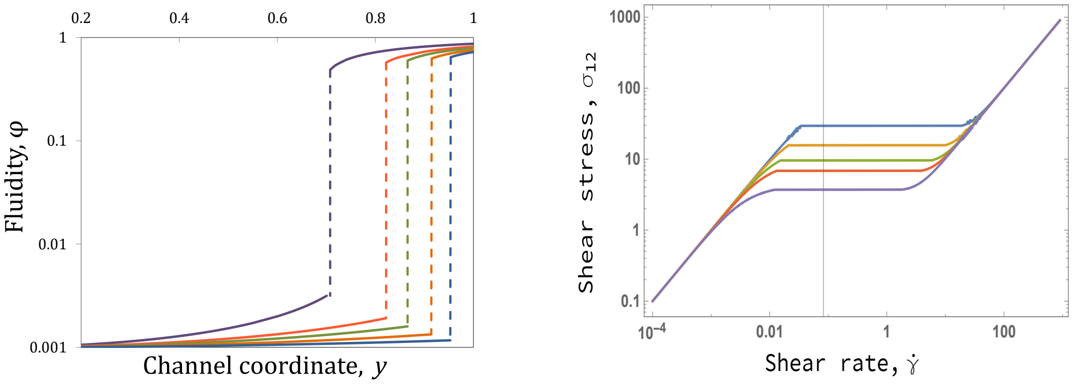

(a) Fluidity profiles (b) Flow curve $\sigma_{12}$ vs $\dot{\gamma}$

Figure 5.7: Fluidity profiles and flow curves for different values of $\Gamma\Lambda$, with $\Phi = 0.001$ and $\theta = 1.0$ fixed. Figure (a) Fluidity profile; from right to left: $\Gamma\Lambda$=$1.6 \times 10^{-4}, 0.001, 0.004, 0.01$ and $0.05$. The dashed lines represent the discontinuity (or jump) in the fluidity values at $\kappa$. Figure (b): flow curves); from top to bottom, $\Gamma\Lambda$ increases.

Finally, in figure 5.7 ,we explore the behaviour of the fluidity profiles and the flow curves with $\Gamma\Lambda$ variable but this time for a much higher value of shear-banding parameter, $\theta = 1.0$. The rest of the parameters are the same as the ones used in figure 5.6. In contrast with the fluidity profiles reported in 5.6c), where continuity is seen for high values of $\Gamma\Lambda$, notice that when $\theta = 1.0$, a jump is still observed, as seen in figure 5.7a). Additionally, for the curve with the lowest $\Gamma\Lambda = 1.6 \times 10^{-4}$, the low-fluidity plateau $\varphi = \Phi = 0.001$ covers most of the channel, until it *jumps* to a much higher fluidity near the wall. This is also evident in its flow curve shown in figure 5.7b), which is located at the top. For these parameter values (low $\Gamma\Lambda$ and high shear-banding parameter), we see that the high-viscosity region is approximately Newtonian right up to the banding interface: that is, the shear-thinning region II described in section 5.2.2.1 has been eliminated.

### 5.3.3 Perturbation flow

We add an infinitesimal perturbation $\varepsilon$ to the base flow, modifying all quantities by a small change :

$$\underline{u} = (U + u\varepsilon, v\varepsilon) \tag{5.34}$$

$$\underline{\underline{\sigma}}^{tot} = \underline{\underline{\sigma}} + \varepsilon\underline{\underline{\Sigma}} \qquad \underline{\underline{\sigma}}^{tot} = \begin{pmatrix} \sigma_{11} + \Sigma_{11}\varepsilon & \sigma_{12} + \Sigma_{12}\varepsilon \\ \sigma_{21} + \Sigma_{21}\varepsilon & \sigma_{22} + \Sigma_{22}\varepsilon \end{pmatrix} \tag{5.35}$$

$$\varphi_p = \varphi + \phi\varepsilon \tag{5.36}$$

$$\underline{\underline{D}} = \underline{\underline{D}}_0 + \underline{\underline{d}}\varepsilon, \tag{5.37}$$

$$\dot{\gamma} = \dot{\gamma}_0 + \dot{\gamma}_p\varepsilon, \tag{5.38}$$

$$P_p = P_0 + \varepsilon p, \tag{5.39}$$

in which all the perturbation quantities are functions of the channel coordinate $y$, and $\varepsilon$ represents a single Fourier mode:

$$\varepsilon = \epsilon \exp\left[\mathrm{i}kx - \mathrm{i}\omega t\right]. \tag{5.40}$$

By introducing the streamfunction $\psi$ (defined in equation (2.41)), the continuity equation (4.23) is automatically satisfied. Discarding terms of order $\epsilon^2$, the remaining governing equations become:

$$\begin{aligned} Re(-\mathrm{i}\omega \mathrm{D}\psi - \mathrm{i}k\psi \mathrm{D}U + \mathrm{i}kU\mathrm{D}\psi) &= -\mathrm{i}kp + \mathrm{i}k\Sigma_{11} + \mathrm{D}\Sigma_{12} && (5.41)\\ Re(-k\omega\psi + k^2U\psi) &= -\mathrm{D}\,p + \mathrm{i}k\Sigma_{12} + \mathrm{D}\Sigma_{22} && (5.42) \end{aligned}$$

$$\begin{aligned} \phi = {} & \frac{\Gamma(1-\varphi)(1+\theta\,\dot{\gamma}_0)\left[\mathrm{i}k\sigma_{11}\mathrm{D}\psi + \sigma_{12}(\mathrm{D}^2+k^2)\psi + \Sigma_{12}\mathrm{D}U\right] + \mathrm{i}k\psi\mathrm{D}\varphi}{\left[-\mathrm{i}\omega + \mathrm{i}kU + \Lambda^{-1} + \Gamma\sigma_{12}\mathrm{D}U(1+\theta\,\dot{\gamma}_0)\right]}\\ & + \frac{\Gamma\sigma_{12}\mathrm{D}U(1-\varphi)\theta\dot{\gamma}_p}{\left[-\mathrm{i}\omega + \mathrm{i}kU + \Lambda^{-1} + \Gamma\sigma_{12}\mathrm{D}U(1+\theta\,\dot{\gamma}_0)\right]} \qquad (5.43) \end{aligned}$$

$$\begin{aligned} \Sigma_{22}(-\mathrm{i}\omega W\eta + \mathrm{i}kUW\eta + 1) &= 2\eta(W\sigma_{12}k^2\psi - \mathrm{i}k\mathrm{D}\psi) && (5.44)\\ \Sigma_{12}(-\mathrm{i}\omega W\eta + \mathrm{i}kUW\eta + 1) &= \eta(\mathrm{D}^2+k^2)\psi - \xi\mathrm{D}U + \mathrm{i}k\psi W\eta\mathrm{D}\sigma_{12}\\ &+ W\eta(\sigma_{11}k^2\psi + \Sigma_{22}\mathrm{D}U) && (5.45)\\ \Sigma_{11}(-\mathrm{i}\omega W\eta + \mathrm{i}kUW\eta + 1) &= 2\eta\mathrm{i}k\mathrm{D}\psi - 2W\xi\sigma_{12}\mathrm{D}U + \mathrm{i}k\psi W\eta\mathrm{D}\sigma_{11}\\ &+ 2W\eta(\mathrm{i}k\sigma_{11}\mathrm{D}\psi + \sigma_{12}\mathrm{D}^2\psi + \Sigma_{12}\mathrm{D}U) && (5.46) \end{aligned}$$

in which $\xi$ and $\dot{\gamma}_p$ are :

$$\xi = \frac{\phi}{\varphi^2} \qquad \dot{\gamma}_p = -\left(\mathrm{D}^2\psi + k^2\psi\right) \qquad (5.47)$$

and the base state quantities $\eta$ and $\sigma_{ij}$ are:

$$\eta = \varphi^{-1} = \frac{1+\Gamma\Lambda(1+\theta\,\dot{\gamma})\sigma_{12}\mathrm{D}U}{\Phi+\Gamma\Lambda(1+\theta\,\dot{\gamma})\sigma_{12}\mathrm{D}U} \qquad \underline{\underline{\sigma}} = \begin{pmatrix} 2W\mathcal{P}^2y^2 & -\mathcal{P}y \\ -\mathcal{P}y & 0 \end{pmatrix}. \qquad (5.48)$$

### 5.3.4 Boundary conditions

The coupled system of equations (5.41)–(5.47) can be combined and the resulting equation is a fourth-order ODE in $\psi$ dependent on $y$. The boundary conditions are conditions of no flow on the boundaries (see equation (2.51)).

This system is governed by seven dimensionless parameters: the Reynolds $Re$ and Weissenberg $W$ numbers, the wavenumber $k$, the thixotropic ratio $\Phi$, the shear-banding parameter $\theta$ and the reformation/destruction parameters $\Lambda$ and $\Gamma$. For fixed values of the parameters mentioned above, we look for the frequency or *eigenvalue* of the system, $\omega$, more specifically, its imaginary part or *growth rate*, $\Im(\omega)$ to deduce whether a flow is stable or not: for $\Im(\omega) > 0$, the flow is said to be unstable as the perturbations grow with time. The opposite is seen when $\Im(\omega) < 0$.

By now, we limit ourselves to only study two-dimensional perturbations as a function of our dimensionless parameters defined in equations (5.20)–(5.21). Potential future work might include carrying out stability analysis of three-dimensional perturbations using a model that allows to calculate a non-zero value of $N_2$.

#### 5.3.4.1 Continuity in the fluidity profile

When the shear-banding parameter $\theta$ had a non-zero value, that does not necessarily mean we will observe shear bands (or a jump in the viscosity). Instead, at some parameter values, we will see a continuous fluidity profile, as we previously analysed in sections 5.3.2.2 and 5.3.2.3. For these cases, the numerical method is simple and is the same we have used in the previous chapters: we solve the ODE using the shooting method of Ho & Denn [81] (described in section 2.9), which consists of integrating the governing equations from the centreline to the channel wall, until we find the correct eigenvalue $\Im(\omega)$ that satisfies the boundary conditions at the wall $y = \pm 1$ and the ones in the centreline.

The boundary conditions at $y = 0$ (considering appropriate symmetry) will depend on the kind of mode that is perturbing the flow; a) varicose modes, for which $\psi$ is an odd function of $y$ (equation (2.52))and b) sinuous modes, for which $\psi$ is an even function of $y$ (equation(2.53)). We use as initial estimations the results obtained in chapter 4 to make parameter continuation in $\theta$, until we observe a jump in fluidity, for which we use the method described below.

#### 5.3.4.2 Shear-band flow

The numerical method drastically changes when there is a discontinuity in the fluidity profiles, which leads to the formation of shear bands, whose interface in the base state is located at $y = \kappa$. As we have previously explained, the location of the interface along the channel depends on our flow parameters $\kappa = \kappa\left(\Gamma, \Lambda, \Phi, \theta\right)$, and its numerical value is found when we satisfy the following equation:

$$R(\kappa) = 0, \tag{5.49}$$

where $R$, see equation (5.27), is an expression that depends on the coefficients of the cubic equation for the fluidity (5.25). When a perturbation is imposed to the base state flow, there will be an infinitesimal displacement $\zeta$ of a fluid particle located in the interface, which leads to a kinematic boundary condition, in which the interface is defined by $y = \overline{\eta} + \zeta\varepsilon$, where $\overline{\eta}$ is a Lagrangian coordinate that satisfies:

$$\frac{D\,\overline{\eta}}{Dt} = \frac{\partial \overline{\eta}}{\partial t} + \underline{u} \cdot \underline{\nabla}\,\overline{\eta} = 0. \tag{5.50}$$

The physical meaning of equation (5.50) is that there is no mass transport through the interface, and therefore, fluid particles on the interface always remain part of the interface. Moreover, equation (5.50) is a common boundary condition used when there is an interface separating two different fluids, but it has also been applied to shear-banded flows [154, 177]. For our linear stability analysis problem, if our interface initially located at $\overline{\eta} = \kappa$ is displaced from $y = \kappa$ to $y = \overline{\eta} + \zeta\varepsilon$, and if $\zeta$ is small, the kinematic boundary condition (after correcting to linear order terms) becomes:

$$-\,\mathrm{i}k\psi - (-\mathrm{i}\,\omega + \mathrm{i}kU)\zeta = 0. \tag{5.51}$$

Furthermore, we require continuity across the interface of the velocity components $U + \underline{u}$ and of the traction (force balance at the interface), $(\underline{\underline{\sigma}} + \varepsilon\underline{\underline{\Sigma}}) \cdot \underline{n}$ (where $\underline{n}$ is the normal to the interface); this requires:

$$[\psi] = 0 \qquad [\mathrm{D}\psi + \zeta\,\mathrm{D}U] = 0 \tag{5.52}$$

$$[\Sigma_{12}] = 0 \qquad [\mathrm{D}\Sigma_{12} + \mathrm{i}k(\Sigma_{11} - \Sigma_{22})] = 0, \tag{5.53}$$

where we use $[x]$ to denote the jump in quantity $x$ across the interface $y = \kappa$. In order to solve our stability problem, we integrate the governing equations (5.41)–(5.47) using the shooting method (described in section 2.9) from the centreline (with boundary conditions for either varicose (2.52) or sinuous modes (2.53)) to the interface, and from the channel wall (with non-slip boundary conditions (2.51)) to the interface. The four jump conditions (5.52)–(5.53) at the interface $y = \kappa$ then become a matrix equation of the form:

$$M\Psi = 0, \tag{5.54}$$

where $\Psi$ is the vector of coefficients of each of the four linearly independent basic functions. Thus, the true solution of the system is found when the determinant of $M(\omega)$ is zero. A Newton-Raphson technique is used to find a zero of the determinant as a function of $\omega$, as in the case without interface.

## 5.4 Results

### 5.4.1 Shear-banding parameter variable

In chapter 4, we studied the isolated and combined effect of the BMP model parameters on the flow instability, and we identified under which conditions it is likely to observe highly unstable flows. Here we will carry out similar calculations and explain the results, but we will begin by varying the new dimensionless number that appears in this chapter: the shear-banding parameter.

In order to illustrate the effects of $\theta$, we simply choose and fix values of the destruction parameter, thixoviscous number, wavenumber, Reynolds and Weissenberg numbers and thixotropic ratio. For the last three cases, we will use a fixed value for almost all the calculations along the paper. For the Reynolds number, we set $Re = 0$ because we are interested in studying elastic instabilities rather than inertial ones. For the Weissenberg number, we will be using $W = 2$, as we know that an increase in $W$ was destabilising for the modes seen in section 5.4.3 (we will show that this is also the case for TVEP fluids that exhibit shear-banding). And lastly, although it is not numerically possible for us to explore the case of a fluid with a true yield stress ($\Phi = 0$), unstable flows are seen when there is a decrease in $\Phi$, so we will fix $\Phi = 0.001$, as this is one of the values that we previously reported where strong instabilities happen. In the subsections below we will show and analyse the results obtained.

#### 5.4.1.1 Critical shear-banding parameter value

In this section, we make parameter continuation in $\theta$, and choose as our initial values base states that are found to be unstable in the absence of shear-banding ($\theta = 0$, see section 4.4.5.3). We select two different values of the destruction parameter: $\Gamma = 0.003$ and $\Gamma = 0.005$. We set $W = 2$, $\Lambda = 1$, $\Phi = 0.001$ and $k = 0.1$. The results for sinuous perturbations are shown in figure 5.8.

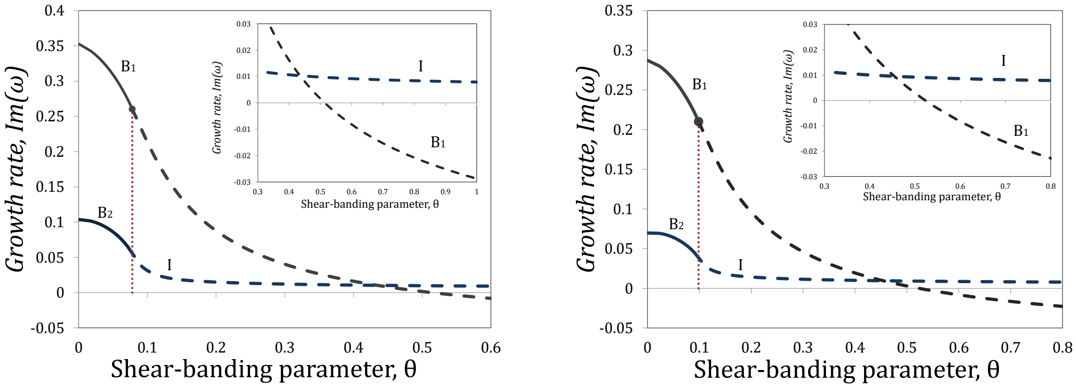

(a) $\Gamma\Lambda = 0.003$ (b) $\Gamma\Lambda = 0.005$

Figure 5.8: Growth rate against shear-banding parameter $\theta$ for sinuous modes, with $W = 2$, $\Lambda = 1$, $\Phi = 0.001$ and $k = 0.1$ fixed. Inertia is neglected ($Re = 0$). Figure (a): $\Gamma = 0.003$; (b): $\Gamma = 0.005$. For both pictures: the solid lines represent base-states without bands; dashed lines indicate that there are bands of fluids with a jump in the fluidity profile; the dotted line shows the location of the critical value of $\theta$.

We can see for both cases that at low values of $\theta$, there are two modes, $B_1$ and $B_2$, which we call *bulk* modes (this definition is explained in section 5.4.1.2). It can be seen that the mode $B_1$ (which is the kind of mode we studied in chapter 4) is always more unstable than the mode $B_2$ (see section 4.4.2). We then increase the values of the shear-banding parameter, and we observe that there is a decrease in the growth rate for both cases. By increasing $\theta$, the slope of the fluidity profiles in the channel is increasing rapidly (as in sections 5.3.2.2 and 5.3.2.3), which means that the fluid is beginning to separate into two bands. Continuity in the fluidity profiles is seen for all the points that are plotted with the solid line. The *jump* in the viscosity (characteristic in shear-banded flows) is first seen at a critical value of $\theta_c \approx 0.078$ for $\Gamma = 0.003$ and $\theta_c \approx 0.0985$ for $\Gamma = 0.005$. These points are indicated in their respective plots with black circles. After these critical values, we observe pure shear-banding fluids (all the points that are in the dashed lines), which become less and less unstable as we increase $\theta$, indicating that a reduction in the value of the stress plateau and its binodals $\dot{\gamma}_1$ and $\dot{\gamma}_2$ reduces the growth rate of instability. The mode $B_1$ in both cases eventually reach stability for high values of the shear-banding parameter, and this happens approximately when $\theta \approx 0.515$ for $\Gamma = 0.003$ and $\theta \approx 0.522$ for $\Gamma = 0.005$.

More interestingly, above the critical shear-banding parameter value, the mode $B_2$ becomes an *interfacial* mode (the reason for this name is explained in section 5.4.1.2). This mode (which is shown in the figures as "I") appears when there is an interface that separates the bands with different shear rates, and this is seen when there is a jump in the fluidity. Although the mode I also becomes less unstable as we increase $\theta$, the decay of the growth rate of this mode is extremely slow compared to the other mode $B_1$, and above a given value of $\theta$, the interfacial mode now will be more unstable than the bulk one (see small figures in 5.8).

We have determined that these interfacial modes will be dominant when the binodal $\dot{\gamma}_1$ (i.e. the low dimensionless shear rate value that corresponds to one of the bands formed when the system reaches the stress plateau $\sigma_p$, see section 5.3.2.2), obeys the condition established in (5.33):

$$\dot{\gamma}_1^2(1 + \theta\dot{\gamma}_1) \ll \frac{\Phi}{\Gamma\,\Lambda}. \tag{5.55}$$

Physically, this means that the shear-thinning behaviour (region II in the flow curve, see figure 5.1) will vanish, and therefore, the fluidity of the low band would be approximately equal to the value of the thixotropic ratio $\Phi$ (see figure 5.5d). The condition (5.55) is satisfied at high values of the shear-banding parameter $\theta$, which will lead to dominant interfacial instabilities rather than bulk ones, where the shear-thinning characteristics are key components, as shown in our previous works. The bulk modes, as we have seen, dominate over the interfacial ones at values of $\theta$ slightly above the critical shear-banding parameter value $\theta_c$.

#### 5.4.1.2 Dispersion relations: bulk and interfacial modes

The generalised BMP model is able to predict two kinds of modes: bulk and interfacial modes. Two bulk modes were found in the non-shear-banding region, $B_1$ and $B_2$, $B_1$ being the more unstable. In addition, $B_1$ is found to still be present in the shear-banding region. On the other hand, the bulk mode $B_2$ becomes an interfacial mode "I" at values of $\theta$ above the critical shear-banding parameter value $\theta_c$ (when there appears a jump in the fluidity). In section 1.8.6, we briefly reviewed a recently published paper by Renardy *et al.* [154], who studied stability analysis of two-dimensional plane Couette flow of viscoelastic fluids with thixotropic yield stress behaviour and shear-banding and they found similar results to ours: *bulk* instabilities in the yielded phase, and for some given values of their model parameters, they also observed unstable *interfacial* instabilities. The main difference with respect to our case is that the interfacial modes they reported are driven by a jump in the normal stress difference across the interface.

A key contributions of their paper is that they establish a criterion that allows us to distinguish between *bulk* and *interfacial* modes: the *interfacial* modes are neutrally stable as $k \to 0$. In this way, we compare the interfacial and bulk modes obtained in figure 5.8 by taking one point of each mode that is within the shear-banding region (dashed lines), and we vary the wavenumber $k$ to study their behaviour. Results can be seen in figure 5.9.

We set a constant low value of shear-banding parameter $\theta = 0.1180$, which ensures that bands of fluid are formed in the base state, and therefore, two modes of instability are present, $B_1$ and I, according to what we saw in figure 5.8. Parameter continuation for the cases $\Gamma\Lambda = 0.003$ and $\Gamma\Lambda = 0.005$ is made for the wavenumber $k$. For both cases, both modes tend to be more unstable for short waves, reaching an asymptotic value for $k > 1.0$. However, there are remarkable differences between the two modes: one of them, the bulk mode (dotted lines) is always a lot more unstable

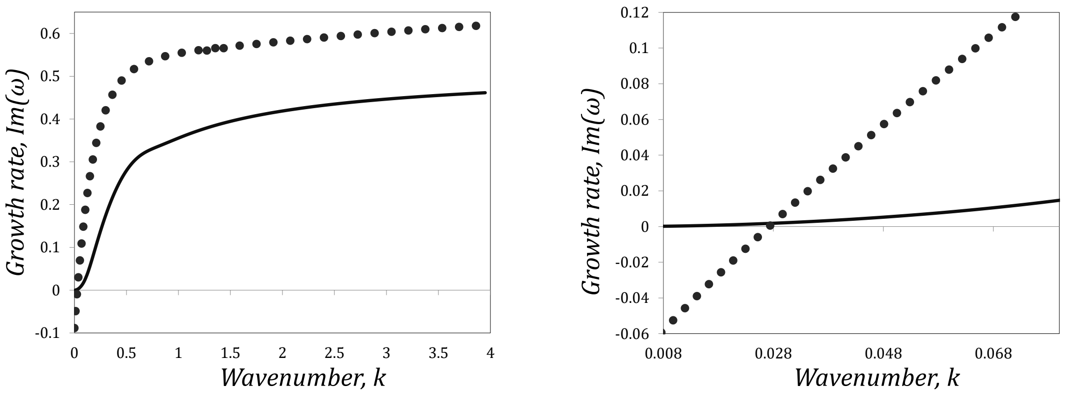

(a) $\Gamma\Lambda = 0.003$ (b) Limit $k \to 0$ for (a)

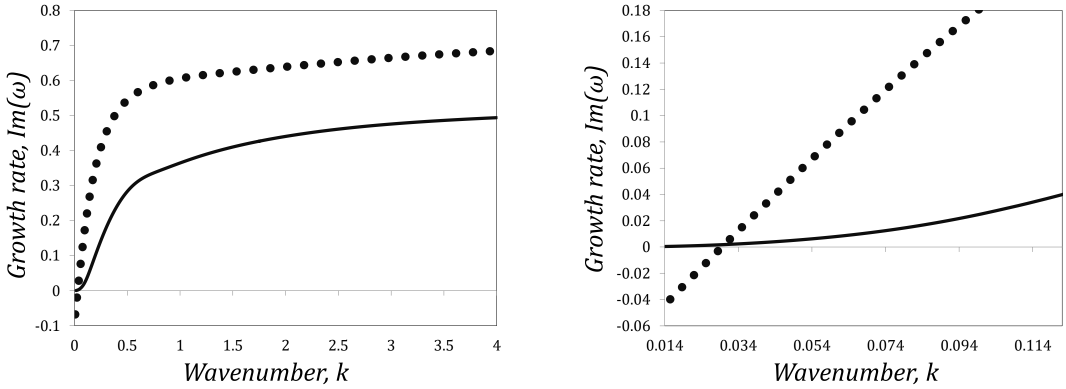

(c) $\Gamma\Lambda = 0.005$ (d) Limit $k \to 0$ for (c)

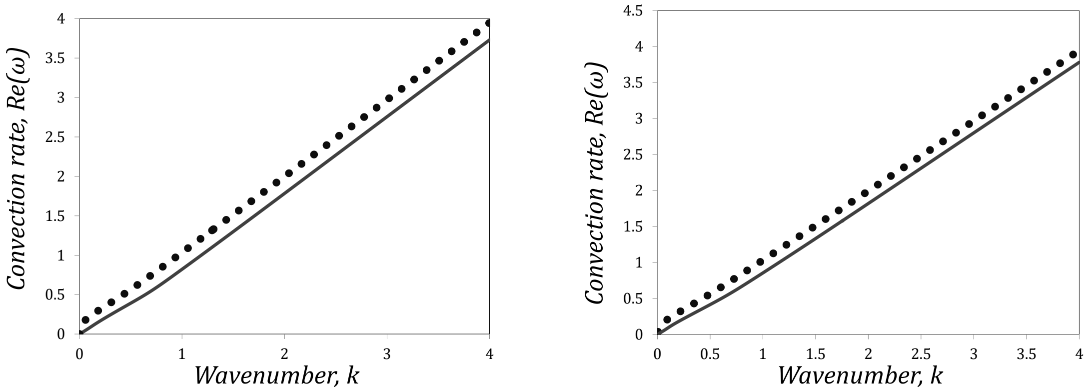

(e) $\Re(\omega)$ vs $k$ for $\Gamma\Lambda = 0.003$ (f) $\Re(\omega)$ vs $k$ for $\Gamma\Lambda = 0.005$

Figure 5.9: Dispersion relations $\Im(\omega)$ vs $k$ for bulk (dotted lines) and interfacial (solid lines) modes, with $\theta = 0.1180$, $W = 2$, $\Lambda = 1$ and $\Phi = 0.001$ fixed. The plots are for sinuous modes. Figure (a), (b) and (e) show the case for $\Gamma = 0.003$, while (c), (d) and (f) are for $\Gamma = 0.005$.

than the interfacial one (solid lines), but more importantly, they behave differently for the long wave case $k \to 0$, see figures 5.9b) and 5.9d). It can be clearly seen that the interfacial modes tend slowly to an asymptotic neutral value of $\Im(\omega) = 0$, meanwhile the bulk ones reach the stability zone, $\Im(\omega) < 0$.

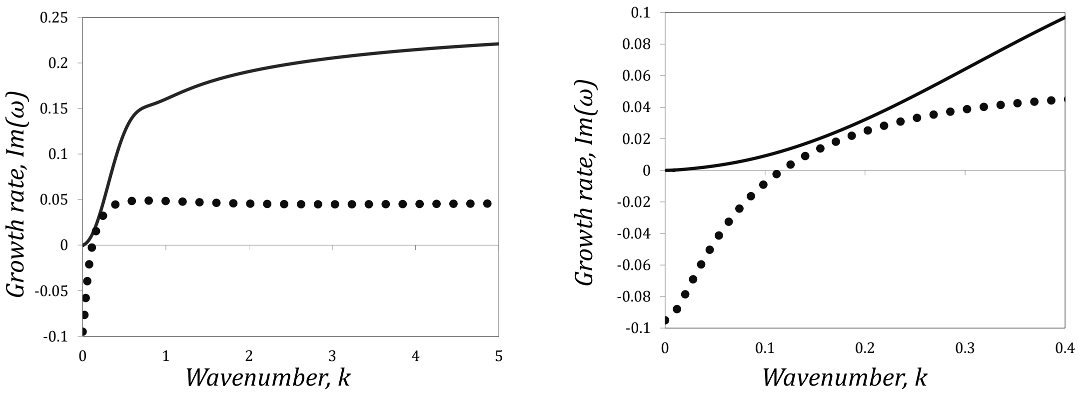

(a) $\Im(\omega)$ vs $k$ (b) $\Im(\omega)$ vs $k$: long waves $k \to 0$

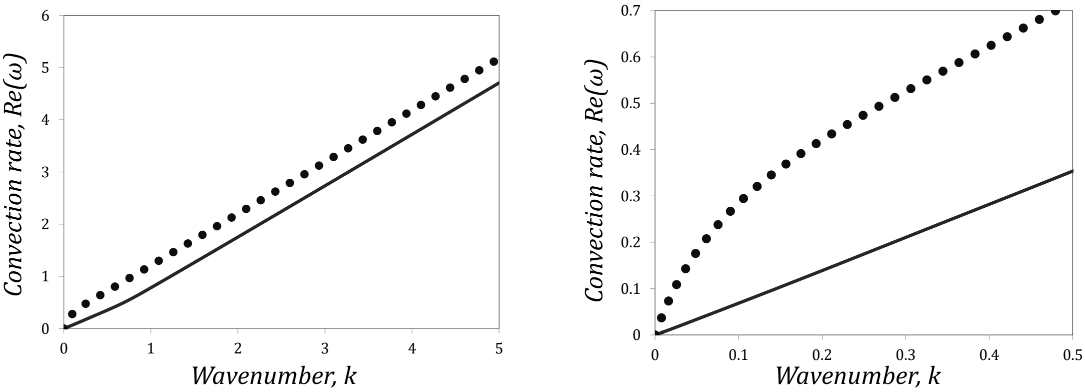

(c) $\Re(\omega)$ vs $k$ (d) $\Re(\omega)$ vs $k$: long waves $k \to 0$

Figure 5.10: Dispersion relations for both sinuous bulk and sinuous interfacial modes with $W = 2$, $\Lambda = 1$, $\Gamma = 0.003$, $\theta = 0.60$ and $\Phi = 0.001$ fixed. For all plots, the solid line depicts the interfacial modes. Figure (a): growth rate against wavenumber. Figure (c): convection rate against wavenumber.

We also plot the convection rate $\Re(\omega)$ against the wavenumber for both modes, see figures 5.9e) and 5.9f). For short waves, notice that the curves adopt a straight line that follows the relation $\Re(\omega) \sim kU(\overline{y})$, which means that the perturbations are localised at a cross-channel position $\overline{y}$ and are convecting with the flow at velocity $U(\overline{y})$ (see [178]). For the interfacial modes (with $k > 2$), we obtain $\Re(\omega) \sim 0.9742\,k = U(0.8976)\,k$ for the case $\Gamma\Lambda = 0.003$, where $\overline{y} = 0.8976 \approx \kappa$ is extremely close to the value of the interface location. Similarly, for $\Gamma\Lambda = 0.005$, we obtain $\Re(\omega) \sim 0.9816\,k = U(0.867)\,k$, with $\overline{y} = 0.867 \approx \kappa$.

On the other hand, the perturbation of the bulk modes seem to be located very close to the interface location but on the yielded region ($y > \kappa$), as we obtain the following relations that approximate well to our results: $\Re(\omega) \sim 0.9756\,k = U(0.8978)\,k$ for $\Gamma\Lambda = 0.003$, and $\Re(\omega) \sim 0.9770\,k = U(0.8693)\,k$ for $\Gamma\Lambda = 0.005$.

We also obtain the dispersion relations for a higher value of the shear-banding parameter $\theta = 0.60$, where the interfacial modes are dominant over the bulk ones, whose results are shown below in figure 5.10a). It can be clearly seen that now the interfacial modes (solid lines) are dominant for all values of the wavenumber.

The convection rate against wavenumber plot is shown in 5.10c), and we notice a behaviour similar to the one from figures 5.9e) and 5.9f): for very short waves, we can fit the results into a linear equation. For the interfacial modes (solid line), we get $\Re(\omega) \sim 0.9863\,k = U(0.889)\,k$, where the cross-channel position $\overline{y}$ is almost equal to the value of the interface location $\kappa = 0.8887$.

Finally, we show the dispersion relation of points that are part of the less unstable bulk mode $\mathrm{B}_2$, which is present in the non-shear-banding zone (see figure 5.8). Results are shown in figure 5.11. Taking a fixed value of $\theta = 0.04$, we illustrate the dispersion relation for two cases: one with $\Gamma = 0.003$ (solid line) and another one with $\Gamma = 0.005$ (dashed line). The main conclusion we can obtain from these results is that the growth rate is negative in the long wave case $k \to 0$, meaning that we have a bulk mode. Above the critical shear-banding parameter value, this bulk mode becomes an interfacial mode, as we previously described in figures 5.8 and 5.9. From now on, when we talk about bulk modes, we will refer to those that are more unstable ($\mathrm{B}_1$).

#### 5.4.1.3 Interfacial instabilities with continuity in the first normal stress difference predicted by the Oldroyd-B model

In the previous section, we discovered two unstable modes: bulk and interfacial instabilities. The first ones have been recently studied by [154] and by ourselves in previous works (without shear-banding), and the second ones have been also observed

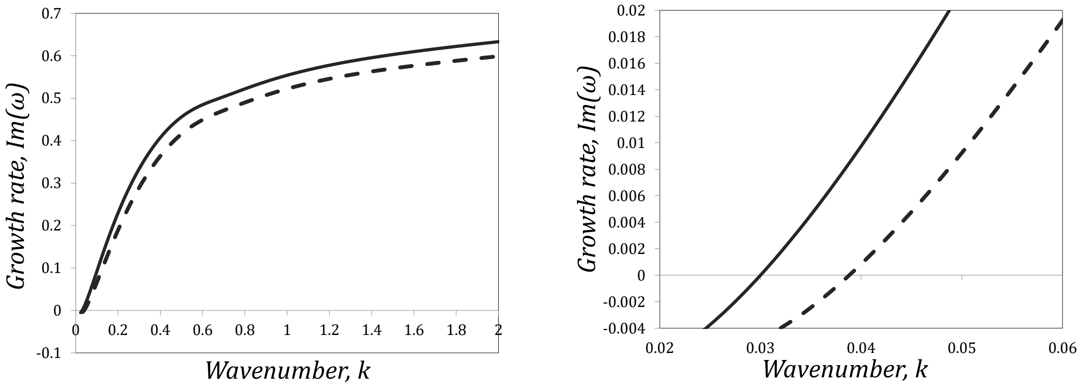

(a) $\Im(\omega)$ vs $k$

(b) $k \to 0$

Figure 5.11: Dispersion relations of the less unstable sinuous bulk mode ($B_2$ in figure 5.8). The parameter model values are $W = 2$, $\Lambda = 1$, $\theta = 0.04$ and $\Phi = 0.001$. The solid line has a value of $\Gamma = 0.003$ and the dashed line is for $\Gamma = 0.005$. Figure (b) shows the behaviour at very long waves.

by multiple research groups [44, 61, 65, 177], in both Poiseuille and Couette shear-banded flows. The mechanism for these interfacial instabilities has been assumed to depend critically on a discontinuity in $N_1$ across the interface, as in the truly interfacial elastic instabilities first discovered in the 90's [36, 80]. But for our fluid, $N_1$ is continuous across the shear-band interface.

The difference, as stated above, is that the instability for the interfacial modes observed by them seems to arise when elasticity varies discontinuously, which is not the case for the BMP model with shear-banding, see figure 5.4c). For these reasons, we decide to explore if the interfacial instabilities that we are observing in section 5.4.1.1 are also predicted by other models that are able to satisfy the conditions of continuity in $N_1$, and of course, a jump in viscosity at the interface.

We use a simple model that can help to achieve this, which is the Oldroyd-B model. In a previous work by Wilson & Rallison [181], this model was used to study the instability of elastic liquids where the concentration of the polymer $C$ (which is proportional to its viscosity) changes across the channel of half-width $L$. We create an artificial scenario that emulates shear-banding phenomenon: a two-layer flow, where two fluids of different viscosities are separated by an interface located at some point $y = \kappa$ in the channel. The fluid near the centreline has a much higher viscosity than the fluid near the channel walls and although both fluids have different Weissenberg number values, there is continuity of the first normal stress difference across the interface.

The full results can be found in the appendix B. Here we briefly mention the main findings: an interfacial instability similar to the one predicted by the generalised BMP model (section 5.4.1.2) is also predicted by the Oldroyd-B model given the proper flow conditions, i.e. a jump in the fluid viscosity at the interface, along with continuity in the first normal stress difference. In addition, we found that the fluid elasticity is a key component of the instability: stability is seen at low values of Weissenberg number, while the opposite is observed if $W$ is increased.

### 5.4.2 Sinuous and varicose modes

In the previous sections, we have been showing only sinuous perturbations. The reason for this is that in section 4.4.3, we found that sinuous perturbations are slightly more unstable than varicose ones for long and intermediate waves, although both reach the same asymptotic value for short waves. Here we simply show that this still seems to hold when the shear-banding phenomenon is present, for both bulk and interfacial modes, see figure 5.12.

For the case of bulk modes, figure 5.12a), the dispersion relation for sinuous perturbations is slightly above the varicose ones, but stability is observed for both perturbations for long waves. For interfacial modes, figure 5.12b) is a bit more complicated to appreciate it, as it seems that the sinuous curve is superimposed over the varicose one, but if we zoom in, we can see that indeed the sinuous perturbations tend to be more unstable.

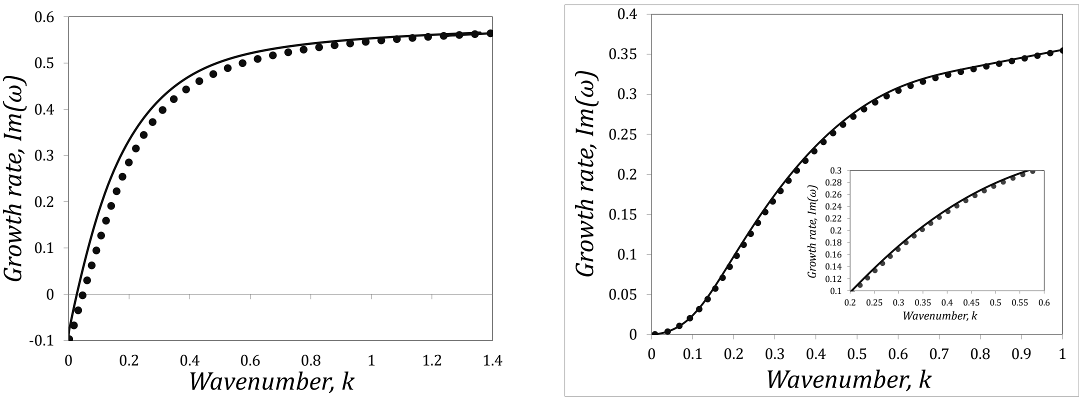

(a) Bulk modes (b) Interfacial modes

Figure 5.12: Growth rate $\Im(\omega)$ against wavenumber $k$ for sinuous (solid lines) and varicose (dotted lines) perturbations, with $W = 2$, $\Phi = 0.001$, $\Lambda = 1$, $\Gamma = 0.003$ and $\theta = 0.118$ fixed. Figure (a): bulk modes. Figure (b): interfacial modes.

### 5.4.3 Variable Weissenberg number

In sections 5.4.3 and 4.4.5, we observed that the flow becomes unstable if the elastic relaxation time scale $\lambda_{ve}$ (and thus, the Weissenberg number) is large, and it becomes even more unstable if the order of magnitude of $\lambda_{ve}$ is much higher compared to the structural relaxation time $\lambda$ and the plastic time scale $\lambda_{tp}$. In this section, we show some examples of this behaviour, which still holds for both bulk modes with sinuous and varicose perturbations, as it can be seen in figure 5.13.

As we concluded in the previous section, sinuous perturbations will be more unstable than varicose ones for either bulk and interfacial modes, and this becomes more evident when the Weissenberg number $W$ is increased, as shown in figures 5.13a) and 5.13b).

At low values of shear-banding parameter, $\theta = 0.118$, and with $k = 0.1$, $\Lambda = 1$, $\Gamma = 0.003$ and $\Phi = 0.001$ fixed, we compare the behaviour of the bulk and interfacial modes as the elastic relaxation time scale (proportional to $W$) grows, see figures 5.13c) and 5.13d). Notice that for sinuous perturbations with values of $W > 0.7$, the growth rate for the bulk modes is much higher compared to the one for the interfacial instabilities. In addition, the thixoelastic number $W_{te} = W/\Lambda$ also

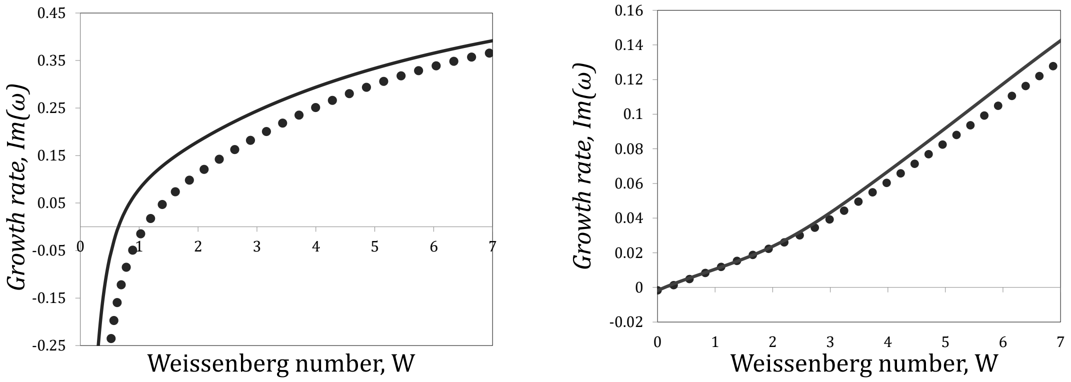

(a) Bulk modes

(b) Interfacial modes

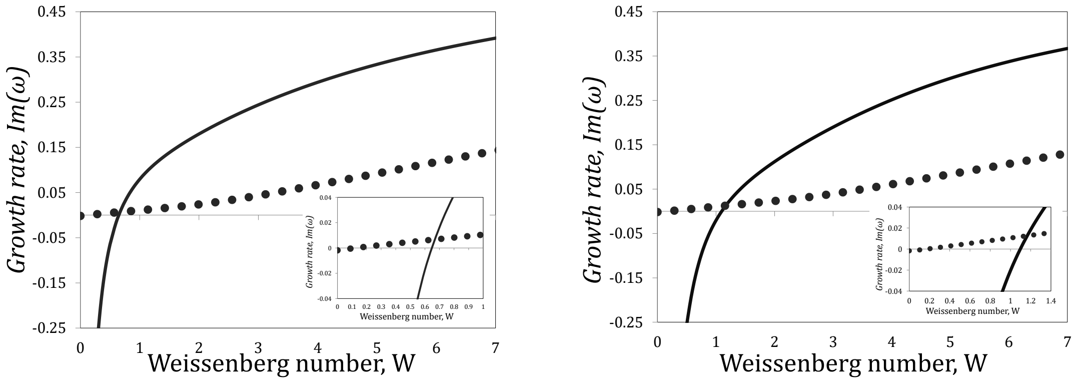

(c) Sinuous perturbations

(d) Varicose perturbations

Figure 5.13: Growth rate $\Im(\omega)$ against Weissenberg number with $\theta = 0.1180$, $k = 0.1$, $\Gamma = 0.003$, $\Lambda = 1$ and $\Phi = 0.001$ fixed. Figure (a): bulk modes. Figure (b): interfacial modes. For figures (a) and (b): solid line is for sinuous perturbations and dotted ones for varicose perturbations. Figure (c): sinuous perturbations. Figure (d): varicose perturbations. For figures (c) and (d): solid lines are bulk modes and dotted lines are interfacial ones.

becomes larger, meaning that the elastic effects overcome the thixotropic effects, leading to instability in both bulk and interfacial modes.

However, for values of $W < 0.7$, the bulk modes reach the stability zone, and the growth rate for interfacial modes is positive with an extremely small value $\Im(\omega) \approx 0.005$, which might indicate that for our very specific set of parameters chosen, the flow is initially slightly unstable due to an interfacial instability at values of $W < 0.7$, but an increase in the Weissenberg number (and thus, of $\lambda_{ve}$) will completely lead to a bulk instability. In order to illustrate this, we calculate the *critical Weissenberg number* $W_c$ defined as the dimensionless flow rate below which the flow is stable to perturbations of all wavenumbers (see [28, 178]). From our calculations, we got that the critical Weissenberg number for the sinuous interfacial mode is $W_c = 0.1105$ (with critical wavenumber $k_c = 1.312$), meanwhile, for the sinuous bulk modes, we obtain $W_c = 0.1562$ and $k_c = 0.837$, which indicates that indeed for our particular case of study ($\theta = 0.118$, $k = 0.1$, $\Lambda = 1$ and $\Phi = 0.001$), an interfacial instability will appear first. We get similar results for varicose perturbations: $W_c = 0.1217$ and $k_c = 1.75$ for interfacial modes, and $W_c = 0.252$ and $k_c = 1.74$ for bulk ones.

Although we have only reported just one case of study, we have found that these trends are robust to changes in the other dimensionless parameters.

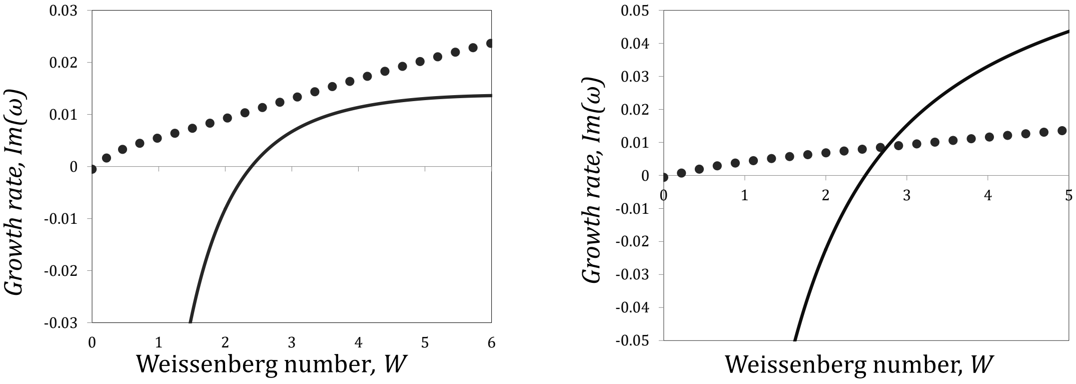

(a) Bulk modes

(b) Interfacial modes

Figure 5.14: Growth rate $\Im(\omega)$ against Weissenberg number for sinuous perturbations with $\theta = 0.60$, $\Phi = 0.001$, $k = 0.1$ and $\Lambda = 1$ fixed. The solid line represents the bulk modes, and the dotted one is for interfacial modes. Figure (a): $\Gamma = 0.003$ with $\kappa \approx 0.89$; figure (b): $\Gamma\Lambda = 0.02$ with $\kappa \approx 0.79$.

Moreover, it also seems that the interfacial modes might not only be caused by a jump in fluidity; elasticity is also a key factor here, as an increase in $W$ involves a rise in the growth rate, for either varicose or sinuous perturbations. This is confirmed by the limit $W \to 0$ of the two-layer flows (see appendix B): elasticity is crucial to interfacial instabilities in the absence of inertia.

Lastly, we also compare the behaviour of the interfacial and bulk modes as the Weissenberg number increases but now with a higher value of shear-banding parameter value $\theta = 0.60$. Results can be seen in figure 5.14, where two comparative cases are reported: one in which the interface location is relatively close to the wall ($\Gamma\Lambda = 0.003$ with $\kappa \approx 0.89$) and another one in which the interface is slightly further away from the channel wall ($\Gamma\Lambda = 0.02$ with $\kappa \approx 0.79$). In contrast with the conclusions obtained from figure 5.13, for the former case, the interfacial modes will be more unstable than the bulk ones for any value of $W$. Additionally, we can observe that the growth rate for the interfacial mode (dotted line) will be mostly positive (with the exception of the limit $W \approx 0$), meanwhile the bulk one is fully stable at $W < 1.5$.

On the other hand, if the interface is no longer so close to the wall, we can notice a similar behaviour to that of figure 5.13: the interfacial modes are weakly unstable but dominant over the bulk ones in the limit of very low Weissenberg number values, while bulk modes become much more unstable at $W > 2.8$. From these observations, we can deduce an important conclusion: the interface location determines whether a bulk or an interfacial mode is dominant.

### 5.4.4 Thixotropic timescales

We have studied flow instabilities and the effect of $\Phi$, $k$, $W$ and $\theta$ on them. In the following sections, we will discuss the effects of the parameters governing structural reformation ($\Lambda$) and destruction ($\Gamma$). We divide the subsections into two parts: 1) we first study the behaviour of the bulk modes, and 2) we focus on interfacial modes, making direct comparisons with respect to the conclusions obtained for the bulk modes.

#### 5.4.4.1 Thixoviscous number: bulk modes

In figure 5.15 we plot the growth rate against the thixoviscous number $\Lambda$ for different low values of shear-banding parameter $\theta$, with $W = 2$, $\Gamma = 0.002$, $\Phi = 0.001$ and $k = 0.1$ fixed. The case $\theta = 0$ is depicted in figure 5.15a), which corresponds to a case that we studied in our previous paper, where we concluded that the flow is linearly stable at both extremes of thixoviscous number: the limit $\Lambda \to 0$, which is the equivalent of a Maxwell fluid with high viscosity ($\eta \approx 1/\Phi$). On the other hand at $\Lambda \to \infty$, the fluid has an extremely slow structural recovery, and thixotropy dominates over viscoelastic effects (low thixoelastic numbers, $\Lambda \gg W$). However, when this condition is not met, the flow can be extremely unstable, as seen in figure 5.15a).

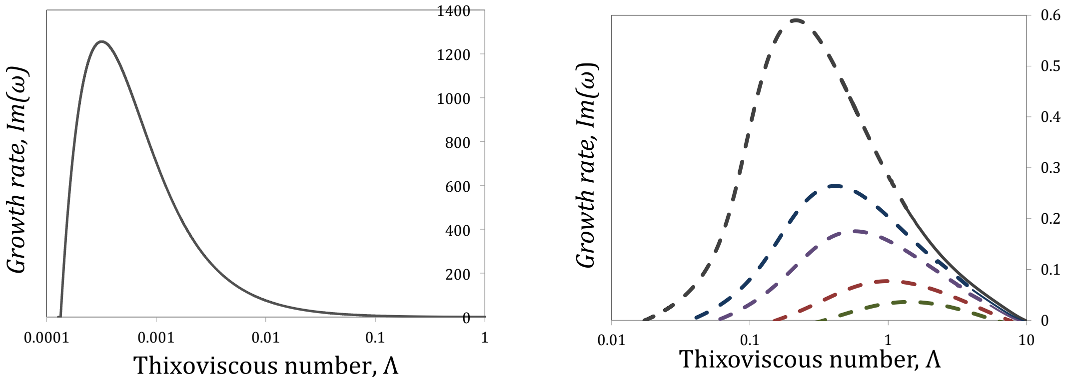

(a) $\theta = 0$ (b) $\theta \neq 0$

Figure 5.15: Growth rate plotted against the thixoviscous number $\Lambda$ for $W = 2$, $\Gamma = 0.002$, $\Phi = 0.001$ and $k = 0.1$. Figure (a): case $\theta = 0$; (b): from top to bottom, $\theta = 0.07, 0.1, 0.1240, 0.20$ and $0.30$. Dashed lines represent base-state shear-band flows.

Similar behaviour is observed for non-zero values of $\theta$, as shown in figure 5.15b): the limits $\Lambda \to 0$ and $\Lambda \to \infty$ are stable, which confirms that thixotropy effects also stabilise flows when shear-banding is present. It is not surprising that an increase in shear-banding parameter value (from top to bottom) leads to less unstable flows until full stability for bulk modes is reached.

Notice that some of the most unstable flows are seen when shear-bands are present (dashed lines), whose interface location is slightly away from the wall ($\kappa \approx 0.8 - 0.9$), meanwhile flows with continuity in the fluidity profile tend to be more stable (see high $\Lambda$ region). Additionally, the curves and their maximum are being displaced from left to right as $\theta$ increases. In order to explain this, we define a new dimensionless number, which is a ratio of two fluid time scales that compares the shear-banding effects over the thixotropic ones, which we will call $\varsigma$:

$$\varsigma = \frac{\theta}{\Lambda} = \frac{\vartheta}{\lambda}. \tag{5.56}$$

We now reframe the growth rate from figure 5.15b) against $\varsigma$, see figure 5.16. Notice that the instability is observed for intermediate values of $\varsigma$, and the most unstable flows have roughly the same value of $\varsigma \approx 0.22$. It is important to point out that this interval is only valid for this case study ($\Gamma = 0.002$, $W = 2$, $k = 0.1$ and $\Phi = 0.001$), and will change if the other parameters take different values, but the conclusions obtained here will remain for bulk modes.

From this plot, we can get additional conclusions: for instance, in order to overcome the instabilities caused by elasticity, highly thixotropic fluids are required to stabilise the flow, as it can be seen in the regions of low $\varsigma$ values (left side of the curve). On the other hand, we know that fluids with extremely quick structural reformation characteristics (low $\Lambda$) tend to be unstable, so in order to compensate for the lack of thixotropy, high shear-banding parameter values $\theta$ are needed to lead to stability of the bulk modes, or in other words, high $\varsigma$ values (right side of the curve). However, in the next subsection, we will see that this extreme involves unstable interfacial modes.

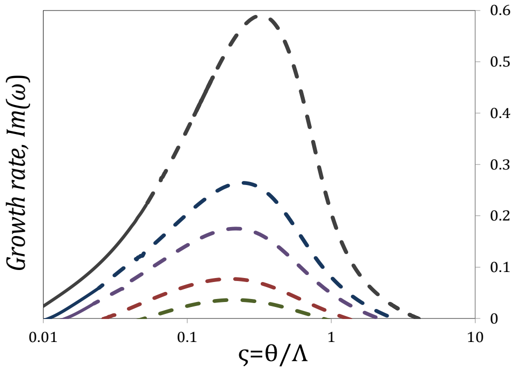

Figure 5.16: Growth rate $\Im(\omega)$ against $\varsigma$ for sinuous perturbations. The parameter values used are the same as in 5.15b).

### 5.4.4.2 Thixoviscous number: interfacial modes

On this subsection, we focus on the regime where the interfacial instabilities are dominant over the bulk ones; this is seen when high values of shear-banding parameter are present. We simply carry out a similar analysis that was carried out in section 5.4.4.1 to study the dependence of the growth rate on the thixoviscous number for interfacial modes. Results can be seen in figure 5.17.

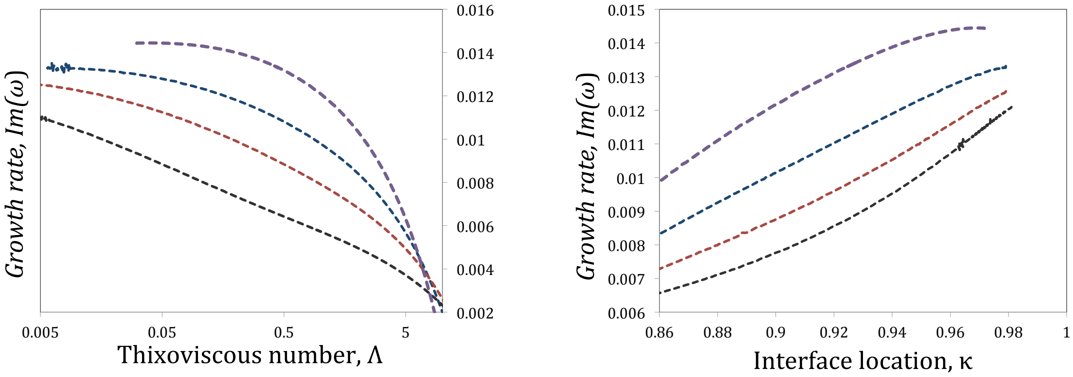

(a) $\Im(\omega)$ vs $\Lambda$ (b) $\Im(\omega)$ vs $\kappa$

Figure 5.17: Figure (a): growth rate plotted against thixoviscous number $\Lambda$ for interfacial modes with $W = 2$, $\Gamma = 0.002$, $\Phi = 0.001$ and $k = 0.1$ fixed. Figure (b): growth rate against interface location $\kappa$. From top to bottom: $\theta = 0.30, 0.50, 1$ and 5.

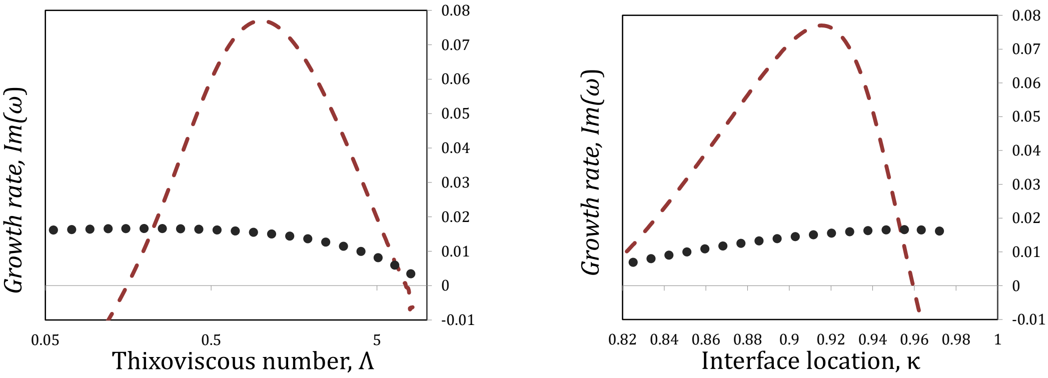

(a) $\Im(\omega)$ vs $\Lambda$ (b) $\Im(\omega)$ vs $\kappa$

Figure 5.18: Behaviour of the interfacial (dotted line) and bulk (dashed lines) modes as a function of the thixoviscous number and the interface location. Figure (a): growth rate plotted against $\Lambda$ for interfacial and bulk modes with $W = 2$, $\theta = 0.20$, $\Gamma = 0.002$, $\Phi = 0.001$ and $k = 0.1$ fixed. Figure (b): growth rate vs interface location $\kappa$.

In contrast with what we saw in figure 5.15, the behaviour of the modes is slightly different: although the modes get more stable as both $\theta$ and $\Lambda$ increase, notice how a decrease in the thixoviscous number leads to highly unstable flows, which means that quick structural recovery is also dangerous for interfacial modes. Thus, interfacial modes are more dangerous at high values of the material time-scale ratio $\varsigma$ defined in equation (5.56). In addition, as we saw in figure 5.7, high shear-banding parameter values and small values of $\Lambda$ lead to an interface location close to the channel wall, so we plot the growth rate against $\kappa$, see figure 5.17b), from which we can see that fluids whose interface location is very close to the wall $\kappa \approx 0.98$ are highly unstable. Unfortunately, we could not reach the limit $\Lambda \to 0$ as the no-slip condition at the channel wall is hard to satisfy as it involves extremely sharp velocity profiles in the base state. However, we can see that for the case $\theta = 0.30$ (curve at the top), the growth rate is slightly decreasing. We believe that the interfacial mode will become neutrally stable (or at least stable) when the interface location reaches the wall, $\kappa = 1$, as predicted by the Oldroyd-B model in appendix B.

Lastly, we simply compare the behaviour of the bulk and interfacial modes as a function of the thixoviscous number with fixed values $W = 2$, $\theta = 0.20$, $\Gamma = 0.002$, $\Phi = 0.001$ and $k = 0.1$, see figure 5.18. As concluded before, it can be clearly seen that although the interfacial modes are weakly unstable, they are dominant at very low values of thixoviscous number, which is the limit in which the interface location is very close to the wall (see figure 5.18b). The bulk modes, on the other hand, are dominant for intermediate values of thixoviscous number and can be highly unstable. Finally, both modes tend to be stable when the thixotropic effects dominate (large $\Lambda$).

#### 5.4.4.3 Thixoplastic number: bulk modes

Now we focus on studying the effect of the destruction parameter on the bulk instabilities for different values of the shear-banding parameter. However, we will plot our results against the timescale associated with the destruction process: the thixoplastic number, previously defined as $W_{tp} = \sqrt{\Gamma\Lambda(1-2\Phi)}$. As explained before, each value of the thixoplastic number involves a unique base state, given that the base-state quantities depend on the product $\Gamma\Lambda$.

We fix the values of $k = 0.1$, $W = 2$, $\Phi = 0.001$, and we choose two representative cases of weakly thixotropic fluids: $\Lambda = 0.1$ and $\Lambda = 0.2$. Results are shown in figure 5.19.

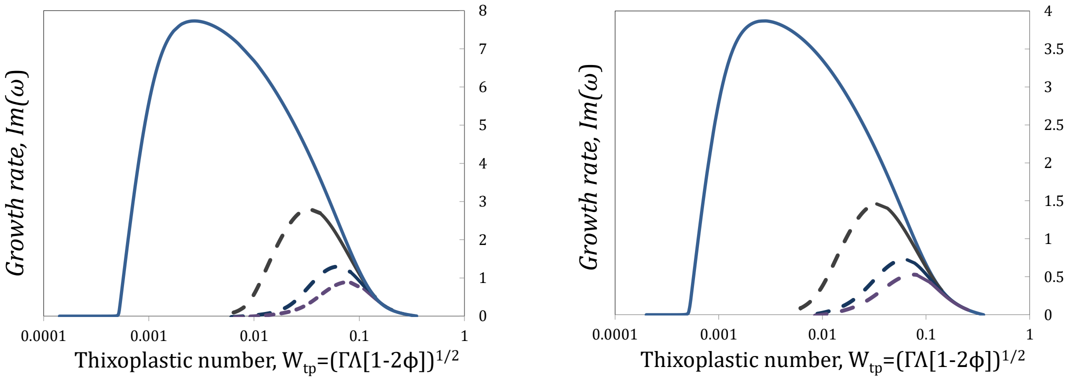

(a) Case $\Lambda = 0.1$ (b) Case $\Lambda = 0.2$

Figure 5.19: Growth rate plotted against thixoplastic number $W_{tp}$ for bulk modes with $W = 2$, $\Phi = 0.001$ and $k = 0.1$ fixed. Figure (a): $\Lambda = 0.1$; (b): $\Lambda = 0.2$. From top to bottom: $\theta = 0, 0.05, 0.1$ and $0.1240$. Solid lines represent base-states with continuity in the fluidity profiles, meanwhile dashed lines indicate a jump in the shear rate at the interface location.

The curves that are found at the top in figures 5.19a) and 5.19b) are the cases with $\theta = 0$ that have been previously studied in section 4.4.5.3. Similarly to figure 5.15a), the extremes $W_{tp} \to 0$ and $W_{tp} \to \infty$ are both stable; the first limit is the equivalent of a Maxwell fluid with low fluidity $\varphi = \Phi$, and the second limit involves high structural destruction and a growth of the yielded region near the walls. Additionally, as reported in [29], the most unstable base state for fixed $\Phi$, $\Lambda$, $W$, $k$ and $\theta = 0$ is found when the dimensionless critical stress $\tau_c = 1/W_{tp}$ is located near the channel wall (around $y \approx 0.98$).

For non-zero values of the shear-banding parameter, the curve behaviour does not change: it is not surprising that an increase in $\theta$ stabilises the flows, and the limits $W_{tp} \to 0$ and $W_{tp} \to \infty$ are stable as well. In addition, the most unstable base states for fixed $\theta \neq 0$ satisfy the condition that the critical stress $\sigma_c$ (whose value is slightly greater than the stress plateau $\sigma_p$) is still close to the wall. The difference with respect to the case $\theta = 0$ is that a rise in $\theta$ diminishes the shear rate and shear stress at $y = 1$, and thus, the critical stress is displaced away from the channel wall. For instance, the most unstable state with fixed $\Lambda = 0.2$ for $\theta = 0.05$ has a value of $\tau_c = 29.91$ and is located at $y = 0.942$; for $\theta = 0.10$, $\tau_c = 16.15$ at $y = 0.904$, and for $\theta = 0.1240$, $\tau_c = 13.32$ located at $y = 0.888$. We also notice that for the cases where $\theta \neq 0$, the most unstable base states are seen when the transition from continuity (solid lines) to a jump in the fluidity profiles (dashed lines) is present, or in other words, the slope of the curve $\varphi$ vs $y$ is extremely high (see section 5.3.2).

It is also evident that $\Lambda$ plays a key role in the bulk instability, as it can be seen that all the curves from figure 5.19a) are much more unstable than the ones in 5.19b). This behaviour will be explored later.

Lastly, we made a similar analysis to the one made in figure 5.16: we define a new dimensionless quantity, $\varpi$, which is a material parameter simply defined as the ratio of two timescales; the time scale representative of plasticity and that for shear-banding effects:

$$\varpi = \frac{W_{tp}}{\theta} = \frac{\lambda_{tp}}{\vartheta}. \tag{5.57}$$

We now simply plot the growth rate of figure 5.19 against $\varpi$. The results are shown in figure 5.20.

We can deduce that high thixoplastic numbers (i.e. when the yielded region grows along the channel) would lead to flow stability, so in order to compensate for weak

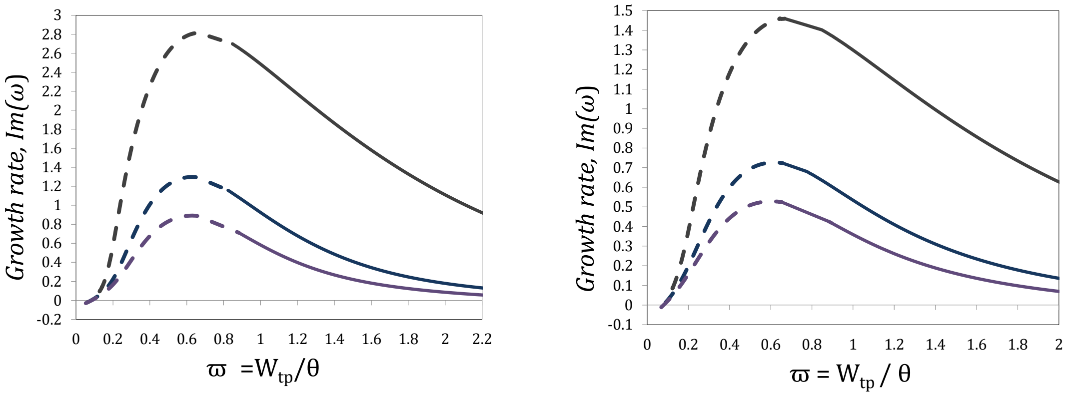

(a) Case $\Lambda = 0.1$

(b) Case $\Lambda = 0.2$

Figure 5.20: Growth rate plotted against $\varpi$ for bulk modes. The model parameter values used are the same that the ones used in figure 5.19.

shear-banding effects, which are usually unstable, high $\varpi$ values are required to stabilise the flow (right side of the plots).

For the other extreme of low thixoplastic numbers, a similar conclusion is obtained: in order to overcome elastic effects and plasticity, low $\varpi$ values are needed to stabilise bulk modes (we will see in the next subsection that this condition will lead to more unstable interfacial instabilities though). More interestingly, intermediate values tend to be highly unstable and the most unstable base-states for all the curves have the same value of $\varpi$: for both cases, $\Lambda = 0.1$ and $\Lambda = 0.2$, the most unstable flows are observed when $\varpi \approx 0.66$. The limit of this instability is the case $\theta = 0$, which we know beforehand is the most unstable case.

#### 5.4.4.4 Thixoplastic number: interfacial modes

Now we focus on studying the effect of variable destruction parameter at high values of the shear-banding parameter, which is the regime in which the interfacial modes are more dominant over the bulk ones. We carry out a similar analysis to that in section 5.4.4.2: we fix the Weissenberg and thixoviscous number, the thixotropic ratio and the wavenumber, and we choose a set of three values of shear-banding parameter $\theta = [0.5, 1, 5]$, and for each case, we vary $\Gamma$. We then plot the growth rate against the timescale characteristic of the destruction process, the thixoplastic number and against the interface location, see figure 5.21.

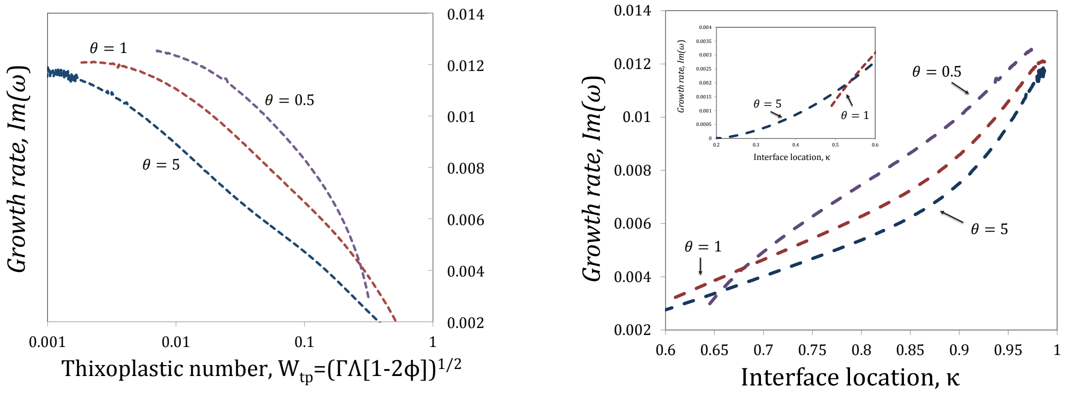

(a) $\Im(\omega)$ vs $W_{tp}$

(b) $\Im(\omega)$ vs $\kappa$

Figure 5.21: Figure (a): growth rate plotted against thixoplastic number $W_{tp}$; (b): growth rate against interface location. The parameter values $W = 2$, $k = 0.1$, $\Phi = 0.001$ and $\Lambda = 1$ are fixed. From top to bottom: $\theta = 0.5, 1$ and $5$.

Similarly to the conclusions obtained from figure 5.17, the most unstable base-state flows seem to be the ones whose interface location $\kappa$ is near the wall, and this is achieved when very low values of thixoplastic number (and therefore, low values of the material time scale ratio $\varpi$ defined in equation (5.57)) are present. However, it was not possible to get to the limit $\kappa \to 1$ due to the sharp velocity profiles. This is evident for the case $\theta = 5$ (bottom curve of figure 5.21a), where there are some fluctuations due to numerical errors.

As expected, the curves with higher $\theta$ value are the less unstable ones. Moreover, we can see that for the curve with the lowest value of shear-banding parameter $\theta = 0.5$ (top curve), the interfacial mode only exists if the interface location is between $0.64 < \kappa < 1$, and it becomes stable at $W_{tp} \leq 0.32$, which coincides with the transition (in the base state) to a continuous fluidity profile. For the other cases, the interfacial modes will still be present for high thixoplastic numbers; for $\theta = 1$, the mode is seen at $W_{tp} \leq 0.6324$ with interface location $0.45 < \kappa < 1$ and lastly, for $\theta = 5$, instability is observed for $W_{tp} \leq 2.41$ with interface location $0.1841 < \kappa < 1$ (see small plot in figure 5.21b)).

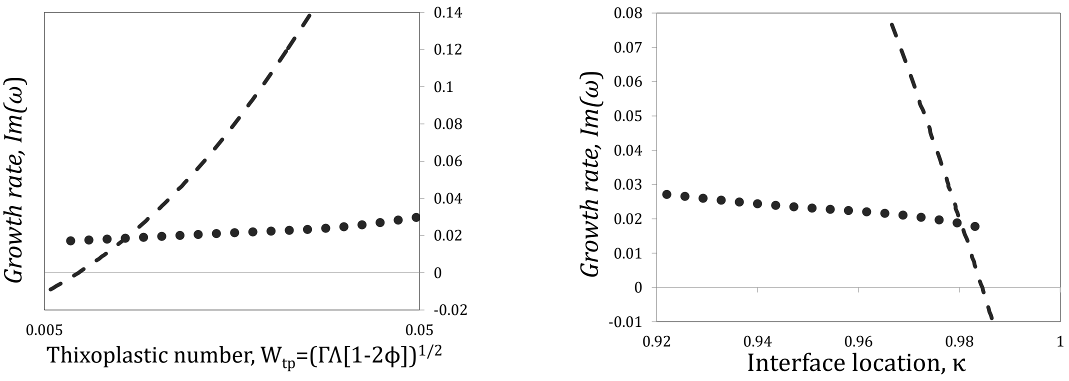

(a) $\Im(\omega)$ vs $W_{tp}$ (b) $\Im(\omega)$ vs $\kappa$

Figure 5.22: Behaviour of the interfacial (dotted line) and bulk (dashed lines) modes as a function of the thixoplastic number and the interface location. Figure (a): growth rate plotted against $W_{tp}$ for interfacial and bulk modes with $W = 2$, $\theta = 0.10$, $\Lambda = 1$, $\Phi = 0.001$ and $k = 0.1$ fixed. Figure (b): growth rate vs interface location $\kappa$.

Finally, as we did in section 5.4.4.2, we compare the behaviour of the bulk and interfacial modes as a function of the thixoplastic number with fixed values of $\theta = 0.10$, $k = 0.1$, $W = 2$, $\Lambda = 1$ and $\Phi = 0.001$. Results are shown in figure 5.22, where we can see that in the limit $W_{tp} \to 0$, the bulk modes (dashed lines) are fully stable, while the interfacial modes are weakly unstable.

From the results obtained here and in section 5.4.4.2, we can conclude that the interfacial modes become more unstable and dominant over the bulk modes if the interface location $\kappa$ is very close to the wall, and small values of destruction parameter and thixoviscous number lead to instability, which is the equivalent of small values of the product $\Gamma\Lambda$: either small destruction and/or poor thixotropy are dangerous, which also satisfies the condition obtained in equation (5.55).

#### 5.4.4.5 Thixoplastic number at fixed shear-banding parameter

In this final subsection, we now explore the behaviour when we vary the thixoplastic number variable with a fixed shear-banding parameter in bulk modes with sinuous perturbations. In the previous chapter (more specifically, in section 4.4.5.4), we analysed this case and we will summarise here what we found. We know that intermediate values of thixoplasticity tend to be unstable, and they become more dangerous if the viscoelastic time scale is much larger than the structural relaxation time scale, $\lambda_{ve} \gg \lambda$. Thus, $\lambda$ play a key role in the bulk instability. For that reason, we studied the effect of the thixoplastic number on the growth rate with multiple combinations of the destruction and reformation parameters. In order to make things easier for the reader, the results obtained in section 4.4.5.4 are shown in figure 5.23.

We took a set of fixed values for $\Lambda = \{0.1, 0.2, 0.5, 1\}$, and for each case, we calculated the growth rate as a function of the thixoplastic number, by varying the destruction parameter $\Gamma$, see figure 5.23a).

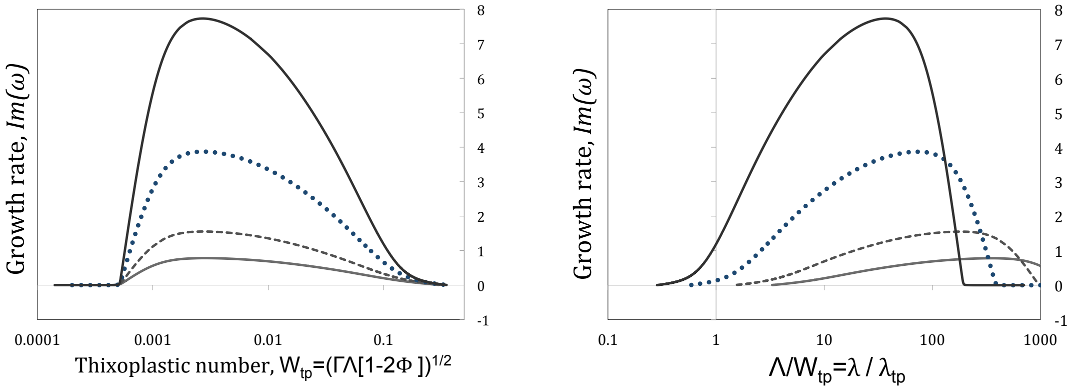

(a) Varying thixoplastic number

(b) Varying $\Lambda/W_{tp}$

Figure 5.23: Dependence of growth rate of bulk sinuous perturbations on thixoplastic number, at fixed $W = 2$, $\Phi = 0.001$, $k = 0.1$ and $\theta = 0$. For each curve $\Lambda$ is constant and $\Gamma$ varies. Main plots, top to bottom: $\Lambda = 0.1$, 0.2, 0.5 and 1. (a) Growth rate against thixoplastic number; (b): growth rate against the ratio $\Lambda/W_{tp}$. These results were originally reported in [29].

The main conclusions we obtained are that there is a strong dependence of the growth rate of the instability on the reformation parameter $\Lambda$, as the instability becomes more dangerous when $\Lambda$ decreases (bottom to top). Additionally, the most unstable point of each curve has the same value of thixoplastic number, which is around $W_{tp} = 0.00269$, which indicate us that there is a small yielded region near the wall $(0.98 < y < 1)$, and the critical stress $\tau_c$ is located at $y \approx 0.98$.

We can also appreciate the strong dependence of the instability on $\Lambda$ and $\Gamma$ in figure 5.23b), where we plot the growth rate against the material parameter $\Lambda/W_{tp}$, which is the ratio of the thixotropic and plastic timescales. From this plot we deduced that the instability follows the scaling observed in section 4.4.5.4: $\Im(\omega) \propto \Lambda^{-1} \propto \Gamma$, and the most unstable points of each curve can be fitted to a single power-law equation that adopts the following form:

$$\Im(\omega) = A\,(\lambda/\lambda_{tp})^{-n}, \tag{5.58}$$

where $A$ and $n$ are coefficients that depend on the Weissenberg number, wavenumber, thixotropic ratio and, as we will see soon, on the shear-banding parameter.

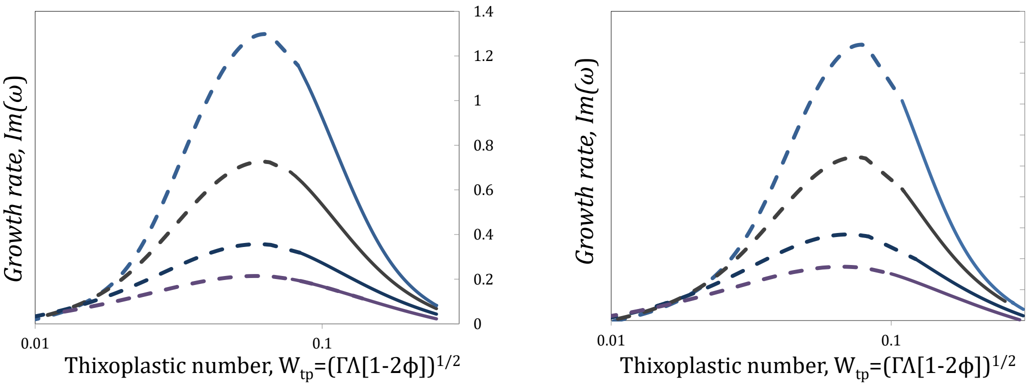

(a) Varying $W_{tp}$ with $\theta = 0.1$

(b) Varying $W_{tp}$ with $\theta = 0.124$

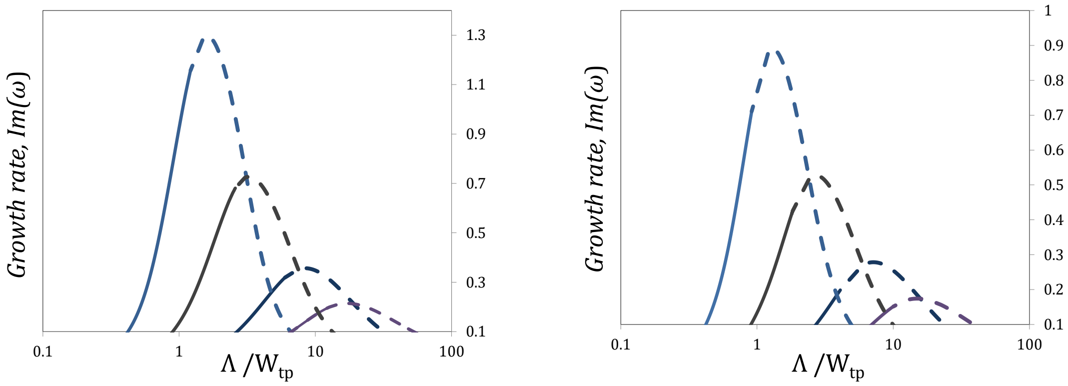

(c) Varying $\Lambda/W_{tp}$ with $\theta = 0.1$

(d) Varying $\Lambda/W_{tp}$ with $\theta = 0.124$

Figure 5.24: Figures (a) and (b): growth rate against thixoplastic number for bulk modes with shear-banding parameter variable fixed. Figures (c) and (d): growth rate plotted against material parameter $\Lambda/W_{tp}$ with fixed $\theta$. For all plots: $W = 2$, $k = 0.1$ and $\Phi = 0.001$; from top to bottom: $\Lambda = 0.1, 0.2, 0.5$ and $1$. Dashed lines represent base-states with a jump in the fluidity profile.

The characteristics of the instability described above are still seen for bulk modes with non-zero shear-banding parameter values, as illustrated in figure 5.24, where we show two different cases: $\theta = 0.1$ and $\theta = 0.1240$. Firstly, we focus on figures 5.24a) and 5.24b), where the growth rate is plotted against thixoplastic number. It can be seen that the behaviour of these curves resembles the one observed in the zero shear-banding case 5.23a): there is a most dangerous thixoplastic number, and therefore, a most dangerous base-state flow for each value of $\theta$; for $\theta = 0.1$, $W_{tp} \approx 0.062$, whose interface is located at $\kappa \approx 0.8791$ with stress plateau value $\sigma_p \approx 15.71$ and critical stress value $\tau_c \approx 16.15$ located at $y = 0.903$, meanwhile for $\theta = 0.1240$, $W_{tp} \approx 0.075$ with interface location $\kappa = 0.8618$, $\sigma_p = 12.94$ and critical stress $\tau_c = 13.31$ located at $y = 0.8871$. Furthermore, we obtain the dispersion relation for these highly unstable flows, and from the plot $\Re(\omega)$ vs $k$, we were able to obtain the location of the perturbation (as we did in section 5.4.1.2). The results show what we have concluded before: bulk perturbations are located in the yielded region which is near the channel wall; more specifically, we found that the perturbation is located roughly in the same position in which the critical stress value is. For the case with $\theta = 0.1$, the perturbation is found at $y = 0.892613$, while for $\theta = 0.1240$, it is located at $y = 0.8871$.

We also note the strong dependence of the instability on the thixoviscous number, and in order to appreciate this better, we reframe these results instead in terms of the material parameter $\Lambda/W_{tp}$, see figures 5.24c) and 5.24d). Similarly to the case $\theta = 0$, figure 5.23b), the maximum growth rate shifts to the left as $\Lambda$ decreases, which is consistent with what we have concluded in our previous work: fluids that exhibit quick structural reformation are highly unstable. For very large values of $\Lambda/W_{tp}$ the flow tends to be stable; this is a limit where thixotropy dominates. The instability for non-zero shear-banding parameter values for bulk modes follows the scaling previously found: $\Im(\omega) \propto \Lambda^{-1} \propto \Gamma$, which establish that highly unstable flows are observed when the following condition is satisfied: high thixoelastic and elastoplastic numbers or $\lambda_{ve} \gg \lambda_p \gg \lambda$. In addition, as concluded in section 5.4.4.3, intermediate values of the material time-scale ratio $\varpi = W_{tp}/\theta$ are present for the most unstable flows with bulk modes, which means that these time-scales are of the same order of magnitude: $\lambda_{tp} \approx \vartheta$.

As explained before, the maximum values of growth rate and their respective values of $\Lambda/W_{tp}$ from figures 5.24c) and 5.24d) can be fitted to a single power-law equation. For the case $\theta = 0.1$, $\Im(\omega) = 1.8045(\lambda/\lambda_{tp})^{-0.756}$ with $R^2 = 0.99912$, meanwhile $\Im(\omega) = 1.0285(\lambda/\lambda_{tp})^{-0.659}$ with $R^2 = 0.99937$ for $\theta = 0.1240$. If we compare these coefficients with the zero-shear banding parameter case, where $\Im(\omega) = 370.92(\lambda/\lambda_{tp})^{-1}$, it can clearly be seen that the power-law coefficients of these functions are decreasing as $\theta$ increases, and are also function of $\Lambda$, $\Gamma$, $\Phi$, $k$ and $W$.

We also have determined that for fixed values of our model parameters, the index $n$ cannot be larger than 1. We demonstrate this empirically by looking at the same parameter values used for the zero-shear banding parameter case. We calculated the maximum values of growth rate for the most dangerous base state for a higher value of wavenumber, $k = 0.7$, which corresponds to a highly dangerous wavenumber when $\theta = 0$, and we obtained the following power-law equation: $\Im(\omega) = 309.17(\lambda/\lambda_{tp})^{-0.999}$ with $R^2 = 1$.

Lastly, we explore the behaviour of thixoplastic number variable at fixed shear-banding parameter in the interfacial modes. As we did with the bulk modes, a set of fixed values for $\Lambda = \{0.1, 0.2, 0.5, 1\}$ is taken and for each case, we calculate the growth rate as a function of the thixoplastic number, by varying the destruction parameter $\Gamma$. Results are shown in figure 5.25a). It is not surprising to see that the most unstable flows are located near the channel wall, and this is observed in the limit of small thixoplastic number ($W_{tp} \propto \Gamma\Lambda \to 0$). Moreover, we notice that although a

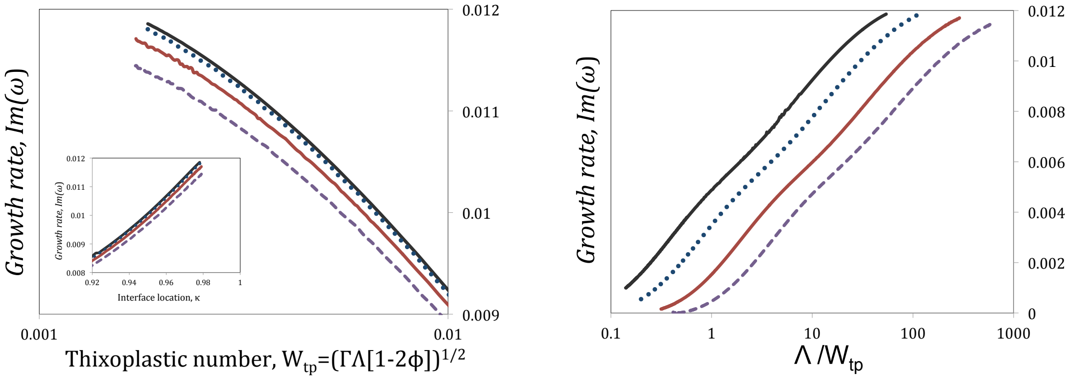

(a) Varying thixoplastic number

(b) Varying $\Lambda/W_{tp}$

Figure 5.25: Figure (a): dependence of growth rate of interfacial sinuous perturbations on thixoplastic number. The inset shows the growth rate versus interface location. Figure (b): growth rate plotted against the material time-scale ratio $\Lambda/W_{tp}$. For both figures, we fix $W = 2$, $\Phi = 0.001$, $k = 0.1$ and $\theta = 5$. For each curve $\Lambda$ is constant and $\Gamma$ varies. Top to bottom: $\Lambda = 0.1$, $0.2$, $0.5$ and $1$.

decrease in the thixoviscous number (from bottom to top) is destabilising, the growth rate values do not rocket like in the bulk modes. In fact, the interfacial modes do not follow the scaling observed for the bulk perturbations, see equation (5.58): they follow the opposite behaviour, see figure 5.25b). In contrast to what we observed in figure 5.24 for the bulk modes, the interfacial modes become slightly more unstable when the material time-scale ratio $\Lambda/W_{tp}$ is large, or in other words, the structural relaxation time is much larger than the plastic time scale, $\lambda \gg \lambda_{tp}$. In addition, as concluded in section 5.4.4.4, these interfacial modes will dominate at low values of the material time scale ratio $\varpi$, or in other words, if the following condition is satisfied: $\lambda_{tp} \ll \vartheta$.

### 5.4.5 Streamlines of the most unstable flows

In this final subsection, we show the streamlines of the perturbation flows for unstable bulk and interfacial modes, see figure 5.26. For the former case, we choose the most unstable flow for the case of $\theta = 0.10$ and $\Lambda = 0.20$ (shown in figure 5.24a). The other parameter values for this case are $\Gamma = 0.0192$, $W = 2$, $\Phi = 0.001$ and

$k = 0.10$. For this set of parameter values, the bulk mode is dominant over the interfacial mode, and we can find the streamlines of this unstable bulk mode in figure 5.26a), where we can see that within the unyielded region near the centreline, there is only vertical motion, which means that the component of the perturbed velocity in $x$-direction is zero. However, near the interface location ($\kappa = \pm 0.8791$), we observe fluid motion in both $x$-and $y$-direction. More interestingly, we can see reverse flow near the channel wall. If we increase the wavenumber to $k = 1$ (which leads to more unstable flows), this becomes more evident, as illustrated in figure 5.26b). The general behaviour away from the wall also changes: there are sections in the channel in which only vertical motion is observed, but motion in both directions is seen close to the centreline.

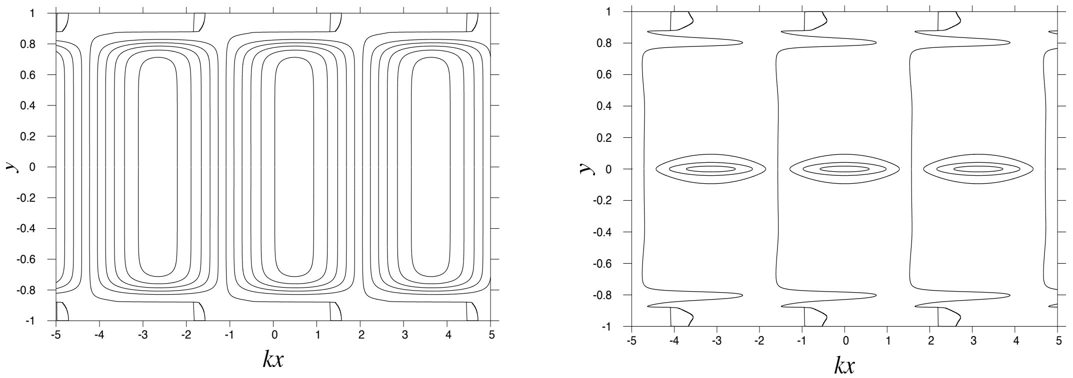

(a) Bulk mode with $k = 0.1$

(b) Bulk mode with $k = 1$

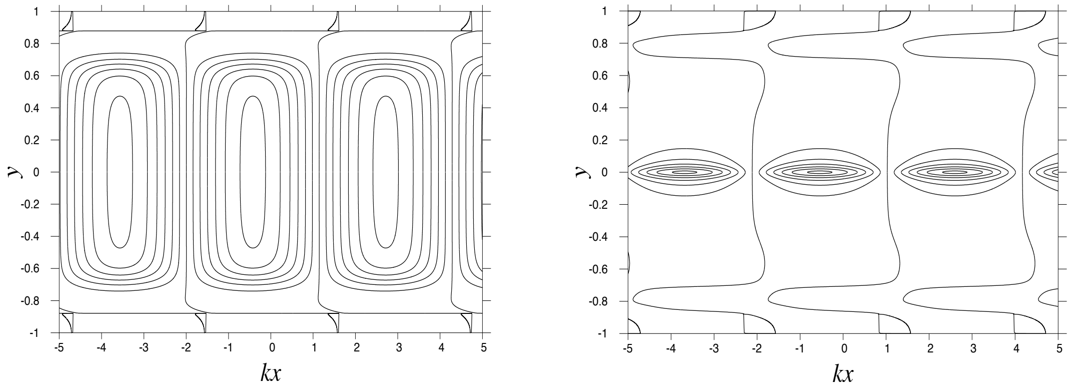

(c) Interfacial mode with $k = 0.1$

(d) Interfacial mode with $k = 1$

Figure 5.26: Streamlines of the perturbation flows for the unstable sinuous bulk and sinuous interfacial modes for different values of wavenumber $k$. The parameter values used are $W = 2$, $\Phi = 0.001$, $\Lambda = 0.20$, $\theta = 0.1$ and $\Gamma = 0.0192$. The interface location is $\kappa = 0.8791$.

We also show the streamlines of the interfacial modes with the same parameter model values used to obtain figures 5.26a) and 5.26b). Although the bulk modes are more unstable than the interfacial perturbations, the latter ones are unstable as well. For the case $k = 0.1$ (see figure 5.26c), vertical motion is seen in the unyielded region near the centreline (similarly to what we observed in figure 5.26a). As we approach the interface location, we notice that there are non-zero values of the perturbed vector velocity in both directions ($u$ and $v$). The major difference with respect to the bulk modes is that we can observe purely horizontal motion exactly at $\kappa = 0.8791$. In the yielded region, reverse flow is also observed.

If we increase the wavenumber to $k = 1$ (figure 5.26d), we obtain a similar picture to that of the bulk mode (figure 5.26b). However, notice that the direction of the perturbed flow near the interface location is different.

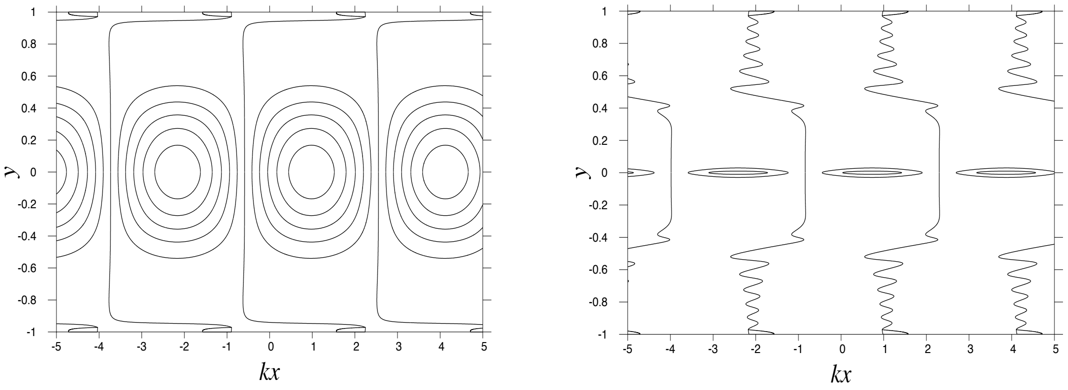

(a) $k = 0.1$ (b) $k = 1$

Figure 5.27: Streamlines of the perturbation flows for the unstable sinuous interfacial modes for different values of wavenumber $k$. The parameter values used are $W = 2$, $\Phi = 0.001$, $\Lambda = 0.20$, $\theta = 0.5$ and $\Gamma = 0.00032$. The interface location is $\kappa = 0.9714$.

We now choose parameter values for which the interfacial modes are dominant over the bulk ones. In order to meet this condition, we previously concluded that low values of $\Gamma\Lambda$ and high values of $\theta$ are needed. On this way, we choose $\Gamma = 0.000032$, $\Lambda = 0.20$ and $\theta = 0.50$, which gives an interface location value of $\kappa = 0.9714$. The other parameter values are $W = 2$, $\Phi = 0.001$. The streamlines for $k = 0.1$ are shown in figure 5.27a). Unlike the case for the bulk mode shown in figure 5.26a), we can observe motion in both directions near the centreline. As we move away from this zone and before reaching the interface location, the $x$-component of the perturbed velocity field is almost null. In the narrow yielded region $1 > y > \kappa = 0.9714$, we can also observe reverse flow. If the wavenumber is increased to $k = 1$ (figure 5.27b), the phenomenon is still present and the flow becomes even more unstable, as fluctuations in the streamlines are observed in the unyielded region close to the interface location.

## 5.5 Conclusions

We extended our previous theoretical work carried out in chapter 4 by studying the stability in pressure-driven channel flow of materials that exhibit shear-banding along with viscoelasto-thixo-plasticity. We used the generalised BMP model, which is an extension of the original model [7] and has been extensively used to describe complex rheological behaviour.

We obtained a set of dimensionless groups ($\Phi$, $\Lambda$, $\Gamma$) from which we constructed key dimensionless quantities that were extremely useful in our previous work to describe the phenomena of viscoelasticity, thixotropy and plasticity present in our material. Alongside those dimensionless quantities, we have derived a new dimensionless number that can be incorporated to the family of timescales proposed by Ewoldt & McKinley [56]: the dimensionless shear-banding parameter, $\theta$, from which we derived more dimensionless quantities for analysis of our results.

We have obtained semi-analytical solutions for the base state quantities for the cases with non-zero shear-banding parameter values that allow us to calculate velocity and fluidity profiles, along with the stress plateau and the interface location. We also provide a physical analysis of the large variety of base states that can be predicted by the combination of our fluid parameters.

We have made an extensive exploration of our model parameters and we have identified key conditions for flow instability/stability. Some of the conditions reported in chapter 4 still hold for fluids that exhibit shear-banding, such as a decrease in the thixotropic ratio and an increase in the wavenumber leading to instabilities, and the limits $k \to 0$ and $W \to 0$ are stable. We have found that for fixed values of thixotropic ratio, wavenumber, Weissenberg number and destruction and reformation parameters, the fluids with $\theta = 0$ are always more unstable compared to those with $\theta \neq 0$, i.e. an increase on $\theta$ will lead to less unstable flows, as there is a decrease of the shear rate and shear stress values at the channel walls. We have also identified two modes of instability: one of them, a highly unstable *bulk* mode $\mathrm{B}_1$, which exists at $\theta = 0$ and is still present in the two flow regimes: a) where there exists continuity in the fluidity profile, and b) where we have a jump in the shear-rate, i.e. the presence of two-bands of fluid that coexist with different shear-rate values at a given stress value. A second mode, which we call the *interfacial* mode was also found, whose perturbation is located at the plateau interface. This mode behaves as an interfacial mode in the flow regime b), but it becomes a bulk mode $\mathrm{B}_2$ in the regime a), which happens to be less unstable than the previously described mode $\mathrm{B}_1$.

Although is not possible to define a general criterion in terms of all our parameters that allow us to determine the onset of instability, we have identified key flow conditions in which one of the modes dominate over the other one: for fixed values of thixotropic ratio, Weissenberg number destruction and reformation parameters, we have observed that the bulk modes are dominant over the interfacial ones at very low values of shear-banding parameter and we concluded that the shear-thinning behaviour is an essential component of the bulk instabilities. On the other hand, interfacial modes will dominate for very large $\theta$ values, and they will start to replace the bulk modes when the shear-thinning characteristics of the low-shear-rate band vanish. This is expected to happen when the following condition is present: $\dot{\gamma}_1^2(1 + \theta\dot{\gamma}_1) \ll \Phi/\Gamma\Lambda$, where $\dot{\gamma}_1$ is the dimensionless shear rate value of the high viscosity band that coexists with the low viscosity band when the system reaches the stress plateau $\sigma_p$.

We have also identified additional dissimilarities and similarities between bulk and interfacial modes: for the latter case, the growth rate becomes neutrally stable at very long waves limit, $k \to 0$, meanwhile the bulk modes are fully stable in the same limit. The sinuous perturbations are always going to be slightly more unstable than the varicose ones for both modes, and for short waves, the perturbations will be localised very close to the location of the interface $\kappa$ for interfacial modes, meanwhile, the perturbations for the bulk modes will be localised in the yielded region $y > \kappa$. More importantly, we determined that the viscoelastic effects are the main cause of instability for both bulk and interfacial modes, as an increase in $W$ leads to unstable flows; for the former case, the instability vanishes when the limit $W \to 0$ has been reached, while for the latter case, the growth rate becomes neutrally unstable at $W = 0$.

We have also shown that the interfacial instability predicted by the generalised BMP model, which does not exhibit a jump in the normal stress difference at the interface, is also predicted by a much simpler rheological model: the Oldroyd-B model.

We explored multiple combinations of the thixotropic timescales derived from the generalised BMP model. For bulk modes, we found that fluids with very low values of thixoviscous number (extremely quick structural relaxation time) tend to be highly unstable, which is something we initially observed for the case $\theta = 0$. We also found that instability will be observed for intermediate values of two new material parameters: a) $\varsigma$, defined as the ratio of the dimensionless timescales $\theta$ and $\Lambda$ (equivalent to the ratio $\vartheta/\lambda$), which compares shear-banding and thixotropic effects and b) $\varpi$, defined as $\varpi = W_{tp}/\theta = \lambda_{tp}/\vartheta$ (ratio of plastic and shear-banding effects). The extremes of these material parameters $\varsigma \to 0$, $\varsigma \to \infty$ and $\varpi \to 0$,

$\varpi \to \infty$ are stable.

For the interfacial modes, on the other hand, which tend to be dominant at high values of the shear-banding parameter and when the interfacial location is very close to the channel wall, we have observed unstable flows if the location of the interface $\kappa$ is extremely close to the wall. This happens when $\Gamma\Lambda \to 0$, which means that either poor thixotropy (low $\Lambda$) and/or poor structural destruction (low $\Gamma$) is dangerous.

Lastly, for bulk modes, we found that there is a most dangerous thixoplastic number for each value of shear-banding parameter $\theta$. The most dangerous $W_{tp}$ depends on the values of $k$, $W$ and $\Phi$, but overall, we have found that intermediate values of thixoplastic number (where the yielded region near the wall grows) lead to the most unstable flows. Under these conditions, this bulk instability becomes even more dangerous if the thixoviscous number is allowed to decrease and if the viscoelastic relaxation time $\lambda_{ve}$ is much longer than both the structural destruction timescale $\lambda_{tp}$ and the thixotropic timescale $\lambda$:

$$\lambda \ll \lambda_{tp} \ll \lambda_{ve}. \tag{5.59}$$

In other words, instability is enhanced by extremely high elastoplastic and thixoelastic numbers. This condition for the time scales was originally found in chapter 4, and although an increase in $\theta$ leads to less unstable flows, we have shown here that this condition for instability still holds for non-zero shear-banding parameter values. In addition, we have observed that the most unstable flows satisfy the condition of intermediate values of the material time-scale ratio $\varpi = W_{tp}/\theta$, or in other words, $\vartheta$ and $\lambda_{tp}$ are of the same order of magnitude:

$$\vartheta \approx \lambda_{tp}. \tag{5.60}$$

On the other hand, we have found that the interfacial modes follow a different timescale condition: given an unstable flow for a given value of $k$, $W$ and $\Phi$, the interfacial instabilities become more dangerous if the structural relaxation time-scale is much bigger than that of plasticity, $\lambda \gg \lambda_{tp}$ and at very low values of $\varpi$ and large values of $\varsigma$, which leads us to propose the following condition of time-scale parameters for unstable interfacial modes with non-zero values of Weissenberg number:

$$\vartheta \gg \lambda \gg \lambda_{tp}. \tag{5.61}$$

Lastly, we have provided evidence that interfacial modes dominate at low values of $W$, $\Gamma$ and $\Lambda$, which leads us to think that for fluids that exhibit the shear-banding phenomenon ($\vartheta \neq 0$), a gradual startup flow of these fluids will be initially unstable due to an interfacial instability, but this can be followed by a bulk instability if the time-scale conditions (5.59)–(5.60) are met. On the other hand, interfacial instabilities will only be observed if the model parameters satisfy equation (5.61).

# Chapter 6

# Conclusions

The main focus of this dissertation is studying purely elastic instabilities that are present in the flow of viscoelastic fluids that exhibit complex rheological behaviour. The main research content of the thesis is split into three main chapters. In chapter 3, we considered the linear stability of a shear-thinning viscoelastic fluid, replicating an instability recently discovered in experimental [16] and theoretical work [178]. Our goal was to know whether the mechanism of the instability was truly elastic or principally as a result of strong shear-thinning. In order to answer this question, we studied the effect of reducing elasticity while maintaining the shear-thinning velocity profile, and we did this by using a shear-thinning modification of the Oldroyd-B model, which allowed us to separate elastic from viscous effects. The difference between the model used in this work with respect to the one used in [178] was that an inelastic shear-thinning solvent contribution was added to the stress, which shear-thins at the same rate as the polymer contribution. We found that the solvent viscosity contribution is always stabilising. Most importantly, we found that the mechanism of the instability is a coupling of elasticity with shear-thinning, in which both components are critically important.

It should be pointed out that the theoretical works carried out in [178, 180] and the content of chapter 3 were restricted to study only modes with no cross-channel motion at the centreline, and this was due to singularities caused by the use of power-law rheometric functions. In addition, the models used there have fluid properties that depend instantaneously on the shear rate. In chapter 4, one of our goals was to tackle some of these issues by using a much more realistic constitutive model that would allow us to attempt to capture the physics of the instabilities observed in channel flow of shear-thinning viscoelastic fluids. Thus, we selected the Bautista-Manero-Puig (BMP) model for many reasons: it predicts a finite value of the zero shear viscosity, which permits cross-channel motion at the centreline, and the model also captures more complex rheological behaviours, such as thixotropic-viscoelasto-plasticity.

The BMP model allowed us to obtain analytic solutions for the base-state quantities, and dimensionless groups were derived which facilitated the analysis of our results and allowed us to compare the effects of thixotropy, plasticity and elasticity on the fluid stability. We showed that our results were in agreement with previous theoretical works as we found that an instability is predicted at very low values of thixotropic ratio, which is an indicator that the fluid exhibits shear-thinning behaviour. We have also shown that sinuous perturbations are slightly more unstable than varicose modes, and we have identified the values of our model parameters for which the instability has its strongest effects. We concluded that dominant thixotropy can be stabilising, but flow instability occurs when the characteristic timescale of viscoelasticity is much longer than both those of plasticity and thixotropy:

$$\lambda \ll \lambda_{tp} \ll \lambda_{ve}, \tag{6.1}$$

indicating that the instability might be enhanced by large values of elastoplastic or thixoelastic numbers and if the plastic and shear-banding time-scales are of the same order of magnitude ($\lambda_{tp} \approx \vartheta$). On the other hand, extremes of many of our flow parameters cause linearly stable flow, in particular, very large or very small values of the thixoviscous number $\Lambda$ or the thixoplastic number $W_{tp}$. We have shown that the most unstable flows have the low to high shear transition point near the wall, resulting in a plug flow with an apparent yield surface within the channel. Lastly, one of the main conclusions of chapter 4 is that we have determined that the thixotropic structure recovery rate plays a key role, as it determines the growth rate of instability.

In the last chapter, we extended the theoretical work of chapter 4 by carrying out linear stability analysis of the generalised BMP model, which incorporates shear-banding phenomenon to the flows of thixotropic-viscoelasto-plastic fluids, which are common behaviours observed in wormlike micellar solutions. Along with the dimensionless groups that were derived in chapter 4, a new dimensionless number was introduced, which is the dimensionless shear-banding parameter $\theta$. We have found that given an unstable flow, this parameter has always a stabilising effect.

More interestingly, above a critical shear-banding parameter value (when the formation of bands with different shear rate appears), two different modes of instability have been observed: a bulk mode (which was studied in chapter 4) and an interfacial mode. We found that the former ones dominate over the latter ones at low shear-banding parameter values, while the interfacial ones become dominant at very high $\theta$ values. More specifically, the interfacial modes are more unstable if the shear-thinning region of the low-shear band begins to vanish, and this is observed when the following condition is satisfied:

$$\dot{\gamma}_1^2(1+\theta\dot{\gamma}_1) \ll \Phi/\Gamma\Lambda, \tag{6.2}$$

where $\dot{\gamma}_1$ is the dimensionless shear rate value of the low fluidity band that coexist with the high fluidity band when the system reaches the stress plateau $\sigma_p$.

We have also identified that these interfacial modes become more dangerous if the interface location $\kappa$ is near the channel wall, and this is seen when the structural relaxation time $\lambda$ is much larger than that of plasticity $\lambda_{tp}$ and if there are present very low values of $\varpi$ and large values of $\varsigma$. These conclusions lead us to propose to the following material time-scale condition for unstable interfacial perturbations:

$$\vartheta \gg \lambda \gg \lambda_{tp} \text{ for } W \neq 0. \tag{6.3}$$

Such condition also satisfies equation (6.2). On the other hand, we found that the time-scale condition for highly unstable flows (equation (6.1)), initially established for fluids without shear-banding, is also valid for the bulk modes in shear-banded flows.

In addition, intermediate values of the material time-scale ratios (shear-banding parameter to thixoviscous number and thixoplastic number to shear-banding parameter) lead to highly unstable flows for the bulk modes. The main conclusion of this chapter is that the two modes of instability seem to follow different time scalings, see equations (6.1) and (6.3).

Lastly, we wish to mention that this dissertation leaves some questions open to future work. For instance, it is still necessary to study the behaviour of bulk and interfacial modes in the short-wave limit ($k \to \infty$) and at extremely high values of Weissenberg number to determine whether our conclusions obtained here still hold. It would also be of great interest to use a model that can be able to predict a jump in the first normal stress difference at the shear-band interface, and study whether this discontinuity will enhance the instability or not. In addition, to our knowledge, no previous theoretical work has studied the dependence of the second normal stress difference on these elastic instabilities present in channel flow, as the majority of the models are unable to predict a non-zero value of $N_2$. A model that can help us to achieve this is a recently published model [70] that couples the flow behaviour, structural parameters and diffusion of species, with full tensorial expressions derived from extended irreversible thermodynamics. Such a model (which is an even more general extension of the BMP model used in the present work) is also able to predict a non-zero second normal stress difference.

In order to prove the validity of our results, we would expect in a near future that experimental rheologists could be able to carry out experiments to study the stability of pressure-driven channel flow of thixotropic-viscoelasto-plastic fluids with and without shear-banding. Another challenging problem still pending is to address the true yield stress case for both zero and nonzero shear-banding cases. Finally, a fully comprehensive mechanism for the instabilities studied here is still elusive, though we have gained valuable insight through the current work.

# Appendix A

# List of Symbols

## General

| | |
|---|---|
| $x$, $y$ | Cartesian coordinates |
| $t$ | Time |
| $T$ | Temperature |
| $g$, $\underline{g}$ | Gravitational acceleration; gravity field |
| $\mathrm{i}$ | Complex number ($\equiv \sqrt{-1}$) |
| $\underline{\nabla}$ | Nabla operator ($\equiv (\partial/\partial x, \partial/\partial y)$) |
| $\mathrm{D}$ | Derivative with respect coordinate $y$ |

## Fluid properties

| | |
|---|---|
| $\rho$ | Density |
| $\mu$ | Newtonian Viscosity |

## Non-Newtonian fluid mechanics

| | |
|---|---|
| $\underline{u}$ | Fluid velocity |
| $\underline{\nabla}\,\underline{u}$ | Velocity gradient tensor |
| $\underline{\nabla}\,\underline{u}^{\top}$ | Transpose of the velocity gradient tensor |
| $D/Dt$ | Material derivative ($\equiv \partial/\partial t + \underline{u} \cdot \underline{\nabla}$) |
| $U(y)$ | Velocity field/Channel-flow velocity |
| $U_0$ | Channel-flow centreline velocity |
| $L$ | Channel half-width |
| $P$ | Pressure |
| $\underline{\underline{I}}$, $\delta_{ij}$ | Identity tensor |
| $\underline{\underline{A}}$ | Conformation tensor |
| $\overset{\nabla}{\underline{\underline{A}}}$ | Upper convected derivative of the conformation tensor |
| $\underline{\underline{\sigma}}$ | Deviatoric or polymer stress tensor |
| $\overset{\nabla}{\underline{\underline{\sigma}}}$ | Upper convected derivative of the stress tensor |
| $\underline{\underline{\tau}}$ | Total stress tensor ($\equiv -P\underline{\underline{I}} + \underline{\underline{\sigma}}$) |
| $\underline{\underline{D}}$ | Deformation tensor ($\equiv \frac{1}{2}[\,\underline{\nabla}\,\underline{u} + \underline{\nabla}\,\underline{u}^{\top}]$) |
| $\dot{\gamma}$ | Shear rate ($\equiv \sqrt{2\underline{\underline{D}} : \underline{\underline{D}}}$) |
| $\dot{\gamma}_0$ | Steady shear rate/Dimensionless shear-rate |
| $\dot{\gamma}_w$ | Dimensionless shear-rate at the wall |
| $I_D$ | First invariant of deformation tensor ($\equiv \operatorname{tr}\underline{\underline{D}}$) |
| $II_D$ | Second invariant of deformation tensor ($\equiv 2\,\underline{\underline{D}} : \underline{\underline{D}}$) |
| $III_D$ | Third invariant of deformation tensor ($\equiv \det\underline{\underline{D}}$) |
| $\mathscr{P}$ | Gradient pressure ($\equiv \mathrm{d}P/\mathrm{d}x$) |
| $\mathcal{P}$ | Dimensionless gradient pressure |
| $\psi$ | Streamfunction |
| $\kappa$ | Location of fluid-fluid interface |
| $\overline{\eta}$ | Lagrangian coordinate |

## Quantities in constitutive equations

| | |
|---|---|
| $\mu(\dot{\gamma})$ | Non-Newtonian solvent viscosity |
| $\mu_0$ | Viscosity coefficient in power-law model |
| $N$ | Power-law coefficient of an inelastic fluid |
| $\lambda_R(\dot{\gamma})$ | Relaxation time function |
| $G(\dot{\gamma})$ | Shear modulus function |
| $K_M$ | Relaxation time coefficient |
| $G_M$ | Shear modulus coefficient |
| $\lambda_s$ | Structural parameter |
| $m$ | Power-law coefficient of an elastic fluid |
| $n$ | Relaxation-time power-law coefficient |
| $G_0$ | Stress modulus |
| $\lambda$ | Structural relaxation time |
| $K_0$ | Structural destruction parameter |
| $\eta_0$ | Viscosity at low-shear-rates |
| $\varphi_0$ | Fluidity at low-shear-rates ($\equiv \eta_0^{-1}$) |
| $\eta_\infty$ | Viscosity at high-shear-rates |
| $\varphi_\infty$ | Fluidity at high-shear-rates ($\equiv \eta_\infty^{-1}$) |
| $\vartheta$ | Shear-banding parameter |
| $\sigma_c$, $\tau_c$ | Dimensional and dimensionless critical shear-stress |
| $\sigma_y$, $\tau_y$ | Dimensional and dimensionless yield stress |
| $\lambda_{ve}$ | Viscoelastic relaxation time ($\equiv (G_0\varphi_\infty)^{-1}$) |
| $\lambda_{tp}$ | Plastic relaxation time |
| $C_i$ | Polymer concentration |
| $C_0(\dot{\gamma}_0)$ | Dimensionless shear viscosity function |
| $\mathcal{W}_0(\dot{\gamma}_0)$ | Dimensionless relaxation time function |

## Material functions

| | |
|---|---|
| $\eta(\dot{\gamma})$ | Non-Newtonian viscosity |
| $\varphi(\dot{\gamma})$ | Fluidity ($\equiv \eta(\dot{\gamma})^{-1}$) |
| $N_1(\dot{\gamma})$ | First normal stress difference |
| $N_2(\dot{\gamma})$ | Second normal stress difference |
| $\Psi_1(\dot{\gamma})$ | First normal stress difference coefficient |
| $\Psi_2(\dot{\gamma})$ | Second normal stress difference coefficient |
| $\eta^+(t,\dot{\gamma})$ | Shear-stress growth coefficient |
| $\Psi_1^+(t,\dot{\gamma})$ | First normal-stress growth coefficient |
| $\Psi_2^+(t,\dot{\gamma})$ | Second normal-stress growth coefficient |
| $\eta^-(t,\dot{\gamma})$ | Shear-stress decay coefficient |
| $\Psi_1^-(t,\dot{\gamma})$ | First normal-stress decay coefficient |
| $\Psi_2^-(t,\dot{\gamma})$ | Second normal-stress decay coefficient |
| $G(t,\dot{\gamma})$ | Relaxation modulus |
| $G_{\Psi_1}(t,\dot{\gamma})$ | First normal stress step shear relaxation modulus |
| $G_{\Psi_2}(t,\dot{\gamma})$ | Second normal stress step shear relaxation modulus |
| $G'(\omega)$ | Storage modulus |
| $G''(\omega)$ | Loss modulus |

## Dimensionless numbers

| | |
|---|---|
| $Re$ | Reynolds number |
| $De$ | Deborah number |
| $W$ | Weissenberg number |
| $\beta$ | Retardation parameter |
| $\Phi$ | Thixotropic ratio |
| $\Lambda$ | Thixoviscous number |
| $\Gamma$ | Dimensionless destruction parameter |

| | |
|---|---|
| $\theta$ | Dimensionless shear-banding parameter |
| $W_{te}$ | Thixoelastic number |
| $W_{tp}$ | Thixoplastic number |
| $\varpi$ | Material time-scale ratio ($\equiv W_{tp}/\theta$) |
| $\varsigma$ | Material time-scale ratio ($\equiv \theta/\Lambda$) |

## Stability analysis

| | |
|---|---|
| $\omega$ | Complex frequency |
| $\Im(\omega)$ | Growth rate; imaginary part of $\omega$ |
| $\Re(\omega)$ | Convection rate; real part of $\omega$ |
| $k$ | Wavenumber |
| $\epsilon$ | Small quantity |
| $\varepsilon$ | Fourier mode ($\equiv \epsilon \exp\left[\mathrm{i}kx - \mathrm{i}\omega t\right]$) |
| $u$ | Perturbed velocity in $x$-direction |
| $v$ | Perturbed velocity in $y$-direction |
| $p$ | Perturbed pressure |
| $\underline{\underline{\Sigma}}$ | Perturbed stress tensor |
| $\phi$ | Perturbed fluidity |
| $\underline{\underline{d}}$ | Perturbed deformation tensor |
| $\underline{\underline{a}}$ | Perturbed conformation tensor |
| $\dot{\gamma}_p$ | Perturbed shear rate |
| $c$ | Perturbed shear-viscosity function |
| $w$ | Perturbed relaxation time function |
| $\zeta$ | Perturbed interface location |

# Appendix B

# Interfacial instabilities in channel flow of two Oldroyd-B liquids with continuous normal stresses

We modify the governing equations used in [181] to adapt them to our problem. The set of equations is:

$$\underline{\nabla} \cdot \underline{u} = 0 \qquad \underline{\nabla} \cdot \underline{\underline{\sigma}} = 0 \tag{B.1}$$

$$\underline{\underline{\sigma}} = -p\underline{\underline{I}} + 2\underline{\underline{D}} + \frac{C}{W}\underline{\underline{A}} \qquad \overset{\triangledown}{\underline{\underline{A}}} = -\frac{1}{W}(\underline{\underline{A}} - \underline{\underline{I}}) \tag{B.2}$$

$$\overset{\triangledown}{\underline{\underline{A}}} = \frac{\partial \underline{\underline{A}}}{\partial t} + \underline{u} \cdot \underline{\nabla}\,\underline{\underline{A}} - \underline{\underline{A}} \cdot (\underline{\nabla}\,\underline{u}) - (\underline{\nabla}\,\underline{u})^{\top} \cdot \underline{\underline{A}}, \tag{B.3}$$

where $\underline{\underline{A}}$ and $\underline{\underline{I}}$ are the conformation and identity tensors, respectively. The other variables of the system are known and have been defined previously here. However, their definition slightly changes for this model; the concentration and the Weissenberg number are defined as:

$$W = \frac{\lambda_M U_0}{L} \qquad C = \frac{\lambda_M G_M U_0^2}{L^3 \mu}, \tag{B.4}$$

where $\lambda_M$ and $G_M$ are the relaxation time and elastic modulus, respectively, and $\mu$ is the solvent viscosity. These equations are used to study instabilities in pressure-driven channel flow, with the same geometry described in section 5.2.3.1, leading us to the following base-state equations:

$$C(y) = \begin{cases} C_1 & |y| > \kappa \\ C_2 & |y| < \kappa \end{cases} \qquad -\dot{\gamma}_0 = U' = Gy/[1 + C(y)] \tag{B.5}$$

$$G = -\mathcal{P} = \frac{-2(1+C_1)(1+C_2)}{(1+C_1)\kappa^2 + (1+C_2)(1-\kappa^2)} \tag{B.6}$$

$$U(y) = \begin{cases} \dfrac{G(y^2-1)}{2(1+C_1)}, & |y| > \kappa \\ \dfrac{G[(1+C_1)(y^2-\kappa^2) - (1+C_2)(1-\kappa^2)]}{2(1+C_1)(1+C_2)}, & |y| < \kappa \end{cases} \tag{B.7}$$

$$W(y) = \begin{cases} W_2 & |y| < \kappa \\ \left[\dfrac{(1+C_1)}{(1+C_2)}\right]^2 \left(\dfrac{C_2 W_2}{C_1}\right) & |y| > \kappa \end{cases} \tag{B.8}$$

$$\underline{\underline{\sigma}} = \begin{pmatrix} -Gx + 2\,C\,W(y)\,U'^{\,2} & Gy \\ Gy & -Gx \end{pmatrix} \qquad N_1 = 2\,C\,W(y)\,U'^{\,2} \tag{B.9}$$

Equation (B.5) shows the concentration profile $C(y)$, which is equivalent to our fluidity profile (5.28). Here, $\kappa$ is the location of the interface where the two fluids meet. Above this value of $\kappa$, the polymer will have a concentration of $C_1$, and below the interface it will have a value of $C_2$. In order to match these equations to our results, the viscosity (which is proportional to the polymer concentration) near the centreline $C_2$ has to be bigger than the one located near the wall, i.e. $C_2 \gg C_1$.

The shear rate $\dot{\gamma}_0$ can be calculated according to (B.5), and it is clearly seen that there will be a jump in $\dot{\gamma}_0$ at the interface $\kappa$, and this is due to the variation in the polymer concentration. The velocity profile obtained from the governing equations is shown in (B.7), and it also depends on the location of the interface. The coefficient

$G$ is the pressure gradient and is shown in (B.6). Unlike our velocity profiles reported in section 5.3.2), here $G$ can be calculated analytically to satisfy $U(0) = 1$.

The most important difference between the equations used in this section and the ones used by Wilson & Rallison in [181] is that here we require continuity in the first normal stress difference $N_1$ to compare the results predicted by the Oldroyd-B model with the ones that were shown in section 5.4.1.1. In order to achieve that, we need a Weissenberg number that is different between the two fluids. Additionally, we have to find the values of $W$ that satisfy the condition $[N_1] = 0$ at $y = \kappa$. The Weissenberg number profile $W(y)$ proposed is shown in equation (B.8), where $W_2$ stands for the Weissenberg number of the layer of fluid with concentration $C_2$, meanwhile the Weissenberg number for $y > \kappa$, $W_1$, depends on $C_1$, $C_2$, $W_2$ and the location of the interface. If the condition $C_2 > C_1$ is satisfied, $W_2$ will also be greater than $W_1$.

We show in figure B.1 the velocity and first normal stress difference coefficient profiles along the channel calculated with equations (B.7) and (B.9). We choose parameter values that can provide us with a base state behaviour similar to the ones predicted by the generalised BMP model. For instance, the fluid viscosity near the centreline $(1 + C_2)$ is much higher than the viscosity near the channel wall $(1 + C_1)$. We also select a value of $\kappa$ relatively near to the channel wall, and we fix $W_2 = 4$, giving us a value of $W_1 = 0.4744$ using equation (B.8).

We see that the velocity profile in figure B.1a) resembles the one reported in figure 5.4a): we observe a plug-flow for values of channel coordinate $|y|$ below $\kappa$ (dotted lines), and the velocity decreases rapidly as the coordinate approaches $|y|= 1$, which is where the polymer concentration $C_1$ is smaller. Furthermore, we can see that figure B.1b) shows a smooth, parabolic and continuous first normal stress difference profile $N_1$ similar to the one predicted by the BMP model in figure 5.4c).

Now that we have demonstrated that these equations satisfy our conditions, we

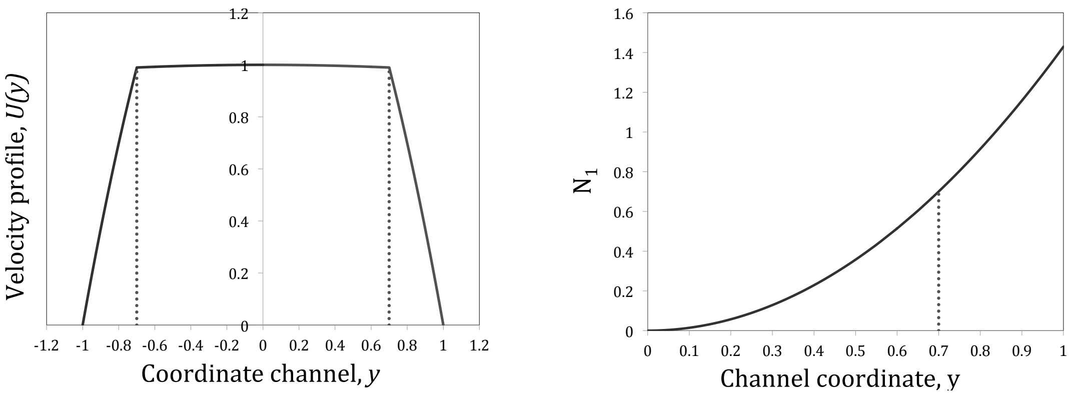

(a) Velocity profile

(b) Normal stress difference profile

Figure B.1: Velocity (a) and first normal stress difference (b) profiles for an Oldroyd-B fluid with concentration and Weissenberg number variable. The parameters used are: $C_1 = 0.1$, $C_2 = 100$, $W_2 = 4$ and $\kappa = 0.7$ (vertical dotted lines).

study the stability of layered Oldroyd-B fluids with differing concentration and Weissenberg number using a similar method described in sections 5.3.3 and 5.3.4.2: an infinitesimal perturbation $\varepsilon$ is added to the base flow, and all the quantities from the governing equations (B.1)–(B.2) and the base state equations (B.5)–(B.9) are modified by a small change. The whole set of perturbed governing equations can be found in [181]. We require non-slip boundary conditions at the channel-wall, boundary conditions for either sinuous or varicose modes (see section 5.3.4), and we must satisfy continuity of the velocity, shear rate and of the traction at the interface $y = \kappa + \zeta\varepsilon$. We show some results below.

We choose two values of interface location $\kappa = [0.7, 0.8]$, and using the same parameter values as the ones used in figure B.1, we obtain the dispersion relation $\Im(\omega)$ vs $k$ for those values of $\kappa$, which are depicted in figure B.2a). Notice that the modes obtained are interfacial, as the growth rate becomes neutrally stable for long waves $k = 0$. As the wavenumber is increased, we see that the flow is stable and remains this way until we reach values of $k \approx 0.6$ for $\kappa = 0.7$ and $k \approx 0.81$ for $\kappa = 0.8$, where the flow becomes unstable. The growth rate reaches a maximum value and then will decrease until flow stability is seen again.

Furthermore, the elasticity of the fluid seems to play a key role in the interfacial

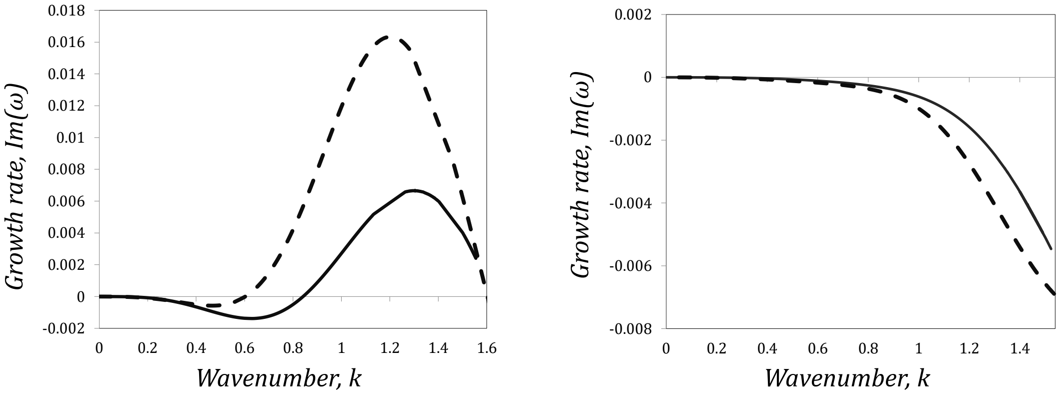

(a) Unstable flows

(b) Stable flows

Figure B.2: Dispersion relation $\Im(\omega)$ vs $k$ for sinuous modes of an Oldroyd-B fluid with polymer concentration and Weissenberg number variable. The parameter values used are: $C_1 = 0.1$ and $C_2 = 100$. For both plots, dashed lines indicate an interface location at $\kappa = 0.7$. Solid lines: $\kappa = 0.8$. Figure (a): $W_2 = 4$, $W_1 = 0.4745$ unstable modes. Figure (b): $W_2 = 1$, $W_1 = 0.1186$ stable modes.

instability. If we keep the same parameter values $C_1 = 0.1$, $C_2 = 100$ and $\kappa = [0.7, 0.8]$ fixed, and now we decrease the Weissenberg number to $W_2 = 1$, we obtain figure B.2b), and the modes are completely stable for the same range of values of $k$ where an instability is observed in B.2a).

The main conclusion here is that an interfacial instability exists indeed and is predicted by the BMP model and the Oldroyd-B model, given the proper flow conditions, i.e. a jump in the fluid viscosity at the interface, along with continuity in the first normal stress difference. However, there are still some remarkable differences between the interfacial modes shown in section 5.4.1.2 and the ones from figure B.2. For instance, for the modes predicted by the generalised BMP model (see figure 5.9), we always observe that the growth rate remains always positive, and reaches an asymptotic value for large values of wavenumber, in contrast to the modes shown in B.2. These dissimilarities might be due to model characteristics; for instance, the effect of solvent viscosity in the Oldroyd-B model in equation (B.2), which is a something that we are ignoring for the BMP model. Perhaps more important is that in the BMP model there is shear-thinning within each phase, whereas the Oldroyd-B model has constant shear viscosity.

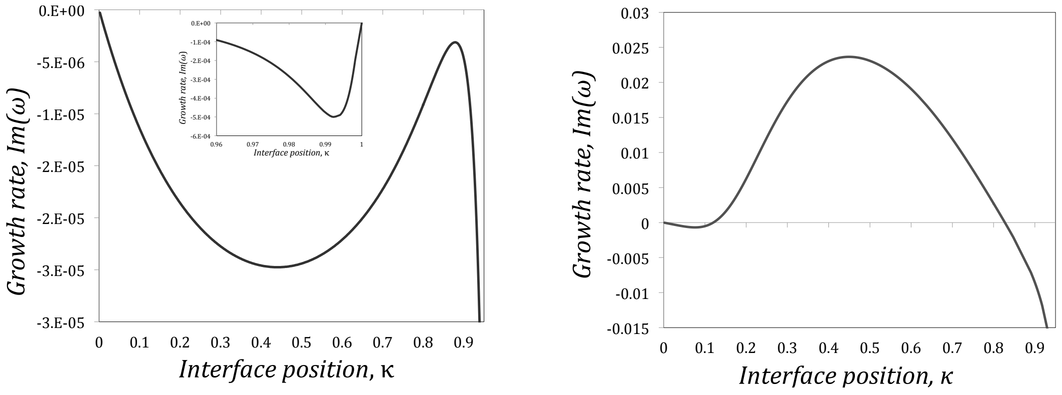

(a) $k = 0.1$

(b) $k = 1$

Figure B.3: Growth rate $\Im(\omega)$ against interface location $\kappa$ for sinuous modes, with $C_1 = 0.1$, $C_2 = 100$, and $W_2 = 4$ fixed. Figure (a): longwaves $k = 0.1$. The small plot shows the behaviour near the wall. Figure (b): $k = 1$.

In figure B.3 we show two cases of growth rate against interface position for the Oldroyd-B model. The parameter values used are the same as those from figure B.2, but here we fix the wavenumber. For long waves (figure B.3a) we can see that the flow is always stable, independently of the value of $\kappa$, and the mode is neutrally stable if there is no fluid interface within the channel ($\kappa = 0$ or $\kappa = 1$). Something similar is observed for the case $k = 1$ in figure B.3b), but the main difference with respect to the long wave case is that an instability is observed for an interval of $0.12 < \kappa < 0.81$. In the next sections, we will see that this is another difference between the modes predicted by the Oldroyd-B and the BMP model, which for the latter it is not possible for us to specify $\kappa$, and the interfacial modes will only exist for appropriate parameter values that lead to the formation of bands.

# Bibliography

[1] Nonlinear Elastic Instability in Channel Flows at Low Reynolds Numbers, author = Pan, L. and Morozov, A. and Wagner, C. and Arratia, P. E. *Phys. Rev. Lett.*, 110:174502, Apr 2013.

[2] D. Acierno, F. P. La Mantia, G. Marrucci and G. Titomanlio. A non-linear viscoelastic model with structure-dependent relaxation times: I. Basic formulation. *Journal of Non-Newtonian Fluid Mechanics*, 1(2):125–146, 1976.

[3] J. M. Adams, S. M. Fielding and P. D. Olmsted. The interplay between boundary conditions and flow geometries in shear banding: Hysteresis, band configurations, and surface transitions. *Journal of Non-Newtonian Fluid Mechanics*, 151(1-3):101–118, 2008.

[4] K. AtalIk and R. Keunings. Non-linear temporal stability analysis of viscoelastic plane channel flows using a fully-spectral method. *Journal of Non-Newtonian Fluid Mechanics*, 102(2):299–319, 2002.

[5] H. A. Barnes. Thixotropy-a review. *Journal of Non-Newtonian Fluid Mechanics*, 70(1-2):1–33, 1997.

[6] H. A. Barnes and K. Walters. The yield stress myth?. *Rheologica Acta*, 24(4):323–326, 1985.

[7] F. Bautista, J. M. De Santos, J. E. Puig and O. Manero. Understanding thixotropic and antithixotropic behavior of viscoelastic micellar solutions and

liquid crystalline dispersions. I. The model. *Journal of Non-Newtonian Fluid Mechanics*, 80(2-3):93–113, 1999.

[8] F. Bautista, J. F. A. Soltero, J. H. Pérez-López, J. E. Puig and O. Manero. On the shear banding flow of elongated micellar solutions. *Journal of Non-Newtonian Fluid Mechanics*, 94(1):57–66, 2000.

[9] L. Becu, D. Anache, S. Manneville and A. Colin. Evidence for three-dimensional unstable flows in shear-banding wormlike micelles. *Physical Review E*, 76(1):011503, 2007.

[10] J. F. Berret. Rheology of wormlike micelles: Equilibrium properties and shear banding transitions. In *Molecular Gels*, pages 667–720. Springer, 2006.

[11] J.-F. Berret, G. Porte and J.-P. Decruppe. Inhomogeneous shear flows of wormlike micelles: A master dynamic phase diagram. *Physical Review E*, 55(2):1668, 1997.

[12] J.-F. Berret, D. C. Roux, G. Porte and P. Lindner. Shear-induced isotropic-to-nematic phase transition in equilibrium polymers. *EPL (Europhysics Letters)*, 25(7):521, 1994.

[13] R. B. Bird, R. C. Armstrong and O. Hassager. *Dynamics of polymeric liquids. Vol. 1: Fluid mechanics.* John Wiley & Sons, New York, 1987.

[14] R. B. Bird, C. F. Curtis, R. C. Armstrong and O. Hassager. *Dynamics of polymeric liquids. Vol. 2: Kinetic theory.* John Wiley & Sons, New York, 1987.

[15] R. B. Bird, W. E. Stewart and E. N. Lightfoot. *Transport phenomena.* John Wiley & Sons, 1960.

[16] H. Bodiguel, J. Beaumont, A. Machado, L. Martinie and A. Kellay, H.and Colin. Flow enhancement due to elastic turbulence in channel flows of shear thinning fluids. *Physical Review Letters*, 114(2):028302, 2015.

[17] D. V. Boger. A highly elastic constant-viscosity fluid. *Journal of Non-Newtonian Fluid Mechanics*, 3(1):87–91, 1977.

[18] D. V. Boger and K. Walters. *Rheological phenomena in focus*, volume 4. Elsevier, 1993.

[19] D. Bonn, F. Ingremeau, Y. Amarouchene and H. Kellay. Large velocity fluctuations in small-Reynolds-number pipe flow of polymer solutions. *Phys. Rev. E*, 84:045301, Oct 2011.

[20] M. M. Britton and P. T. Callaghan. Two-phase shear band structures at uniform stress. *Physical Review Letters*, 78(26):4930, 1997.

[21] M. M. Britton, R. W. Mair, R. K. Lambert and P. T. Callaghan. Transition to shear banding in pipe and Couette flow of wormlike micellar solutions. *Journal of Rheology*, 43(4):897–909, 1999.

[22] F. Calderas, E. E. Herrera-Valencia, A. Sanchez-Solis, O. Manero, L. Medina-Torres, A. Renteria and G. Sanchez-Olivares. On the yield stress of complex materials. *Korea-Australia Rheology Journal*, 25(4):233–242, 2013.

[23] P. T. Callaghan, M. E. Cates, C. J. Rofe and J. B. A. F. Smeulders. A study of the "Spurt Effect" in wormlike micelles using Nuclear Magnetic Resonance Microscopy. *Journal de Physique II*, 6(3):375–393, 1996.

[24] E. Cappelaere, J. F. Berret, J. P. Decruppe, R. Cressely and P. Lindner. Rheology, birefringence, and small-angle neutron scattering in a charged micellar system: Evidence of a shear-induced phase transition. *Physical Review E*, 56(2):1869, 1997.

[25] P. J. Carreau. Rheological equations from molecular network theories [Ph. D. thesis]. *University of Wisconsin, Madison*, 1968.

[26] L. Casanellas, C. J Dimitriou, T. J. Ober and G. H. McKinley. Spatiotemporal dynamics of multiple shear-banding events for viscoelastic micellar flu-

ids in cone-plate shearing flows. *Journal of Non-Newtonian Fluid Mechanics*, 222:234–247, 2015.

[27] H. A. Castillo, J. C. Tejas, J. P. García-Sandoval, O. Matus, F. Bautista, J. E. Puig and O. Manero. Derivation of the mechanical and thermodynamic potentials from the generalized BMP model under shear-banding flow. *Journal of Non-Equilibrium Thermodynamics*, 39(4):231–248, 2014.

[28] H. A Castillo and H. J. Wilson. Towards a mechanism for instability in channel flow of highly shear-thinning viscoelastic fluids. *Journal of Non-Newtonian Fluid Mechanics*, 247:15–21, 2017.

[29] H. A. Castillo and H. J. Wilson. Elastic instabilities in pressure-driven channel flow of thixotropic-viscoelasto-plastic fluids. *Journal of Non-Newtonian Fluid Mechanics*, 261:10–24, 2018.

[30] J. Castillo-Tejas, S. Carro and O. Manero. Shear banding in telechelic associative polymers by molecular dynamics. *ACS Macro Letters*, 6(3):190–193, 2017.

[31] M. E. Cates. Reptation of living polymers: dynamics of entangled polymers in the presence of reversible chain-scission reactions. *Macromolecules*, 20(9):2289–2296, 1987.

[32] M. E. Cates and S. J. Candau. Statics and dynamics of worm-like surfactant micelles. *Journal of Physics: Condensed Matter*, 2(33):6869, 1990.

[33] M. E. Cates and S. M. Fielding. Rheology of giant micelles. *Advances in Physics*, 55(7-8):799–879, 2006.

[34] A. Chekila, C. Nouar, E. Plaut and A. Nemdili. Subcritical bifurcation of shear-thinning plane Poiseuille flows. *Journal of Fluid Mechanics*, 686:272–298, 2011.

[35] I.-J. Chen, G. E. Hagler, L. E. Abbott, D. C. Bogue and J. L. White. In-

terpretation of tensile and melt spinning experiments on low density and high density polyethylene. *Transactions of the Society of Rheology*, 16(3):473–494, 1972.

[36] K. Chen. Elastic instability of the interface in Couette flow of viscoelastic liquids. *Journal of Non-Newtonian Fluid Mechanics*, 40(2):261–267, 1991.

[37] K. Chen and D. D. Joseph. Elastic short wave instability in extrusion flows of viscoelastic liquids. *Journal of Non-Newtonian Fluid Mechanics*, 42(1-2):189–211, 1992.

[38] L. B. Chen, C. F. Zukoski, B. J. Ackerson, H. J. M. Hanley, G. C. Straty, J. Barker and C. J. Glinka. Structural changes and orientaional order in a sheared colloidal suspension. *Physical Review Letters*, 69(4):688–693, 1992.

[39] D. C. H. Cheng. The effect of secondary flow on the viscosity measurement using the cone-and-plate viscometer. *Chemical Engineering Science*, 23(8):895–899, 1968.

[40] P. Chokshi, S. Gupta, S. Yadav and A. Agrawal. Interfacial instability in two-layer Couette–Poiseuille flow of viscoelastic fluids. *Journal of Non-Newtonian Fluid Mechanics*, 224:17–29, 2015.

[41] P. Coussot. Yield stress fluid flows: A review of experimental data. *Journal of Non-Newtonian Fluid Mechanics*, 211:31–49, 2014.

[42] P. Coussot, J. S. Raynaud, F. Bertrand, P. Moucheront, J. P. Guilbaud, H. T. Huynh, S. Jarny and D. Lesueur. Coexistence of liquid and solid phases in flowing soft–glassy materials. *Physical Review Letters*, 88(21):218301, 2002.

[43] C. Craver and C. Carraher. *Applied polymer science: 21st century.* Elsevier, 2000.

[44] M. Cromer, L. P. Cook and G. H. McKinley. Interfacial instability of pressure-

driven channel flow for a two-species model of entangled wormlike micellar solutions. *Journal of Non-Newtonian Fluid Mechanics*, 166(11):566–577, 2011.

[45] C. Y. David Lu, P. D. Olmsted and R. C. Ball. Effects of nonlocal stress on the determination of shear banding flow. *Physical Review Letters*, 84(4):642–645, 2000.

[46] P.-G. de Gennes. Reptation of a polymer chain in the presence of fixed obstacles. *The Journal of Chemical Physics*, 55(2):572–579, 1971.

[47] P. R. de Souza Mendes. Thixotropic elasto-viscoplastic model for structured fluids. *Soft Matter*, 7(6):2471–2483, 2011.

[48] P. R. de Souza Mendes and R. L. Thompson. A critical overview of elasto-viscoplastic thixotropic modeling. *Journal of Non-Newtonian Fluid Mechanics*, 187:8–15, 2012.

[49] P. R. de Souza Mendes and R. L. Thompson. A unified approach to model elasto-viscoplastic thixotropic yield-stress materials and apparent yield-stress fluids. *Rheologica Acta*, 52(7):673–694, 2013.

[50] J. P. Decruppe, R. Cressely, R. Makhloufi and E. Cappelaere. Flow birefringence experiments showing a shear-banding structure in a CTAB solution. *Colloid and Polymer Science*, 273(4):346–351, 1995.

[51] M. M. Denn and J. J. Roisman. Rotational stability and measurement of normal stress functions in dilute polymer solutions. *AIChE Journal*, 15(3):454–459, 1969.

[52] P. G. Drazin and W. H. Reid. *Hydrodynamic stability*. Cambridge University Press, 1981.

[53] P. G. Drazin and W. H. Reid. *Hydrodynamic stability*. Cambridge university press, 2004.

[54] J. I. Escalante, E. R. Macias, F. Bautista, J. H. Pérez-López, J. F. A. Soltero,

J. E. Puig and O. Manero. Shear-banded flow and transient rheology of cationic wormlike micellar solutions. *Langmuir*, 19(17):6620–6626, 2003.

[55] I. D. Evans. Letter to the editor: On the nature of the yield stress. *Journal of Rheology*, 36(7):1313–1318, 1992.

[56] R. H. Ewoldt and G. H. McKinley. Mapping Thixo-Visco-Elasto-Plastic behavior. *Rheological Acta*, 256:195–210, 2017.

[57] M.-A. Fardin, L. Casanellas, B. Saint-Michel, S. Manneville and S. Lerouge. Shear-banding in wormlike micelles: Beware of elastic instabilities. *Journal of Rheology*, 60(5):917–926, 2016.

[58] M.-A. Fardin and S. Lerouge. Instabilities in wormlike micelle systems. *The European Physical Journal E*, 35(9):1–29, 2012.

[59] M.-A. Fardin, T. J. Ober, C. Gay, G. Grégoire, G. H. McKinley and S. Lerouge. Potential “ways of thinking about the shear-banding phenomenon. *Soft Matter*, 8(4):910–922, 2012.

[60] K. W. Feindel and P. T. Callaghan. Anomalous shear banding: multidimensional dynamics under fluctuating slip conditions. *Rheologica Acta*, 49(10):1003–1013, 2010.

[61] S. M. Fielding. Linear instability of planar shear banded flow. *Physical Review Letters*, 95(13):134501, 2005.

[62] S. M. Fielding. Complex dynamics of shear banded flows. *Soft Matter*, 3(10):1262–1279, 2007.

[63] S. M. Fielding. Viscoelastic Taylor-Couette instability of shear banded flow. *Physical Review Letters*, 104(19):198303, 2010.

[64] S. M. Fielding. Criterion for extensional necking instability in polymeric fluids. *Physical Review Letters*, 107(25):258301, 2011.

[65] S. M. Fielding and H. J. Wilson. Shear banding and interfacial instability in planar Poiseuille flow. *Journal of Non-Newtonian Fluid Mechanics*, 165(5-6):196–202, 2010.

[66] A. Franck. Understanding rheology of structured fluids. *Book of TA instruments*, pages 1–17, 2004.

[67] A. G. Fredrickson. A model for the thixotropy of suspensions. *AIChe journal*, 16(3):436–441, 1970.

[68] I. A. Frigaard, K. G. Paso and P. R. de Souza Mendes. Binghams model in the oil and gas industry. *Rheologica Acta*, 56(3):259–282, 2017.

[69] J. P. García-Sandoval, F. Bautista, J. E. Puig and O. Manero. The interface migration in shear-banded micellar solutions. *Rheologica Acta*, 56(9):765–778, 2017.

[70] J. P. García-Sandoval, F. Bautista, J. E. Puig and O. Manero. Inhomogeneous flow of wormlike micelles: predictions of the generalized BMP model with normal stresses. *Fluids*, 4(1):45, 2019.

[71] H. Giesekus. Die elastizität von flüssigkeiten. *Rheologica Acta*, 5(1):29–35, 1966.

[72] S. J. Haward, F. J. Galindo-Rosales, P. Ballesta and M. A. Alves. Spatiotemporal flow instabilities of wormlike micellar solutions in rectangular microchannels. *Applied Physics Letters*, 104(12):124101, 2014.

[73] M. E. Helgeson, P. A. Vasquez, E. W. Kaler and N. J. Wagner. Rheology and spatially resolved structure of cetyltrimethylammonium bromide wormlike micelles through the shear banding transition. *Journal of Rheology*, 53(3):727–756, 2009.

[74] M. Hellsten. Drag-reducing surfactants. *Journal of Surfactants and Detergents*, 5(1):65–70, 2002.

[75] E. J. Hemingway and S. M. Fielding. Edge-induced shear banding in entangled polymeric fluids. *Physical Review Letters*, 120(13):138002, 2018.

[76] E. J. Hemingway and S. M. Fielding. Edge fracture of entangled polymeric fluids: onset criterion and possible mitigation strategy. *arXiv preprint arXiv:1903.02037 [cond-mat.soft]*, 2019.

[77] E. J. Hemingway, H. Kusumaatmaja and S. M. Fielding. Edge fracture in complex fluids. *Physical review letters*, 119(2):028006, 2017.

[78] E. E. Herrera-Valencia, F. Calderas, L. Medina-Torres, M. Pérez-Camacho, L. Moreno and O. Manero. On the pulsating flow behavior of a biological fluid: human blood. *Rheologica Acta*, 56(4):387–407, 2017.

[79] G. Heuser and E. Krause. The flow field of Newtonian fluids in cone and plate viscometers with small gap angles. *Rheologica Acta*, 18(5):553–564, 1979.

[80] E. J. Hinch, O. J. Harris and J. M. Rallison. The instability mechanism for two elastic liquids being co-extruded. *Journal of Non-Newtonian Fluid Mechanics*, 43(2-3):311–324, 1992.

[81] T. C. Ho and M. M. Denn. Stability of plane Poiseuille flow of a highly elastic liquid. *Journal of Non-Newtonian Fluid Mechanics*, 3(2):179–195, 1977.

[82] W. M. Holmes, M. R. Lopez-Gonzalez and P. T. Callaghan. Fluctuations in shear-banded flow seen by NMR velocimetry. *Europhysics Letters*, 64(2):274, 2003.

[83] P. Huerre, M. Rossi, C. Godrèche and P. Manneville. Hydrodynamics and nonlinear instabilities. *Aléa Saclay*, pages 81–386, 1998.

[84] J. F. Hutton. Fracture and secondary flow of elastic liquids. *Rheologica Acta*, 8(1):54–59, 1969.

[85] K. P. Jackson, K. Walters and R. W. Williams. A rheometrical study of boger fluids. *Journal of Non-Newtonian Fluid Mechanics*, 14:173–188, 1984.

[86] S. Jeong, J. M. Kim and C. Baig. Molecular characteristics of stress overshoot for polymer melts under start-up shear flow. *The Journal of Chemical Physics*, 147(23):234901, 2017.

[87] M. W. Johnson Jr and D. Segalman. A model for viscoelastic fluid behavior which allows non-affine deformation. *Journal of Non-Newtonian Fluid Mechanics*, 2(3):255–270, 1977.

[88] B. Khomami. Interfacial stability and deformation of two stratified power law fluids in plane Poiseuille flow Part I. Stability analysis. *Journal of Non-Newtonian Fluid Mechanics*, 36:289–303, 1990.

[89] B. Khomami and M. M. Ranjbaran. Experimental studies of interfacial instabilities in multilayer pressure-driven flow of polymeric melts. *Rheologica Acta*, 36(4):345–366, 1997.

[90] Y. Kim, A. Adams, W. H. Hartt, R. G. Larson and M. J. Solomon. Transient, near-wall shear-band dynamics in channel flow of wormlike micelle solutions. *Journal of Non-Newtonian Fluid Mechanics*, 232:77–87, 2016.

[91] W.-M. Kulicke, H.-E. Jeberien, H. Kiss and R. S. Porter. Visual observation of flow irregularities in polymer solutions at theta-conditions. *Rheologica Acta*, 18(6):711–716, 1979.

[92] W. M. Kulicke and R. S. Porter. Irregularities in steady flow for non-newtonian fluids between cone and plate. *Journal of Applied Polymer Science*, 23(4):953–965, 1979.

[93] W.-M. Kulicke and U. Wallbaum. Determination of first and second normal stress differences in polymer solutions in steady shear flow and limitations caused by flow irregularities. *Chemical engineering science*, 40(6):961–972, 1985.

[94] R. G. Larson. A constitutive equation for polymer melts based on partially extending strand convection. *Journal of Rheology*, 28(5):545–571, 1984.

[95] R. G. Larson. *Constitutive equations for polymer melts and solutions.* Elsevier, 1988.

[96] R. G. Larson. Instabilities in viscoelastic flows. *Rheologica Acta*, 31(3):213–263, 1992.

[97] R. G. Larson. The structure and rheology of complex fluids (topics in chemical engineering). *Oxford University Press, New York, Oxford*, 86:108, 1999.

[98] R. G. Larson. Constitutive equations for thixotropic fluids. *Journal of Rheology*, 59(3):595–611, 2015.

[99] R. G. Larson, S. J. Muller and E. S. G. Shaqfeh. The effect of fluid rheology on the elastic Taylor-Couette instability. *Journal of Non-Newtonian Fluid Mechanics*, 51(2):195–225, 1994.

[100] R. G. Larson, E. S. G. Shaqfeh and S. J. Muller. A purely elastic instability in Taylor–Couette flow. *Journal of Fluid Mechanics*, 218:573–600, 1990.

[101] H. M. Laun. Description of the non-linear shear behaviour of a low density polyethylene melt by means of an experimentally determined strain dependent memory function. *Rheologica Acta*, 17(1):1–15, 1978.

[102] B.-L. Lee and J. L. White. An experimental study of rheological properties of polymer melts in laminar shear flow and of interface deformation and its mechanisms in two-phase stratified flow. *Transactions of the Society of Rheology*, 18(3):467–492, 1974.

[103] C.-S. Lee, B. C. Tripp and J. J. Magda. Does N1 or N2 control the onset of edge fracture? *Rheologica acta*, 31(3):306–308, 1992.

[104] S. Lerouge, M. Argentina and J.-P. Decruppe. Interface instability in shear-banding flow. *Physical Review Letters*, 96(8):088301, 2006.

[105] M. P. Lettinga and S. Manneville. Competition between shear banding and wall slip in wormlike micelles. *Physical Review Letters*, 103(24):248302, 2009.

[106] M. R. López-González, W. M. Holmes and P. T. Callaghan. Rheo-NMR phenomena of wormlike micelles. *Soft Matter*, 2(10):855–869, 2006.

[107] M. R. López-González, W. M. Holmes, P. T. Callaghan and P. J. Photinos. Shear banding fluctuations and nematic order in wormlike micelles. *Physical Review Letters*, 93(26):268302, 2004.

[108] C. W. Macosko. *Rheology: principles, measurements, and applications.* Vch New York, 1994.

[109] J. J. Magda and R. G. Larson. A transition occurring in ideal elastic liquids during shear flow. *Journal of Non-Newtonian Fluid Mechanics*, 30(1):1–19, 1988.

[110] R. W. Mair and P. T. Callaghan. Observation of shear banding in worm-like micelles by NMR velocity imaging. *EPL (Europhysics Letters)*, 36(9):719, 1996.

[111] O. Manero, J. H. Pérez-López, J. I. Escalante, J. E. Puig and F. Bautista. A thermodynamic approach to rheology of complex fluids: The generalized bmp model. *Journal of Non-Newtonian Fluid Mechanics*, 146(1-3):22–29, 2007.

[112] S. Manneville, L. Bécu and A. Colin. High-frequency ultrasonic speckle velocimetry in sheared complex fluids. *The European Physical Journal-Applied Physics*, 28(3):361–373, 2004.

[113] G. H. McKinley, J. A. Byars, R. A. Brown and R. C. Armstrong. Observations on the elastic instability in cone-and-plate and parallel-plate flows of a polyisobutylene Boger fluid. *Journal of Non-Newtonian Fluid Mechanics*, 40(2):201–229, 1991.

[114] G. H. Mckinley, A. Öztekin, J. A. Byars and R. A. Brown. Self-similar spiral

instabilities in elastic flows between a cone and a plate. *Journal of Fluid Mechanics*, 285:123–164, 1995.

[115] G. H. McKinley, P. Pakdel and A. Öztekin. Rheological and geometric scaling of purely elastic flow instabilities. *Journal of Non-Newtonian Fluid Mechanics*, 67:19–47, 1996.

[116] E. V. Menezes and W. W. Graessley. Nonlinear rheological behavior of polymer systems for several shear-flow histories. *Journal of Polymer Science: Polymer Physics Edition*, 20(10):1817–1833, 1982.

[117] B. Meulenbroek, C. Storm, A. N. Morozov and W. van Saarloos. Weakly nonlinear subcritical instability of visco-elastic Poiseuille flow. *Journal of Non-Newtonian Fluid Mechanics*, 116(2-3):235–268, 2004.

[118] J. Mewis and N. J. Wagner. *Colloidal suspension rheology.* Cambridge University Press, 2012.

[119] J. C. Miller and J. M. Rallison. Instability of coextruded elastic liquids at high Weissenberg number. *Journal of Non-Newtonian Fluid Mechanics*, 143(2-3):88–106, 2007.

[120] J. C. Miller and J. M. Rallison. Interfacial instability between sheared elastic liquids in a channel. *Journal of Non-Newtonian Fluid Mechanics*, 143(2-3):71–87, 2007.

[121] J. C. Miller and J. M. Rallison. Interfacial instability between sheared elastic liquids in a channel. *Journal of Non-Newtonian Fluid Mechanics*, 143(2-3):71–87, 2007.

[122] W. Minoshima and J. L. White. Instability phenomena in tubular film, and melt spinning of rheologically characterized high density, low density and linear low density polyethylenes. *Journal of Non-Newtonian Fluid Mechanics*, 19(3):275–302, 1986.

[123] H. Mohammadigoushki and S. J. Muller. A flow visualization and superposition rheology study of shear-banding wormlike micelle solutions. *Soft Matter*, 12(4):1051–1061, 2016.

[124] F. Moore. The rheology of ceramic slip and bodies. *Trans. Brit. Ceram. Soc.*, 58:470–492, 1959.

[125] A. Moriel and E. Bouchbinder. Necking instabilities in elastoviscoplastic materials. *Physical Review Materials*, 2(7):073602, 2018.

[126] A. Morozov and W. van Saarloos. Subcritical instabilities in plane Poiseuille flow of an Oldroyd-B fluid. *Journal of Statistical Physics*, pages 1–24, 2018.

[127] A. N. Morozov and W. van Saarloos. Subcritical finite-amplitude solutions for plane Couette flow of viscoelastic fluids. *Physical Review Letters*, 95(2):024501, 2005.

[128] F. A. Morrison. *Understanding rheology.* Oxford University Press, New York, 2001.

[129] A. Mujumdar, A. N. Beris and A. B. Metzner. Transient phenomena in thixotropic systems. *Journal of Non-Newtonian Fluid Mechanics*, 102(2):157–178, 2002.

[130] S. J. Muller. Elastically-influenced instabilities in Taylor-Couette and other flows with curved streamlines: a review. *Korea-Australia Rheology Journal*, 20(3):117–125, 2008.

[131] S. J. Muller, R. G. Larson and E. S. G. Shaqfeh. A purely elastic transition in Taylor-Couette flow. *Rheologica Acta*, 28(6):499–503, 1989.

[132] P. Nghe, S. M. Fielding, P. Tabeling and A. Ajdari. Interfacially driven instability in the microchannel flow of a shear-banding fluid. *Physical Review Letters*, 104(24):248303, 2010.

[133] A. Nicolas and A. Morozov. Nonaxisymmetric instability of shear-banded Taylor-Couette flow. *Physical Review Letters*, 108(8):088302, 2012.

[134] C. Nouar, A. Bottaro and J. P. Brancher. Delaying transition to turbulence in channel flow: revisiting the stability of shear-thinning fluids. *Journal of Fluid Mechanics*, 592:177–194, 2007.

[135] C. Nouar and I. Frigaard. Stability of plane Couette–Poiseuille flow of shear-thinning fluid. *Physics of Fluids*, 21(6):064104, 2009.

[136] D. O. Olagunju. Elastic instabilities in cone-and-plate flow: small gap theory. *Zeitschrift für angewandte Mathematik und Physik ZAMP*, 46(6):946–959, 1995.

[137] J. G. Oldroyd. On the formulation of rheological equations of state. *Proceedings of the Royal Society of London. Series A. Mathematical and Physical Sciences*, 200(1063):523–541, 1950.

[138] A. Öztekin and R. A. Brown. Instability of a viscoelastic fluid between rotating parallel disks: analysis for the Oldroyd-B fluid. *Journal of Fluid Mechanics*, 255:473–502, 1993.

[139] A. Öztekin, R. A. Brown and G. H. McKinley. Quantitative prediction of the viscoelastic instability in cone-and-plate flow of a Boger fluid using a multi-mode Giesekus model. *Journal of Non-Newtonian Fluid Mechanics*, 54:351–377, 1994.

[140] P. Pakdel and G. H. McKinley. Elastic instability and curved streamlines. *Physical Review Letters*, 77(12):2459–2462, 1996.

[141] J. Peng and K.-Q. Zhu. Instability of the interface in co-extrusion flow of two UCM fluids in the presence of surfactant. *Journal of Non-Newtonian Fluid Mechanics*, 166(1-2):152–163, 2011.

[142] C. Perge, M.-A. Fardin and S. Manneville. Surfactant micelles: Model sys-

tems for flow instabilities of complex fluids. *The European Physical Journal E*, 37(4):23, 2014.

[143] C. J. S. Petrie and M. M. Denn. Instabilities in polymer processing. *AIChE Journal*, 22(2):209–236, 1976.

[144] L. Picaut, O. Ronsin, C. Caroli and T. Baumberger. Experimental evidence of a helical, supercritical instability in pipe flow of shear thinning fluids. *Physical Review Fluids*, 2(8):083303, 2017.

[145] C. J. Pipe, N. J. Kim, P. A. Vasquez, L. P. Cook and G. H. McKinley. Wormlike micellar solutions: II. Comparison between experimental data and scission model predictions. *Journal of Rheology*, 54(4):881–913, 2010.

[146] R. J. Poole. The Deborah and Weissenberg numbers. *The British Society of Rheology. Rheology Bulletin*, 53:32–39, 2012.

[147] R. J. Poole. Elastic instabilities in parallel shear flows of a viscoelastic shear-thinning liquid. *Physical Review Fluids*, 1(4):041301, 2016.

[148] C. Pujolle-Robic and L. Noirez. Observation of shear-induced nematic–isotropic transition in side-chain liquid crystal polymers. *Nature*, 409(6817):167–171, 2001.

[149] Boyang Qin and Paulo E Arratia. Characterizing elastic turbulence in channel flows at low Reynolds number. *Physical Review Fluids*, 2(8):083302, 2017.

[150] M. Reiner. The Deborah number. *Physics today*, 17(1):62, 1964.

[151] M. Renardy. The mathematics of myth: Yield stress behavior as a limit of non-monotone constitutive theories. *Journal of Non-Newtonian Fluid Mechanics*, 165(9-10):519–526, 2010.

[152] Y. Renardy. The thin-layer effect and interfacial stability in a two-layer Couette flow with similar liquids. *The Physics of Fluids*, 30(6):1627–1637, 1987.

[153] Y. Renardy. Stability of the interface in two-layer Couette flow of upper convected Maxwell liquids. *Journal of Non-Newtonian Fluid Mechanics*, 28(1):99–115, 1988.

[154] Y. Renardy and M. Renardy. Stability of shear banded flow for a viscoelastic constitutive model with thixotropic yield stress behavior. *Journal of Non-Newtonian Fluid Mechanics*, 244:57–74, 2017.

[155] L. D. Rhein, M. Schlossman, A. O'Lenick and P. Somasundaran. *Surfactants in personal care products and decorative cosmetics*, volume 135. crc press, 2007.

[156] M. J. Rosen and M. Dahanayake. *Industrial utilization of surfactants: principles and practice.* American Oil Chemists' Society, 2000.

[157] R. Seto, G. G. Giusteri and A. Martiniello. Microstructure and thickening of dense suspensions under extensional and shear flows. *Journal of Fluid Mechanics*, 825, 2017.

[158] E. S. G. Shaqfeh. Purely elastic instabilities in viscometric flows. *Annual Review of Fluid Mechanics*, 28(1):129–185, 1996.

[159] E. S. G. Shaqfeh, S. J. Muller and R. G. Larson. The effects of gap width and dilute solution properties on the viscoelastic Taylor-Couette instability. *Journal of Fluid Mechanics*, 235:285–317, 1992.

[160] S. E. Spagnolie. *Complex fluids in biological systems: experiment, theory, and computation*, volume 6. 2015.

[161] J. Sprakel, E. Spruijt, M. A. Stuart Cohen, N. A. M. Besseling, M. P. Lettinga and J. Van Der Gucht. Shear banding and rheochaos in associative polymer networks. *Soft Matter*, 4(8):1696–1705, 2008.

[162] Z.-S. Sun and M. M. Denn. Stability of rotational couette flow of polymer solutions. *AIChE Journal*, 18(5):1010–1015, 1972.

[163] R. Sureshkumar and A.N. Beris. Linear stability analysis of viscoelastic

Poiseuille flow using an Arnoldi-based orthogonalization algorithm. *Journal of Non-Newtonian Fluid Mechanics*, 56(2):151–182, 1995.

[164] R. I. Tanner. *Engineering Rheology.* Oxford Press, New York, 1985.

[165] R. I. Tanner and M. Keentok. Shear fracture in cone-plate rheometry. *Journal of Rheology*, 27(1):47–57, 1983.

[166] R. I. Tanner and M. Keentok. Shear fracture in cone-plate rheometry. *Journal of Rheology*, 27(1):47–57, 1983.

[167] G. I. Taylor. Stability of a viscous liquid contained between two rotating cylinders. *Philosophical Transactions of the Royal Society of London. Series A.*, 223(605-615):289–343, 1923.

[168] A. K. Townsend and H. J. Wilson. The fluid dynamics of the chocolate fountain. *European Journal of Physics*, 37(1):015803, 2015.

[169] P. A . Vasquez, G. H. McKinley and L. P. Cook. A network scission model for wormlike micellar solutions: I. Model formulation and viscometric flow predictions. *Journal of Non-Newtonian Fluid Mechanics*, 144(2-3):122–139, 2007.

[170] L. M. Walker. Rheology and structure of worm-like micelles. *Current opinion in colloid and interface science*, 6(5-6):451–456, 2001.

[171] N. D. Waters and A. M. Keeley. The stability of two stratified non-Newtonian liquids in Couette flow. *Journal of Non-Newtonian Fluid Mechanics*, 24(2):161–181, 1987.

[172] K. Weissenberg. Proceedings. *First International Rheological Congress. North-Holland, Amsterdam*, 1:29, 1949.

[173] G. M. Wilson and B. Khomami. An experimental investigation of interfacial instabilities in multilayer flow of viscoelastic fluids: Part I. Incompatible polymer systems. *Journal of Non-Newtonian Fluid Mechanics*, 45(3):355–384, 1992.

[174] H. J. Wilson. *Shear flow instabilities in viscoelastic fluids.* PhD thesis, University of Cambridge, 1998.

[175] H. J. Wilson. Instabilities and constitutive modelling. *Philosophical Transactions of the Royal Society A: Mathematical, Physical and Engineering Sciences*, 364(1849):3267–3283, 2006.

[176] H. J. Wilson. Shear thickening in non-shear flows: the effect of microstructure. *Journal of Fluid Mechanics*, 836:1–4, 2018.

[177] H. J. Wilson and S. M. Fielding. Linear instability of planar shear banded flow of both diffusive and non-diffusive Johnson–Segalman fluids. *Journal of Non-Newtonian Fluid Mechanics*, 138(2-3):181–196, 2006.

[178] H. J. Wilson and V. Loridan. Linear instability of a highly shear-thinning fluid in channel flow. *Journal of Non-Newtonian Fluid Mechanics*, 223:200–208, 2015.

[179] H. J. Wilson and J. M. Rallison. Short wave instability of co-extruded elastic liquids with matched viscosities. *Journal of Non-Newtonian Fluid Mechanics*, 72(2-3):237–251, 1997.

[180] H. J. Wilson and J. M. Rallison. Instability of channel flow of a shear-thinning White–Metzner fluid. *Journal of Non-Newtonian Fluid Mechanics*, 87(1):75–96, 1999.

[181] H. J. Wilson and J. M. Rallison. Instability of channel flows of elastic liquids having continuously stratified properties. *Journal of Non-Newtonian Fluid Mechanics*, 85(2-3):273–298, 1999.

[182] H. J. Wilson, M. Renardy and Y. Renardy. Structure of the spectrum in zero Reynolds number shear flow of the UCM and Oldroyd-B liquids. *Journal of Non-Newtonian Fluid Mechanics*, 80(2-3):251–268, 1999.

[183] M. Wyart and M. E. Cates. Discontinuous shear thickening without inertia

in dense non-Brownian suspensions. *Physical Review Letters*, 112(9):098302, 2014.

[184] T. Yamamoto, T. Hashimoto and A. Yamashita. Flow analysis for wormlike micellar solutions in an axisymmetric capillary channel. *Rheologica Acta*, 47(9):963–974, 2008.

[185] K. Y. Yasuda, R. C. Armstrong and R. E. Cohen. Shear flow properties of concentrated solutions of linear and star branched polystyrenes. *Rheologica Acta*, 20(2):163–178, 1981.

[186] C.-S. Yih. Instability due to viscosity stratification. *Journal of Fluid Mechanics*, 27(2):337–352, 1967.

[187] A. Ziabicki and R. Takserman-Krozer. Mechanism of breakage of liquid threads. *Kolloid-Zeitschrift und Zeitschrift für Polymere*, 198(1-2):60–65, 1964.